Ionic currents and intrinsic properties of key interneurons and their influence on network activity in a chain of coupled oscillators

Inaugural – Dissertation

zur Erlangung des Doktorgrades

der Mathematisch-Naturwissenschaftlichen Fakultät

der Universität zu Köln

vorgelegt von

Laura Schläger

aus Starnberg

Köln, 2018

Berichterstatter/in: Dr. Carmen Wellmann

Prof. Dr. Ansgar Büschges

Tag der mündlichen Prüfung: 03.09.2018

Content

Zusammenfassung

Der Post-Inhibitorische Rebound (PIR) stellt einen essentiellen Mechanismus in der Generierung rhythmischer Aktivitäten von neuronalen Netzwerken dar. Erzeugt durch eine Phase hemmender Eingänge, kann dieser Mechanismus neue neuronale Erregung erzeugen und fördert daher, zellautonom, rhythmische Aktivität. In dieser Arbeit habe ich den Mechanismus des PIRs im Zusammenhang mit rhythmischer Bewegung der vier Schwimmbeinpaare am Flusskrebs untersucht. Das neuronale Netzwerk welches die sehr gleichmäßige und koordinierte Schwimmbeinbewegung erzeugt ist weitestgehend identifiziert. Des Weiteren ist bekannt, dass alle Neurone die bei der Generierung dieser Bewegung involviert sind, ein ähnliches Aktivitätsmuster zeigen. Das Membranpotential aller dieser Neurone oszilliert in der gleichen Frequenz wie die Beinbewegung. Es ist daher davon auszugehen, dass die Generierung dieser Oszillationen ein wichtiges Phänomen für den Erhalt der rhythmischen Schwimmbeinbewegung darstellt. Es ist jedoch nicht bekannt ob und in wie fern zellulären Eigenschaften, wie z. B. ein PIR, an der Generierung beteiligt sind. Um dies zu untersuchen habe ich das abdominale Nervensystem isoliert und intrazelluläre Ableitungen an den Neuronen, welche bewiesenermaßen die Schwimmbeinbewegung generieren und koordinieren, durchgeführt. Um einen PIR zu erzeugen wurden die Neurone durch eine negative Strominjektion für 3 Sekunden hyperpolarisiert. Dies induzierte in fast allen Neuronen, die hemmende synaptische Eingänge erhalten, ein „sag-Potential“ während der Stimulation und anschließend einen PIR. Dies waren sowohl zwei exzitatorische Gruppen von Motoneuronen, Power Stroke Erreger (PSE) und Return Stroke Erreger (RSE), als auch die koordinierenden Neurone, das Aszendierende- (ASC_E) und das Deszendierende Koordinierende Neuron (DSC). Im Gegensatz dazu wurde nicht in allen der untersuchten Neurone des Zentralen Mustergenerators (CPG), die Inhibitoren des Power Stroke (IPS), ein PIR erzeugt. In jenen IPS jedoch die einen PIR erzeugten, konnte ein Einfluss des Halte-Membran Potentials auf die Größe des PIR erkannt werden. In einer weiteren Neuron Gruppe, dem Kommissuralen Interneuron 1 (ComInt1), welches erregende synaptische Eingänge bekommt, konnte unerwarteter Weise auch ein PIR erzeugt werden.

Im weiteren Verlauf der Experimente erforschte ich welche Ionenströme der Generierung der beobachteten PIRs zugrunde liegen. Dabei untersuchte ich

klassische Ionenströme welche in anderen Nervensystemen an der Generierung von PIRs beteiligt sind. Dies sind der L-typ Calciumstrom (I_{CaL}), der hyperpolarisiert-aktivierte Kationenstrom (I_H) als auch der persistierende Natriumstrom (I_{NaP}).

Bei einer Hemmung von I_{CaL} durch Applikation des bekannten Antagonisten Nifedipin, konnte eine Zunahme des PIR in 13 von 21 aktionspotential-generierenden Neuronen beobachtet werden. Der PIR in den übrigen 8 Neuronen wurde durch die Hemmung von I_{CaL} reduziert. Der PIR des CPG Neurons, IPS, wurde nicht durch Nifedipin beeinflusst. Bei einer anschließenden Zugabe eines bekannten Antagonisten von I_H, Zd7288, reduzierte sich der PIR in allen Motorneuronen, IPS wie auch in 4 ASC_Es. In den übrigen ASC_Es und DSCs konnte die Hemmung von I_H den induzierten PIR nicht reduzieren. Dies wurde jedoch erreicht als I_{NaP} durch die Hinzugabe von Riluzole, geblockt wurde.

Um die Bedeutung der identifizierten Ionenströme für die Generierung dieser Aktivitätsmuster zu verifizieren, wurden die oben beschriebenen Ionenkanalblocker einzeln, während rhythmischer Motoraktivität, appliziert. Dabei wurden sowohl die Aktivitäten einzelner Neurone, die Koordination zwischen den Segmenten als auch die Rhythmus-Eigenschaften des gesamten Netzwerkes analysiert. Hemmung von allen vorherigen Ionenströmen (I_{CaL}, I_H, I_{NaP}), sowie eines transienten Auswärtsstroms I_A durch 4-AP, hatte weitreichende Effekte auf die Rhythmusgenerierung. Ein Effekt auf die intersegmentale Koordination konnte bei einer Hemmung von I_H, I_{NaP} und I_A beobachtet werden. Während die Blockierung von I_{CaL}, I_H, und I_A ebenfalls eine Reduzierung der Aktionspotential Weiterleitungsgeschwindigkeit verursachte.

Die beschriebenen Ergebnisse zeigen, dass der PIR einen wichtigen Mechanismus der Neurone im Schwimmbeinsystem des Flusskrebses darstellt. Hervorgerufen durch unterschiedliche Ionenströme, induziert der PIR neue neuronale Erregung welche wahrscheinlich essentiell für rhythmische Aktivitätsmuster der Neurone ist.

Abstract

Post-inhibitory rebound (PIR) plays an important role in producing rhythmic network activity. By inducing new excitation, following a phase of inhibition it promotes generation of rhythmic cellular activity. I investigated this property in identified neurons of the swimmeret system. These neurons are characterized by membrane potential oscillations and account for the well-coordinated generation of Power- and Return-Stroke movements of four pairs of pleopods (swimmerets) at the abdomen of crayfish. I isolated the abdominal nervous system and performed current clamp recordings with sharp electrodes at the dendritic aborizations of the neurons. To induce a PIR, hyperpolarizing current pulses at different holding potentials and with different amplitudes were applied. All spiking neurons that are known to receive inhibitory synaptic input possessed the ability to produce a PIR, which was accompanied by a small sag potential during the hyperpolarization. These are the Coordinating Neurons, Ascending Coordinating Neuron ($ASC_{E)}$ and Descending Coordinating Neuron (DSC) and the motor neurons Power Stroke Exciter (PSE) and Return Stroke Exciter (RSE). In contrast, not all neurons of the central pattern generator (CPG), Inhibitor of Power Stroke (IPS), generated rebound responses when being released from hyperpolarizing current injections. PIR rebounds elicited in IPS, depended on the holding potentials. This was contrary to the spiking neurons, which were not affected by changes in holding potentials.

One neuron in the swimmeret system, the Commissural Interneuron1 (ComInt1), which is characterized solely by excitatory synaptic input, and was therefore not expected to have a PIR, also showed the ability to produce one.

Different ionic currents are shown in various studies to account for the generation of a PIR. Those are the L-type calcium current (I_{CaL}), the hyperpolarization activated cation current (I_H), and in some systems the persistent sodium current (I_{NaP}). In the following experiments, I investigated the ionic basis of the PIR in the above described neuron groups of the swimmeret system.

Blocking I_{CaL}, by applying the channel antagonist Nifedipine, increased PIR responses in 13 of 21 spiking neurons, while there was no effect on PIR in IPS. In the remaining spiking neurons blocking I_{CaL} reduced PIR responses. In all MNs, IPS, as well as in 4 ASC_Es the subsequent block of I_H completely suppressed all PIR

responses. Blocking I_H failed to abolish PIRs in two ASC_Es and two DSCs. The remaining PIR responses in those Coordinating Neurons were either abolished or reduced when blocking I_{NaP} by additional treatment with Riluzole.

To test the significance of the identified ionic conductances for generation of rhythmic motor output, I blocked the respective ionic currents individually while monitoring fictive locomotion of the system on the network-, as well as on the single cell level. During this series of experiments also the contribution of the transient potassium current, I_A, was investigated by application of 4-AP. Confirming the importance of the above identified currents (I_{CaL}, I_H and I_{NaP}), all ion channel blockers altered the ability of the entire system to produce a steady motor rhythm. Similar strong effects were observed when blocking I_A.

These results of this study demonstrate that PIR is an essential mechanism for the neurons in the swimmeret system to induce new excitability after a phase of inhibition. This suggests that PIR plays a crucial role in establishing rhythmic cellular activity. Furthermore, I could show that PIR responses were mediated by different ionic current depending on the neuron group.

1. Introduction

Escaping predators-, or rivals, seeking new food sources or mating partners, the ability to locomote is essential for every organism to survive. During all modes of locomotion the muscle synergies, controlled by the central nervous system, perform rhythmically reoccurring cycles of activities. To ensure functional motor output the rhythmic activity patterns controlling individual limb movements need to be precisely controlled, but, additionally, coordinated with other limbs, similarly taking part during the same process of locomotion. Thereby, biophysical properties of the neurons involved in the induction, coordinating, and execution of rhythmic motor commands are of tremendous importance. Such properties like ionic conductances, as principal creators of single neuronal activities need to be precisely regulated. Therefore, when trying to unveil how the nervous system generates behaviors, like locomotion, it is essential to identify the underlying ionic conductances.

1.1 Central mechanisms for rhythm generation and coordination

Great progress has been made to discover the neuronal networks behind the generation of motor commands. Much of this progress has been achieved by work on lower vertebrates and invertebrate nervous systems. With their characteristics small number of participating neurons essential elements for the generation of functional motor output were identified (Johnston and Levine, 1996; Skinner and Mulloney, 1998; Stein, 2008; Wallén and Williams, 1984). In particular, small neuronal networks were detected that tightly control rhythmically occurring movements without the need of sensory information or central drive from higher brain regions (Bucher, 2009; Büschges et al., 1995). In the swimmeret system, for example, interneurons were identified that generate rhythmic activity of antagonistic muscles during swimming. More precisely, it was shown that two groups of interneurons in each hemi segment mutual inhibit each other to induce alternating activity of the corresponding motor neurons (MNs) (Heitler and Pearson, 1980). Such micro circuits, generating organized and repetitive motor patterns are called central pattern generators (CPGs) (Marder et al., 2005). Some of the best understood rhythm generating neuronal networks for locomotion are those, driving crayfish swimmeret beating (Mulloney and Smarandache-Wellmann, 2012), leech- (Kristan and Calabrese, 1976), lamprey- (Cohen and Wallén, 1980; Grillner, 2003) and tritonia swimming (Getting et al., 1980;

Sakurai and Katz, 2009), stick insect walking (Büschges, 2012), and locust flight (Ramirez and Pearson, 1993).

Critical factors for the generation of rhythmic neuronal network activities are synaptic transmissions that promote the expression of intrinsic electrical properties in postsynaptic neurons. Such intrinsic electrical properties are able to shape the final form of neuronal output. For example, spike frequency adaptation intrinsically reduces the activity of a neuron by reducing the instantaneous spike frequency during prolonged excitation (el Manira et al., 1994). Thereby, this process can ultimately result in the termination of a burst of action potentials (APs). On the other hand different membrane properties can increase the excitation of a neuron. In some neurons, brief depolarizing stimuli elicit the generation of plateau potentials. In crayfish, plateau potentials of abdominal stretch receptor neurons have the characteristic to outlast the duration of the stimulus, which in turn result in stronger transmitter release to the postsynaptic neuron (Barrio et al., 1991). Another membrane property, that is particularly important for the activity pattern of CPGs based on mutual inhibition, is the post-inhibitory rebound (PIR). This property evokes a depolarization of the membrane potential, elicited by prior hyperpolarizing stimuli (Friesen, 1994). Thereby, it serves as a mechanism to escape from inhibitory synaptic input. The PIR has been shown to be of particular importance for rhythmically active neurons (Angstadt et al., 2005; Ascoli et al., 2010; Bertrand and Cazalets, 1998; Wang et al., 2011).

All neurons that are part of a rhythmically active neuronal network express one or several of these intrinsic properties. Thereby, in addition to CPG neurons, MNs, transmitting information about motor commands to the muscles, but also neurons responsible for the correct coordination of different CPGs rely on such properties.

The latter are of particular importance to establish a functional motor output. Moving body segments or limbs can be only properly coordinated to achieve different kinds of synchronicity if rhythm generating networks “talk to one another”. The mechanism for the coordination of CPGs has been thoroughly investigated in terrestrial as well as aquatic living systems. However, the cellular basis for coordination is fairly understood in most systems. In terrestrial living animals, like the stick insect for example, intersegmental coordination primarily relies on sensory information, while central coupling between CPG networks are rather week (Borgmann et al., 2007,

2012; Büschges and Gruhn, 2007; Büschges et al., 1995; Mantziaris et al., 2017). Similar high importance of sensory feedback for intersegmental coordination has been found in the locust (Macmillan and Kien, 1983) and cat (Andersson et al., 1978; Conway et al., 1987).

In aquatically living systems, the analysis of the central network architecture is facilitated, given the homogeneous environment and thereby the resulting minor role of sensory information. In the leech, intersegmental projection neurons, spanning asymmetrically through several body segments, have been identified to be essential for the proper induction of antiphasic dorsal and ventral muscle contractions during swimming (Brodfuehrer et al., 1995; Friesen, 1989). Forward movement of the lamprey on the other hand, is produced by alternating muscle contractions between the two body sides (Wallén and Williams, 1984). Intersegmental coupling, through ascending and descending fibers, is believed to produces the caudally propagating undulatory wave that propels the animal forward (Cohen et al., 1992; Dale, 1986; Guan et al., 2001). This is supported by a gradient of excitability from caudal to rostral, which is reversed, when the animal swims backwards (Matsushima and Grillner, 1992). However, the exact neuronal network establishing rhythm generation and coordination of segments has not been identified.

Although, plenty of research has been done to unveil the mechanisms of rhythm generation and coordination in many systems, the sheer complexity of most nervous systems obstructs its understanding to its full capacity. Only if all neurons responsible for rhythm generation, coordination, and execution of motor commands can be identified, and their different tasks properly assigned, the important biophysical properties that are crucial for neuronal activity, can be unveiled. Only hereby a full understanding can be gained of how the nervous system generates behaviors.

1.2 The swimmeret system of the crayfish

The abdominal nervous system of the crayfish contains neuronal networks, in which all cellular components mediating rhythm generation and intersegmental coordination for locomotion are identified. This network generates rhythmic beating of four pairs of swimmerets that are used for forward thrust of the animal through the water. The activity happens in a strictly coordinated manner. All pairs of swimmerets move

synchronously in a metachronal wave from posterior to anterior during each cycle of activity.

Swimmerets are pleopods at the abdomen of the crayfish that are organized into the protopod at the base and more distal segment, comprised of the endopod and the exopod (Storch and Welsch, 2014). The swimmerets move in two phases, the Power Stroke (PS, retraction) and the Return Stroke (RS, protraction) when the animal swims (Mulloney et al., 2003; Paul and Mulloney, 1985a, 1985b; Smarandache-Wellmann et al., 2013). During the PS, the swimmerets extend from the flexed resting position and produce a posterior fluid thrust. During the RS, the swimmerets move back to their original starting position.

The PS and RS muscles are innervated by 70 MNs, 32 excitatory Power Stroke Exciter (PSE) and 33 excitatory Return Stroke Exciter (RSE) (Figure 1) as well as three inhibitory Power Stroke Inhibitor (PSI) and two inhibitory Return Stroke Inhibitor (RSI) (Mulloney et al., 2003; Smarandache-Wellmann et al., 2013). The axons of the MNs innervating the PS muscles project through the posterior branch of Nerve1. The axons of the MN innervating the RS muscles project through the anterior branch (Mulloney and Hall, 2000; Mulloney et al., 2003).

The alternating PS and RS activity of each swimmeret is driven by its own local, central pattern generating circuit (CPG), which is located in each segments' hemiganglion (Heitler, 1978; Mulloney et al., 2003; Paul and Mulloney, 1985a, 1985b; Smarandache-Wellmann et al., 2013). The CPGs consists of five identified unilateral non-spiking interneurons: Three Inhibitors of Power stroke (IPS: IPS_{Wedge}, $IPS_{Tangent}$, $IPS_{Orthogonal}$) and two Inhibitors of Return Stroke (IRS: IRS_{Hook}, IRS_{NoHook}) (Smarandache-Wellmann et al., 2013). These neurons form reciprocal inhibitory synaptic connections, thereby creating a half center oscillator (Figure1). At this point the functional relevance of three homolog copies of IPS and two of IRS has not been unveiled. Despite slight differences in their morphology, all neurons have a similar influence on the motor output (Smarandache-Wellmann et al., 2013). However, IRS_{Hook} has been shown to be of specific importance for the intersegmental coordination (Smarandache-Wellmann et al., 2014) (see below).

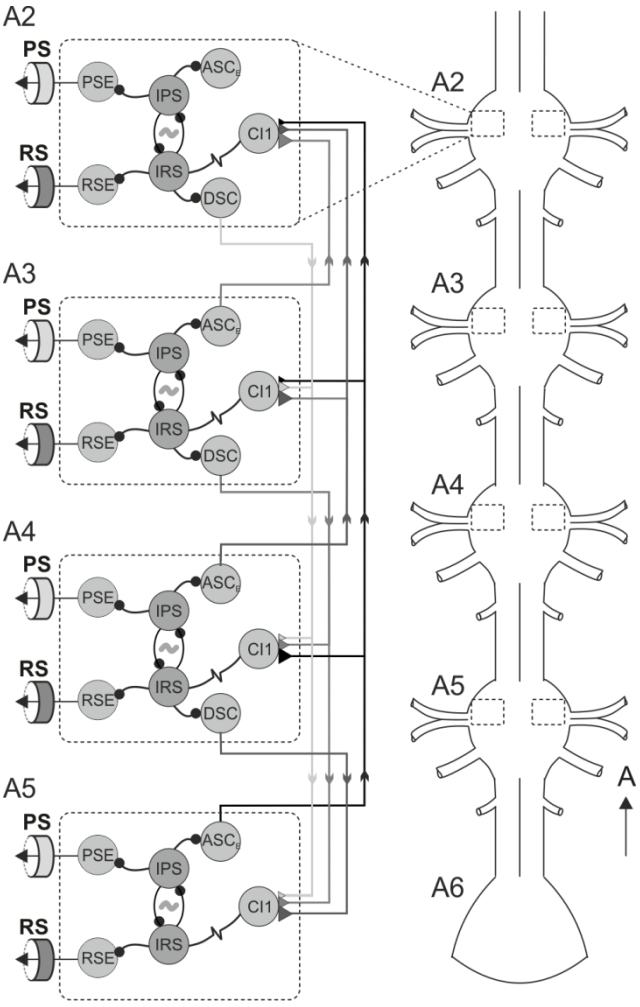

Figure 1 Ipsilateral connectivity between each microcircuit. IPS and IRS inhibit each other, forming the pattern generating kernel. IPS inhibits PSE and ASC_E, IRS inhibits RSE and DSC. ASC_E and DSC send excitatory long range projections to ComInt1 in all other ganglia. Dashed boxes show the location of the Lateral Neuropil. IPS: Inhibitor of Power Stroke, IRS: Inhibitor of Return Stroke, PSE: Power Stroke Exciter, RSE: Return Stroke Exciter, ASC_E: Ascending Coordinating Neuron, DSC: Descending Coordinating Neuron, ComInt1: Commissural Interneuron 1, PS: Power Stroke, RS: Return Stroke, A1 – A6: abdominal ganglia 1 – 6.

The coordination between the segments is established by the neurons of the coordinating network, composed of the Coordinating Neurons, Ascending Coordinating Neuron (ASC_E) and Descending Coordinating Neuron (DSC), and the nonspiking Commissural Interneuron 1 (ComInt1) (Figure1) (Namba and Mulloney, 1999; Tschuluun et al., 2001). Both Coordinating Neurons receive inhibitory synaptic input from the CPG; ASC_E from IPS, and DSC from IRS (Smarandache-Wellmann and Grätsch, 2014). Hence, both neurons carry efference copies of their home ganglions motor output and transmit this information about timing, duration, and strength of the motor output to their target ganglia. This information is then decoded by excitatory postsynaptic potentials (EPSPs) in ComInt1 (Mulloney et al., 2006, 2006; Namba and Mulloney, 1999; Smarandache et al., 200). The intersegmental coordination between each ipsilateral swimmeret group is achieved by the long range projections of ASC_E and DSC (Mulloney et al., 2003; Namba and Mulloney, 1999). Each ASC_E and DSC projects to all anterior (ASC_E) or posterior (DSC) abdominal

ganglia (Figure1). Therefore, each ComInt1 receives the information from Coordinating Neurons from three different ganglia (Smarandache et al., 2009). A crucial factor for the proper coordinated activity is the gradient of synaptic strength between different Coordinating Neurons in ComInt1 (Smarandache et al., 2009). The size of EPSPs, elicited in ComInt1, differs depending on the distance and position of the home module of the respective Coordinating Neuron. EPSPs with the largest amplitudes are always elicited by the nearest posterior ASC_E. Smaller EPSPs are elicited from Coordinating Neurons originating from more remote segments. The coordinating information received by ComInt1 is then transmitted to the local CPG via an electrical synapse to IRS_{Hook} (Mulloney and Hall, 2003; Smarandache et al., 2009; Smarandache-Wellmann et al., 2014). The coordinating network of ASC_E, DSC, and ComInt1 is necessary and sufficient to establish precisely coordinated swimmeret movement that maintains its phase delay of 0.23 ± 0.07 independent of the frequency (Blumenthal and Smarandache-Wellmann, in preparation, Hughes and Wiersma, 1960; Ikeda and Wiersma, 1964).

1.3 Cellular activity pattern of swimmeret neurons

The swimmeret system generates rhythmic and coordinated motor output even deprived of sensory and central input. All neurons that take part in rhythm generation, coordination, or execution of motor commands, have oscillating membrane potentials around voltages between approximately -55 mV and -45 mV (Mulloney et al., 2006; Paul and Mulloney, 1985; Sherff and Mulloney, 1997; Smarandache-Wellmann et al., 2013, 2014). At a closer look, similarities as well as disparities between membrane potential oscillation shapes in different neuron groups become apparent. Oscillations generated by PSE, RSE, and IPS are characterized by similar shape and shallow depolarizing slope (Figure 2 A, B, E), while oscillations in ASC_Es are mostly characterized by steeper slopes (Figure 2 C) (Schneider, 2017; Sherff and Mulloney, 1997). However, some ASC_Es are characterized by the same steepness as observed in PSE and RSE (Schneider, 2017; Sherff and Mulloney, 1997). Oscillations in DSC have a broader depolarized phase compared to the other neuron types (Figure 2 D) (personal communication C. Smarandache-Wellmann).

Oscillations in ComInt1 are accompanied by different sized EPSPs (Smarandache-Wellmann et al., 2014). However, ComInt1 recordings vary with regard to proportion

of oscillation amplitude and EPSP amplitudes (Figure 2 F) (personal communication F. Blumenthal).

All spiking neurons produce bursts of action potentials (APs) during the most depolarized phase of the oscillation. ASC_E is characterized by a higher amount of generated APs than the remaining spiking neurons, PSE, RSE, and DSC (personal communication F. Blumenthal), while PSE and RSE produce the least amount of APs. The elicited spike train in each spiking neuron is characterized by spike frequency adaptation and reduced first spike threshold in ASC_E, PSE and RSE, but not in DSC (Schneider, 2017).

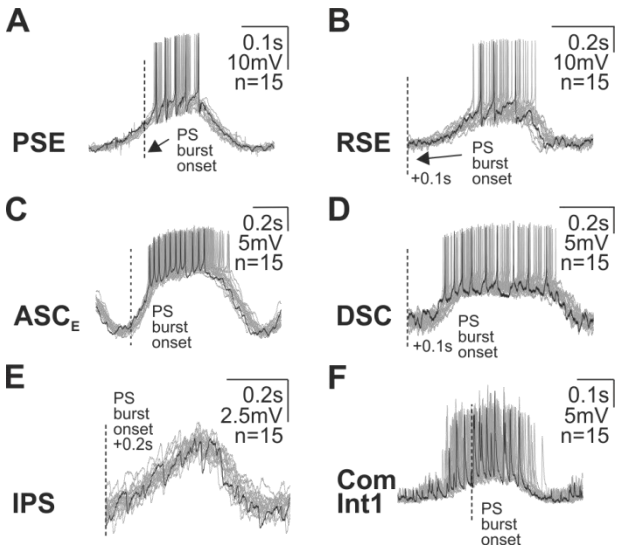

Figure 2: Neurons in the swimmeret system oscillate. A, B, C, D, E, F Overdraws of four representative spiking neurons (PSE, RSE, ASC_E, and DSC) and two nonspiking neurons (IPS and ComInt1) triggered to PS burst onset (each n = 15). PSE: Power Stroke Exciter, RSE: Return Stroke Exciter, ASC_E: Ascending Coordinating Neuron, DSC: Descending Coordinating Neuron, IPS: Inhibitor of Power Stroke, ComInt1: Commissural Interneuron 1, PS: Power Stroke.

Experimental depolarizing current injections differentially affect membrane potential oscillations in the different neurons groups, especially when comparing IPS to the other neuron groups. Depolarizing current injections in IPS is shown to decrease membrane potential oscillations strongly, while the amplitudes remain similar or even tend to increase in in the other neurons of the swimmeret system (IRS, PSE, RSE, ASC_E, DSC, and ComInt1) (Mulloney, 2003; Schneider, 2017; Smarandache-Wellmann et al., 2013; personal communication F. Blumenthal).

1.4 Cellular properties of rhythmic neuronal networks

Despite our good understanding of the cellular components and synaptic contacts in each microcircuit of the crayfish abdominal nervous system, it remains unknown how single cell activity is established. Although some neuron groups have been shown to

receive the same synaptic input from the CPG, their activity patterns differ. Therefore it seems likely that the discrepancies in neuronal activity pattern arise from discrete ion channel compositions in the respective neuron groups.

Ion channels are specialized proteins in the membrane of neurons that are able to respond to very small stimuli. Once activated, they can open within milliseconds to mediate fast diffusion of ions across the membrane leading to rapid change in potential. Ions will either enter the cell or diffuse out of the cell according to their electro-chemical gradient between the cytoplasmic side and the extracellular space. In the case of sodium for example the ionic concentration is much higher in the extracellular space than inside the neuron. When channels open, sodium will diffuse into the cell and thereby cause an accumulation of positively charged ions inside the cell, leading to a depolarization of the membrane (Alberts et al., 2002).

Ion channels are highly specific with regard to their permeability for ions. Depending on their pore lining structure, some channels are selectively permeable to one ion type, while others are less specific and will allow more than one ion type to diffuse through the pore of the channel. Essential for proper signaling, mediated by ions channels are the gating mechanisms of the channel. Depending on the type of ion channel, they will open or close caused by chemical or electrical signals. Ligand-gated ion channels open when a ligand binds to specific binding site on the channel itself, or to a binding site in close proximity to the channel. Those ligands can either be transmitters in the extracellular space or intracellular mediators such as ions or nucleotides (Alberts et al., 2002).

Voltage-gated ion channels opens upon voltage changes of the membrane potential. If membrane potentials de- or hyperpolarize, e.g. due to excitatory or inhibitory synaptic input, the likelihood of intrinsic ion channels to open changes. Some ion channels open at more depolarized potentials, while other channels are sensitive to hyperpolarized potentials. Likewise, closing of ion channel can be similarly depending on the membrane potential. Other ion channels are constantly open and allow continuing diffusion of ions across the membrane (Alberts et al., 2002).

1.5 Ion channels mediating inward currents

1.5.1 Sodium channels

Sodium channels play a crucial role during membrane potential depolarization of a neuron, thereby, enabling the neuron to transmit electrical signals over long distances (Marban et al., 1998). Properties of sodium channels were first characterized by Hodgkin and Huxley, when discovering voltage-gated ion channels in the squid axon (Hodgkin and Huxley, 1952). Mammalian sodium channels consist of the α, and the smaller auxiliary β1 and β2 subunits, whereas the principle α subunit is necessary for functionality of the channel (Catterall, 1992; Marban et al., 1998). The α subunit is composed of four homologous domains, each consisting of six transmembrane domains. Four of these transmembrane domains form the central pore that ensures the selectivity and conductance properties of the channel by their pore lining domain P between the fifth and the sixth transmembrane domain (Marban et al., 1998). Experiments in *Xenopus* oocytes expressing sodium channels revealed that the fourth transmembrane domain with its positively charged arginin and lysine residues serves as a voltage sensor (Stühmer et al., 1989).

Experiments treating the intracellular surface of the squid neuronal membranes with pronase, or site-directed antibodies against the intracellular loop between domains III and IV, blocked inactivation of sodium channels (Armstrong et al., 1973; Vassilev et al., 1988). Rescue experiments adding a synthetic peptide consisting of three amino acids (Ile-Phe-Met) that resembled the same sequence of the hydrophobic loop between domains III and IV, could reestablish inactivation (Eaholtz et al., 1994). These experiments led to the conclusion that the inactivation site lies between those two domains.

However, not all sodium channels are characterized by fast opening and closing kinetics. In experiments on vertebrate guinea pig cerebellar Purkinje neurons (Kay et al., 1998), dorsal root ganglion neuron of the rat (Elliott and Elliott, 1993; Roy and Narahashi, 1992), as well as different mollusk neurons (Gilly et al., 1997; Kiss, 2003) and jellyfish MNs (Anderson, 1987), sodium channels were detected with slow activating kinetics and were either noninactivating or slowly inactivating. Furthermore, in cat layer V pyramidal neurons, persistent sodium channels were shown to activate at more negative membrane voltages than the transient sodium channels (Crill, 1996). Persistent sodium channels were shown to have important functions in setting

the resting membrane potential in cerebellar Purkinje neurons (Kay et al., 1998). Furthermore, they were found to be involved in rhythmically active neurons during maintenance of pacemaker activities in neurons of the preBötzinger Complex (Del Negro et al., 2002; Peña et al., 2004), promotion of subthreshold oscillation in the leech heart interneurons (Opdyke and Calabrese, 1994), generation of plateau potentials in crayfish abdominal stretch receptor neurons (Barrio et al., 1991), and PIR responses of leech MNs (Angstadt and Simone, 2014).

The transient sodium current, as well as one type of I_{NaP} were shown to be sensitive to Tetrodotoxin (TTX) application (Gilly et al., 1997; Kiss, 2003). In a modeling study the target site of TTX at the sodium channel could be identified as the extracellular loop between S5 and S6 (Lipkind and Fozzard, 1994). Another subgroup of persistent sodium channels was not TTX-sensitive but could be blocked by low concentrations of Riluzole (Harvey et al., 2006; Miles et al., 2005; Tsuruyama et al., 2013; Urbani and Belluzzi, 2000). Because the effect of Riluzole was predominantly seen after sodium channels were activated and entered the inactivation state, it was concluded that Riluzole binds at the inactivation loop of the channel (Benoit and Escande, 1991).

1.5.2 Calcium channels

Five classes of voltage activated calcium channels give rise to a depolarizing inward current carried by calcium ions. These channels are the L-type, P/Q type, N- type, R-type, and the T-type channels (Simms and Zamponi, 2014). Calcium channels are composed of different proteins that determine their ion selectivity, as well as their opening and closing kinetics. The α_1 subunit, a homologue to the α subunit of sodium channels, is comprised of four domains, each with six transmembrane domains, including the voltage sensor in S4 and the pore lining P region. The auxiliary subunits α_2, β, γ, and δ modify the specific channel properties of the different channel types (Catterall, 2011).

The voltage sensitivity varies between the different channels types. P/Q-type, N-type, and R-type calcium channels open at depolarized membrane voltages. They are therefore often referred to as high-voltage activated calcium channels. Depending on the system, the L-type calcium channel has been shown to be either high- (Snutch et al., 2013) or low voltage activated (Wang et al., 2011; Xu and Lipscombe, 2001).

Together with the T-type calcium channel, which also opens at hyperpolarized voltages (Armstrong and Matteson, 1985), they were both shown to be involved in PIR responses in lamprey commissural interneurons and MNs (Wang et al., 2011) and rat caudal hypothalamic neurons (Fan et al., 2000). The L-type calcium current (I_{CaL}), without interference of the T-type calcium current (I_{CaT}), was furthermore seen to induce PIR responses in cerebellar nuclei neurons (Zheng and Raman, 2011). Furthermore, the L-type calcium channel was shown to be involved the generation of plateau potentials in rat deep dorsal horn neurons (Morisset and Nagy, 1999), and pacemaker activity in dopaminergic Substantia Nigra neurons (Branch et al., 2014), generating membrane potential oscillations in striatal neurons (Song et al., 2016) and unidentified neurons of the swimmeret system of the crayfish (Chrachri, 1995). L-type calcium channels have been shown to be blocked by different dihydropyridines, Nitrendipine, Nifedipine, and Nimodipine by binding to a specific region close to the pore and the hypothesized activation gate at the α1- subunit (Snutch et al., 2013; Tikhonov and Zhorov, 2009; Wang et al., 2011).

1.5.3 HCN channels

Hyperpolarization-activated cyclic-nucleotid-gated (HCN) channels activate slowly at hyperpolarized membrane voltages and give rise to slow inward currents depolarizing the neurons (I_H) (Angelo and Margrie, 2011). Therefore, they contribute to several processes in non-pacing-, as well as rhythmically active neurons in the brain. HCN channels contribute to long term potentiation (Mellor et al., 2002) and modulation of synaptic transmission (Beaumont and Zucker, 2000). In rhythmically active neurons, they were shown to modulate pacemaker activity in preBötzinger complex neurons (Thoby-Brisson et al., 2000), thalamocortical relay neurons during sleep (McCormick and Pape, 1990), and CA1 hippocampal stratum oriens-alveus interneurons. They also contribute to membrane resonance in inferior olive neurons (Matsumoto-Makidono et al., 2016). Furthermore, this current often mediates PIR responses in pyloric neurons of the stomatogastric nervous system (Harris-Warrick et al., 1995), leech heart interneurons (Angstadt and Calabrese, 1989), CA1 pyramidal neurons (Surges et al., 2006), and neonatal rat MNs (Bertrand and Cazalets, 1998).

HCN channels are not selective for one specific ion type but allow both sodium and potassium to diffuse through the membrane. HCN channels are comprised of six transmembrane domains (S1 – S6), forming a tetrameric complex (Biel, 2010). The

channels are characterized by a pore lining loop between S5, S6, and a cyclic nucleotide binding domain at the C- terminal region. The positively charged fourth transmembrane domain functions as the voltage sensor and shares close homology with the voltage sensor in voltage-gated potassium channels (Kaupp and Seifert, 2001). HCN channels typically open at hyperpolarization of the membrane. Depending on the neuron type, the half-maximal activation voltages vary between -65 mV and -95 mV (Pape, 1996) and inactivate at -43 mV in thalamocortical relay neurons (McCormick and Pape, 1990), -50 mV in neurons of preBötzinger complex (Thoby-Brisson et al., 2000), or -35 mV in dorsal gastric MNs of the stomatogastric nervous system (Kiehn and Harris-Warrick, 1992). When open, HCN channel conduct sodium and potassium in a ratio of 1:4 to 1:6, which is blocked by millimolar concentrations of cesium (Edman et al., 1987; Gauss et al., 1998; Ludwig et al., 1998) or Zd7288 by binding at the residues Ala425 and Ile432 located at the S6 transmembrane domain at the inner pore of the channel (Cheng et al., 2007).

1.6 Ion channels mediating outward currents

Potassium-carried outward currents are of equal importance for the generation of rhythmic neuronal activity. Leading to outward diffusion of positively charged ions, these channels are key mediators to hyperpolarize the membrane.

Voltage-gated potassium channels ($K_{(V)}$-channels) are comprised of four α subunits, each consisting of six transmembrane domains (S1 – S6) and a diverse number auxiliary β subunits that are arranged barrel-like and embedded into the membrane of the neuron to form a pore (Biggin et al., 2000). Despite the variety of different potassium channels, all show the same structural attributes that ensure the selectivity of these channels for potassium. This main structure is the pore loop between the fifth and sixth transmembrane domain (Biggin et al., 2000). The S4 transmembrane domain is the voltage sensor of the channel. Furthermore, the β subunit influences the conductance through the channel by serving as an inactivation gate that blocks the channel after activation or by influencing the cell surface expression of the α subunit (Biggin et al., 2000).

The first voltage-gated potassium channel was found by the detection of a mutated *shaker* gene in *Drosophila melanogaster* (Ferrus et al., 1990). After the

characterization of the *shaker* gene, three other related potassium channel genes were cloned, *shab, shaw,* and *shal* (Salkoff et al., 1992; Wicher et al., 2001; Xu et al., 1995). All four are highly conserved between flies, mice, and humans (Salkoff et al., 1992). The genes *shaker* and *shal* encode for transient potassium currents (I_A) with fast activation and inactivation kinetics. The genes *shab* and *shaw* encode for moderate activation and slow inactivation kinetics of potassium currents (Hille, 2001). Depending on the cell, different compositions of these genes are expressed.

An important feature of transient potassium channels is their sensitivity to hyperpolarized membrane voltages. At subthreshold membrane potentials transient potassium channels open rapidly, reducing the amount of positively charged ions inside the cell (Kim et al., 2005). Thereby, the activity of this channel is important for shaping APs, spike frequency, delay of rebound firing, and rhythmic bursting (Ascoli et al., 2010; Harris-Warrick et al., 1995; Hartline and Gassie, 1979; Hille, 1992; Kim et al., 2005; Serrano and Getting, 1989; Tierney and Harris-Warrick, 1992). A selective antagonist of I_A is 4-Aminopyridine (4-AP), which has been shown to block the transient potassium channel from the cytoplasmatic site when the channels are open (Kiss et al., 2002; Yao and Tseng, 1994).

Another group of potassium channels open due to accumulation of intracellular Ca^{2+} ions. The outward current counteracts depolarizations mediated by calcium influx. Calcium-gated potassium channels play an important role in inducing spike afterhyperpolarizations, which directly affects spike frequency adaptation and finally termination of AP bursts (el Manira et al., 1994). The family of calcium gated potassium channels can be divided into three groups, the big conductance (BK) intermediate (IK), and the small conductance (SK) channels (Vergara et al., 1998). IK and SK channels open solely to changes in intracellular calcium concentrations while the BK channel is also sensitive to changes in the membrane voltage. The structure of calcium- gated potassium channels is similar to those of voltage-gated potassium channels, besides a calcium binding site at the C-terminal region (Schreiber and Salkoff, 1997).

1.7 Computational model of the swimmeret system

The fundamental aim of working on the neuronal network controlling swimmeret movements is to achieve a better understanding of how the nervous system

generates behavior. Regarding the extensive investigations in this system and accumulation of new insight about the network architecture, we are getting closer to understanding basic principles for rhythmogenesis, and coordination. Thereby a lot of progress has been made about possible intersegmental connections, mediating the 0.25 phase difference between the segments, by the used of simplified mathematical models (Skinner and Mulloney, 1998; Zhang et al., 2014).

In the stomatogastric nervous system extensive theoretical work has been performed identifying possible ionic currents that take part in evolving neuronal activity pattern. Thereby it was revealed how the same firing pattern can be generated by variable ionic current compositions (Prinz et al., 2004; Soofi et al., 2012), but also, how homeostatic plasticity is able to adapt ionic conductances to maintain phase constancy between neurons (Marder and Prinz, 2002).

At this point, little is known about intrinsic neuronal properties that contribute to the generation of rhythmic and coordinated motor output in the swimmeret system. Regarding that most of the identified synaptic connections between individual network components are shown to be inhibitory (Mulloney, 2003; Murchison et al., 1993; Skinner and Mulloney, 1998; Smarandache-Wellmann and Grätsch, 2014), suggest that either escape- or a release mechanism could play a role during rhythmic neuronal activities of the participating neurons. Especially the activity pattern of the half center oscillator formed by IPS and IRS neurons is likely to depend on either of these two processes. A study by Daun and colleagues simulated the activity of half center oscillators based on different combinations of ionic currents (Daun et al., 2009). Thereby it could be learned that particularly the half center oscillator based on I_{NaP} and I_L was able to perform the greatest range of oscillations periods.

1.8 Objectives

Ionic currents and synaptic input cooperatively establish the activity of individual neurons within a network. This is achieved, foremost, by a precise interplay of intrinsic ionic conductances, which fine-tune single neuronal activities to meet the correct phasing and magnitude needed for a functional network activity. At this point little is known about any ionic currents that contribute to generating neuronal activities in the swimmeret system. However, in order to fully comprehend, how the neuronal network of the swimmeret system operates, the intrinsic properties

underlying the activity pattern of each neuron need to be identified. Thereby, the expression of specific membrane responses, upon de- or hyperpolarizing stimuli, can facilitate the analysis of the contributing ionic conductances.

In other systems, like clione (Pirtle and Satterlie, 2004), leech (Angstadt et al., 2005), lamprey (Matsushima et al., 1993), or xenopus tadpole (Li and Moult, 2012), key neurons for rhythmogenesis are shown to receive inhibitory synaptic input, and additionally, have the ability to escape from this inhibition. Thereby, induced by negative potential changes, hyperpolarization-activated ion channels open, and allow influx of positively charged ions, which ultimately depolarizes the neuron and thus promotes the next oscillation. Possible ion channels with low voltage sensitivities are the T-type calcium channel, the L-type calcium channel, and/or the HCN channel.

Because most of the neurons in the swimmeret system are shown to receive inhibitory synaptic input (Mulloney, 2003; Murchison et al., 1993; Skinner and Mulloney, 1998; Smarandache-Wellmann and Grätsch, 2014), the question arises, whether these neuron possess the ability to escape from inhibition, as well. This could represent a possible mechanism to escape the hyperpolarized membrane potential during the oscillation and promote the depolarization. Furthermore, by a correct interplay of underlying ionic conductances the specific phasing of the oscillation could be established.

Analyzing the expression of PIR responses represents a means to gain a better understanding of escape mechanisms and the underlying ionic conductances. In a variety of neuronal networks, the presence PIR responses, mediated by one or several different ionic currents have been described. One ionic current, I_H, has been shown to underlie or contribute to PIR generation in several vertebrate (Ascoli et al., 2010; Johnson and Getting, 1991; Matsushima et al., 1993) and invertebrate species (Calabrese et al., 1995; Golowasch et al., 1992; Harris-Warrick et al., 1995). However, in other species or even in other neurons types of the same species, PIR responses have been shown to be mediated by calcium or sodium carried currents (Angstadt and Simone, 2014; Angstadt et al., 2005; Fan et al., 2000; Wang et al., 2011; Zheng and Raman, 2011).

In the first part of this thesis I explored the presence PIR responses in key neurons of the swimmeret system for rhythm generation, intersegmental coordination and

execution of motor commands. I monitored the voltage responses of synaptically isolated neurons to hyperpolarizing current injections in discontinuous current clamp mode.

In the second part of this thesis, I performed occlusion experiments to unveil the ionic bases of the evoked PIR responses, and in addition, tested the significance of identified ionic currents for the generation of fictive locomotion in the third part of this thesis.

In a reduced mathematical model, I furthermore tested the capability of swimmeret CPGs to perform similar network activities with disparate underlying ionic conductances.

2. Material and Methods

The experiments were carried out on adult crayfish, Pacifastacus leniusculus. The animals were caught in nearby rivers and ponds and kept in fresh water tanks at temperatures of 14 °C and a 12 hour day / night cycle.

2.1 Dissection

All experiments were performed on isolated abdominal nerve cord preparations. To prepare the dissection, the animals were anesthetized by keeping them on ice for 20 – 30 min. Afterwards the claws were cut at the base near the thorax and the left and right uropodes were removed (Seichter et al., 2014). To exsanguinate the animal 50 ml cold ringer solution containing (in mM): 195.0 NaCl, 5.4 KCl, 13.5 $CaCl_2$, 2.6 $MgCl_2$ (ph: 7.4) was rinsed though the claw opening. In a next step the animal was decapitated and the walking legs were cut near the base. A following transverse cut through the thorax at the level of the second walking leg separated the abdomen with the last three thoracic segments from the remaining cephalothorax. By separating the ventral and dorsal abdomen from another the ventral nerve cord could be exposed and removed from the abdominal plate. The abdominal nerve cord (including abdominal ganglia 1 to 6 as well as the last two thoracic ganglia) was then pinned down with the dorsal side facing up in a Sylgard lined Petri dish filled with cold ringer solution. The anterior and posterior branches of N1 were separated to record the RS (anterior branch) and PS (posterior branch) activities. In order to facilitate intracellular recordings at the region of the Lateral Neuropil and to allow diffusion of superfused drugs into the tissue, the ganglia sheaths from ganglia A2 - A5 were removed with fine scissors.

2.2 Electrophysiology

2.2.1 Extracellular recordings

I performed up to fourteen simultaneous extracellular recordings (Figure 3 A, B). I used two differential stainless steel pin electrodes to record the activity pattern of all motor neurons (MNs) innervating the Power Stroke (PS) and Return Stroke (RS) muscles. Thereby, I placed the electrodes either at the anterior branch of Nerve1

(N1) for RS recordings, or at the posterior branch of N1 for PS recordings (Figure 3 A, B). The nerve endings were wrapped around each of the pin electrodes and insulated from surrounding saline with petroleum jelly. RS activities were only recorded from ganglia A3 and A4. The signals from the pin electrodes were amplified 1000 fold (Model MA 102, Electronics laboratory, University of Cologne) and band pass filtered from 300 Hz to 2 kHz.

Additionally to MN recordings I performed extracellular recordings of the axons of the Coordinating Neurons, Ascending Coordinating Neuron (ASC_E) and Descending Coordinating Neuron (DSC). Therefore I placed two differential suction electrodes (MWE-F15B, Warner Instruments, Hamden, CT, USA, M-3333, Narishige, Tokio, Japan) on the dorsal surface of the ganglia (Figure 3 A, B). Suction electrodes were pulled from a P-87 micropipette puller (Sutter Instruments, Novato, CA, USA) from borosilicate capillaries (outer diameter: 1.5 mm, inner diameter: 0.86 mm, Sutter) and broken until the tip diameter was slightly larger than the Lateral Giant Axon. In order to record from ASC_E I placed the electrode dorsally to the Lateral Giant Axon on the anterior Minuscule Tract, during DSC recordings on the posterior Minuscule Tract (Figure 3 A, B). To increase the recording quality I applied negative air pressure to the electrode which improved the contact of the electrode to the tissue. The recorded signal was 50 - fold preamplified (MA103, Electronics laboratory, University of Cologne) and transmitted to the extracellular amplifier.

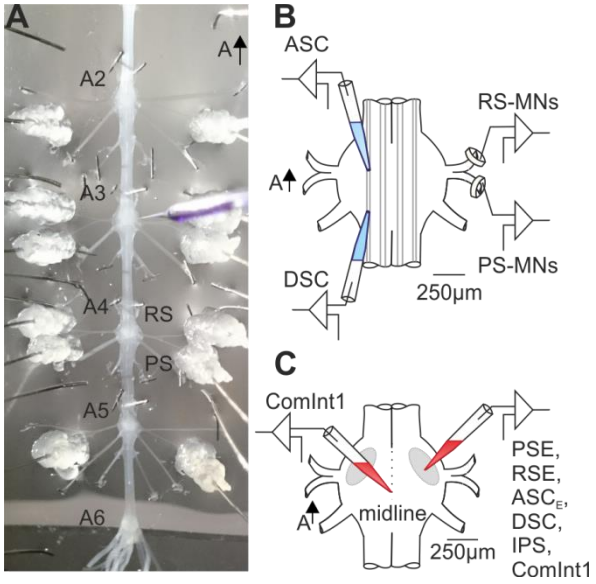

Figure 3. Experimental setup and recording sites. A: Isolated abdominal nervous system (A2 to A6) with intracellular electrode and extracellular pin electrodes at anterior and posterior branches of N1. B: Schematic illustration of ganglion shows the placement of ASC & DSC suction electrode as well as differential pin electrodes for RS- and PS MNs recordings. C: Sharp electrode placement for intracellular recordings from PSE, RSE, ASC_E, DSC, IPS and ComInt1. A2 to A6: abdominal ganglion 2 to abdominal segment 6, N1: Nerve 1, RS: Return Stroke, PS: Power Stroke, MN: motor neurons, PSE: Power Stroke Exciter, RSE: Return Stroke Exciter, ASC: Ascending Coordinating Neuron, DSC: Descending Coordinating Neuron, IPS: Inhibitor of Power Stroke, ComInt1: Commissural Interneuron 1.

Signals of suction electrode and pin electrode recordings were digitized in a sampling frequency of 10 kHz with an analogue/digital (A/D) converter (Digidata 1440A, Molecular Devices, Sunnyvale, CA, USA) and recorded on a personal computer with Clampex (Molecular Devices).

2.2.2 Intracellular recordings

To analyze the cellular properties of the different neurons in the swimmeret system I performed intracellular recordings at the dendritic aborizations in the Lateral Neuropil or at the midline of the ganglion (Figure 3 C). The intracellular electrodes were pulled from borosilicate glass capillaries with filaments (outer diameter: 1 mm; inner diameter: 0.5 mm). The electrodes were filled with intracellular electrode solution containing 1 M KAc and 0.1 M KCl and 1% Dextran Texas Red with resistances between 30 – 60 MΩ. Electrode liquid junction potential and capacitance were compensated prior neuron penetration. During intracellular recordings electrode capacitance was compensated in regular intervals. The intracellular signal was amplified 1000 fold (SEC-05X, npi electronic, Tamm Germany), digitized (10 kHz) and recorded with Clampex (Molecular Devices). The recordings were performed in discontinuous single electrode current clamp with switching frequencies of 35 kHz.

Based on different electrophysiological properties of the recorded neurons (effect of de- or hyperpolarizing current injections on the PS / RS motor output of the home ganglion (PSE, RSE, and ComInt1) or the target ganglion (ASC_E and DSC)) and specific phase relationships to the PS MNs bursts they could be classified during the experiment to the different neuron classes. The classifications during the experiments were later verified by their morphology through single neuron labeling by intracellular dye injection (PSE, RSE (Sherff and Mulloney, 1997), ASC_E, DSC (Namba and Mulloney, 1999), IPS (Smarandache-Wellmann et al., 2013), ComInt1 (Smarandache-Wellmann et al., 2014)).

2.3 Morphology

To verify the identity of the intracellularly recorded neurons by their morphology I stained the neurons iontophoretically with 1 % Dextran Texas Red, by delivering depolarizing current pulses (1 nA; pulse durations: 250 ms, frequency: 2 Hz).

Ganglia in which neurons were labeled were subsequently fixed in 4 % paraformaldehyde at least 2 h at room temperature, washed 3 times in PBS for 15 min each, and dehydrated in an ascending ethanol series of 30 %, 50 %, 70 %, 90 % and 100 %. Additionally the ganglia were cleared with methyl salicylate to improve the visibility of the stained neurons. Images were taken in 10 fold to 20 fold magnification either on a fluorescence microscope (BX61, Olympus, Hamburg, Germany) or confocal laser scanning microscope (LSM 500 Meta, Zeiss, Oberkochen, Germany), installed on an inverted Zeiss Axiovert 100M. Z-stacks were converted of 20 to 25 optical slices by the image processing software Image J (Version 1.45s).

2.4 Experimental Procedure

After a settling period of up to 15min following membrane penetration with the intracellular electrode the superfusion of the preparation with different bathing solutions was initialized with a peristaltic pump (Alitea, Sweden). When searching for neurons intracellularly, the volumetric flow rate was set to 0.5 ml / min and increased to maximum flow rates of 2 ml / min during the experiment. To achieve comparable effects of applied blockers, all preparations were superfused with 2 µM carbachol diluted in ringer solution.

During the experiments ringer solution containing different drugs were applied to the abdominal nervous system while analyzing cellular and system properties.

Drugs

A mixture of different synaptic blockers with concentrations of (in µM): 10 Picrotoxin (PTX), 10 6-cyano-7-nitroquinoxaline-2,3-dione (CNQX), 10 6,7-dinitroquinoxaline-2,3-dione (DNQX), 10 D-2-amino-5-phosphonopentanoic acid (D-AP5), and 10 Tubocurarin was applied to the abdominal nervous system to achieve synaptic isolation. The synaptic blockers were mixed just prior to application from defrosted stock solutions. To investigate the contribution of specific ion channels during characteristic membrane responses Nifedipine, 4-(N-ethyl-N-phenylamino)-1,2-dimethyl-6-(methylamino) pyrimidinium chloride (Zd7288) and Riluzole were added to the synaptic blocker solution and subsequently applied to the preparation.

The channel blockers were prepared as 40 mM (Nifedipine), 50 mM (Zd7288), and 70 mM (Riluzole) stock solutions, dissolved either in DMSO or ringer solution. Defrosted drugs were diluted to the synaptic blocker solution immediately before application and kept in light shielded containers (40 µM Nifedipine, 200 µM Zd7288, and 70 µM Riluzole).

During system analysis the drugs mentioned above, as well as 4 mM 4-Aminopytidine (4-AP) (diluted from 4 M stock solution in ringer) were added to ringer solution without synaptic blockers and applied to the preparation individually during each experimental approach.

Protocols

While superfusing the abdominal nervous with synaptic blockers and/or ion channel blockers the cellular input resistance (R_{IN}) was measured by applying brief hyperpolarizing current pulses of -1 nA for 200 ms at an interval of 0.2 Hz (Cornerstone, S-900 Stimulator, Dragan Corporation, USA). The membrane potential was always set to similar values, allowing the neurons to oscillate around -50 mV to increase comparability between cells and experimental conditions.

Cellular properties

Post-inhibitory rebound (PIR) responses were induced, in order to characterize membrane properties of the neurons in the swimmeret system. Each protocol consisted of 15 sweeps at three different holding potentials (V_H)(V_H = -40 mV, V_H = -50 mV, and V_H = -60 mV). Negative currents were injected hyperpolarizing the neurons for 3 s to three different test potentials (V_T) (V_T = -80 mV, V_T = -90 mV, and V_T = -100 mV) to elicit PIR responses (Figure 4). Protocols were executed with the build in stimulation tool in Clampex. The injected current had to be adjusted from cell to cell to reach the aimed test potentials. Due to large differences in currents needed to reach V_T values between different neurons and neuron groups the emphasis during analysis was put on membrane potentials reached, not currents amplitudes injected.

The above mentioned channel blockers (Nifedipine, Zd7288, and Riluzole) were applied to the preparation while PIR responses were evoked in order to evaluate the contribution of different ionic currents for PIR generation.

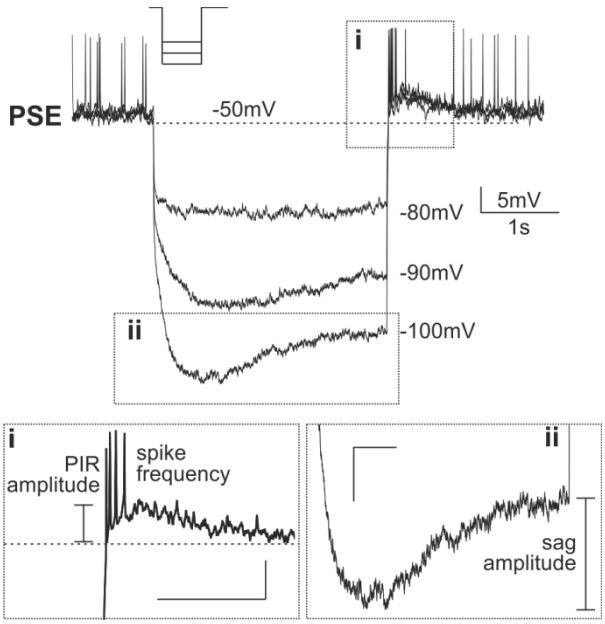

Figure 4. PIR response of a PSE. Intracellular recording of a PSE during hyperpolarizing current injection leading to a PIR response. The holding potential of this neuron was set to V_H = -50 mV. During the protocol the neuron was step wise hyperpolarized to V_T = -80 mV, V_T = -90 mV, and V_T = -100 mV for 3 s. Dashed boxes (i, ii) indicate the analyzed parameters during the PIR stimulations. i: PIR amplitude and spike frequency, ii: sag potential amplitude, PSE: Power Stroke Exciter, V_H: holding potential, V_T: test potential.

Analysis

In all cells the following parameters of the evoked PIR were analyzed in matlab (version R2014b, MathWorks, Natick, MA, USA). Figures were processed with Corel Draw X6 (Corel Corporation, Ottawa, Canada). Voltage traces of all 15 sweeps were taken for calculation of the median and interquartile ranges (IQR).

Holding Potential (V_H)

V_H values were identified by calculating the mean voltage potentials for each 15 sweeps in a time range between 1.5 s before onset of the stimulation, and onset of the stimulation. In order to reduce false depolarized V_H values due to strong depolarizations during action potentials (APs), APs were removed from the voltage traces by smoothing single voltage traces with a sliding window calculating the mean voltage data points between each neighboring data point in a factor of 900.

Test Potential (V_T)

V_T was detected by calculating the mean maximum hyperpolarized membrane potential during the current injection. Single voltage traces were smoothed to keep consistency for PIR- and sag amplitude calculations (below).

PIR amplitude

PIR depolarization amplitudes were measured between V_H and the maximum depolarized potential (between termination of current injection and 2.5 s post

termination of stimulation) (Figure 4 i). This time period was taken for analysis to be certain that all PIR responses had already ended during the measurement.

Sag amplitude

Mean voltage values between beginning of current injection and 1 s after beginning current injection, were subtracted from mean voltage values between 1 s before current injection termination and termination of current injection, in order to calculate sag potential amplitudes (Figure 4 ii).

Spiking characteristics

Spiking cells (PSE, RSE, ASC_E and DSC) elicited rebound spikes when released from hyperpolarizing current injections. One parameter that was analyzed was the latency until first rebound spikes were elicited. This value was measured as the time period of release from hyperpolarizing current pulse until the first APs occurred. The other parameter analyzed was the mean instantaneous APs frequency before and after PIR stimulation (Figure 4 i). In control condition, the maximum instantaneous spiking frequency was compared between the three different V_T at V_H = -40 mV to ensure all neurons reached spike threshold. During experiments identifying ionic conductances mediating PIR responses, maximum instantaneous frequencies were compared between experimental conditions elicited from V_H = -50 mV to V_T = -100 mV. This more hyperpolarized V_H was used for comparison because channel blocker application tented to increase instantaneous spike frequencies in many cells and some neurons seemed to enter sodium block at V_H = -40 mV.

System properties

During ion channel blocker application the following parameters were analyzed to assess the contribution of different ion channels for the generation of rhythmic motor output. The synchronicity between two PS recordings (in neighboring segments), as well as the relative time delay between two segments, were compared in order to analyze intersegmental coordination. Changes in rhythm generation were monitored by calculating, in single segments, period, burst duration and duty cycles. To explore which ionic currents where contributing to rhythmogenesis and coordination, Nifedipine (40 µM), Zd7288 (200 µM), Riluzole (70 µM) and 4-AP (4 mM) were applied individually to the abdominal nervous system.

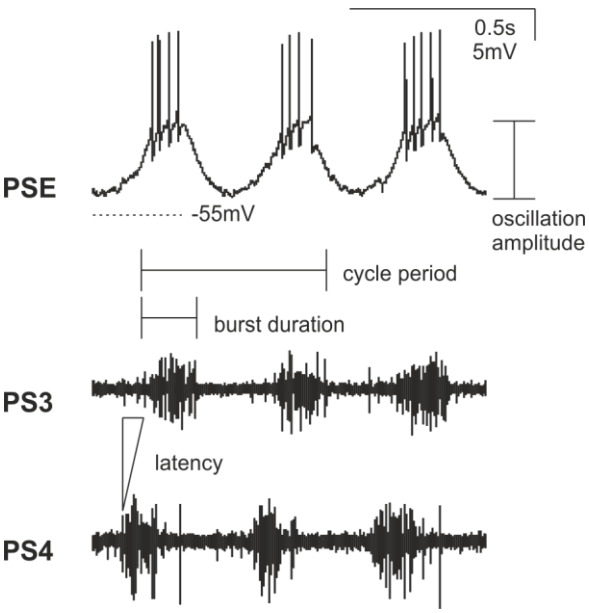

Figure 5. Cellular and system properties. Simultaneous intracellular recording of PSE during extracellular recording of PS in A3 and A4. Oscillation amplitudes were analyzed of intracellular traces. Latency, burst durations and period were measured from the extracellular PS traces. PSE: Power Stroke Exciter, A3 & A4: Abdominal Ganglion 3 and 4, PS: Power Stroke.

Phase analysis and Cross-Correlation

In preparations with a good signal to noise ratio, the coordination between segments was analyzed with a manual phase analysis. The phase was calculated as the relative fraction of time from the onset of a PS burst in one segment to the onset of a burst in the next anterior segment (phase= latency / period) (Figure 5). In preparations with a poor signal to noise ratio and diverse numbers of bursts in different segments a cross correlation analysis between two PS signals was performed in matlab. The traces were shifted along themselves until maximum correlation was reached, to test the synchronicity between the signals. The absolute correlation values were then plotted as a function of time delay. During the cross correlation analysis always data periods of 30 s were analyzed in control and experimental condition. If rhythmic patterns were analyzed with very large cycle periods, the analyzed time frame was increased to 100 s in control and experimental condition.

Period

The period was measured as the time between the onset of a PS burst and the onset of the consecutive burst (Figure 5). In preparations where bursts could not be distinguished visually period values were obtained from cross correlation analysis.

Burst Duration

The burst duration was measured as the interval from the beginning of a burst to the end of a burst. Only bursts were included that consisted of at least 5 APs and possessed no longer inter spike intervals than 5 ms.

Duty Cycle

The duty cycle was calculated by dividing the burst duration by the period.

Single cell activity

When blocking ionic currents in the swimmeret system, the activity patterns of individual neurons were analyzed with regard to the generation of membrane potential oscillations. Therefore 15 consecutive membrane potential oscillations were each triggered to PS burst onset and superimposed. To assess quantitatively AP generation in spiking cells event correlations were calculated. Hence the distribution of generated APs was plotted over the duration of a cycle (aligned to the PS burst onset, bin sizes = 8 ms).

Oscillation amplitude

The amplitude of the intracellular recorded membrane potential oscillations was measured from the trough potential to the maximum depolarized potential. During oscillation amplitude measurements, voltage traces were smoothed to avoid false depolarized voltage values due to AP generation of the cell.

2.5 Statistics

All statistical tests were performed assuming that all obtained datasets are characterized by nonparametric distribution. The two-sided Wilcoxon rank sum test was used, to test for significant differences between two unpaired data sets in control- and experimental condition. Paired datasets were analyzed using the two-sided Wilcoxon sign rank test. A Kruskal-Wallis test and multiple comparison test was used, to compare the differences between unpaired multiple datasets. When

evaluating the differences between multiple paired data sets a Friedman test was used. The H0 hypothesis was accepted if P values reached 0.05.

Median values from single cells and boxplots of all cells were created. Black dotted median values represent significant changes in evaluated parameters between experimental conditions. Grey dotted median values failed the H0 hypothesis for significant difference. Median values are plotted in dark grey if data points were collected during cross correlation analysis. When analyzing the contribution of ionic currents during generation of PIR and rhythmic motor output median values were normalized to the median of the control values.

Traditional 'box style' box plots were created in matlab, showing the calculated median from all cells as well as representing with box edges the 25 %, 75 % percentiles and most extreme data points with the upper whisker and lower whisker. Outliers are plotted individually and marked by a cross.

If datasets from one single cell were shown in one graph, dot density plots were created. Median values were plotted as a horizontal line.

In plots analyzing instantaneous spike frequencies, second-degree polyfits were created from control data sets. Exponential fits second degrees were created from strongly declining instantaneous spike frequencies after PIR stimulations were executed. In one experiment a polynomial fit fourth degree was modeled from the experimental data during blocker application.

All graphs were created and statistical test were performed using matlab. Figures were created with Corel Draw X (Corel Cordporation, Ottawa, Canada).

2.6 Computational modeling of a half center CPG model

Simulations were performed using matlab. To simulate the alternating activities of IPS and IRS a half center CPG model, based on I_{NaP} and I_L, was used (Daun et al., 2009). I_H and I_A were integrated into the model, based on experimental findings.

Model equations

The ionic currents were descried by the following differential equations:

$$I_A(V) \quad = g_A A\, m_A(V)(V - E_A),$$

$$A' = \frac{(A_\infty(V)-A)}{\tau_A(V)},$$

$$\tau_A = \frac{1}{\epsilon \cosh(\gamma_{\tau A}(V-V_{A_{1/2}}))},$$

$$m_A(V) = \frac{1}{1+\exp(\gamma_A(V-V_{Am_{1/2}}))}$$

$$A_\infty(V) = \frac{1}{1+\exp(\gamma_{hA}(V-V_{A_{1/2}}))}$$

$g_A = 0.580$, $E_A = -80.0$, $\gamma_A = 0.1$, $\gamma_{hA} = -\frac{1.0}{1.6} = -0.625$, $\gamma_{\tau A} = 2.5\gamma_{hA}$,

$V_{Am_{1/2}} = -27.0$, $V_{A_{1/2}} = -74.0$.

$$I_H(V) = g_H H(V-E_H),$$

$$H' = \frac{(H_\infty(V)-H)}{\tau_H(V)},$$

$$\tau_H = \frac{1}{\epsilon \cosh(\gamma_{\tau H}(V-V_H))},$$

$$H_\infty(V) = \frac{1}{1+\exp(\gamma_H(V-V_H))}$$

$g_H = 2.153$, $E_h = -43.0$, $\gamma_H = -\frac{1}{15.5}$, $\gamma_{\tau H} = \gamma_H/2.8$, $V_H = -64.0$

where V is the membrane voltage, E the equilibrium potential of the respective current. Variable m indicates the activation variable of the transient potassium channel. Parameters values for I_A and I_H were obtained from Izhikevich (2007).

3. Results

The swimmeret system of crayfish provides a powerful tool to study rhythm generation and coordination of neuronal networks. The abdominal nervous system innervating the swimmerets is characterized by a small number of neurons. The nervous system mediates a very robust rhythmic activity that is highly coordinated. All neurons that are responsible for rhythm generation and coordination are identified and generate characteristic regular activity. Yet, it is not known to what degree single cell activity arises from synaptic input or how much intrinsic mechanisms of single neurons are necessary. Such intrinsic properties are crucial for proper generation of rhythmogenesis, coordination between the segments as well as for the transmission of information from the central pattern generator (CPG) to the muscles to execute the swimmeret movement.

With the help of electrophysiological methods, I aimed at unveiling such intrinsic properties in two groups of motor neurons (MNs) (Power Stroke Exciter (PSE), Return Stroke Exciter (RSE)), the neurons from the coordinating network (Ascending Coordinating Neuron (ASC_E), and Descending Coordinating Neuron (DSC), and Commissural Interneuron 1 (ComInt1)) as well as in one representative CPG neuron Inhibitor of Power Stroke (IPS).

The following work introduces a membrane property, the post-inhibitory rebound (PIR) in the swimmeret system that likely contributes to the generation of rhythmic motor activity. I systematically analyzed the presence of rebound responses in all neuron groups in the swimmeret system and continued identifying the underlying ionic conductances. Finally, I tested the significance of the identified ionic conductances for generation of a rhythmic motor output.

3.1 Unveiling the PIR phenotype in an intact swimmeret network

I injected a negative current during ongoing rhythmic activity, to test whether neurons in the swimmeret system produce a PIR. After hyperpolarizing the membrane for 3 s to test potentials (V_T) V_T = -100 mV the investigated neurons (PSE, ASC_E and IPS) responded with a PIR phenotype (Figure 6 Aii, Bii, C). I observed elevated initial firing frequency post stimulation of PSE and ASC_E, (peak frequency post stimulation: PSE: 22.3 Hz (Ai); ASC_E: 36.1 Hz (Bi)) compared to pre stimulation (peak frequency pre

stimulation: PSE: 16.6 Hz; ASC_E: 27.8 Hz; Figure 6). The increase in spike frequency was accompanied by a slight depolarization of the first oscillation peak values post stimulation (peak oscillation post stimulation as medians: PSE: -43.9 mV (Aii); ASC_E: -40.4 mV (Bii)) compared to amplitudes measured before the stimulation (oscillation amplitude pre stimulation as medians: PSE: -45.1 mV; ASC_E: -41.9 mV). A similar increase in oscillation amplitude post stimulation was observed in IPS (oscillation amplitude pre stimulation as medians: -36.7 mV; post stimulation: -34.9 mV (C)).

However, one major attribute that is almost always described in the context of generation of a PIR response, a sag potential, seemed to be missing in these neurons. Because the generation of a sag potential could possibly be masked by network effects, I applied synaptic blockers to the abdominal nerve cord to shut down the activity of all central pattern generating kernels to explore the characteristics of PIR responses in the previous described neurons groups of the swimmeret system but also of RSE, DSC and ComInt1.

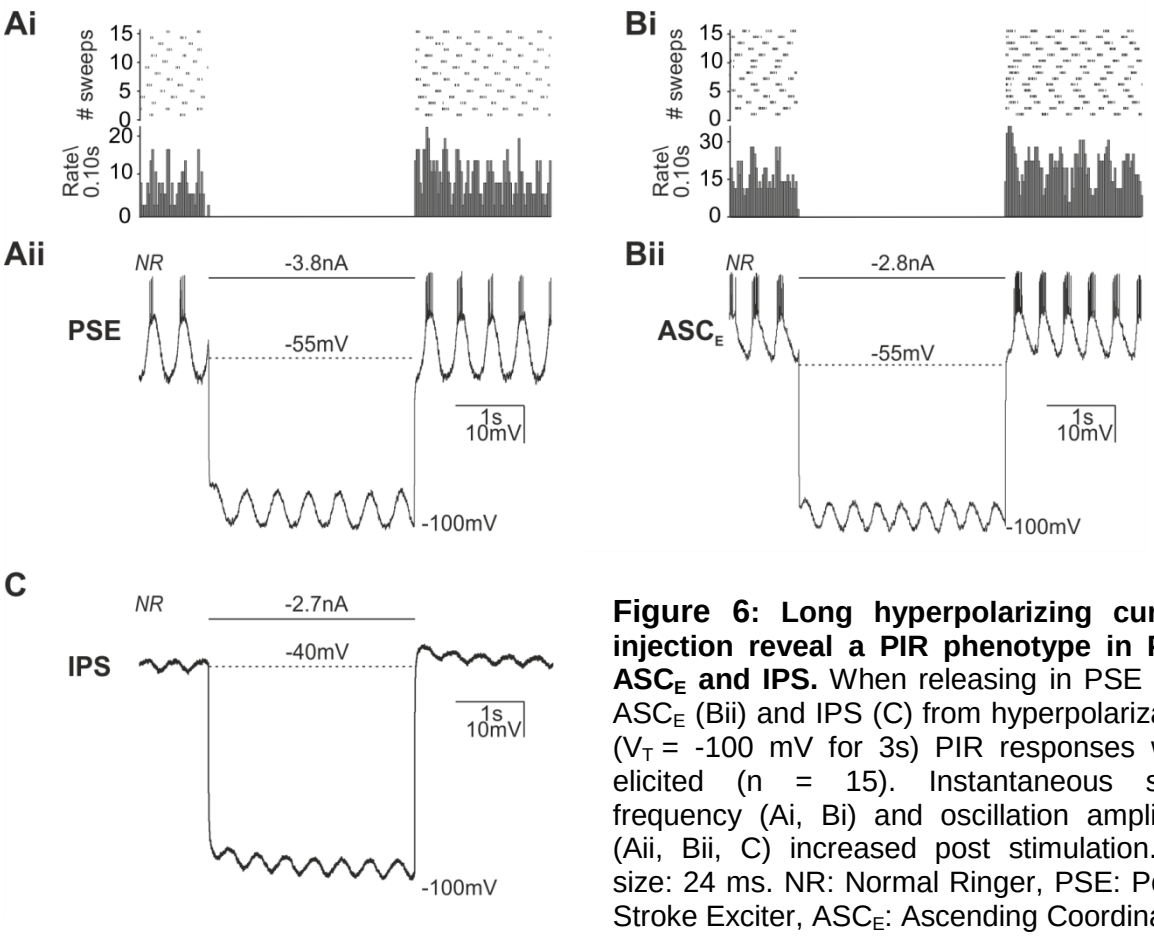

Figure 6: Long hyperpolarizing current injection reveal a PIR phenotype in PSE, ASC_E and IPS. When releasing in PSE (Aii), ASC_E (Bii) and IPS (C) from hyperpolarization (V_T = -100 mV for 3s) PIR responses were elicited (n = 15). Instantaneous spike frequency (Ai, Bi) and oscillation amplitude (Aii, Bii, C) increased post stimulation. bin size: 24 ms. NR: Normal Ringer, PSE: Power Stroke Exciter, ASC_E: Ascending Coordinating Neuron, IPS: Inhibitor of Power Stroke.

3.1.1 Breaking down network activity to elucidate cellular properties

I replaced the bathing solution with ringer solution containing a mixture of different synaptic blockers, to be able to analyze electrophysiological properties, like the generation of the PIR in the neurons of the swimmeret system without interference of rhythmic synaptic input and possible modulations.

The only transmitter identified so far is present in the Coordinating Neurons and presumably released from the Coordinating Neurons ASC_E and DSC at the synapse to ComInt1. This transmitter is Acetylcholine (Schneider et al., 2018). The transmitters at the remaining synapses have not been identified so far. However, puff application of glutamate and GABA on swimmeret MNs induced a hyperpolarization of membrane potentials (Sherff and Mulloney, 1996). Therefore likely transmitters at the synapses between the pattern generating kernel and the MNs are Glutamate and GABA. However, confirming evidence supporting this hypothesis is still missing. The transmitter used within the central pattern generator (CPG) as well as at the synapses to the Coordinating Neurons is unknown. Consequently synaptic blockers against all three common transmitters were used, that also covered different types of glutamate receptors.

Application of glutamatergic, cholinergic and GABAergic receptor blockers (CNQX, DNQX, DL-AP4, Tubocurarin, Picrotoxin, see Material and Methods, chapter 2.4) led to tonic motor output (Figure 7). In all intracellularly recorded neurons, regular oscillatory activity was abolished (PSE, N = 10 (Ai); RSE, N = 6 (Bi); ASC_E, N = 7 (Ci); DSC, N = 3 (Di); IPS, N = 9 (Ei); ComInt1, N = 9 (Di)), and all spiking neurons responded with tonic activity. In PSEs, RSEs, IPSs and ComInt1s the abolishment of oscillatory activity was accompanied by an increase in normalized input resistance (R_{IN}) (Figure 7 Aii, Bii, Eii, Fii). However, a significant increase was observed only in PSEs (as medians with interquartile range (IQR), Wilcoxon rank sum test: PSE: 1.39, 1.3 - 1.5, N = 10, $p < 0.002$; RSE: 1.26, 1.0 - 1.5, N = 6, $p > 0.05$; IPS: 1.1, 1.1 - 1.3, N = 9, $p > 0.05$, ComInt1: 1.0, 1.0 - 1.4, N = 9, $p > 0.05$). In ASC_{Es} (ASC_E: 0.9, 0.9 - 1.3, N = 7, $p > 0.05$) and DSCs (DSC: 0.9, 0.9 – 1.0, N = 3) R_{IN} were not reliably affected. No statistical test was performed in DSC, because of the low sample size.

After synaptic blocker application, varying degrees of membrane noise were observed in all recordings. Especially in ComInt1s such observations were obvious,

leading to the conclusion that synaptic transmission from Coordinating Neurons to ComInt1 was partially still functional. Regarding this and the sometimes variable effects of synaptic blocker application on R_{IN} indicates that synaptic isolation was not complete. Nevertheless, the obvious abolishment of oscillatory activity suggests that CPG activity had paused. Therefore I started analyzing PIR responses without interference of rhythmic synaptic input mediated by the CPGs.

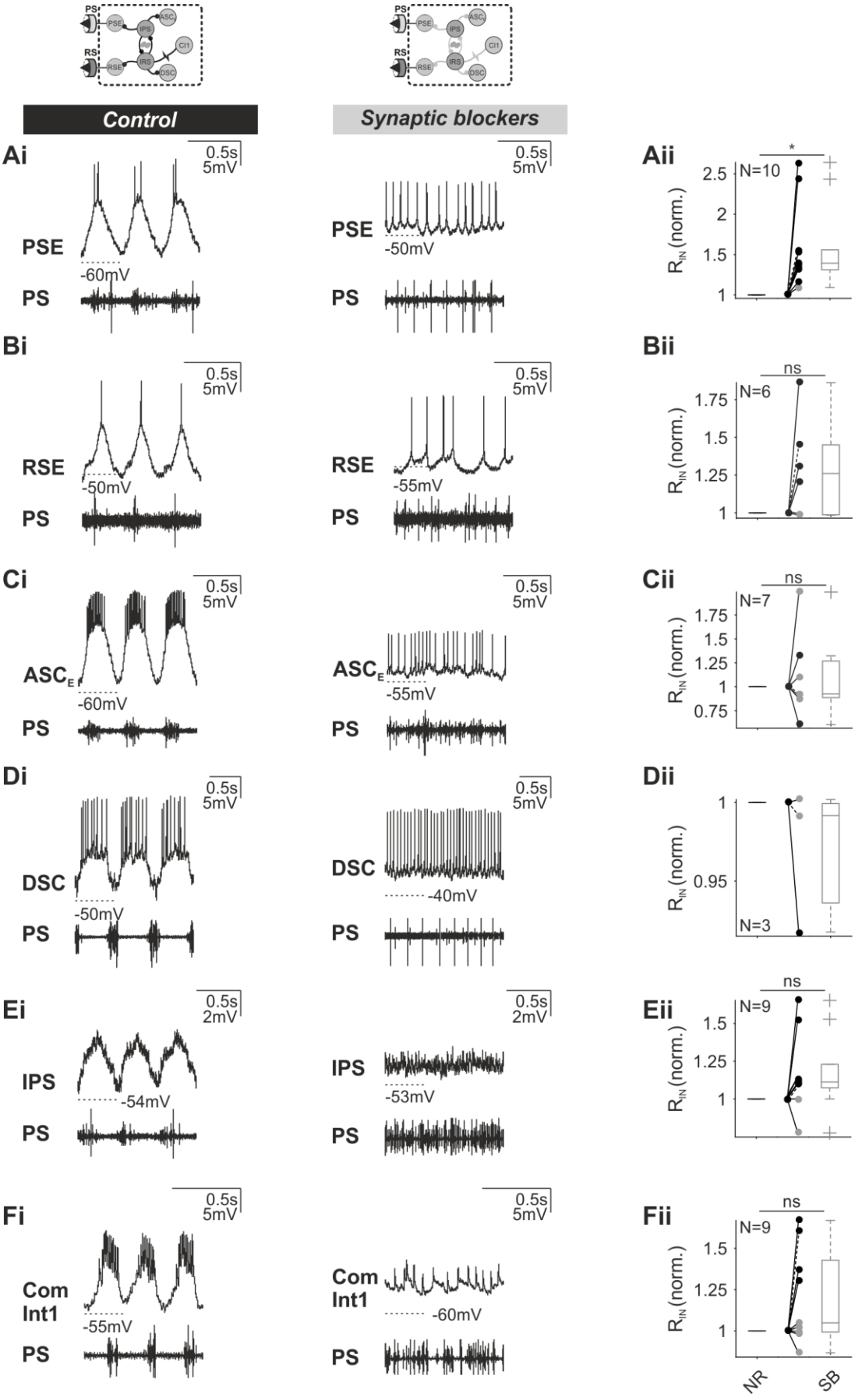
Control
Synaptic blockers
Ai
PSE
-60mV
PS
0.5s
5mV
-50mV
Aii
N=10
*
Bi
RSE
-50mV
-55mV
Bii
N=6
ns
Ci
ASC$_E$
-60mV
-55mV
Cii
N=7
Di
DSC
-50mV
-40mV
Dii
N=3
Ei
IPS
-54mV
-53mV
0.5s
2mV
Eii
N=9
Fi
Com Int1
-55mV
-60mV
Fii
R$_{IN}$ (norm.)
NR
SB

3.2 Cellular properties in neurons of the swimmeret system – PIR

After observing a PIR response of PSE, ASC_E and IPS in normal ringer solution, the question was raised whether other neurons in the swimmeret system (DSC and RSE, and ComInt1) display a PIR as well.

In the first part of this chapter (chapter 3.2.1), I examined the presence of PIR responses in four spiking neurons of the swimmeret system (PSE, RSE, ASC_E, DSC). In the second part (chapter 3.2.2), I analyzed PIR responses in non-spiking interneurons (IPS, ComInt1).

3.2.1 PIR in four types of spiking neurons in the swimmeret system

After recording intracellularly from PSE, RSE, ASC_E and DSC, I applied synaptic blockers to the abdominal nervous system to study PIR responses in these cells.

The expression of PIR with regard to its dependency to pre stimulus holding potentials (V_H) was analyzed by setting the membrane potential of all neurons to three different holding potentials (V_H = -40 mV, V_H = -50 mV and V_H = -60 mV) (Figure 8 A - D). For each V_H, I injected a series of negative current pulses with incrementing amplitudes, hyperpolarizing the neurons to approximately three different test potentials (V_T) (V_T = -80 mV, V_T = -90 mV, and V_T = -100 mV), to test the dependence of PIR responses on the test potential.

Figure 7: Synaptic isolation of swimmeret neurons. Intracellular recordings of swimmeret neurons during control condition (NR) and during synaptic isolation (SB) (Ai, Bi, Ci, Di, Ei, Fi). Rhythmic motor output became tonic and oscillatory activity of neurons was abolished. R_{IN} increased in PSEs (N = 10, Aii), RSE (N = 6, Bii), IPSs (N = 9, Eii), and ComInt1s (N = 9, Fii). Blocker application did not affect R_{IN} in ASC_{Es} (N = 7, Cii) and DSCs (N = 3, Dii). Box plots compare R_{IN} during NR and during SB condition. Markers: normalized median values of single experiments (black markers: significant change of evaluated parameter, grey makers: represent failed statistical test), dashed lines: results from exemplary recording, PSE: Power Stroke Exciter, RSE: Return Stroke Exciter, ASC_E: Ascending Coordinating Neuron, DSC: Descending Coordinating Neuron, IPS: Inhibitor of Power Stroke, ComInt1: Commissural Interneuron 1, PS: Power Stroke, R_{IN}: input resistance, NR: normal ringer, SB: synaptic blocker, Wilcoxon rank sum test *: $p < 0.05$, ns: $p > 0.05$ (Supplemental Figures 1 – 6).

Most neurons responded with a voltage sag during the hyperpolarization. The sag potential was slowly activating and was only detected during stimulations longer than 300 ms (not shown). Following the end of hyperpolarizing current injection, the neurons (PSE, RSE, ASC_E and DSC) depolarized above the V_H level (Figure 8 A - D). At more depolarized V_Hs, all neurons responded with an increase in instantaneous firing frequency compared to pre stimulation (Figure 8 A - D). At V_Hs below spike threshold some neurons responded with a rebound burst of spikes (Figure 8 A, B, D, third column). Some neurons, like ASC_E (Figure 8 C, third column) on the other hand remained sub spike threshold.

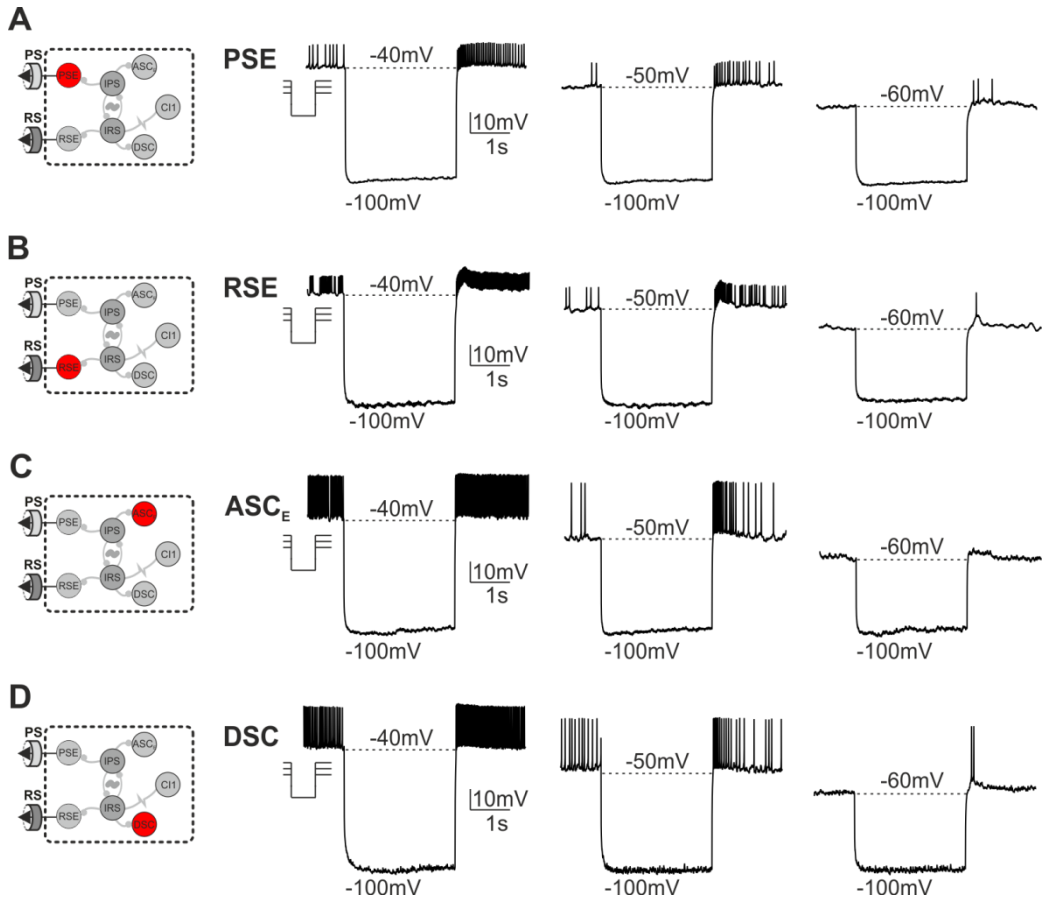

Figure 8: PIR responses in four groups of spiking neurons. Schematic of recorded neuron group. Representative PIR responses at different holding potentials (V_H = -40 mV, V_H = -50 mV and V_H = -60 mV) to V_T = -100mV are shown for single spiking neurons PSE (A), RSE (B), ASC_E (C) and DSC (D). All neurons displayed voltage sag, PIR depolarization, and rebound firing. PSE: Power Stroke Exciter, RSE: Return Stroke Exciter, ASC_E: Ascending Coordinating Neuron, DSC: Descending Coordinating Neuron, PIR: post-inhibitory rebound, V_H: holding potential, V_T: test potential.

3.2.1.1 Post-inhibitory rebound amplitudes

The evoked PIR depolarization amplitudes varied between preparations as well as between neuron groups (Figure 11). Figure 11 shows exemplary PSE, RSE, ASC_E and DSC recordings, respectively. First shown are the voltage traces of 15 executed sweeps during PIR stimulations from a fixed holding potential (V_H = -40 mV) to different test potentials (V_T = -100 mV, V_T = -90 mV, and V_T = -80 mV) (Fig 11 Ai - Di). Presented second are the voltage traces from different holding potentials (V_H = -40 mV, V_H = -50 mV, and V_H = -60 mV) to a specific test potential (V_T = -100 mV) (Fig 11 Aii – Dii). Single voltage traces were smoothed to erase APs, to facilitate examinations of PIR depolarizations.

In figure 11 Aiii - Diii, the median PIR amplitude values of single neurons are plotted against the pulse potential reached during the stimulation and sorted according to V_H (left graph: V_H = -40 mV, center graph: V_H = -50 mV, right graph: V_H = -60 mV). Note that Y-axis labeling was adjusted in each graph instead of keeping consistent during the analysis, to facilitate the visibility of changes observed during the different stimuli.

Motor neurons (PSE) All PSEs neurons that were tested elicited rebound depolarizations upon release from hyperpolarizing current pulses (Figure 9 Aiii). PIR stimulations from holding potentials of V_H = -40 mV to V_T = -100 mV and V_T = -80 mV caused a significant reduction in generated PIR amplitudes that correlated to less hyperpolarized test potentials (V_H = -40 mV: V_T -100 mV - V_T -80 mV, Friedman test: $p < 0.0013$; Figure 9 Ai, Aiii, left graph, and Table 1, left column).

However, changing V_T during PIR stimulation from the other V_H = -50 mV and V_H = -60 mV did not cause a correlated change in PIR depolarization amplitudes (Figure 9 Aiii, center and right graph; Table 1, center and right column).

To assess the dependence of the holding potential on the generated PIR amplitudes, PIR amplitude values were compared between the different V_Hs, induced by maximum stimulations reaching V_T = -100 mV (Figure 9, Aii, Aiii, Table 1). Here, PIR amplitudes elicited between holding potentials did not change significantly. A high variance in evoked rebound depolarizations was apparent, between different PSE neurons.

One neuron showed a clear increase in PIR amplitude at more negative V_H = -60 mV compared to more depolarized V_H = -50 mV and V_H = -40 mV. Furthermore it showed prominently larger PIR amplitude values than all other PSEs. PIR depolarizations amplitudes reached up to 17 mV at V_H = -60 mV.

PSE	V_H = -40 mV			V_H = -50 mV			V_H = -60 mV		
V_T [mv]	-100	-90	-80	-100	-90	-80	-100	-90	-80
25 IQR [mV]	2.15	1.72	0.73	1.58	2.03	1.35	0.82	1.23	0.84
mdn [mV]	2.9	2.32	1.33	2.38	2.93	1.98	2.4	2.71	2.08
75 IQR [mV]	4.04	3.61	1.99	3.42	3.73	2.41	3.49	5.3	4.65

Table 1: Summary of median PIR amplitudes elicited in PSEs during PIR stimulations from three different holding potentials (V_H = -40 mV, V_H = -50 mV, and V_H = -60 mV) to three different test potentials (V_T = -100 mV, V_T = -90 mV, and V_T = -80 mV).

Motor neurons (RSE) In all recorded RSE neurons, no significant changes in the median PIR amplitudes were observed for any of the tested PIR stimulations (V_H = -40 mV, V_H = -50 mV, V_H = -60 mV) (Figure 9 Bii, Biii; Table 2). Furthermore median PIR amplitudes did not depend on different test potentials (V_T = -100 mV, V_T = -90 mV, V_T = -80 mV) at neither of the tested holding potentials (Figure 9 Bi, Biii and Table 2). Only minor reductions in PIR amplitudes were observed when stimulating RSE to less hyperpolarized V_T during different PIR stimulations.

RSE	V_H = -40 mV			V_H = -50 mV			V_H = -60 mV		
V_T [mv]	-100	-90	-80	-100	-90	-80	-100	-90	-80
25 IQR [mV]	2.29	1.85	1.26	1.27	1.4	1.47	0.66	0.45	0.69
mdn [mV]	4.2	3.35	2.18	4.47	3.37	2.21	1.98	1.67	1.35
75 IQR [mV]	5.28	4.81	3.52	5.42	4.38	3.04	3.73	3	2.35

Table 2: Summary of median PIR amplitudes elicited in RSEs during PIR stimulations from three different holding potentials (V_H = -40 mV, V_H = -50 mV, and V_H = -60 mV) to three different test potentials (V_T = -100 mV, V_T = -90 mV, and V_T = -80 mV).

Coordinating Neurons (ASC_E, DSC) In both ASC_{Es} and DSCs, PIR stimulations of different holding potentials, *i.e.* V_H = -40 mV, V_H = -50 mV, and V_H = -60 mV, did not cause a reliable change in PIR amplitudes at V_T = -100 mV (Figure 9 Cii, Ciii, Dii, Diii; Table 3, 4). Additionally, no significant correlation was found between different test potentials elicited from constant V_H (Figure 9 Ci, Ciii, Di, Diii and Table 3, 4). Only a slight decrease in PIR amplitudes with less hyperpolarized V_T was observed in single trials in both neuron groups.

ASC_E	V_H = -40 mV			V_H = -50 mV			V_H = -60 mV		
V_T [mv]	-100	-90	-80	-100	-90	-80	-100	-90	-80
25 IQR [mV]	2.23	1.5	1.21	2.98	2.57	1.93	2.09	1.74	1.62
mdn [mV]	2.99	2.8	2.47	3.42	2.99	3.08	3.67	2.68	1.75
75 IQR [mV]	4.03	3.89	2.8	4.03	4.93	4.51	4.26	3.54	2.99

Table 3: Summary of median PIR amplitudes elicited in ASC_Es during PIR stimulations from three different holding potentials (V_H = -40 mV, V_H = -50 mV, and V_H = -60 mV) to three different test potentials (V_T = -100 mV, V_T = -90 mV and V_T = -80 mV).

DSC	V_H = -40 mV			V_H = -50 mV			V_H = -60 mV		
V_T [mv]	-100	-90	-80	-100	-90	-80	-100	-90	-80
25 IQR [mV]	1.37	1.01	0.53	1.84	1.2	1.33	1.59	1.58	1.19
mdn [mV]	3.46	1.97	0.58	4.43	3.07	3.46	3.3	3.79	2.85
75 IQR [mV]	4.49	3.54	3.03	7.05	5.82	3.77	3.94	4.04	3.43

Table 4: Summary of median PIR amplitudes elicited in DSCs during PIR stimulations from three different holding potentials (V_H = -40 mV, V_H = -50 mV, and V_H = -60 mV) to three different test potentials (V_T = -100 mV, V_T = -90 mV and V_T = -80 mV).

All recorded neurons responded with PIR when being released from hyperpolarizing current pulses. However, in the different neuron types changes in membrane voltages (V_H or V_T) did not alter PIR amplitudes reliably.

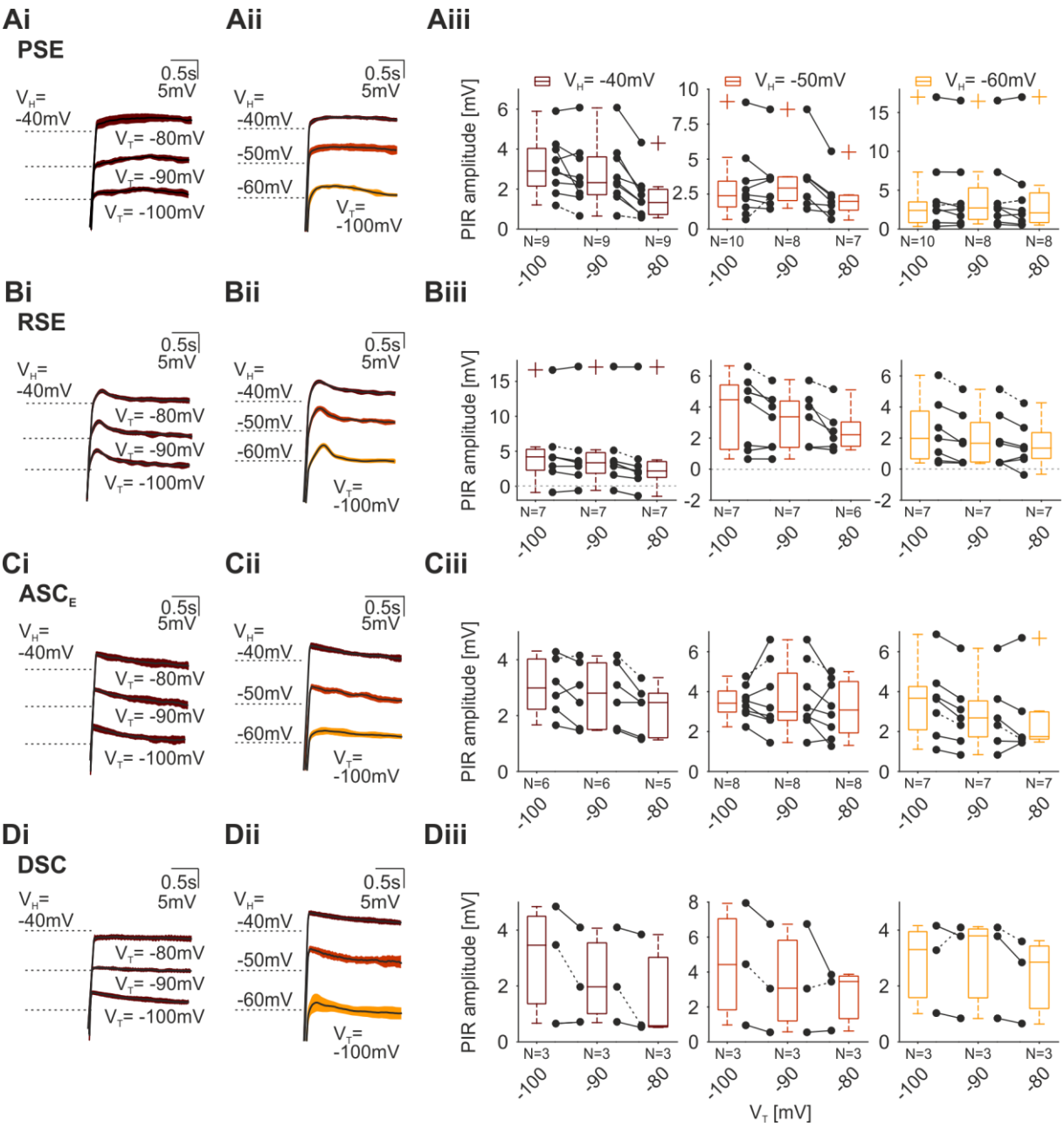

Figure 9: PIR amplitudes in four types of spiking neurons in the swimmeret system. After the termination of hyperpolarizing current pulses, all tested spiking neurons depolarized above V_H level. In the majority of experiments, changes in V_T and V_H did not cause reliable changes in PIR amplitudes. Mean intracellular voltage traces of 15 consecutive PIR stimulations (black line) for PSE (Ai, Aii), RSE (Bi, Bii), ASC_E (Ci, Cii), and DSC (Di, Dii). Standard deviation of voltage traces are shown in color coded areas. Color codes represent different V_H. Voltage traces are smoothed to erase APs. Box plots compare PIR amplitudes between different V_Hs and V_Ts (V_H = -40 mV, V_H = -50 mV and V_H = -60 mV to V_T = -100 mV, V_T = -90 mV, and V_T = -80 mV). Markers: median PIR amplitudes of single experiments, dashed lines: results from exemplary recording, PIR: post-inhibitory rebound, PSE: Power Stroke Exciter, RSE: Return Stroke Exciter, ASC_E: Ascending Coordinating Neuron, DSC: Descending Coordinating Neuron, V_H: holding potential, V_T: test potential (Supplemental Figures 7 – 10).

3.2.1.2 Sag potential amplitude

When performing PIR stimulations, most of the neurons displayed a sag potential during the hyperpolarizing current pulses. However, for each tested group of neurons, some cells where identified that did not express a sag potential and some of them even tended to hyperpolarize during the pulse. In those recordings it remained inconclusive whether these neurons lacked the ability to produce a sag potential or whether it was masked by ionic currents that counteracted a sag depolarization. Hence from all neurons the voltage difference between the beginning of the current injection and the end was calculated. If a sag potential was detected, this resulted in a positive sag potential amplitude. In those cells where no sag potential was detected, this lead to 0 mV changes or negative amplitudes.

As in the previous chapter, mean voltage traces (15 sweeps) of evoked sag potentials from single exemplary neurons are illustrated in figure 10. Here, sag potentials during stimulations from a fixed holding potential (V_H = -40 mV) to three different test potentials (V_T = -100 mV, V_T = -90 mV, V_T = -80mV) are presented in figure 10 Ai - Di, while stimulations from three different holding potentials (V_H = -40 mV, V_H = -50 mV, and V_H = -60 mV) to only one test potential (V_T = -100 mV) are shown in figure 10 Aii - Dii.

Motor neurons (PSE, RSE) During hyperpolarizing current pulses voltage sags were elicited in most of the tested PSEs and RSEs.

Changing the test potentials (V_T) (V_T = -100 mV, V_T = -90 mV, V_T = -80mV) during PIR stimulations at holding potentials of V_H = -40 mV, V_H = -50 mV, or V_H = -60 mV did not cause a reliable change in evoked sag potential amplitudes (Figure 10 Ai, Aiii, Bi, Biii; Table 5, 6). However voltage sag amplitudes tended to decrease at more depolarized V_T compared to more hyperpolarized V_T. No significant change in voltage sag amplitudes was observed between different holding potentials (Figure 10 Aii, Aiii, Bii, Biii; Table 5, 6). However, median sag amplitudes slightly declined with more hyperpolarized V_H = -50 mV and V_H = -60 mV compared to V_H = -40 mV.

PSE	V_H = -40 mV			V_H = -50 mV			V_H = -60 mV		
V_T [mV]	-100	-90	-80	-100	-90	-80	-100	-90	-80
25 IQR [mV]	-0.16	-0.27	0.16	-0.13	0.28	0.19	0.24	0.15	-0.05
mdn [mV]	0.63	0.54	0.43	0.5	0.92	0.27	0.49	0.46	0.19
75 IQR [mV]	2.24	1.11	0.6	2.4	2.09	0.37	2.16	1.82	1.03

Table 5: Summary of median sag potential amplitudes elicited in PSEs during PIR stimulations from three different holding potentials (V_H = -40 mV, V_H = -50 mV, and V_H = -60 mV) to three different test potentials (V_T = -100 mV, V_T = -90 mV and V_T = -80 mV).

RSE	V_H = -40 mV			V_H = -50 mV			V_H = -60 mV		
V_T [mV]	-100	-90	-80	-100	-90	-80	-100	-90	-80
25 IQR [mV]	-1.34	-0.8	-0.13	-1.02	-0.65	-0.25	-0.63	-0.33	-0.14
Mdn [mV]	0.39	0.44	0.2	0.54	0.33	0.18	0.47	0.53	0.28
75 IQR [mV]	1.67	1.24	0.3	1.63	0.8	0.32	1.22	0.82	0.53

Table 6: Summary of median sag potential amplitudes elicited in RSEs during PIR stimulations from three different holding potentials (V_H = -40 mV, V_H = -50 mV, and V_H = -60 mV) to three different test potentials (V_T = -100 mV, V_T = -90 mV and V_T = -80 mV).

Coordinating Neurons (ASC_E, DSC) Similarly as in the above described MN groups, no significant change in median sag potential amplitudes was observed at different test potentials (V_T) in the Coordinating Neurons ASC_Es and DSCs (Figure 10 Ci, Ciii, Di, Diii; Table 7, 8). Only a slight decline in sag potential amplitudes was observed when changing V_T to more depolarized holding potentials. Furthermore, median sag amplitudes elicited at V_T = -100 mV between different V_H = -40 mV, V_H = -50 mV, and V_H = -60 mV did not show a consistent change (Figure 10 Cii, Ciii, Dii, Diii, Table 7, 8).

ASC_E	V_H = -40 mV			V_H = -50 mV			V_H = -60 mV		
V_T [mv]	-100	-90	-80	-100	-90	-80	-100	-90	-80
25 IQR [mV]	0.76	0.95	1	0.51	0.72	0.66	0.49	0.42	0.12
Mdn [mV]	1.19	1.1	1.04	0.83	1.13	0.84	1.21	0.61	0.64
75 IQR [mV]	1.96	1.61	1.62	2.48	2.21	1.17	2.13	1.43	1.31

Table 7: Summary of median sag potential amplitudes elicited in ASC_Es during PIR stimulations from three different holding potentials (V_H = -40 mV, V_H = -50 mV, and V_H = -60 mV) to three different test potentials (V_T = -100 mV, V_T = -90 mV and V_T = -80 mV).

DSC	V_H = -40 mV			V_H = -50 mV			V_H = -60 mV		
V_T [mv]	-100	-90	-80	-100	-90	-80	-100	-90	-80
25 IQR [mV]	-0.39	-0.16	-0.29	0.05	-0.39	-0.3	0.23	0.14	-0.16
Mdn [mV]	0.83	0.38	0.24	0.18	-0.34	0.03	0.43	0.26	0.07
75 IQR [mV]	2.58	1.76	0.49	2.01	1.33	0.47	1.7	1.14	0.69

Table 8: Summary of median sag potential amplitudes elicited in DSCs during PIR stimulations from three different holding potentials (V_H = -40 mV, V_H = -50 mV, and V_H = -60 mV) to three different test potentials (V_T = -100 mV, V_T = -90 mV and V_T = -80 mV).

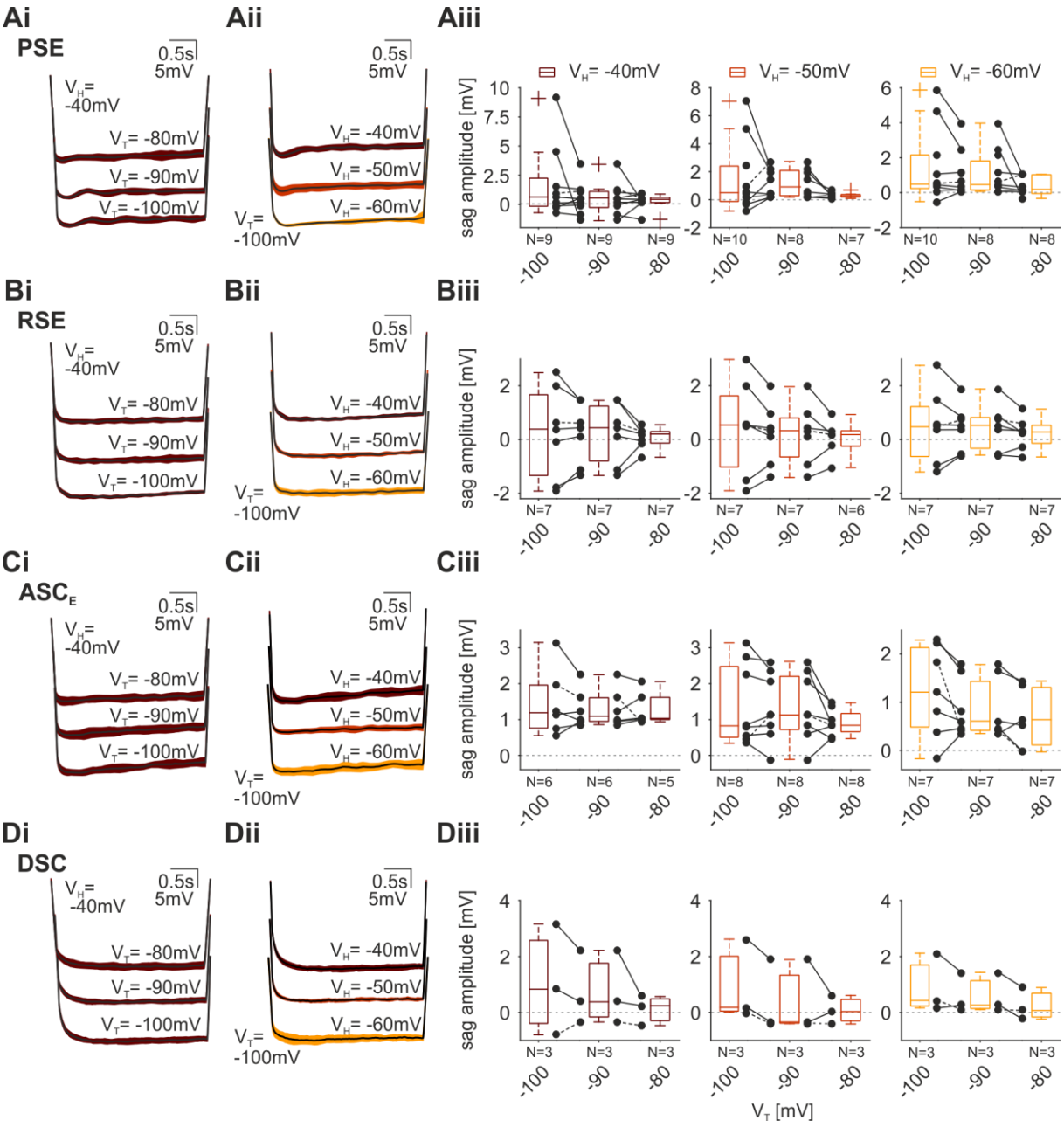

Figure 10: Voltage sags in four spiking neuron groups of the swimmeret system. During hyperpolarizing current pulses sag potentials are elicited. Changes in sag amplitudes did not correlate to changes in V_T or V_H. Mean intracellular voltage traces of 15 consecutive PIR stimulations (black line), PSE (Ai, Aii), RSE (Bi, Bii), ASC_E (Ci, Cii), DSC (Di, Dii). Standard deviation of voltage traces are shown in color coded areas. Color codes represent different V_H. Voltage traces are smoothed. (Aiii - Diii) Box plots compare sag amplitudes between different V_Hs and V_Ts (V_H = -40 mV, V_H = -50 mV and V_H = -60 mV to V_T = -100 mV, V_T = -90 mV, and V_T = -80 mV). Markers: median sag amplitudes of single experiments, dashed lines: results from exemplary recording, PSE: Power Stroke Exciter, RSE: Return Stroke Exciter, ASC_E: Ascending Coordinating Neuron, DSC: Descending Coordinating Neuron, PIR: post-inhibitory rebound, V_H: holding potential, V_T: test potential (Supplemental Figures 13 – 16).

3.2.1.3 Firing activity

All neurons of the examined groups showed a modulation of firing frequency post hyperpolarizing current injection compared to pre current injection.

In PSEs, RSEs, ASC_ES, and DSCs, instantaneous AP generation frequencies were compared at V_H = -40 mV elicited by PIR stimulations reaching different V_T (Figure 11). Note, that only those frequency modulations were analyzed that were characterized by rather constant baseline firing frequency throughout the stimulations. Therefore, the number of samples varies with regard to rebound and voltage sag potential amplitude measurements.

Motor neurons (PSE) PIR stimulations in PSEs resulted in an increase in instantaneous firing frequency when releasing the neuron from hyperpolarizing current pulses. Exemplary PIR stimulations from a fixed holding potential (V_H = -40 mV) to three different test potentials (V_T = -80 mV, V_T = -90 mV, and V_T = -100 mV) are shown in figure 11 Ai. Mean instantaneous spike frequencies of 15 executed PIR stimulations, measured in Figure 11 Ai are shown in figure 11 Aii. Current injections to strongly hyperpolarized test potentials resulted in higher instantaneous rebound frequencies than current injections to more depolarized test potentials (V_T = -100 mV: 33.6 Hz ± 4.9; V_T = -90 mV: 32.8 Hz ± 5.0; V_T = -80 mV: 31.2 Hz ± 4.1; Figure 11 Aii). After reaching maximum firing frequency, AP generation declined exponentially until the baseline frequencies of 9.4 Hz were reached. All of the eight PSEs tested, generated rebound spikes when stimulated to V_T = -100 mV and V_T = -90 mV. When stimulating to V_T = -80 mV two neurons were depolarized sub spike threshold. In all PSEs a significant higher maximum instantaneous firing frequency was detected when hyperpolarizing to V_T = -100 mV compared to V_T = -90 mV and V_T = -80 mV (Friedman test: V_T = -100 mV - V_T = -90 mV: $p < 0.0471$, $N = 8$; V_T = -90 mV - V_T = -80 mV: $p < 0.0395$, $6 < N < 8$; Figure 11 Aiii).

Motor neurons (RSE) Similar to what has been observed in PSEs, recordings in RSEs revealed an increase in firing frequency when releasing the neurons from hyperpolarizing current injections (Figure 11 Bi, Bii). This increase in

firing frequency correlated with the test potential (Figure 11 Bii). During more hyperpolarized V_T a higher mean instantaneous firing frequency was elicited (V_T = -100 mV: 92.1 Hz ± 6.8) compared to more depolarized test potentials (V_T = -90 mV: 82.6 Hz ± 8.2; V_T = -80 mV: 76.7 Hz ± 7.3). Instantaneous firing frequencies decreased exponentially during all stimulations until baseline firing frequencies of 40.5 Hz ± 5.3 were reached. In four out of six RSEs maximum instantaneous firing frequency decreased between V_T = -100 mV, V_T = -90 mV, and V_T = -90 mV, V_T = -80 mV (Friedman test: $p > 0.05$, N = 6; Figure 11 Biii).

Coordinating Neurons (ASC_E) ASC_Es responded with a similar modulation in rebound burst discharges when the neurons were stimulated with hyperpolarizing current pulses. When hyperpolarizing ASC_Es from V_H = -40 mV to three different test potentials (V_T = -100 mV, -90 mV, and -80 mV), an increase in instantaneous firing frequency was observed that slightly depended on the test potential (Figure 11 Ci, Cii, Ciii). Instantaneous firing frequencies increased when hyperpolarizing the neuron to more negative test potentials compared to less hyperpolarized test potentials (V_T -100 mV: 165.6 Hz ± 9.1; V_T -90 mV: 162.2 Hz ± 9.9; V_T -80 mV: 159.6 Hz ± 9.4). All instantaneous firing frequencies declined after PIR stimulations until baseline firing frequencies were reached at 42.2 Hz ± 4.33. The decline was characterized by a second-order exponential fit (Figure 11 Cii).

Out of six ASC_Es tested, four showed a decrease in maximum instantaneous rebound frequency when hyperpolarized to V_T = -90 mV compared to V_T = -100 mV (Friedman test: $p > 0.05$, N = 6; Figure 11 Ciii). Five ASC_Es showed a further reduction when hyperpolarizing the neurons to V_T = -80 mV.

Coordinating Neurons (DSC) In DSCs an increase in instantaneous frequency was detected when releasing the neuron from hyperpolarizing current pulses (Figure 11 Dii, Diii). When hyperpolarizing the neuron to most hyperpolarized test potentials the strongest acceleration in rebound firing was detected (V_T = -100 mV: 123 Hz ± 8.0). Stimulations to more depolarized test potentials elicited lower firing frequencies (V_T = -90 mV: 50.6 Hz ± 5.1; V_T -80 mV: 23.3 Hz ± 4.8; Figure 11 Dii). Note that baseline firing frequency showed a slight reduction between

V_T = -100 mV (26.6 Hz ± 7.2) and V_T = -90 mV (15.8 Hz ± 2.9) and V_T = -80 mV (15.1 Hz ± 4.1). Instantaneous firing frequency elicited from all three test potentials declined exponentially (Figure 11 Dii). Maximum instantaneous firing frequencies in both DSCs decreased between PIR stimulations reaching V_T = -100 mV and V_T = -90 mV (Figure 11 Diii). A further reduction in maximum instantaneous firing frequency was observed when hyperpolarizing to V_T = -90 mV and V_T = -80 mV. No statistical test was performed because of the low sample size.

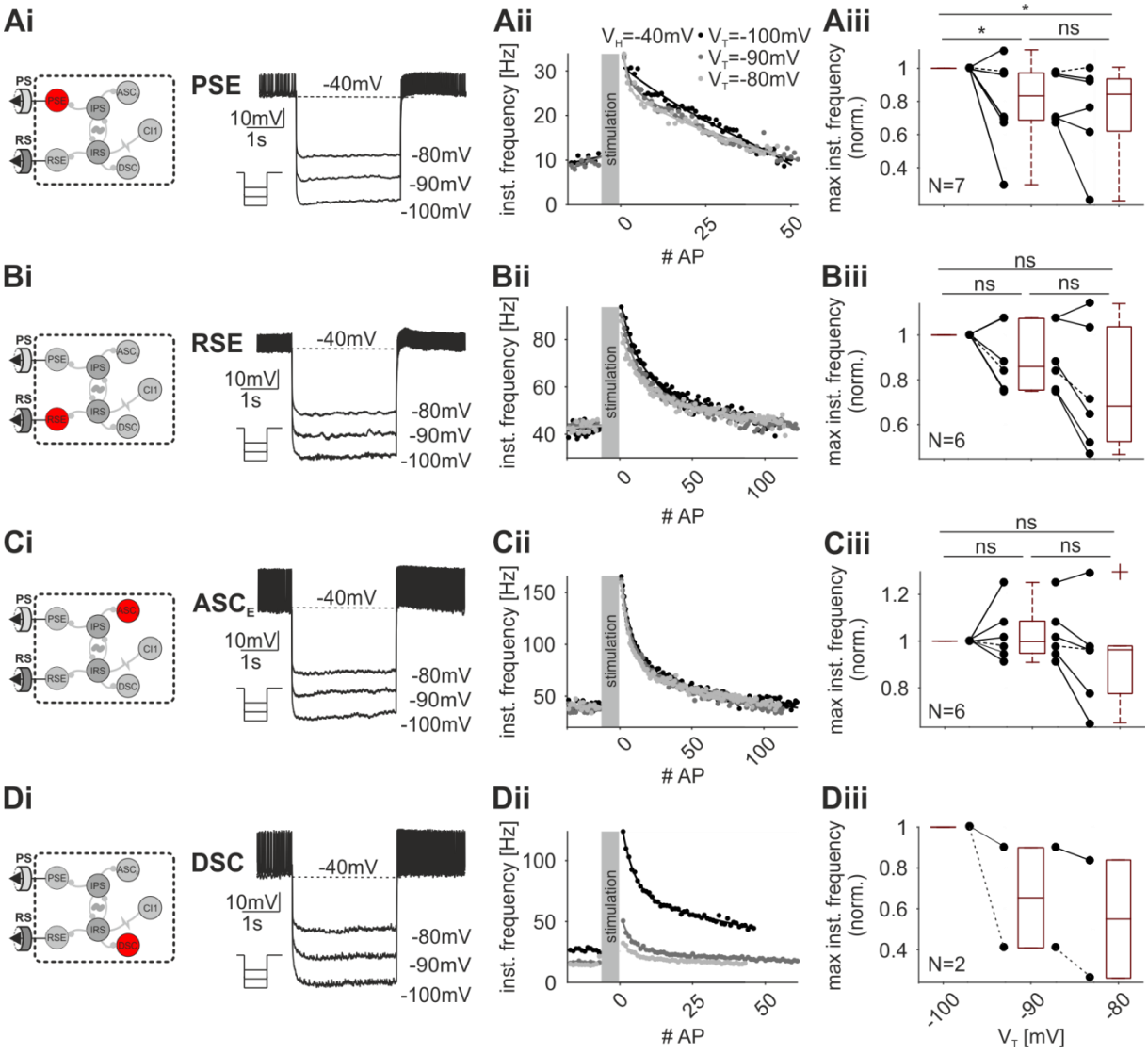

Figure 11: Modulation fast rebound firing by changes in V_T. Schematic of recorded neurons. Representative PIR responses at holding potentials of V_H = -40 mV reaching different test potentials V_T = -100 mV, V_T = -90 mV, and V_T = -80 mV are shown of single spiking neurons PSE (Ai), RSE (Bi), ASC_E (Ci) and DSC (Dii). Mean instantaneous firing frequencies are plotted against the number of APs following the stimulation. Spike frequencies declined until baseline frequencies were reached and was characterized by a second-order exponential fit for all three V_Ts. PSE (Aii), RSE (Bii), ASC_E (Cii) and DSC (Dii).

Color codes represent different V_T at constant V_H = -40 mV. Maximum instantaneous firing frequencies in most neurons correlated to changes in V_T (Aiii, Biii, Ciii, Diii). Markers: normalized median maximum instantaneous frequency of single experiments, dashed lines: results from exemplary recording. PSE: Power Stroke Exciter, RSE: Return Stroke Exciter, ASC_E: Ascending Coordinating Neuron, DSC: Descending Coordinating Neuron, PIR: post-inhibitory rebound, V_H: holding potential, V_T: test potential, AP: action potential, Wilcoxon rank sum test *: $p < 0.05$, ns: $p > 0.05$ (Supplemental Figures 19 – 22).

3.2.1.4 Latency of the first spike after hyperpolarizing current pulses

One other spiking feature that was modulated during the different PIR stimulations was the rebound latency. Depending on the holding potentials and the test potential a change in the interval to the first rebound spike was observed in some neurons. In Figure 12, representative recordings of neurons are shown for each of the four tested spiking neuron groups, as well as median values of first spike latencies plotted against the different V_T and arranged according to V_H. Comparing median first spike latencies in the different neuron groups at different membrane potentials never induced a significant change due to high variances in single neuron latencies. However, depending on different V_H and V_T, slight changes in the duration until the first rebound spikes were elicited.

Motor neurons (PSE) PIR stimulations in PSEs resulted in fast rebound firing with slightly modulated rebound latencies correlating to changes in V_T (Figure 12 Ai, Aii, Aiii; Table 9). PIR stimulation executed from a fixed holding potential (V_H = -40 mV) to most hyperpolarized test potentials (V_T = -100 mV) depolarized all PSEs supra spike threshold and led to rebound firing (Figure 12 Ai, Aiii, left graph; Table 9). When hyperpolarizing the neurons from the same membrane potential to more depolarized test potentials rebound latencies decreased slightly (Figure 12 Aiii, left graph; Table 9, left column). At more hyperpolarized holding potentials of V_H = -50 mV and V_H = -60 mV no correlation of first spike latencies was seen when changing V_T (Figure 12 Aiii, center and right graph; Table 9, center and right column).

Between different holding potentials all PSEs were characterized by longer first spike latencies at more hyperpolarized V_H compared to more depolarized V_H when stimulating to V_T= -100mV (Figure 12 Aii, Aiii; Table 9).

PSE	V_H = -40 mV			V_H = -50 mV			V_H = -60 mV		
V_T [mV]	-100	-90	-80	-100	-90	-80	-100	-90	-80
25 IQR [ms]	25	23	19	29	22	20	73	81	95
mdn [ms]	34	32	26	50	41	41	138	85	158
75 IQR [ms]	58	58	44	93	81	116	216	252	278

Table 9: Summary of median rebound spike latencies elicited in PSEs during PIR stimulations from three different holding potentials (V_H = -40 mV, V_H = -50 mV, and V_H = -60 mV) to three different test potentials (V_T = -100 mV, V_T = -90 mV and V_T = -80 mV).

Motor neurons (RSE) In RSEs, slightly varying rebound latencies were elicited when the neurons were released from hyperpolarizing current pulses. In contrast to PSEs, no reliable modulation in rebound latencies was observed when changing test potentials at a fixed holding potential (V_H = -40 mV) (Figure 12 Bi, Biii left graph; Table 10). At more hyperpolarized holding potentials of V_H = -50 mV not all neurons reached spike threshold. Those that did, showed slightly longer rebound latencies at more depolarized V_T compared to more hyperpolarized V_T (Figure 12 Biii center graph and Table 10, center column). At V_H = -60 mV even less neurons were depolarized above AP threshold, but similar tendencies on rebound durations was observed between different V_T, as seen at V_H = -50 mV (Figure 12 Biii right graph; Table 10). Similar as in PSEs, rebound latencies slightly increased at more hyperpolarized holding potentials compared to more depolarized holding potentials when releasing the neurons from test potentials of V_T = -100 mV (Figure 12 Bii, Biii; Table 10).

RSE	V_H = -40 mV			V_H = -50 mV			V_H = -60 mV		
V_T [mV]	-100	-90	-80	-100	-90	-80	-100	-90	-80
25 IQR [ms]	29	27	19	51	65	48	301	289	907
mdn [ms]	42	48	39	94	118	177	456	590	907
75 IQR [ms]	108	130	62	131	154	290	611	890	907

Table 10: Summary of median rebound spike latencies elicited in RSEs during PIR stimulations from three different holding potentials (V_H = -40 mV, V_H = -50 mV, and V_H = -60 mV) to three different test potentials (V_T = -100 mV, V_T = -90 mV and V_T = -80 mV).

Coordinating Neurons (ASC_E) ASC_Es responded with a similar modulation in rebound spike latencies as previously described in PSEs at more depolarized holding potentials (V_H = -40 mV). When hyperpolarizing ASC_Es from a fixed holding potential (V_H = -40 mV) to three different test potentials (V_T = -100 mV, V_T = -90 mV, and V_T = -80 mV) rebound latencies slightly decreased with depolarizing test potential (Figure 12 Ci, Ciii left graph; Table 11, left column). At more hyperpolarized holding potentials (V_H = -50 mV and V_H = -60 mV) no reliable change in rebound spike latencies was observed when changed V_T potentials (V_T = -100 mV, V_T = -90 mV, and V_T = -80 mV) (Figure 12 Ci, Ciii left graph; Table 11, center-, right column). Similar as PSE and RSE, rebound latencies slightly increased at more hyperpolarized holding potentials compared to more depolarized holding potentials when releasing the neurons from test potentials of V_T = -100 mV (Figure 12 Cii, Ciii; Table 11).

ASC_E	V_H = -40 mV			V_H = -50 mV			V_H = -60 mV		
V_T [mV]	-100	-90	-80	-100	-90	-80	-100	-90	-80
25 IQR [ms]	17	16	13	19	19	19	41	44	35
Mdn [ms]	28	22	21	27	34	25	61	58	67
75 IQR [ms]	36	24	23	55	67	51	108	164	228

Table 11: Summary of median rebound spike latencies elicited in ASC_Es during PIR stimulations from three different holding potentials (V_H = -40 mV, V_H = -50 mV, and V_H = -60 mV) to three different test potentials (V_T = -100 mV, V_T = -90 mV and V_T = -80 mV).

Coordinating Neurons (DSC) No reliably change in rebound latencies between different holding- or test potentials was observed in DSCs (Figure 12 Di, Dii, Diii; Table 12).

DSC	V_H = -40 mV			V_H = -50 mV			V_H = -60 mV		
V_T [mV]	-100	-90	-80	-100	-90	-80	-100	-90	-80
25 IQR [ms]	32	30	31	58	72	111	192	200	211
mdn [ms]	51	54	57	104	173	261	2,15	1,77	211
75 IQR [ms]	125	166	103	869	504	806	4,12	3,34	211

Table 12: Summary of median rebound spike latencies elicited in DSCs during PIR stimulations from three different holding potentials (V_H = -40 mV, V_H = -50 mV, and V_H = -60 mV) to three different test potentials (V_T = -100 mV, V_T = -90 mV and V_T = -80 mV).

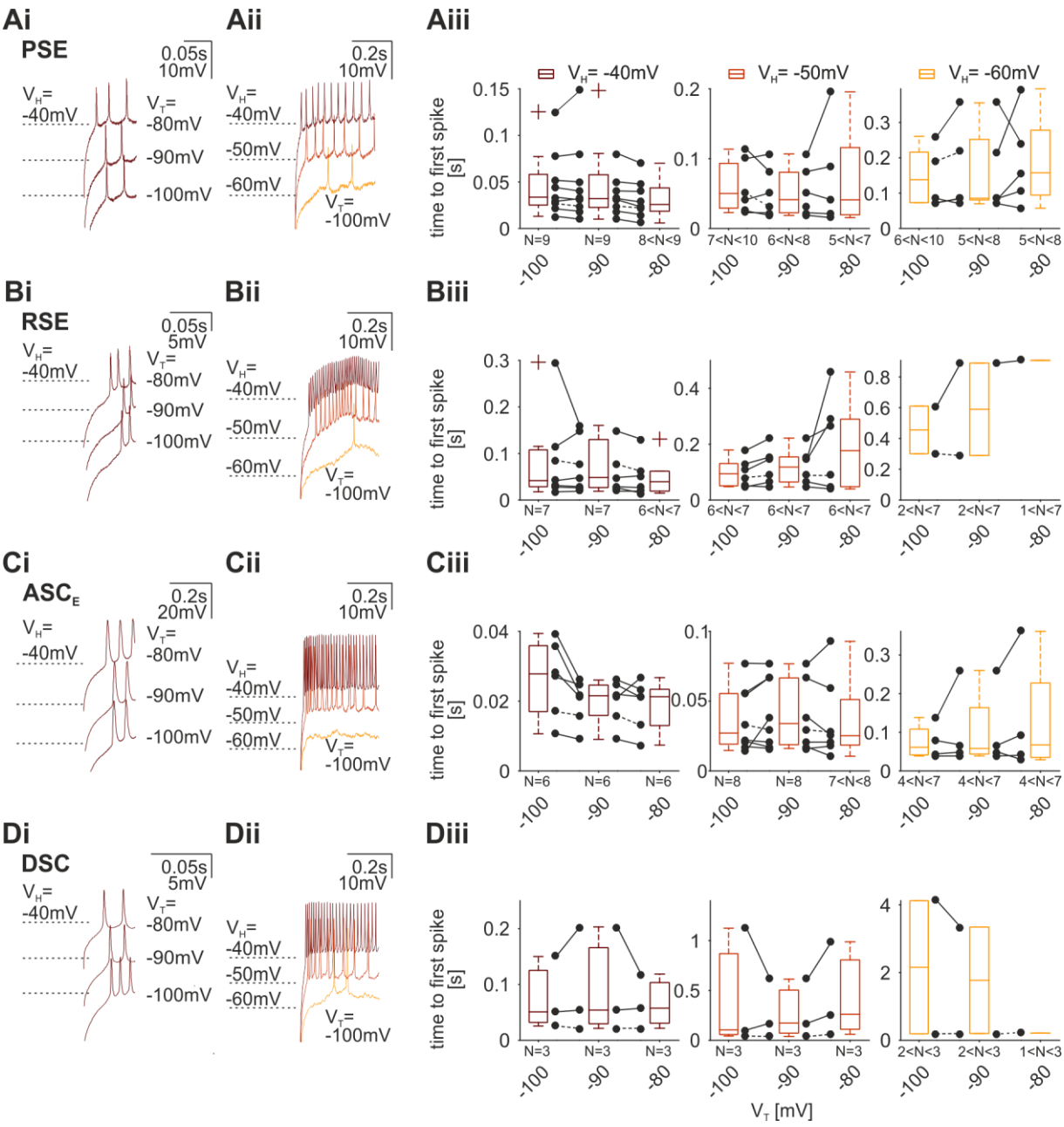

Figure 12: Slight modulation of rebound spike latencies in PSEs and ASC_Es. Representative voltage traces of single PIR stimulations are shown after termination of current injection PSE (Ai, Aii), RSE (Bi, Bii), ASC_E (Ci, Cii), DSC (Di, Dii). Color codes represent different V_H. Aiii, Biii, Ciii, Diii Box plots compare rebound latencies between different V_Hs and V_Ts (V_H = -40 mV, V_H = -50 mV and V_H = -60 mV to V_T = -100 mV, V_T = -90 mV, and V_T = -80 mV). Markers: median time to first spikes of single experiments, dashed lines: results from exemplary recording, PSE: Power Stroke Exciter, RSE: Return Stroke Exciter, ASC_E: Ascending Coordinating Neuron, DSC: Descending Coordinating Neuron, PIR: post-inhibitory rebound, V_H: holding potential, V_T: test potential (Supplemental Figures 23 – 26)

3.2.1.5 Summary – Characterizing PIR properties of spiking neurons

In this chapter I demonstrated the presence of PIR responses in all tested spiking neuron groups of the swimmeret system that were characterized by a sag potential in most neurons during the hyperpolarizing current injection. Moreover, a depolarization greater than $V_{H,}$ was elicited when releasing the neurons from hyperpolarization, that promoted rebound spikes. During the experiments no consistent influence of command or test potentials on evoked sag and PIR amplitudes was identified. Yet, a weak correlation between different V_H and the latency until first rebound spikes occurred was observed in PSEs and ASC_Es.

The presence of rebound properties indicates that all tested neurons possess an intrinsically generated mechanism that promotes new excitability after a phase of inhibitory synaptic input. Therefore, this property is likely to resemble particular importance in generating the oscillatory activity of the tested neuron groups.

3.2.2 PIR in two types of nonspiking neurons of the swimmeret system

CPG neurons (IPS) In the previous chapter, I demonstrated that all tested spiking neurons in the swimmeret system possess the ability to produce a PIR response. Because all of these neurons are known to receive inhibitory synaptic input from the CPG, it seems likely that this membrane mechanism plays a role in the escape from inhibitory synaptic input. But what about the neurons that are actually part of the rhythm generating circuit themselves? Rhythm generation in each module of the swimmeret system is mediated by mutual inhibition from the CPG neurons (three IPS and two IRS neurons). It has been shown that neurons forming a half center oscillator are either able to release the other neuron from inhibition or themselves being able to escape from inhibitory synaptic input. Given that, I wanted to examine the mechanism behind mutual inhibition in the swimmeret system. Since the spiking neurons seem to rely on escape mechanisms, the goal of the following experiments was to see whether the CPG neurons use a similar mechanism. In one representative type of CPG neurons, namely in IPSs, I tested the presence of PIR responses in the same way as previously done in spiking neurons (Figure 13).

The membrane potential of recorded neurons was set to three different V_Hs to analyze PIR responses. Simultaneously, a series of incrementing negative current

pulses was injected, hyperpolarizing the membrane potential to three different test potentials (V_T = -100 mV, V_T = -90 mV and V_T = -80 mV).

Interestingly, I identified different PIR responses in IPSs. In two out of five recorded IPSs, a PIR response as well as a sag potential was elicited (Figure 13 A). The remaining examined IPSs lacked this ability and they neither depolarized during the hyperpolarization (sag potential) nor depolarized above V_H (PIR amplitude) when released from current pulses (Figure 13 B).

One IPS that expressed a PIR depolarization showed a significant voltage dependence to changes in V_Hs. In contrast to the spiking neurons, during more depolarized V_Hs, IPS responded with smaller PIR amplitudes (V_H = -40 mV: mdn = 6.7 mV, IQR = 4.25 mV – 7.3 mV, V_H = -50 mV: mdn = 12.4 mV, IQR = 11.8 mV –12.8 mV, 1 < N < 8, Kruskal-Wallis test: $p < 0.032$) than during more hyperpolarized V_Hs (V_H = -60 mV: mdn = 15.5 mV, IQR = 12.75 mV - 17.9 mV, 1 < N < 8, Kruskal-Wallis test: $p << 0.001$; Figure 13 A, Cii, Ciii). Sag potential amplitudes were not affected by changes in V_Hs (Figure 13 Dii, Diii; Table 14). Furthermore, no consistent influence on PIR amplitudes as well as sag potential amplitudes (Figure 13 Ci, Ciii, Di, Diii; Table 13, 14) were observed when changing V_T at neither of V_H. Unfortunately, I was not able to assign the recorded IPSs to one of the three published IPS neuron types due to severe loss of intracellularly injected dye during the fixation process.

In summary, a divergence of membrane mechanisms seems to be present in IPSs. Some IPSs were able to produce PIR responses when released from hyperpolarizing current pulses, and some were not. Therefore this indicates that some IPSs rely on escape from inhibition that possibly plays a role during rhythm generation in the system. However, it seems that either not all IPSs have the same functional role during rhythm generation or that some IPSs are dependent on other mechanisms supporting mutual inhibition.

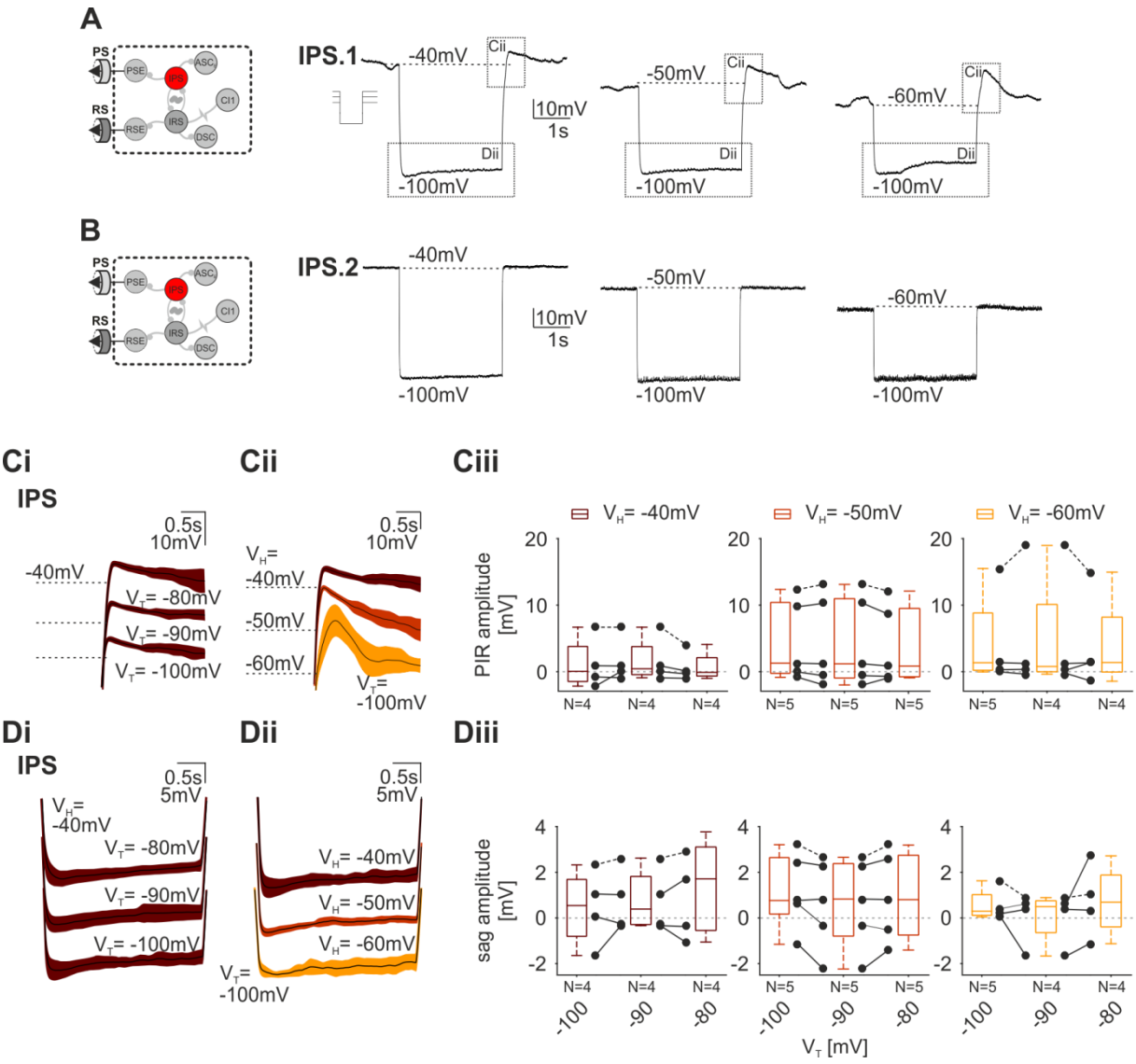

Figure 13: Variability of PIR expression in IPS. Schematic of recorded neurons. Not all IPSs produced a PIR. Two representative examples of IPSs that either elicited a PIR (A) or not (B). PIR stimulations were elicited at three different holding potentials (V_H = -40 mV, V_H = -50 mV, and V_H = -60 mV, reaching V_T = -100 mV) to test potentials of V_T = -100 mV are shown. PIR amplitudes and sag potential of IPS in A correlated to changes in V_H but not V_T. Dashed boxes indicate analyzed PIR parameters. Ci, Cii, Di, Dii Mean intracellular voltage traces of 15 consecutive PIR stimulations (black line). Standard deviation of voltage traces are shown in color coded areas. Color codes represent different V_H. Box plots compare PIR amplitudes (Ciii) and sag potential amplitudes (Diii) evoked at different V_Hs and V_Ts (V_H = -40 mV, V_H = -50 mV and V_H = -60 mV to V_T = -100 mV, V_T = -90mV, V_T = -80mV). Markers: median values of single experiments, dashed lines: results from exemplary recording in A, IPS: Inhibitor of Power Stroke, PIR: post-inhibitory rebound, V_H: holding potential, V_T: test potential (Supplemental Figures 11, 17).

IPS	V_H = -40 mV			V_H = -50 mV			V_H = -60 mV		
V_T [mV]	-100	-90	-80	-100	-90	-80	-100	-90	-80
25 IQR [mV]	-1.48	-0.45	-0.66	-0.25	-0.95	-0.77	0.21	-0.01	-0.05
mdn [mV]	0.05	0.44	-0.1	1.27	1.18	0.85	1.34	0.79	1.38
75 IQR [mV]	3.8	3.78	2.11	10.41	10.97	9.51	8.83	10.1	8.19

Table 13: Summary of median PIR amplitudes elicited in IPSs during PIR stimulations from three different holding potentials (V_H = -40 mV, V_H = -50 mV, and V_H = -60 mV) to three different test potentials (V_T = -100 mV, V_T = -90 mV, and V_T = -80 mV).

IPS	V_H = -40 mV			V_H = -50 mV			V_H = -60 mV		
V_T [mV]	-100	-90	-80	-100	-90	-80	-100	-90	-80
25 IQR [mV]	-0.81	-0.29	-0.55	0.17	-0.8	-0.75	0.11	-0.65	-0.39
mdn [mV]	0.54	0.39	1.71	0.76	0.83	0.8	0.29	0.49	0.69
75 IQR [mV]	1.69	1.82	3.11	2.64	2.38	2.74	1.02	0.75	1.88

Table 14: Summary of median sag amplitudes elicited in IPSs during PIR stimulations from three different holding potentials (V_H = -40 mV, V_H = -50 mV, and V_H = -60 mV) to three different test potentials (V_T = -100 mV, V_T = -90 mV, and V_T = -80 mV).

ComInt1 The last neuron analyzed with regard to its ability to produce a PIR response upon release from hyperpolarizing current pulses was the non-spiking interneuron ComInt1. ComInt1 is known to receive monosynaptic excitatory synaptic input from Coordinating Neurons ASC_E and DSC (Smarandache-Wellmann et al., 2014). Therefore, an intrinsic mechanism that would help this neuron to escape from an inhibitory input seemed unlikely. However, in order, to test this hypothesis, I examined PIR responses in ComInt1s (n = 7) similarly as in all previous described neurons. Surprisingly, ComInt1s responded with a rebound depolarization after termination of hyperpolarizing current injections (Figure 14 A), but the measured PIR amplitudes were rarely as large as those measured in other neuron groups (Figure 14 Bi, Bii, Biii left graph; Table 15). PIR amplitudes slightly declined when changing

test potentials from V_T = -100 mV to more depolarized V_T (Figure 14 Biii). Similar observations were made between different V_T = -100 mV, V_T = -90 mV, and V_T = -80 mV, but originating from more hyperpolarized V_H = -50 mV (Figure 14 Biii, center graph; Table 15 center column). At V_H = -60 mV changes in V_T did not cause reliable changes in PIR amplitudes (Figure 14 Biii right graph; Table 15 right column). A weak dependence of evoked PIR amplitudes towards changes in V_Hs was present in ComInt1 (Figure 14 Bii, Biii; Table 15). At more depolarized V_H levels, ComInt1s responded with increased PIR amplitudes compared to more hyperpolarized V_Hs.

In most ComInt1s hyperpolarizing current injections caused the induction of a sag potential. However, no correlation to changes in V_T was observed at neither of V_H (Figure 14 Cii, Ciii; Table 16).

Given that ComInt1s receive excitatory synaptic input it seems unlikely that a PIR response would play a functional role in modulating ComInt1 activities. Therefore I categorize the observed responses in ComInt1s as 'PIR-like' responses.

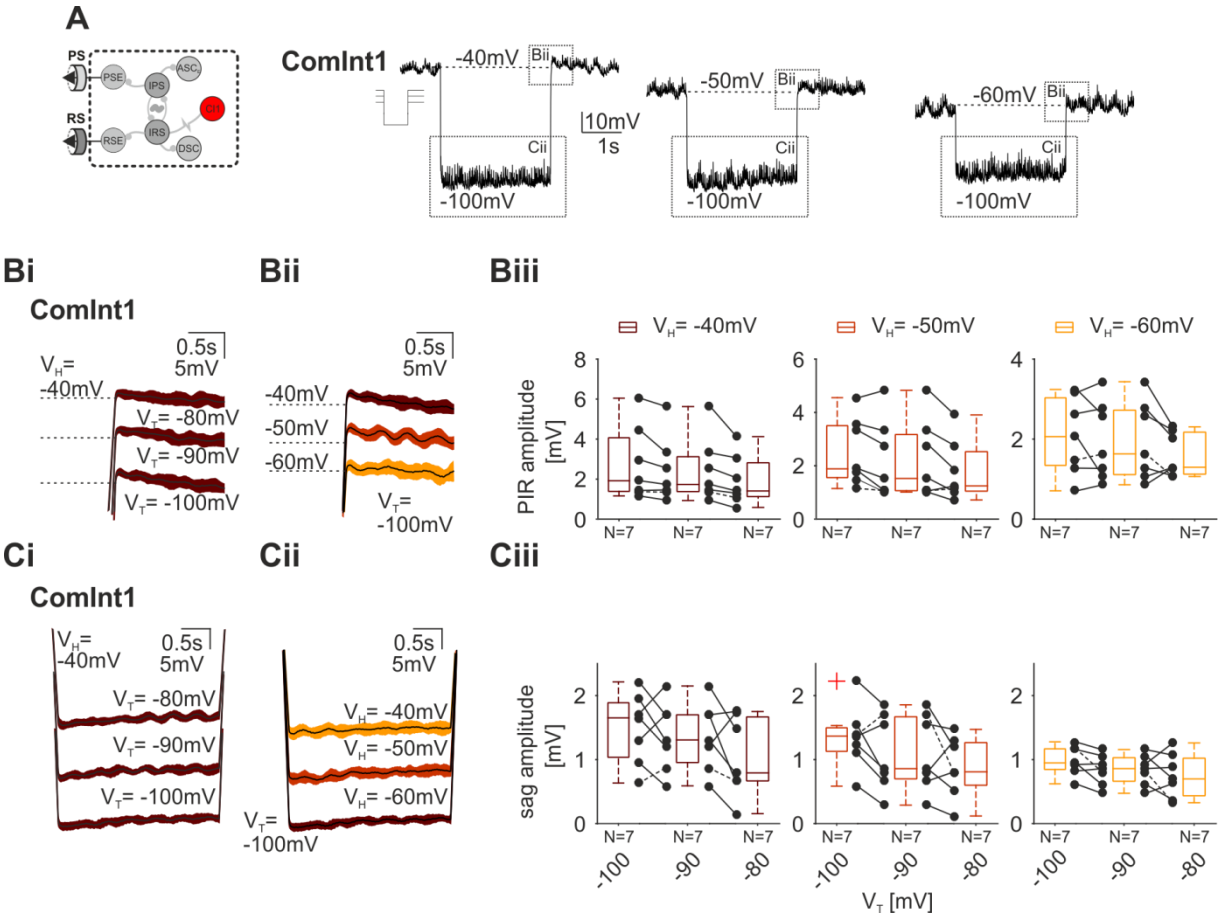

ComInt1	V_H = -40 mV			V_H = -50 mV			V_H = -60 mV		
V_T [mV]	-100	-90	-80	-100	-90	-80	-100	-90	-80
25 IQR [s]	1.39	1.38	1.13	1.56	1.07	1.05	1.34	1.11	1.12
mdn [s]	1.92	1.73	1.41	1.88	1.52	1.25	2.06	1.63	1.3
75 IDQ [s]	4.07	3.12	2.82	3.5	3.17	2.53	3.03	2.72	2.17

Table 15: Summary of median PIR amplitudes elicited in ComInt1s during PIR stimulations from three different holding potentials (V_H = -40 mV, V_H = -50 mV, and V_H = -60 mV) to three different test potentials (V_T = -100 mV, V_T = -90 mV, and V_T = -80 mV).

ComInt1	V_H = -40 mV			V_H = -50 mV			V_H = -60 mV		
V_T [mV]	-100	-90	-80	-100	-90	-80	-100	-90	-80
25 IQR [s]	1.04	0.95	0.67	1.13	0.7	0.6	0.85	0.66	0.43
mdn [s]	1.65	1.31	0.79	1.37	0.86	0.81	0.95	0.86	0.7
75 IDQ [s]	1.89	1.7	1.67	1.5	1.67	1.27	1.17	1.03	1.02

Table 16: Summary of median sag amplitudes elicited in ComInt1s during PIR stimulations from three different holding potentials (V_H = -40 mV, V_H = -50 mV, and V_H = -60 mV) to three different test potentials (V_T = -100 mV, V_T = -90 mV, and V_T = -80 mV).

Figure 14: 'Rebound-like' responses in ComInt1. Schematic of recorded neuron (Ai). ComInt1 generated a PIR when released from hyperpolarizing current injection. Representative example of ComInt1s during PIR stimulations at different V_H = -40 mV, V_H = -50 mV, and V_H = -60 mV, reaching V_T = -100 mV (Aii). Dashed boxes indicate analyzed PIR parameters. Mean intracellular voltage traces of 15 consecutive PIR stimulations (black line) (Bi, Bii, Ci, Cii). Standard deviation of voltage traces are shown in color coded areas. Color codes represent different V_H. Box plots compare PIR amplitudes (Biii) and sag potential amplitudes (Ciii) evoked at different V_Hs and V_Ts (V_H = -40 mV, V_H = -50 mV, and V_H = -60 mV to V_T = -100 mV, V_T = -90 mV, V_T = -80 mV). Markers: median values of single experiments, dashed lines: results from exemplary recording, ComInt1: Commissural Interneuron 1, PIR: post-inhibitory rebound, V_H: holding potential, V_T: test potential (Supplemental Figures 12, 18).

3.3 Ionic bases for PIR phenotype

In order to better understand the contribution of PIR as a possible mechanism of the neurons to escape from periods of inhibitory synaptic input it is necessary to characterize the mechanisms behind the PIR. Consequently, I wanted to identify the underlying hyperpolarization-activated ionic conductances and elucidate possible dissimilarities between the ionic currents in the different neuron groups. This could reveal important insights into how the neurons accomplish their diverse tasks in the network.

In other systems several hyperpolarization-activated ionic currents play a role in shaping PIR responses. In lamprey commissural interneurons as well as MNs, the combination of two different calcium currents (T-type calcium current (I_{CaT}) and L-type calcium current (I_{CaL})) gives rise to PIR induction in those neuron types (Wang et al., 2011). In work by Chrachri, 1995, the presence of I_{CaL} in the soma of dissociated swimmeret MNs was shown. However, no functional implication of I_{CaL} has been investigated in this study. Furthermore, it is questionable how much the presence of I_{CaL} in the soma of an invertebrate like the crayfish would contribute to neuron activity in the dendritic branches, as it is expected to be the localization of all synaptic integration. In other system, like rat olfactory bulb mitral cells (Angelo and Margrie, 2011), or CA1 pyramidal neurons (Ascoli et al., 2010) also I_H was detected to play an essential role for the generation of PIR responses. In leech heart interneurons (Angstadt and Calabrese, 1989) also the hyperpolarization-activated nonselective cation current (I_H) contributed to PIR generation while in dorsal excitatory MNs, the persistent sodium current (I_{NaP}) was involved (Angstadt et al., 2005)

Given the aforementioned studies on I_{CaL}, I tested whether I_{CaL} is present in the dendritic aborizations of MNs and whether there is actually a functional relevance of this current for PIR generation. I performed the same current protocols as previously described, while I superfused the abdominal nervous system with Nifedipine, a blocker against I_{CaL} to identify its contribution during PIR generation. Afterwards, I analyzed the additional contribution of I_H and the I_{NaP} during PIR induction by subsequent application of Zd7288 and Riluzole.

All presented median values were normalized to the median value of the control condition, to increase comparability between animals.

3.3.1 Motor neurons

3.3.1.1 I_{CaL} and I_H contribute to PIR responses in PSE

After observing the presence of PIR in PSEs I aimed to identify the ionic currents that mediate this intrinsically generated neuronal excitability (Figure 15, A – D). The most reliable PIR responses in all neurons were elicited at intermediate holding potentials (V_H = -50 mV) with most hyperpolarized test potentials (V_T = -100 mV). Therefore I used this stimulation protocol to test further which ionic conductances contribute to the induction of PIR responses. After characterizing PIR I superfused Nifedipine (40 µM, diluted in a mixture of synaptic blockers, see Material and Methods, chapter 2.4) over the abdominal nerve cord to investigate a possible contribution of I_{CaL} during PIR generation. During these experiments, blocking I_{CaL} caused diverse effects on the evoked rebound responses. The normalized median (mdn) PIR amplitudes across all eight PSE decreased (mdn = 0.9, IQR = 0.7 - 1.9, N = 8, Friedman test: $p > 0.05$; Figure 15 C, Ei). Nevertheless, this effect was not consistent across all preparations. In five of the eight tested PSEs the PIR amplitudes decreased during Nifedipine treatment while in the remaining three PSEs PIR amplitudes increased.

On the other hand Nifedipine treatment induced a significant reduction of sag amplitude in all eight neurons (mdn = -0.005, IQR = -2.2 - 0.5, N = 8, Friedman test: $p < 0.0055$; Figure 15 Fi, Fii), while it had not consistent effect on the normalized rebound spike latencies (mdn = 0.9, IQR = 0.6 – 1.1, N = 8, Friedman test: $p > 0.05$; Figure 15 Gi, Gii). Instantaneous frequency increased (114 Hz ± 22.7) with Nifedipine compared to control condition (106 Hz ± 15.05) and decayed exponentially as shown in the representative example in figure 15 (Hi). Such an increase in peak instantaneous frequency was seen in all PSE post PIR stimulation (mdn = 1.6, IQR = 1.4 – 4.0, $7 < N < 8$, Friedman test: $p < 0.0097$; Figure 15 Hii).

Nifedipine application failed to abolish PIR generation in all of the tested PSE. Therefore I tested the contribution of I_H during PIR generation and added a common blocker against the I_H, Zd7288 (200 µM, to the saline containing Nifedipine, see Material and Methods, chapter 2.4), to the bathing solution. With this I was able to evaluate the combined effects of both blockers on PIR generation (Figure 15 D). In all PSEs the additional superfusion with Zd7288 abolished all PIR depolarizations (mdn = 0.2, IQR = 0.1 – 0.3, N = 8, Friedman test: $p < 0.0313$; Figure 15 D, Ei, Eii),

as well as rebound spiking (Figure 15 D). Addition of Zd7288 resulted in a further reduction of sag amplitudes in all cells (mdn = -1.0, IQR = -11.7 - -0.1, N = 8, Friedman test: $p > 0.05$; Figure 15 D, Fi, Fii).

In these experiments I demonstrated that the generation of PIR responses in PSEs was mediated by a combination of I_{CaL} and I_H.

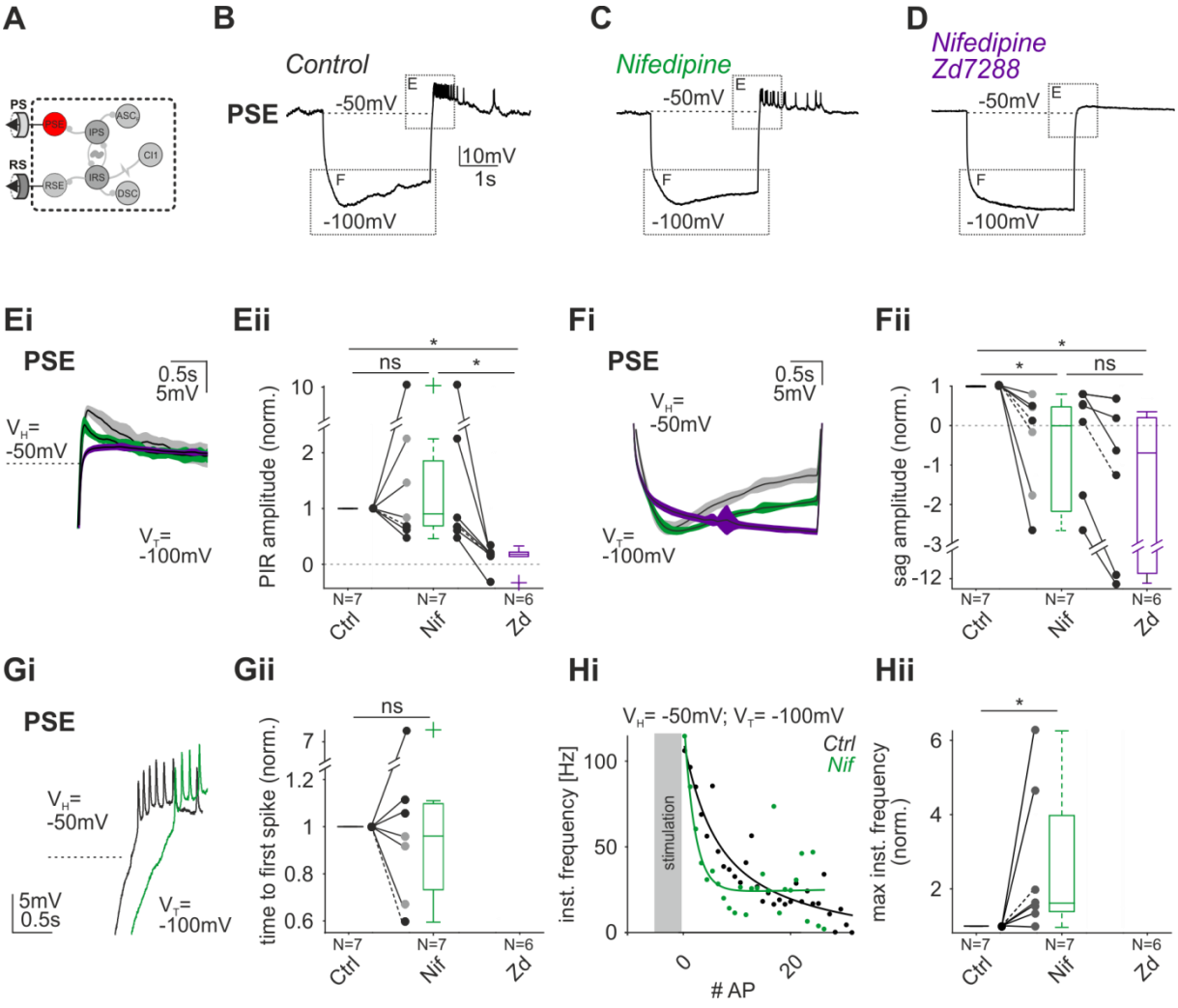

Figure 15: I_{CaL} and I_H contribute to PIR responses in PSE. Schematic of recorded neuron (A). PIR responses were elicited by releasing the neurons from hyperpolarizing current pulses (V_H = -50 mV, V_T = -100 mV) (B). Successively Nifedipine (40 µM) and Nifedipine (40 µM) + Zd7288 (200 µM) were superfused over the abdominal nerve cord to elucidate the ionic bases for the PIR (C, D). Dashed boxes indicate analyzed PIR parameters. Mean voltage traces of 15 subsequent PIR stimulations are shown in Ei, Fi. Voltage traces are smoothed to erase APs. PIR amplitudes and rebound spike latencies decreased in four and increased in three PSE, during Nifedipine treatment (C, Ei, Eii, Gi, Gii). Sag potential amplitudes declined, while maximum instantaneous frequency increased in all PSE (Hii). Mean instantaneous firing frequencies are plotted against the number of APs following the stimulation (Hi). Decline of instantaneous spike frequency in control and Nifedipine condition was characterized by a second-order exponential fit. Adding Zd7288 reduced PIR-, sag potential amplitudes (D, Ei, Eii, Fi, Fii) and rebound spiking was abolished. Box plots compare normalized PIR amplitudes (Eii), sag potential amplitudes (Fii), time to first spike

(Gi), and maximum instantaneous frequency (Hii) between experimental conditions. Markers: normalized median values of single experiments (black markers: a significant change of evaluated parameter, grey makers: represent failed statistical test), dashed lines: results from exemplary recording, PSE: Power Stroke Exciter, Ctrl: Control, Nif: Nifedipine, Zd: Zd7288, AP: action potential, PIR: post-inhibitory rebound, V_H: holding potential, V_T: test potential, Wilcoxon rank sum test *: $p < 0.05$, ns: $p > 0.05$ (Supplemental Figures 27, 32, 37, 41).

3.3.1.2 I_{CaL} and I_H contribute to PIR responses in RSEs

In RSEs the contribution of I_{CaL} and I_H during PIR generation was analyzed with the same protocol as previously executed in PSEs. After characterizing PIR responses in RSEs I first applied Nifedipine and then added Zd7288 to the bathing solution (Figure 16 B, C, D). During control and blocker condition I compared PIR responses elicited from V_H = -50 mV to V_T = -100 mV. During block of I_{CaL} I observed an overall increase in normalized PIR amplitudes (mdn = 1.5, IQR = 0.7 – 4.5, N = 6, Friedman test: $p > 0.05$). Three out of six neurons elicited a plateau-like depolarization when released from hyperpolarization (Figure 16 B, Ei, Eii). In one of the remaining RSEs, PIR amplitudes increased without generation of a plateau potential. In the remaining two RSE neurons tested PIR amplitudes declined during Nifedipine treatment. Sag potential amplitudes were not reliably affected by Nifedipine treatment (mdn = 0.8, IQR = 0.5 – 1.4, N = 6, Friedman test: $p > 0.05$; Figure 16 C, Fi, Fii).

All neurons responded with rebound spikes when being released from hyperpolarizing current pulses. However no consistent change in rebound latency was evoked during Nifedipine treatment and the induction of plateau potentials had also no influence on the latency (mdn = 1.0, IQR = 0.7– 1.3, N = 6, Friedman test: $p > 0.05$; Figure 16 B, Gi, Gii). Blocking I_{CaL} increased initial instantaneous spike frequency in the exemplary PSE recording from 49 Hz ± 6.4 (control) to 205 Hz ± 8.4 (Nifedipine) before dropping to baseline frequencies of 47 Hz ± 23.8 that was also elevated compared to control 7.3 Hz ± 6.2 (Figure 16 B, Hi). The decline in instantaneous spike frequencies was characterized by a second-order exponential fit (Figure 16 D). The maximum instantaneous spike frequency increased due a block of I_{CaL} in all but one RSE (mdn = 2.8, IQR = 0.5 - 4.9, N = 6, Friedman test: $p > 0.05$; Figure 16 B, Hi, Hii). Regarding that Nifedipine application failed to abolish PIR generation I subsequently added Zd7288 to the preparation to test whether the remaining PIR responses were mediated by I_H as previously shown in PSEs (Figure

16 C). I_H blocker application, Zd7288, either abolished all PIR depolarizations or caused a steep decrease (mdn = 0.3, IQR = -0.2 – 0.7, N = 6, Friedman test: $p > 0.05$; Figure 16 B, Ei, Eii). Furthermore with Zd7288 treatment all rebound spiking was abolished (Figure 16 D).

Zd7288 had varying effects on evoked sag potentials amplitudes (mdn = -0.2, IQR = 4.3 - 1.7, N = 6, Friedman test: $p > 0.05$) (Figure 16 D, Fi, Fii). In three RSEs the elicited sag potential declined by blockage of I_H while in the other three RSEs voltage sag amplitudes increased.

Taken together the experimental findings for PSEs and RSEs represent promising evidence that PIR in both MN groups are elicited by I_{CaL} as well as I_H. Regarding this I_{CaL} and I_H seem to be important currents that help both MN groups to depolarize following a phase of inhibitory synaptic input during CPG neuron activity.

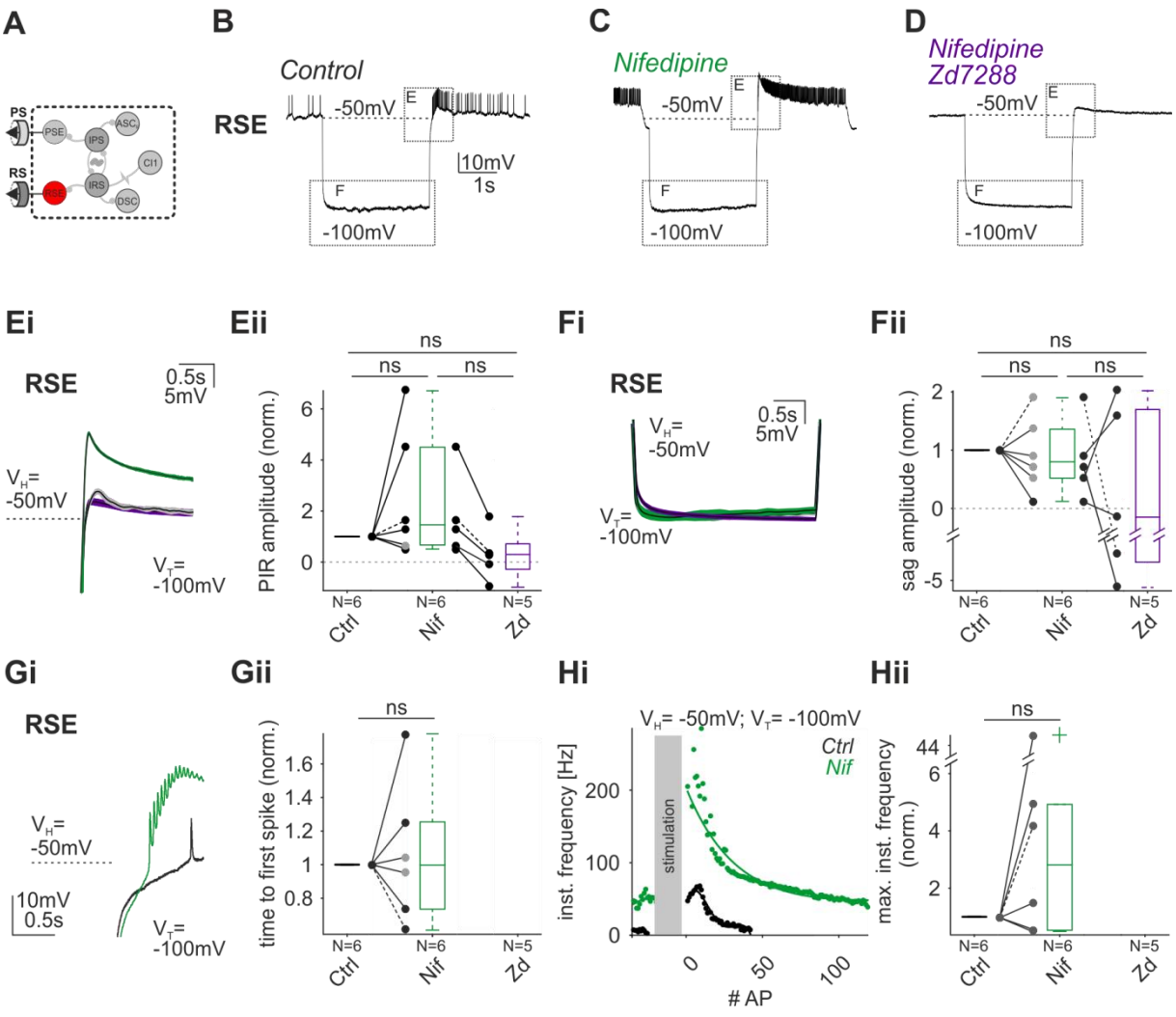

Figure 16: I_{CaL} and I_H contribute to PIR responses in RSE. Schematic of recorded neuron (A). PIR responses were elicited by releasing the neurons from hyperpolarizing current pulses (V_H = -50 mV, V_T = -100 mV) (B). Successively Nifedipine (40 µM) and Nifedipine (40 µM) + Zd7288 (200 µM) were superfused over the abdominal nerve cord in order to elucidate the ionic bases for the PIR (C, D). Dashed boxes indicate analyzed PIR parameters. Mean voltage traces of 15 subsequent PIR stimulations are shown in Ei, Fi. Voltage traces are smoothed to erase APs. Blocking I_{CaL} had variable effects on PIR-, sag potential amplitudes, first spike latencies and maximum instantaneous frequency (C, Ei, Eii, Fi, Fii, Gi, Gii, Hii). Mean instantaneous firing frequencies are plotted against the number of APs following the stimulation (Hi). Decline of instantaneous frequency in control and Nifedipine condition was characterized by a second-order exponential fit. Superfusion of Zd7288 reduced PIR amplitude and sag potential amplitudes (D, Ei, Eii, Fi, Fii). Rebound spiking was abolished. Box plots compare normalized PIR amplitudes (Eii), sag potential amplitudes (Fii), time to first spike (Gi), and maximum instantaneous frequency (Hii) between experimental conditions. Markers: normalized median values of single experiments (black markers: significant change of evaluated parameter, grey makers: represent failed statistical test, dark grey markers: unpaired median values were not compared in a statistical test), dashed lines: results from exemplary recording, RSE: Return Stroke Exciter, Ctrl: Control, Nif: Nifedipine, Zd: Zd7288, AP: action potential, PIR: post-inhibitory rebound, V_H: holding potential, V_T: test potential, Wilcoxon rank sum test *: $p < 0.05$, ns: $p > 0.05$ (Supplemental Figures 28, 33, 38, 42).

3.3.2 Coordinating Neurons

In the previous chapter evidence was found that I_{CaL} and I_H are present in MNs and play a major role in shaping PIR responses. It is likely that these currents play a role to accomplish their task in the network, *i.e*. to transmit information from the pattern generating kernel to the muscles. But how about the Coordinating Neurons which are important to synchronize the rhythmic activity between the different ganglia? What are the ionic currents that help shape their activity in order to accomplish their task in the network? In the following chapter this issue is addressed by analyzing the mediating ionic conductances during PIR responses in the Coordinating Neurons, ASC_E and DSC.

3.3.2.1 Different currents contribute to PIR responses in ASC_E

The influence of different ionic conductances on PIR expression was investigated in ASC_Es by performing similar current protocols as described during PIR characterization (Figure 17). PIR responses were most reliably generated at intermediate holding potentials (V_H = -50 mV) with most hyperpolarized test potentials (V_T = -100 mV). Subsequently different ion channel blockers were applied to the preparation to elucidate the underlying ionic conductances. Most ASC_Es (4 of 6 ASC_E) responded in the same way to a block in ion channels as previously seen in MNs. However it seemed that in some ASC_Es (2 of 6 ASC_E), I_{NaP} was responsible for PIR generation in addition to of I_{CaL} and I_H. In these ASC_Es not all PIR responses was abolished by combined treatment with Nifedipine and Zd7288. Additional superfusion of Riluzole (70 µM, see Material and Methods), thereby blocking I_{NaP}, was required to eliminate PIR responses.

In figure 17 two representative ASC_Es recordings from two separate animals and recording sites, are shown. PIR responses in the first ASC_E were elicited by the same ionic currents as in MNs (Figure 17 Ai, Bi, Ci). Their PIR responses were analyzed first during Nifedipine- (Figure 17 Bi) and then following Zd7288 superfusion (Figure 17 Ci).

Blocking I_{CaL} caused diverse effects on PIR amplitudes over all tested ASC_Es (mdn = 1.2, IQR = 0.7 – -0.2, N = 6, Friedman test: $p > 0.05$; Figure 17 Eii). In the exemplary ASC_E (Figure 17 Bi, Ei, upper traces) as well the majority of the remaining ASC_Es (4 of 6) normalized PIR amplitudes increased. Similarly, diverse effects on

sag potential amplitudes were observed when blocking I_{CaL} (mdn = 1.1, IQR = -0.5 - 2.2, N = 6, Friedman test: $p > 0.05$; Figure 17, Eii). An exemplary increase in sag potential amplitudes is shown in figure 17 Bi, Ei (upper traces). Baseline AP generation frequency of 22.8 Hz ± 5.2 (Ctrl: 19.2 Hz ± 9.4; Figure 17 Hi, upper trace) as well as rebound peak spike frequency of 73.3 Hz ± 8.2 (Ctrl: 53.3 Hz ± 18.2) was elevated attributable to Nifedipine in the exemplary ASC_E recording, but also over all ASC_Es tested (mdn = 1.3, IQR = 0.9 - 1.7, N = 6, Friedman test: $p > 0.05$; Figure 17 Bi, Hi upper graph). However this effect was not consistent. In three ASC_Es rebound spike frequency was either reduced or not affected. Rebound instantaneous spike frequency was characterized by a second-order exponential fit. Rebound spike latency was not reliably affected when blocking I_{CaL} (mdn = 0.9, IQR = 0.8 – 2.0, N = 6, Friedman test: $p > 0.05$).

With a following block of I_H by additional treatment with Zd7288, PIR depolarization was abolished in four of six ASC_Es (mdn = 0.3, IQR = -0.2 – 2.0, N = 6, Friedman test: $p > 0.05$; Figure 17 Bi, Ei upper graph), sag potential amplitudes were further reduced in all six ASC_Es (mdn = -1.79, IQR = -5.0 – -0.5, N = 6, Friedman test: $p > 0.05$; Figure 17 Bi, Fi upper graph) and rebound spiking was eliminated.

In the other recorded ASC_Es Nifedipine evoked similar effects on PIR generation. PIR depolarizations increased (Figure 17 Bii, Ei lower graph), sag amplitudes decreased (Figure 17 Bii, Fi, lower graph) and rebound firing was elevated when I_{CaL} was blocked (Figure 17 Bii, Hi lower graph). However, during block of I_H I observed obvious differences to the other four recorded ASC_Es.

Instead of abolishing rebound responses, Zd7288 increased some, but not all PIR features (Figure 17 Cii). When inhibiting I_H the amplitude of normalized PIR amplitudes increased (Figure 17 Ci, Ei lower graph). This increase was reflected in an enhancement in instantaneous spike frequency (mdn = 1.0, IQR = 0.7 – 1.4, N = 6, Friedman test: $p > 0.05$; Figure 17 Ci, Hi lower graph). A fourth-order polynomial fit showed an initial increase in instantaneous frequency starting from 113.23 Hz ± 8.9 (Ctrl: 110.19 Hz ± 9.40; Nif: 78.0 Hz ± 11.6) before declining to baseline firing of 65.4 Hz ± 33.0 (Ctrl: 36.0 Hz ± 15.2; Nif: 20.0 Hz ± 17.5). The rebound spike latency increased with additional block of I_H (mdn = 3.7, IQR = 1.8 – 5.7, N = 6, Friedman test: $p > 0.05$). During Zd7288 condition sag potential amplitude was further reduced (Figure 17 Ci, Fi lower graph). When applying Riluzole to the

preparation, to suppress I_{NaP} currents (70 µM, see Material and Methods), I observed a full abolishment of PIR responses (mdn = -0.2, IQR = 0.2 – 0.2, 1 < N < 6, Friedman test: p > 0.05; Figure 17 Di). In this experimental condition the remaining ASC_Es did not elicit a rebound depolarization (Figure 17 Di, Ei lower graph) nor could the generation of rebound spikes be observed. Furthermore an additional reduction in sag potential amplitudes was seen (mdn = -8.3, IQR = -8.3 - -8.3, 1 < N < 6, Friedman test: p > 0.05; Figure 17 Di, Fi lower graph).

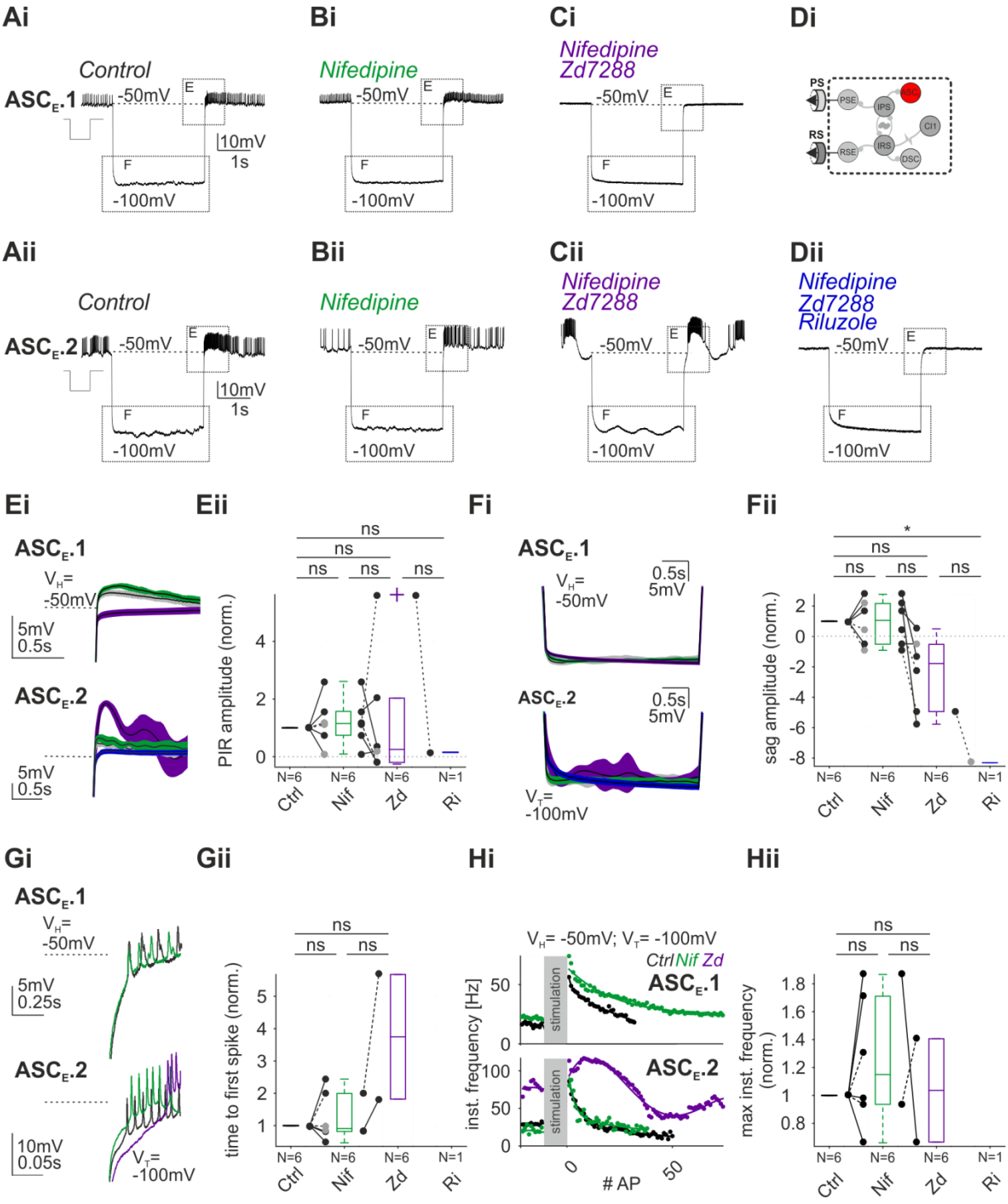

Regarding the previous section I classified PIR responses in ASC_Es into two different categories. In one category PIR were mediated by I_{CaL} & I_H and in the other by a combination of I_{CaL}, I_H and additionally I_{NaP}. When searching for further dissimilarities I found a striking correlation when qualitatively comparing shapes of generated membrane potential oscillations during control activities. ASC_Es that performed PIR responses, mediated by I_{CaL} and I_H, showed oscillatory activity with smaller amplitudes and shallower slopes (Figure 18 A). Comparing activities in the other ASC_E group I found larger amplitudes and steeper slopes of the membrane potential oscillations (Figure 18 B).

Figure 17: I_{CaL}, I_H, and I_{NaP} contribute to PIR responses in ASC_E PIR responses were elicited by releasing the neurons from hyperpolarizing current pulses (V_H = -50 mV, V_T = -100 mV) (Ai, Aii). Successively Nifedipine (40 µM), Nifedipine (40 µM) + Zd7288 (200 µM) and in one case Nifedipine (40 µM) + Zd7288 (200 µM) + Riluzole (70 µM) were superfused over the abdominal nerve cord to elucidate the ionic bases for the PIR. PIR responses in four recordings ASC_Es were mediated by I_{CaL} & I_H (Ai, Bi, Ci) and in the other by I_{CaL} & I_H & I_{NaP} (Aii, Bii, Cii). Dashed boxes indicate analyzed PIR parameters. Schematic of recorded neuron (Di). Mean voltage traces of 15 subsequent PIR stimulations are shown in Ei, Fi. Voltage traces are smoothed to erase APs. Blocking I_{CaL} had variable effects on PIR-, sag potential amplitudes, rebound spike latencies and maximum instantaneous frequency (C, Ei, Eii, Fi, Fii, Gi, Gii, Hii). Mean instantaneous firing frequencies are plotted against the number of APs following the stimulation (Hi). Decline of instantaneous frequency in control and Nifedipine condition was characterized by a second-order exponential fit (Hi, upper graph). Changes in instantaneous frequency during Zd7288 condition (lower graph) were characterized by a fourth-order polynomial fit. Blocking I_H reduced all sag potential amplitudes but only partially PIR amplitudes (D, Ei, Eii, Fi, Fii). Rebound spiking was abolished in four ASC_Es. Riluzole abolished remaining PIR responses (N = 1). Box plots compare normalized PIR amplitudes (Eii), sag potential amplitudes (Fii), time to first spike (Gi), and maximum instantaneous frequency (Hii) between experimental conditions. Markers: normalized median values of single experiments (black markers: significant change of evaluated parameter, grey makers: represent failed statistical test, dark grey markers: unpaired median values were not compared in a statistical test), dashed lines: results from exemplary recordings of ASC_E.1 and ASC_E.2, ASC_E: Ascending Coordinating Neuron, Ctrl: Control, Nif: Nifedipine, Zd: Zd7288, Ri: Riluzole AP: action potential, PIR: post-inhibitory rebound, V_H: holding potential, V_T: test potential, Wilcoxon rank sum test *: $p < 0.05$, ns: $p > 0.05$ (Supplemental Figures 29, 34, 39, 43).

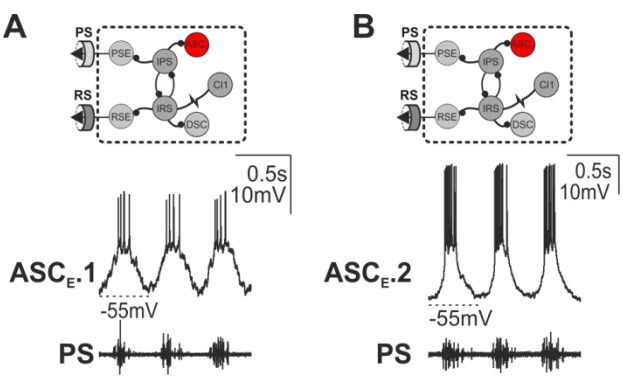

Figure 18: Different oscillations shapes in ASC$_E$. Schematic of recorded neuron (Ai, Bi). Exemplary recordings show oscillatory activity of two ASC$_E$s during three cycles of rhythmic activity and their corresponding PS traces. Oscillation shapes in one ASC$_E$ are characterized by gentle slopes and small oscillations amplitudes (Aii) while the other ASC$_E$ is characterized by large amplitudes and steep oscillation slopes (Bii). ASC$_E$: Ascending Coordinating Neuron, PS: Power Stroke.

3.3.2.2 I_{CaL}, I_H and I_{NaP} contribute to PIR responses in DSC

When aiming at identifying the hyperpolarization-activated ionic conductances mediating PIR responses in DSCs I observed similar effects as in the second category of PIR responses in ASC$_E$s. In DSCs it was apparent that also three different ionic currents give rise to PIR responses. During the experiments I studied two different DSCs and stimulated PIR responses at V_H = -50 mV by injecting negative current pulses for 3 s to decrease the membrane potential to V_T = -100 mV. I subsequently blocked I_{CaL}, I_H and I_{NaP} by successively adding Nifedipine, Zd7288, and Riluzole to the bathing solution in order to identify the underlying ionic currents (Figure 19 A - D). As seen in some of the previously investigated neurons, blocking I_{CaL} increased normalized PIR amplitudes in both DSCs (mdn = 1.4, IQR = 1.1 – 2.0, N = 2; Figure 19 B, Ei, Eii). In one of two analyzed DSCs I observed the generation of a plateau potential upon release from negative current pulses. Comparable effects were observed in three RSE MNs.

In the presence of Nifedipine, DSCs responded with an increase in sag amplitudes during the hyperpolarizing pulse (mdn = 1.9, IQR = 1.4 – 2.4, N = 2; Figure 19 B, Fi, Fii) and high frequency rebound spikes post stimulation of 230 Hz ± 4.0 (Ctrl: 89.9 Hz ± 13.0; Figure 19 B, Hi, Hii). Rebound spikes were generated earlier (mdn = 0.4, IQR = 0.1 - 0.7, N = 2) and the maximum instantaneous frequency increased (mdn = 1.8, IQR = 1.0 – 2.7, N = 2). The decline in instantaneous firing frequency was characterized by a second-order exponential fit until baseline frequencies were reached of 192.0 Hz ± 8.7 (Figure 19 B, Hi). One DSC (not shown) elicited only one rebound AP in control conditions but produced rebound bursts of spikes in Nifedipine. Therefore maximum instantaneous spike frequencies were not

measured in control condition. Firing characteristics in the following experimental conditions, during Zd7288 and Riluzole treatment were consequently normalized to frequencies measured in Nifedipine condition (Figure 19 Hii).

When subsequently blocking I_H by superfusing the nervous system with Zd7288, I observed a decrease in PIR amplitude in either DSCs (mdn = 1.6, IQR = 1.1 - 2.0, N = 2; Figure 19 C, Ei, Eii). Sag potential amplitudes increased in one DSC and decreased in the other DSC (mdn = 1.5, IQR = 0.5 – 2.5, N = 2; Figure 19 C, Fi, Fii). In one DSC AP generation was blocked during Zd7288 condition (Figure 19 C) while the other showed a significant increase in instantaneous spike frequency (mdn = 11.1, IQR = 11.1 – 11.1, N = 2; Figure 19 Hii) while rebound spike latency increased (mdn = 2.3, IQR = 2.3 - 2.3, N = 2; Figure Gi, Gii).

In both DSCs PIR amplitudes became much smaller during application of Riluzole, a blocker against I_{NaP} (mdn = 1.05, IQR = 0.74 - 1.36, N = 2; Figure 19 D, Ei, Eii). Furthermore sag potential amplitudes decreased (mdn = 0.8, IQR = -1.47 – -0.45, N = 2; Figure 19 D, Fi, Fii) and rebound spikes in the remaining DSC were abolished (Figure 19 D).

The presented results indicate that a combined action of I_{CaL}, I_H, and I_{NaP} mediate PIR responses in DSCs.

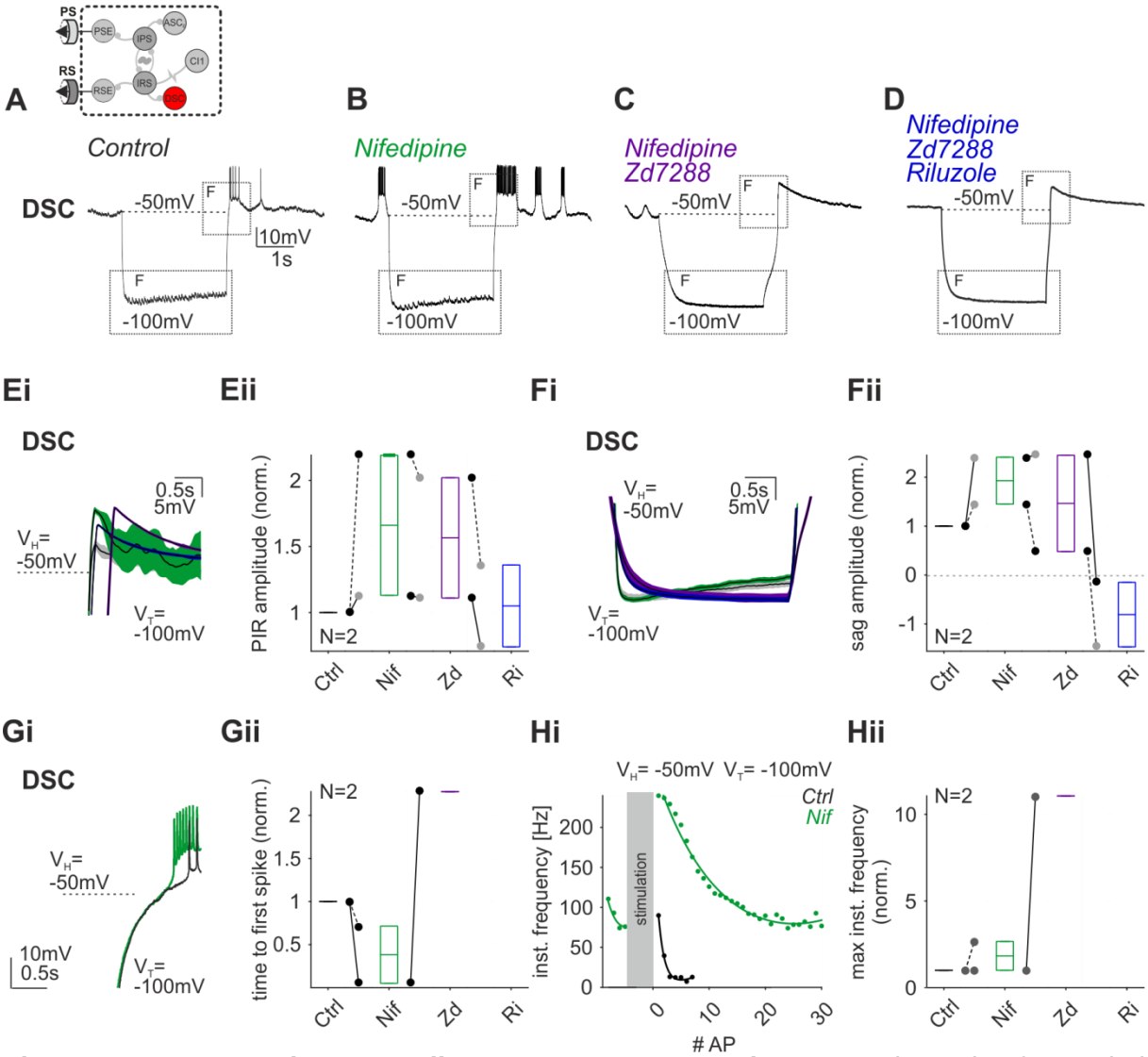

Figure 19: I_{CaL}, I_H, and I_{NaP} contribute to PIR responses in DSC. Schematic of recorded neuron. PIR responses were elicited by releasing the neurons from hyperpolarizing current pulses (V_H = -50 mV, V_T = -100 mV) (A). Successively Nifedipine (40 µM) (B), Nifedipine (40 µM) + Zd7288 (200 µM) (C) and Nifedipine (40 µM) + Zd7288 (200 µM) + Riluzole (70 µM) (D) were superfused over the abdominal nerve cord, in order to elucidate the ionic bases for the PIR. Dashed boxes indicate analyzed PIR parameters. Mean voltage traces of 15 subsequent PIR stimulations are shown in Ei, Fi. Voltage traces are smoothed to erase APs. Blocking I_{CaL} increased PIR amplitudes and sag potential amplitudes (C, Ei, Eii, Fi, Fii). First spike latencies increased and maximum instantaneous frequency decreased (Gi, Gii, Hii). Mean instantaneous firing frequencies are plotted against the number of APs following the stimulation (Hi). Decline of instantaneous frequency in control and Nifedipine condition was characterized by a second-order exponential fit. Zd7288 reduced PIR amplitudes but only partially sag potential amplitudes (Ei, Eii, Fi, Fii). Blocking I_H increased first spike latency (Gi) and enhanced instantaneous spike frequency (Hi). Riluzole treatment reduced remaining PIR responses in DSC. Box plots compare normalized PIR amplitudes (Eii), sag potential amplitudes (Fii), time to first spike (Gi), and maximum instantaneous frequency (Hii) between experimental conditions. Markers: normalized median values of single experiments (black markers: significant change of evaluated parameter, grey makers: represent failed statistical test, dark grey markers: unpaired median values were not compared in a statistical test), dashed lines: results from exemplary recording,DSC: Descending Coordinating Neuron, Ctrl: Control, Nif: Nifedipine, Zd: Zd7288, Ri: Riluzole, AP: action potential,

PIR: post-inhibitory rebound, V_H: holding potential, V_T: test potential, Wilcoxon rank sum test *: $p < 0.05$, ns: $p > 0.05$ (Supplemental Figures 30, 35, 40, 44).

3.3.3 **CPG neuron – I_H contributes to PIR responses in IPS**

In the previous chapter I found differences concerning the hyperpolarization-activated ionic current composition mediating PIR responses between MNs and Coordinating Neurons. In MNs I_{CaL} and I_H mediated all rebound responses, while in some ASC_Es and all DSCs also I_{NaP} was important, in addition to I_{CaL} and I_H. When analyzing underlying features in a rhythmically active system it is most certainly of crucial importance to understand how rhythm generation itself is established.

In chapter 3.2.2 I found evidence that in some IPSs of the pattern generating kernel a PIR response was induced when the neuron was stimulated with hyperpolarizing current pulses. Because in many systems PIR is an important mechanism of a neuron to escape from inhibition, this could be essential for establishing mutual inhibition between the CPG neurons forming the half center oscillator, IPSs and IRSs, in the swimmeret system. Therefore, I wanted to identify the underlying ionic conductances and test whether the same currents contribute as in the previously described neurons.

In control condition, of five IPSs tested only two IPSs responded with a rebound response when the neurons were released from hyperpolarizing current pulses. Consequently, I could only investigate the underlying hyperpolarization-activated ionic conductances in these IPSs. In this chapter one IPS was successfully examined and the underlying current mediating PIR responses identified.

In the presence of different ion channel blockers the generation of PIR responses was analyzed in IPS (Figure 20). PIR responses were evoked by hyperpolarizing this neuron from V_H = -50 mV to V_T = -100 mV for a period of 3 s (Figure 20 B). Blocking I_{CaL}, by Nifedipine application, caused no change in normalized rebound amplitudes (mdn = 1.1, IQR = 1.0 – 1.1, N = 1, Kruskal-Wallis test: $p > 0.05$; Figure 20 C, Ei, Eii). However the variation in measured PIR amplitudes declined under Nifedipine treatment. Sag potential amplitudes showed a significant reduction when blocking I_{CaL} (mdn = -0.7, IQR = -0.7 - -0.6, N = 1, Kruskal-Wallis test: $p << 0.001$ Figure 20 C, Fi, Fii).

Zd7288 was added to the bathing solution, to test for the contribution of I_H during PIR expression in IPS. Normalized rebound depolarization amplitudes significantly

decreased during block of I_H (mdn = 0.3, IQR = 0.3 – 0.3, N = 1, Kruskal-Wallis test: p << 0.001; Figure 20 D, Ei, Eii) while no further reduction in sag amplitudes was visible (mdn = -0.6, IQR = -0.6 - -0.5, N = 1, Kruskal-Wallis test: p > 0.05; Figure 20 D, Fi, Fii).

Because of the limited number of IPS neurons that showed PIR responses only insufficient repetition of ionic current analysis were made. Because Nifedipine failed to interfere with PIR amplitudes it remains inconclusive whether I_{CaL} is actually involved in generating PIR responses in IPS.

However, a clear diminishing effect on PIR responses could be observed when I_H was blocked by Zd7288. Therefore, I_H seems to be major current establishing PIR responses in one group of IPS. Instead of I_{CaL} & I_H in MNs and I_{CaL}, I_H and I_{NaP} in some Coordinating Neurons, only I_H seems to be a promising current establishing PIR responses in IPS.

The remaining IPS did not elicit PIR responses when being released from hyperpolarizing current pulses. This indicates heterogeneity of intrinsic mechanisms within the groups of IPS. This observation could possible correlate with the classification of IPS into the three groups, published by Smarandache-Wellmann and colleagues (2013), but remains to be elucidated.

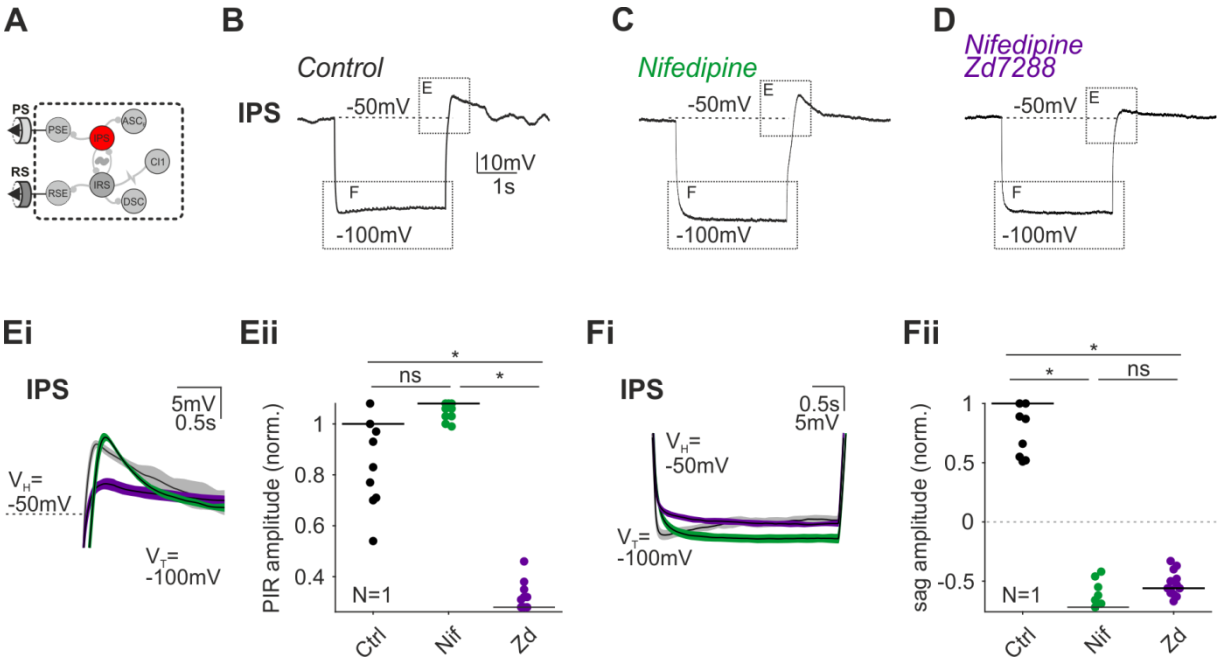

Figure 20: I_H contributes to PIR responses in IPS. Schematic of recorded neuron (A). PIR responses were elicited by releasing IPS from hyperpolarizing current pulses (V_H = -50 mV, V_T = -100 mV) (B). Successively Nifedipine (40 µM) (C) and Nifedipine (40 µM) + Zd7288

(200 µM) (D) were superfused over the abdominal nerve cord. Dashed boxes indicate analyzed PIR parameters. Mean voltage traces of 15 subsequent PIR stimulations are shown in Ei, Fi. The application of Nifedipine decreased membrane noise and voltage sag amplitudes (C, Fi, Fii). Nifedipine did not interfere with PIR amplitudes (Ei, Eii). Additional treatment with Zd7288 reduced PIR amplitudes but had no further effect on sag potential amplitudes (D, Ei, Eii, Fi, Fii). Plots compare PIR amplitudes (Eii) and sag potential amplitudes (Fii) between experimental conditions. Dots represent normalized PIR amplitude and sag potential values, during single PIR stimulations. Horizontal lines represent median values. IPS: Inhibitor of Power Stroke, Ctrl: Control, Nif: Nifedipine, Zd: Zd7288, AP: action potential, PIR: post-inhibitory rebound, V_H: holding potential, V_T: test potential, Wilcoxon rank sum test *: $p < 0.05$, ns: $p > 0.05$.

3.3.4 I_{NaP} contributes to PIR responses in ComInt1

I wanted to unveil the mediating ionic conductances, because ComInt1s were characterized by the ability to produce a 'PIR-like' response when being released from hyperpolarizing current pulses. As in all above described neurons, reliable PIR responses were elicited in ComInt1s by injecting hyperpolarizing current pulses from V_H = -50 mV to V_T = -100 mV. After observing rebound responses I subsequently applied different ion channel blockers to the preparation.

Regarding the unexpected observation that ComInt1s were able to produce PIR-like responses, though it is known to receive only excitatory synaptic, I wondered whether the underlying ionic currents might be different to the other neuron groups.

Therefore, I partially altered the order of the applied channel blockers between different experiments. However, to keep consistency with experiments in the other groups I started off in the first experiment with the same order as in the previously performed experiments (Figure 21 B, C, D). Therefore, I started with bath application of Nifedipine, then successively added Zd7288, and finally, added Riluzole to the bathing solution.

When the abdominal nervous system was superfused with Nifedipine I observed a reduction in membrane noise. This suggests that either remaining synaptic transmission was blocked during Nifedipine treatment or that spiking activity of the Coordinating Neurons was abolished (Figure 21 B). With regard to PIR-like responses, treatment with Nifedipine caused an increase in normalized PIR amplitude (mdn = 2.4, IQR = 2.3 – 2.5, N = 4, Kruskal-Wallis test: $p << 0.001$; Figure 21 B, Ei, Eii (1)) as well as a reduction in sag potential amplitudes (mdn = 0.8, IQR = 0.8 – 0.9, N = 4, Kruskal-Wallis test: $p > 0.05$; Figure 21 B, Fi, Fii (1)). When

adding Zd7288 to the bathing solution PIR amplitudes did not change (mdn = 2.3, IQR = 2.2 – 2.4, N = 4, Kruskal-Wallis test: $p > 0.05$; Figure 21 C, Ei, Eii (1)) but sag potential amplitudes decreased (mdn = 0.4, IQR = 0.3 – 0.6, N = 4, Kruskal-Wallis test: $p < 0.05$; Figure 21 C, Fi, Fii (1)). Because both previous blockers failed to abolish PIR-like responses in ComInt1 I tested the contribution of I_{NaP} by adding Riluzole to the bathing solution (Figure 21 D). During treatment with Riluzole rebound depolarizations were blocked (mdn = 0.6, IQR = 0.5 – 0.6, N = 4, Kruskal-Wallis: $p << 0.001$; Figure 21 D, Ei, Eii (1)) however no additional effect on sag potential amplitudes was observed (mdn = 0.2, IQR = 0.1 – 0.2, N = 4, Kruskal-Wallis test: $p > 0.05$; Figure 21 D, Fi, Fii (1)).

To confirm this effect of Riluzole I changed the order of the applied channel blockers and started off with Riluzole in the next two experiments. Doing so I observed that Riluzole was able to reduce PIR-like responses in one of the two ComInt1s tested (mdn = 0.7, IQR = 0.63 – 0.8, N = 4, Kruskal-Wallis test: $p < 0.01$; Figure 21 Eii (2)), while sag potential amplitudes slightly increased (mdn = 1.5, IQR = 1.0 – 1.9, N = 4, Kruskal-Wallis test: $p > 0.05$; Figure 21 Fii (2)).

Unexpectedly, PIR-like amplitudes in the other ComInt1 increased after Riluzole treatment and sag potential amplitudes decreased (mdn = 2.0, IQR = 1.8 - 2.1, N = 4, Kruskal-Wallis test: $p < 0.01$; Figure 21 Eii (3), Fii (3)).

The voltage traces of both ComInt1 recordings showed a prominent decrease in membrane noise (not shown) leading to the conclusion that synaptic input was abolished during this experimental condition.

To test whether the remaining PIR-like responses in this second ComInt1 depended on I_{CaL} I added Nifedipine to the bathing solution. Nifedipine treatment did not alter PIR-like responses in this ComInt1 (mdn = 2.1, IQR = 2.0 – 2.1, N = 4, Kruskal-Wallis test: $p > 0.05$; Figure 21 Eii (3)), however sag potential amplitudes slightly decreased (mdn = -0.1, IQR = -0.2 – 0.0, N = 4, Kruskal-Wallis test: $p < 0.003$; Figure 21 Fii (3)).

Another experiment was performed under Tetrodotoxin (TTX) application to further elucidate the role of I_{CaL} and I_H during PIR-like responses in ComInt1 (Figure 21 Eii, Fii (4)). Assuming that no transient sodium channels are present in ComInt1, this ion channel blocker was added to the bathing solution in order to abolish AP generation

in the Coordinating Neurons and would therefore block synaptic transmission to ComInt1. This was done in order to facilitate the observation of possible effects blocking I_H and I_{CaL} on 'PIR-like' responses. As hypothesized, TTX abolished all membrane noise in the ComInt1 recording, similar to the previous experiments in which Nifedipine or Riluzole was applied. This suggests a successful block of synaptic transmission. Regarding its effect on PIR- and sag potential amplitudes, TTX caused an increase in PIR depolarization (mdn = 1.6, IQR = 1.5 - 1.7, N = 4, Kruskal-Wallis test: $p < 0.002$; Figure 21 Eii (4)) and a decrease in voltage sag (mdn = 0.8, IQR = 0.8 - 0.9, N = 4, Kruskal-Wallis test: $p > 0.05$; Figure 21 Fii (4)). The additional treatment with Zd7288 increased rebound depolarization (mdn = 2.4, IQR = 2.3 – 2.4, N = 4, Kruskal-Wallis test: $p < 0.003$) and decreased voltage sag amplitudes in ComInt1 (mdn = 0.1, IQR = 0.1 – 0.2, N = 4, Kruskal-Wallis test: $p << 0.001$). During additional superfusion with Nifedipine, PIR depolarizations were reduced (mdn = 1.5, IQR = 1.5 – 1.6, N = 4, Kruskal-Wallis test: $p << 0.001$), however still remained more elevated than during control condition. Sag potential amplitudes on the other hand were not affected by Nifedipine application (mdn = 0.1, IQR = 0.1 – 0.2, N = 4, Kruskal-Wallis test: $p > 0.05$).

During the above described experiments diverse and sometimes contradictory effects of ion channel blockers on rebound responses in ComInt1s were observed. However, a strong reduction of generated PIR depolarizations was observed in two experiments during Riluzole treatment. Regarding the powerful influence of this applied blocker, I_{NaP} seems to be an important contributor during rebound generation in ComInt1s. During treatment with the other ion channel blockers less clear effects were seen. Neither Nifedipine nor Zd7288 were able to reliably diminish PIR depolarizations. Sometimes, however, slight reducing effects of these blockers were observed. Therefore, the actual contribution of I_{CaL} and I_H during rebound responses remains inconclusive.

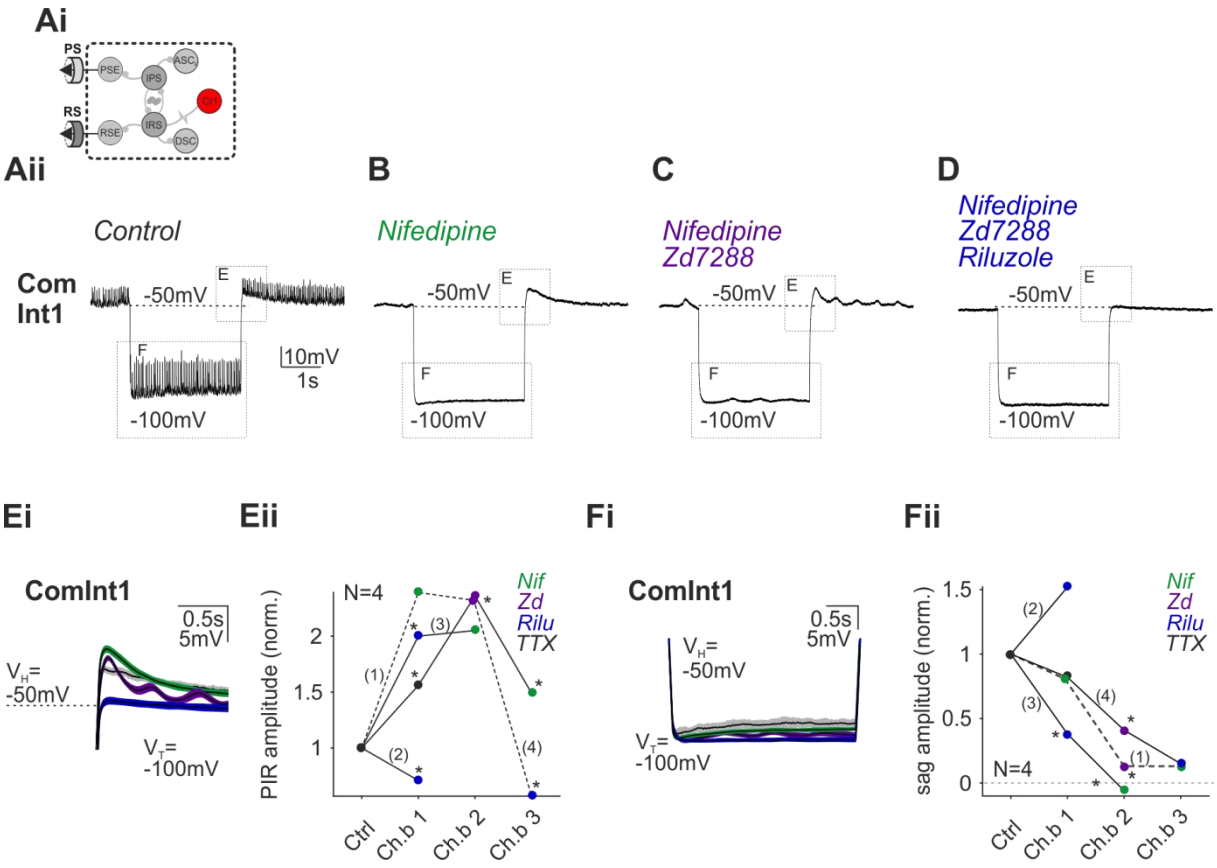

Figure 21: I_{NaP} contributes to PIR responses in ComInt1. Schematic of recorded neuron (Ai). PIR responses were elicited by releasing the neurons from hyperpolarizing current pulses (V_H = -50 mV, V_T = -100 mV) (Aii). Successively different ion channel blockers were applied (Nifedipine (40 µM), Zd7288 (200 µM), Riluzole (70 µM)) in order to elucidate the ionic bases for the PIR. The order of applied channel blockers was individually adjusted in each experiment. In one experiment a new ion channel blocker was introduced. A blocker against I_{NaT} was added to the bathing solution (TTX 0.5 µM). However this was done to abolish synaptic transmission to ComInt1 and was not expected to interfere with rebound responses. Intracellular recordings show one exemplary order of applied ion channel blockers and their effects on PIR generation in ComInt1. Dashed boxes indicate analyzed PIR parameters. Mean voltage traces of 15 subsequent PIR stimulations of exemplary channel blocker order are shown in Ei, Fi. Different channel blockers caused different effects on PIR- and voltage sag amplitudes however also partially within the same ion channel blocker application (B, C, D, Ei, Eii, Fi, Fii). Plots compare PIR amplitudes (Eii) and sag potential amplitudes (Fii) between experimental conditions. Dots represent normalized median amplitudes during single experiments. Dashed lines: results from exemplary recording, ComInt1: Commissural Interneuron 1, Ctrl: Control, Nif: Nifedipine, Zd: Zd7288, TTX: Tetrodotoxin, AP: action potential, PIR: post-inhibitory rebound, V_H: holding potential, V_T: test potential, Kruskal-Wallis test *: $p < 0.05$ (Supplemental Figures 31, 37, 42).

3.3.5 Other cellular properties affected by ion channel blocker application – effects on membrane input resistances

While identifying the underlying ionic current during PIR generation in the different neuron groups of the swimmeret system I simultaneously examined the effects of the different channel blockers on other cellular properties, namely the R_{IN}. In synaptically isolated neurons this provides information on whether the applied blockers were actually able to reduce the fraction of opened ion channels in the membrane. Therefore, this would add evidence to my results identifying the ionic bases for PIR responses in the different neurons. Furthermore, this could provide information on possible secondary effects of reduced ionic conductance on other ligand-gated or voltage-gated channels.

During application of different ion channel blockers I set the membrane potential of each neuron to -50 mV while I delivered short negative current injections of -1 nA. The following figure (22) shows the calculated R_{IN} normalized to the median of the control condition.

When blocking I_{CaL}, by Nifedipine superfusion, the R_{IN} in four of six tested PSE neurons increased (mdn = 1.2, IQR = 1.1 – 1.4, N = 4, Kruskal-Wallis test: $p > 0.05$; Figure 22 A). R_{IN} significantly increased further in all PSE when Zd7288 was applied, blocking I_H (mdn = 1.6, IQR = 1.4 – 2.8, N = 4, Friedman test: $p > 0.05$). Compared to PSEs, ion channel blockers had varying influences on RSE's R_{IN} (Figure 22 B). Blocking I_{CaL} increased R_{IN} in four RSEs while in two RSEs R_{IN} decreased (mdn = 1.2, IQR = 0.8 - 1.6, N = 4, Friedman test: $p > 0.05$). With addition of Zd7288 R_{IN} in all but one RSE increased (mdn = 1.6, IQR = 1.5 – 1.7, N = 4, Friedman test: $p > 0.05$).

In ASC_Es R_{IN} increased in all but one neuron during Nifedipine was treatment (mdn = 1.2, IQR = 1.1 – 1.4, N = 4, Friedman test: $p > 0.05$; Figure 22 C). Interestingly the one neuron that showed a decrease in R_{IN} belonged to the group of ASC_Es in which I_{CaL}, I_H and I_{NaP} generated PIR responses. During superfusion with Zd7288 varying effects on R_{IN} were observed. R_{IN} declined in three ASC_Es while two ASC_Es R_{IN} increased (mdn = 1.3, IQR = 1.0 – 1.4, N = 6, Friedman test: $p > 0.05$). No correlation was found between in- or decreasing effects of Zd7288 on R_{IN} and the two ASC_E categories. In one ASC_E R_{IN} were measured during bath application of

Riluzole. Blocking I_{NaP} led to a significant increase in R_{IN} (mdn = 1.2, IQR = 1.2 – 1.2, N = 6, Friedman test: $p > 0.05$).

During the experiments elucidating the ionic channel composition of PIR responses in DSCs similar observations to treatment with Nifedipine and Zd7288 was observed as in PSE neurons (Figure 22 D). One DSC responded with a strong increase in R_{IN} while R_{IN} in the other DSC only slightly increased (mdn = 1.08, IQR = 1.0 – 1.5, N = 2, Friedman test: $p > 0.05$). R_{IN} of both DSC increased significantly during subsequent treatment with Zd7288 (mdn = 1.87, IQR = 1.4 – 2.3, N = 2, Friedman test: $p > 0.05$) and declined when blocking $I_{NaP,}$ by Riluzole (mdn = 1.4, IQR = 1.1 - 1.9, N = 2, Friedman test: $p > 0.05$).

R_{IN} in IPS increased when blocking I_{CaL} (mdn = 1.5, IQR = 1.5 - 1.6, N = 1, Friedman test: $p > 0.05$; Figure 22 E) as well as during additional application of Zd7288 (mdn = 1.7, IQR = 1.7 – 1.8, N = 1, Friedman test: $p > 0.05$). R_{IN} in ComInt1 increased in all but one experiments (Figure 22). In one experiment (4), only TTX caused an increase in R_{IN}. Adding Zd7288 or Nifedipine in the same experiment did not alter R_{IN} further.

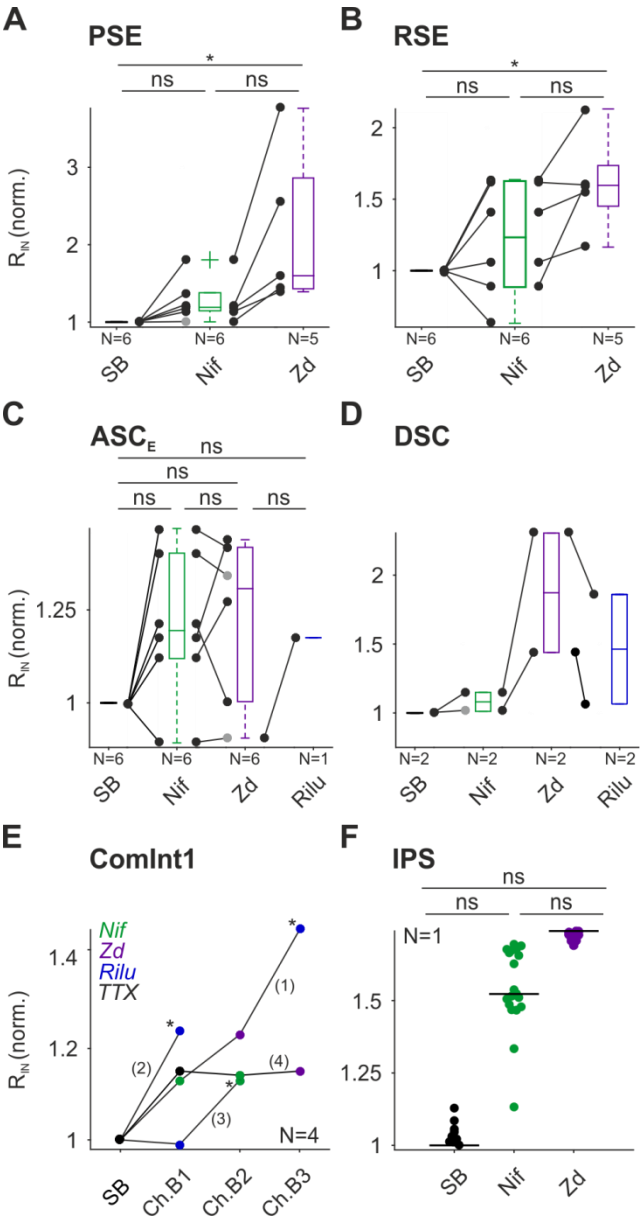

Figure 22 Input resistances mostly increased with application ion channel blocker application. R_{IN} was measured by giving a series of short hyperpolarizing current pulses. With few exceptions the R_{IN} of most neurons increased when ion channel blockers were subsequently added to the bathing solution (A - F). No consistent effect on R_{IN} was seen during Riluzole treatment. Box plots compare R_{IN} during different experimental conditions. Markers: normalized median values of single experiments (black markers: significant change of evaluated parameter, grey makers: represent failed statistical test), dashed lines: results from exemplary recording, R_{IN}: input resistance, PSE: Power Stroke Exciter, RSE: Return Stroke Exciter, ASC_E: Ascending Coordinating Neuron, DSC: Descending Coordinating Neuron, SB: Synaptic blockers, Nif: Nifedipine, Zd: Zd7288, Ri: Riluzole, Wilcoxon rank sum test *: $p < 0.05$, ns: $p > 0.05$, (Supplemental Figures 45 - 49).

3.3.6 Summary ionic currents contributing to PIR responses

In this chapter I identified ionic currents mediating PIR in key neurons of the swimmeret system. Furthermore I demonstrated that between neuron groups as well as within a group, heterogeneity in the ionic current composition exists that enable the neurons to produce PIR responses.

In the group of MNs (PSE, RSE) a combined contribution of I_{CaL} and I_H was seen to evoke PIR responses. PIR responses in the group of Coordinating Neurons were generated by different sets of ionic conductances. In ASC_Es PIR generation was either dependent on the same ionic currents as in MNs, namely I_{CaL} and I_H, or on a combination of I_{CaL} and I_H and additionally I_{NaP}. In the other Coordinating Neuron, DSC, also all three of the previously mentioned ionic conductances were found to

evoke PIR responses. Different findings were observed in IPS. Instead of being mediated by diverse ionic currents, only I_H was a promising current responsible for PIR generation in IPS. Similarly in ComInt1s only one ionic current, namely I_{NaP}, was convincingly identified to contribute to PIR generation. Supporting evidence of the above identified ionic currents during PIR generation was gathered when monitoring cellular R_{IN}.

3.4 Functional relevance of identified ionic conductances during fictive locomotion

In the previous chapters I gained important knowledge about possible cell autonomous mechanisms to depolarize the neuron when receiving phases of inhibitory synaptic input. These PIR responses were shown to be mediated by different ionic currents.

I evaluated the effects of previous described channel blockers during ongoing rhythmic and coordinated activity to test the functional implications of the above identified ionic currents.

3.4.1 Contribution of I_{CaL} during rhythmic motor activity

3.4.1.1 Blocking I_{CaL} alters rhythmogenesis but not coordination

In the previous investigation I discovered the contribution of I_{CaL} in shaping PIR responses in MNs as well as Coordinating Neurons. In the following chapter I tested whether I_{CaL} would be important during the generation of rhythmic motor activity. Therefore, I monitored the motor output of the system by extracellular recordings of Power Stroke (PS) nerve branches without synaptic isolation. After a control period, Nifedipine (40 µM diluted in normal saline with 2 µM carbachol, see Material and Methods, chapter 2.4) was superfused over the abdominal nerve cord to gain universal block of I_{CaL} in all modules of the swimmeret system. A phase analysis and a cross correlation of extracellular signals was performed to analyze changes in the motor output induced by blocking I_{CaL} (Figure 23). The cross correlation was used as an estimation of similarity and measurement of synchronicity between two PS signals.

In the control condition stable rhythmic PS bursting activity was observed. It was characterized by typical metachronal wave from posterior to anterior with a phase lag of 25 ± 0.15 (N = 5) between the segments (Figure 23 Ai, Aii, Ci, Ei). In PS4 and PS5 recordings, large amplitude APs were seen that appeared in the PS interburst interval. From this phase relation is can be assumed that these APs originate from the Power Stroke Inhibitor MNs (PSI). No recruitment of PSIs was apparent in the PS3 recording. During Nifedipine application PS bursts became less defined and

PSIs activity increased (Figure 23 Bi). When comparing all extracellular activities (PSE & PSI activity) between PS4 and PS3 during control condition and during Nifedipine treatment in a cross correlation, over periods of 30 s (Figure 23 Ci), the activity became less correlated (Figure 25 Cii, Di). Normalized peak absolute correlation values decreased compared to control condition (mdn = 0.6, IQR = 0.6 - 0.9, N = 9, Wilcoxon signed rank test: $p < 0.01$, Figure 25 Di). However, the coordination of PS bursts between segments maintained, even though the normalized mean phase lags between segments decreased slightly (mdn = 1.0, IQR = 0.6 – 1.3, N = 5, Wilcoxon signed rank test: $p > 0.05$; Figure 23 Bii, Ei). In detail, in three animals a tendency to slight face advance was detected. Varying effects on normalized PS periods (mdn = 0.9, IQR = 0.8 – 1.0, N = 9, Wilcoxon signed rank test: $p > 0.05$; Figure 23 Dii), as well as burst durations (mdn = 1.2, IQR = 0.8 – 1.4, N = 5, Wilcoxon signed rank test: $p > 0.05$; Figure 23 Eii) were seen by blocking I_{CaL}. Blocking I_{CaL} prolonged normalized PS periods in two preparations and shortened them in eight. The normalized burst duration increased in three preparations and decreased in the remaining two. The duty cycle slightly increased in four animals when blocking I_{CaL} and slightly decreased in one animal, however not significantly (mdn = 1.2, IQR = 1.0 – 1.5, N = 5, Wilcoxon signed rank test: $p > 0.05$; Figure 23 Eiii). Note that the discrepancy between sample sizes arises from two different analysis techniques. Maximum correlation values and period were gained with a cross correlation analysis comparing 30 s of PS3 and PS4 traces, while the remaining data values (phase lag, burst duration and duty cycle) were analyzed manually. During manual phase analysis the signal to noise ratio and clearly distinguishable bursts of APs are crucial for a successful accomplishment. Hence, not all experiments were used for manual analysis but were nevertheless used for the cross correlation analysis.

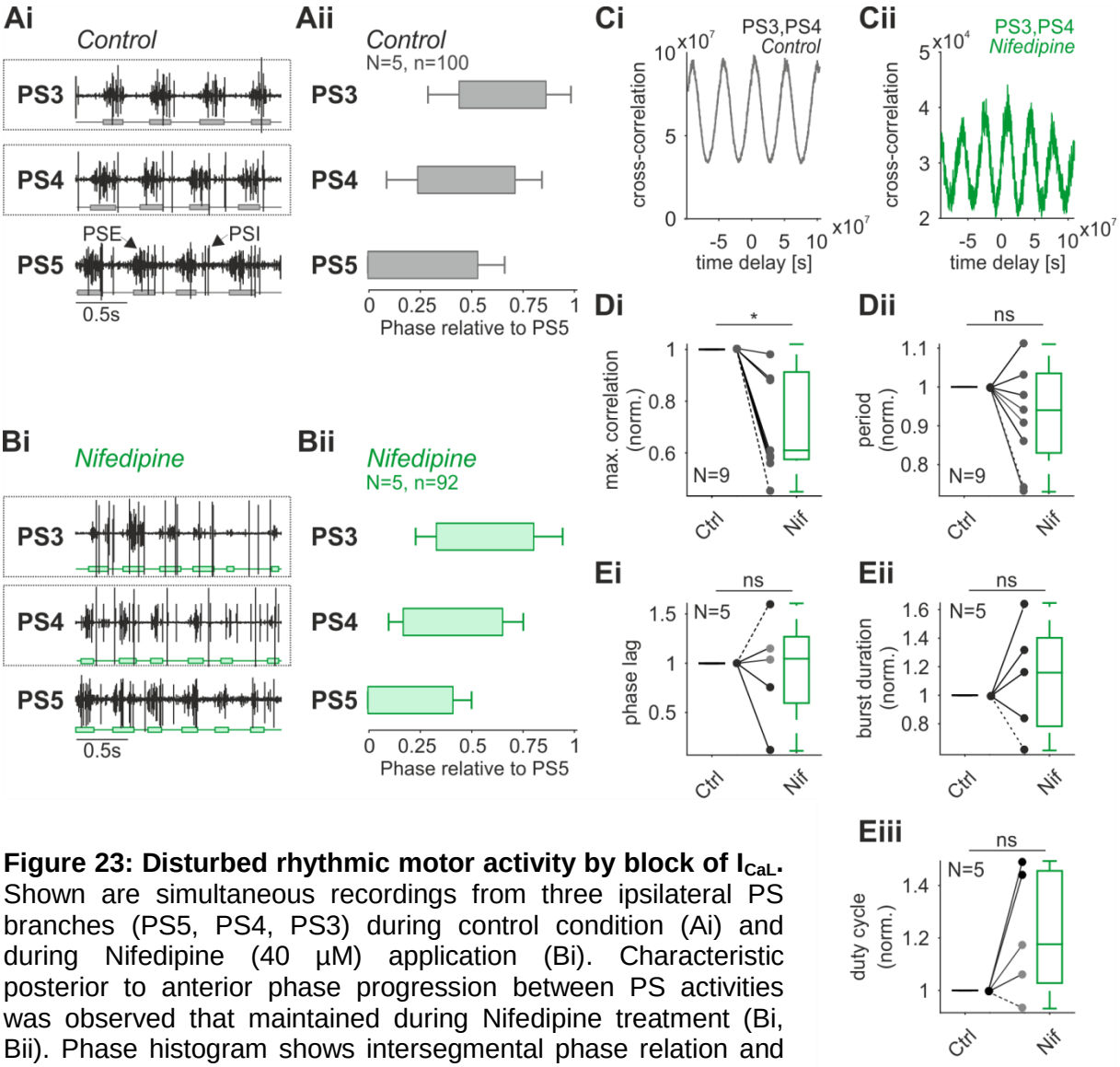

Figure 23: Disturbed rhythmic motor activity by block of I_{CaL}. Shown are simultaneous recordings from three ipsilateral PS branches (PS5, PS4, PS3) during control condition (Ai) and during Nifedipine (40 µM) application (Bi). Characteristic posterior to anterior phase progression between PS activities was observed that maintained during Nifedipine treatment (Bi, Bii). Phase histogram shows intersegmental phase relation and duty cycle of PS bursts with reverence to PS5 (N = 5). Ci, Cii Cross correlation as a function of time delay compares similarity and synchronicity of PS3 vs.PS4 activity in control and during Nifedipine application (dashed boxes in Ai, Bi). Box plots compare normalized peak absolute cross correlation values (Di), period (Dii), phase lag (Ei), burst duration (Eii), and duty cycle (Eiii) between experimental conditions. Markers: normalized median values of single experiments (black markers: significant change of evaluated parameter, grey makers: represent failed statistical test, dark grey markers: unpaired median values were not compared in a statistical test), dashed lines: results from exemplary PS4 recording, PS: Power Stroke, Ctrl: Control, Nif: Nifedipine, Wilcoxon signed rank test *: $p < 0.05$, ns: $p > 0.05$ (Supplemental Figures 50 - 53).

3.4.1.2 Blocking I_{CaL} alters single cell activity

By analyzing the effects of systematic Nifedipine application on single cell activity I observed that membrane potential oscillation shapes were altered. Intracellular recording of a PSE is shown during control- (Figure 24 Bi) and Nifedipine condition (Figure 24 Ci). In control condition the recorded PSE neuron showed large membrane potential oscillations and APs were generated during the most depolarized phase of the oscillation, whereas the first AP was always elicited at a more hyperpolarized membrane potential than the following APs (Figure 24 Bii). Blocking I_{CaL} reduced normalized oscillation amplitudes in the four PSEs analyzed (mdn = 0.8, IQR = 0.6 – 0.9, N = 4, Wilcoxon signed rank test: $p > 0.05$; Figure 24 Ci, Cii, Dii), less APs were elicited and the distribution the generated APs became broader during the oscillation (Figure 24 Cii). The initial high frequency spiking at the beginning of the PSE AP burst was absent during block of I_{CaL}. The difference in neuronal activity was accompanied by an increase in R_{IN} in three of four PSEs (mdn = 1.15, IQR = 1.0 – 1.8, N = 4, Wilcoxon signed rank test: $p > 0.05$; Figure 24 Di).

Action potential propagation along the axon increased from 2.38 ms (Ctrl) to 3.38 ms (Nifedipine) by blocking I_{CaL} (Figure 25 A, B). Latencies were measured between the peak of the intracellularly measured AP until they reached the location of the extracellular recording electrode at the posterior nerve branch of N1 in one exemplary experiment.

With the experiments described above I demonstrated the functional relevance of I_{CaL} for the generation of a functional motor output as well as for a proper generation of single cell activity and the propagation of APs along axons. Blocking I_{CaL} altered rhythm generation as well as the oscillatory activity of single MNs. However intersegmental coordination was maintained despite the difference in conduction velocities, which could also apply to the Coordinating Neurons.

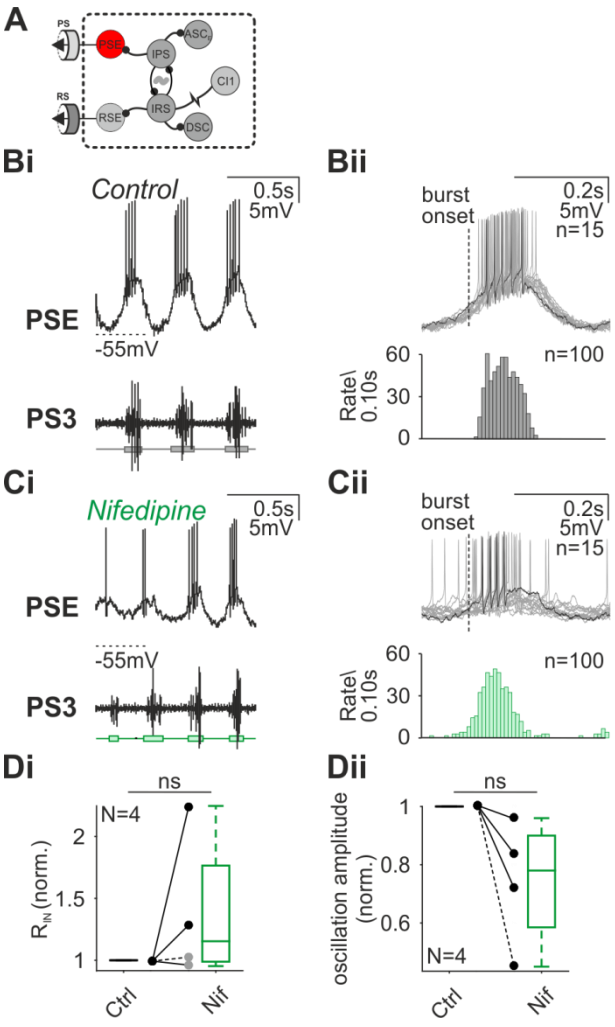

Figure 24: Decreased oscillatory activity of PSE by block of I_{CaL}. Schematic of recorded neuron (A). The contribution of I_{CaL} during generation of oscillatory activity in PSE was investigated by superfusing Nifedipine (40 µM) over the abdominal nerve cord. Shown are simultaneous intra- and extracellular recordings of a PSE (upper trace) and its corresponding PS branch (lower trace) in control condition (Bi), and during application of Nifedipine (Ci). Multiple recordings from PSE aligned to PS burst onset (15 traces superimposed) emphasize the difference of oscillatory activity between control (Bii) and Nifedipine condition (Cii). Spike correlation triggered to PS burst onset show distribution of APs during the oscillation (bin size = 8 ms). Box plots compare R_{IN} (Di) and oscillation amplitude (Dii) between experimental conditions. Markers: normalized median values of single experiments (black markers: significant change of evaluated parameter, grey makers: represent failed statistical test), dashed lines: results from exemplary recording, PSE: Power Stroke Exciter, PS: Power Stroke, R_{IN}: input resistance, Ctrl: Control, Nif: Nifedipine, Wilcoxon signed rank test *: $p < 0.05$, ns: $p > 0.05$ (Supplemental Figures 54).

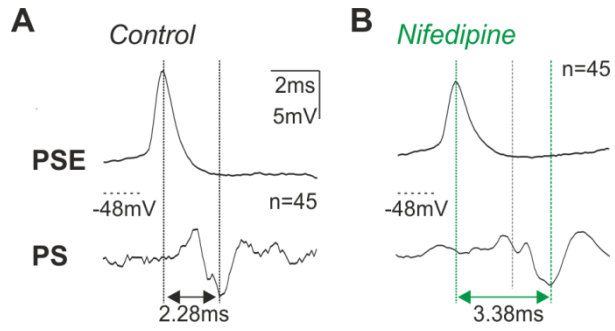

Figure 25: Reduced action potential propagation velocity by block of I_{CaL}. Single PSE APs recorded intracellularly and mean voltage traces from extracellularly recorded PS branch (n = 45) in control condition (A) and during Nifedipine treatment (B). PSE: Power Stroke Exciter, PS: Power Stroke, AP: action potential.

3.4.2 Contribution of I_H during rhythmic motor activity

3.4.2.1 Blocking I_H alters rhythmogenesis and coordination

Next to I_{CaL} I showed in the previous chapters that I_H is involved in generating rebound responses in most of the neurons in the swimmeret system. However, the activation kinetics of HCN channels is described to be far more negative than the normal working ranges of neurons. Neurons in the swimmeret system oscillate, as described in the introduction, around membrane potentials between maximum -45 mV and minimum -55 mV. As described in literature the fraction of activated HCN channels at such elevated membrane potentials is rather small. Therefore, the question remained whether I_H actually contributes to activities of the neurons for rhythmogenesis, coordination and information conduction from the CPG to the exercising muscles. Is perhaps a limited fraction of activated HCN channels enough to support neuronal activity?

To test this the motor output of the system was monitored as described in the previous chapter, 3.4.1. After analyzing the rhythmic motor bursts in control situation (Figure 26 Ai, Aii), the antagonist against I_H, Zd7288 (200 µM, see Material and Methods, chapter 2.4), was superfused over the abdominal nerve cord. Blocking I_H induced stochastic bursting activity (Figure 26 Bi) with loss of coordination between the segments (Figure 26 Bii, Cii). Normalized maximum correlation values declined significantly (mdn = 0.7, IQR = 0.6 – 0.7, N = 6, Wilcoxon signed rank test: $p < 0.03$; Figure 26 Di), while phase delays from posterior to anterior segment declined in four preparations and increased in two (mdn = 0.9, IQR = 0.7 – 1.7, N = 6, Wilcoxon signed rank test: $p > 0.05$; Figure 26 Diii). Zd7288 showed varying effects on periods (Figure 26 Dii). Blocking I_H increased periods in five of six preparations (mdn = 1.24, IQR = 1.1 – 1.5, N = 6, Wilcoxon signed rank test: $p > 0.05$), while burst durations increased in all preparations tested (mdn = 2.3, IQR = 1.5 - 4.2, N = 6, Wilcoxon signed rank test: $p < 0.03$; Figure 26 Ei). In three preparations duty cycles increased, however, in three other preparations they were not affected (mdn = 1.2, IQR = 1.0 - 1.7, N = 6, Wilcoxon signed rank test: $p < 0.03$; Figure 26 Eii). Values for periods and phase lags were gathered during cross correlation analysis comparing PS3 with PS4 traces (30 s), while burst duration and duty cycles were measured from PS4 traces in 6 experiments.

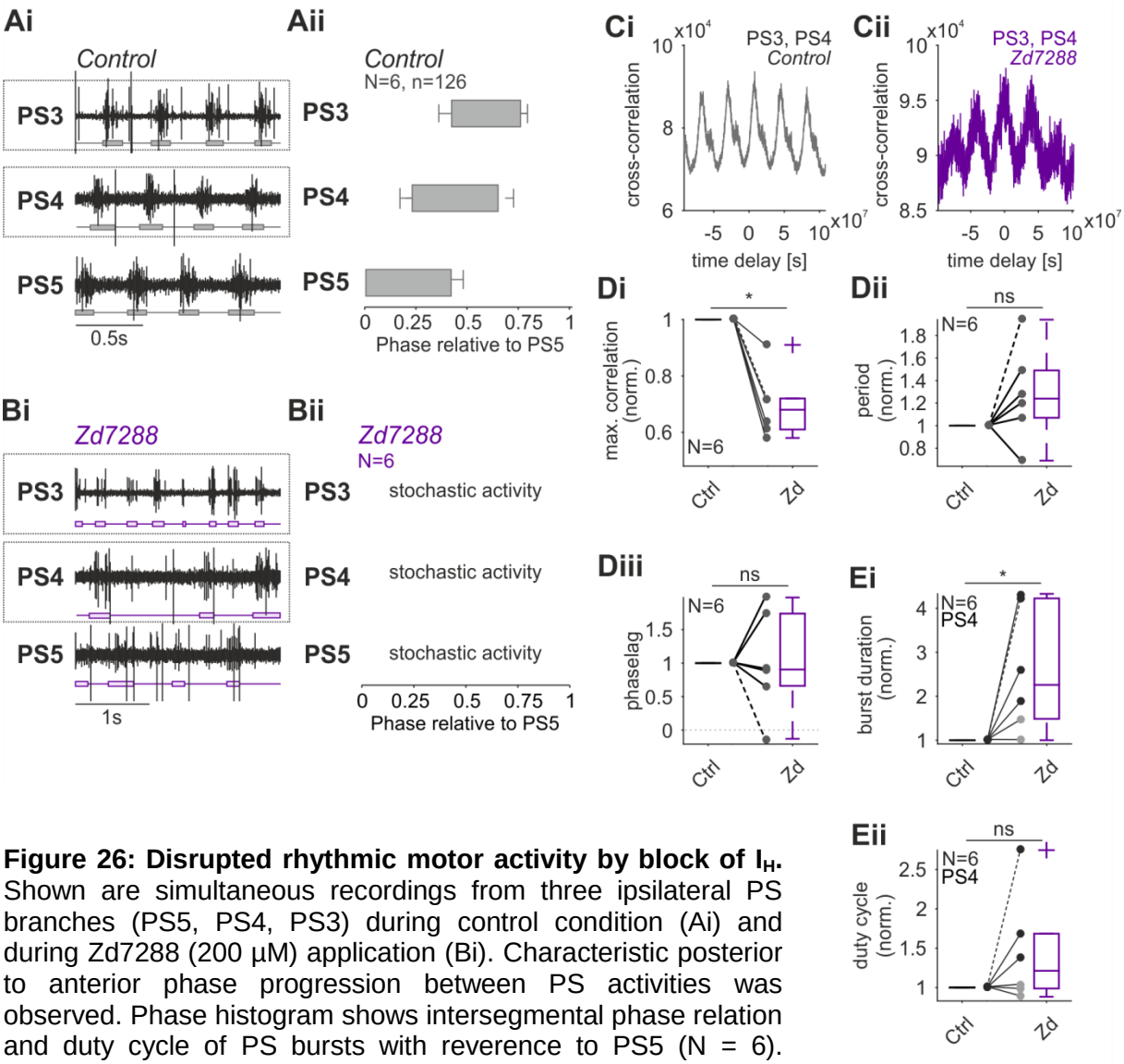

Figure 26: Disrupted rhythmic motor activity by block of I_H. Shown are simultaneous recordings from three ipsilateral PS branches (PS5, PS4, PS3) during control condition (Ai) and during Zd7288 (200 µM) application (Bi). Characteristic posterior to anterior phase progression between PS activities was observed. Phase histogram shows intersegmental phase relation and duty cycle of PS bursts with reverence to PS5 (N = 6). Rhythmic activity in each segment as well as intersegmental coordination was affected when blocking I_H. Ci, Cross correlation as a function of time delay compares similarity and synchronicity of PS3 vs. PS4 activity in control and during Zd7288 application (dashed boxes in Ai, Bi). Box plots compare normalized peak absolute cross correlation values (Di), period (Dii), phase lag (Diii), burst duration (Ei) and duty cycle (Eii) between experimental conditions. Markers: normalized median values of single experiments (black markers: significant change of evaluated parameter, grey makers: represent failed statistical test, dark grey markers: unpaired median values were not compared in a statistical test), dashed lines: results from exemplary PS4 recording, PS: Power Stroke, Ctrl: Control, Zd: Zd7288, Wilcoxon signed rank test *: $p < 0.05$, ns: $p > 0.05$ (Supplemental Figures 55 - 57).

3.4.2.2 Blocking I_H alters single cell activity

Next I analyzed the impact of I_H during oscillatory activity of single neurons. I performed intracellular recordings from PSEs during rhythmic control condition and then applied Zd7288 to the nervous system, to block I_H.

In control condition the intracellular recorded PSE was characterized by regular occurring membrane potential oscillations (Figure 27 Bi, Bii) with two to three APs generated at the maximum depolarized phase of the oscillation. The activity of MNs became irregular, during treatment with Zd7288 (Figure 27 Ci, Cii). Membrane potential oscillations broadened and normalized amplitudes tended to decrease in three of the four cells tested (mdn = 0.8, IQR = 0.7 – 1.0, N = 4, Wilcoxon signed rank test: $p > 0.05$; Figure 27 Dii). AP generation increased during Zd7288 application, however, some oscillations failed to reach spike threshold. All MNs tested, showed an increase in R_{IN} attributable to block of I_H, though significance level was not reached (mdn = 1.3, IQR = 1.2 - 2.3, N = 4, Wilcoxon signed rank test: $p > 0.05$; Figure 27 Di).

AP propagation along the axon became slower during Zd7288 superfusion (Figure 28). The latency from intracellular recorded spikes until they were measured in the extracellular MN recording of the nerve almost doubled from 3.2 ms in control condition to 5.6 ms. The presented voltage traces and propagation latency measurements were performed on one representative PSE example.

A strong influence on rhythmogenesis, intersegmental coordination and single cell oscillatory activity was observed when blocking I_H uniformly in the swimmeret system. These effects reveal an important influence of I_H during generation of a proper motor output during fictive locomotion.

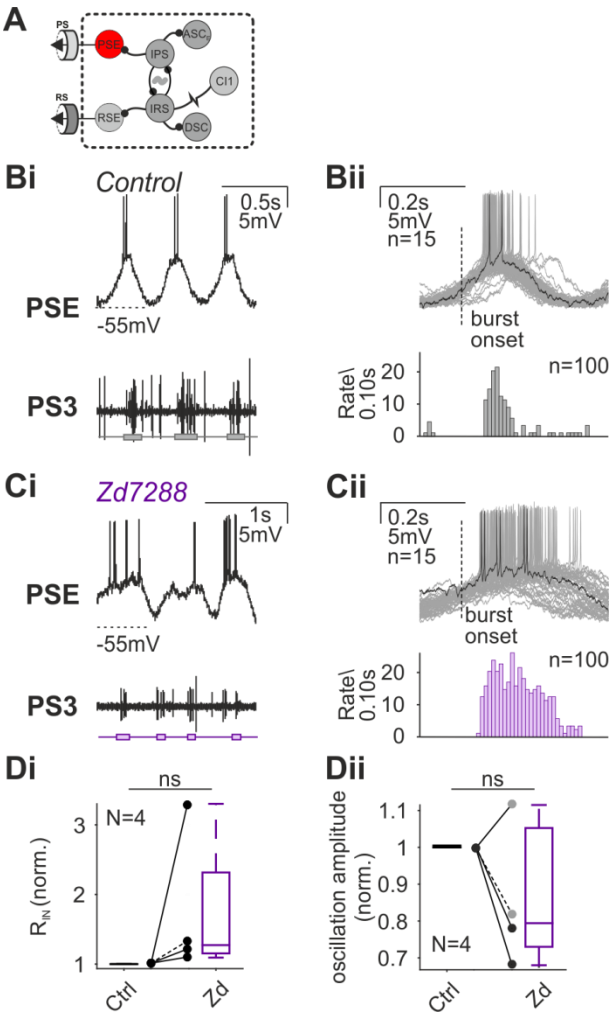

Figure 27: Disrupted oscillatory activity of PSE by blocking I_H. Schematic of recorded neuron (A). The contribution of I_H during generation of oscillatory activity in PSE was investigated by superfusing Zd7288 (200 µM) over the abdominal nerve cord. Shown are simultaneous intra- and extracellular recordings from a PSE (upper trace) and its corresponding PS branch (lower trace) in control condition (Bi) and during application of Zd7288 (Ci). Multiple recordings from PSE aligned to PS burst onset (15 traces superimposed) emphasize the difference between control (Bii) and block of I_H (Cii) during oscillatory activity. Spike correlation triggered to PS burst onset show distribution of APs during the oscillation (bin size = 8 ms). Box plots compare R_{IN} (Di) and oscillation amplitude (Dii) between experimental conditions. Markers: normalized median values of single experiments (black markers: significant change of evaluated parameter, grey makers: represent failed statistical test), dashed lines: results from exemplary PSE recording, PSE: Power Stroke Exciter, PS: Power Stroke, R_{IN}: input resistance, Ctrl: Control, Zd: Zd7288, Wilcoxon signed rank test *: $p < 0.05$, ns: $p > 0.05$ (Supplemental Figures 58).

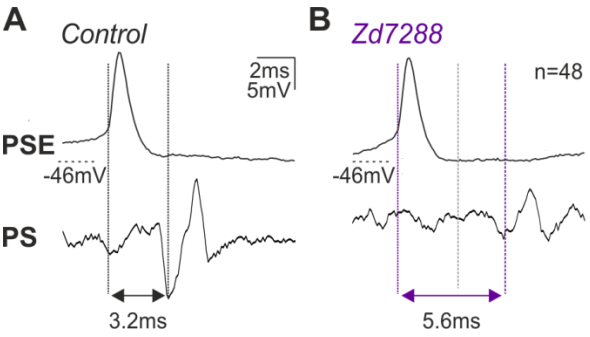

Figure 28: Reduced action potential propagation velocity by block of I_H. Single PSE APs recorded intracellularly and mean voltage traces from extracellularly recorded PS branch (n = 45) in control condition (A) and during Zd7288 treatment (B). PSE: Power Stroke Exciter, PS: Power Stroke, AP: action potential.

3.4.3 Contribution of I_{NaP} during rhythmic motor activity

3.4.3.1 Blocking I_{NaP} abolishes rhythmic motor output

When identifying the ionic conductances mediating PIR responses, the contribution of I_{NaP} was observed in some neuron groups. In some ASC_Es, as well as in DSCs, and in some ComInt1s blocking of I_{NaP} caused a reduction or even abolishment of rebound responses. These results indicate that I_{NaP} has particular importance for the activity pattern of the neurons of the coordinating network. The influence of Riluzole treatment was evaluated during ongoing coordinated and rhythmic activity. If neurons from the coordinating network relied in their activity on $I_{NaP,}$ I hypothesized to see rhythmic but uncoordinated activity.

Extracellular recordings of the PS were performed at different abdominal ganglia (Figure 29 Ai, Aii). After observing fictive locomotion Riluzole (70 µM, see Material and Methods) was bath applied over the abdominal ganglia chain to block uniformly I_{NaP} in all modules of the system. After Riluzole superfusion PS activity strongly declined and became tonic. Only rarely small, uncoordinated bursts of impulses were observed (Figure 29 Bi, Bii).

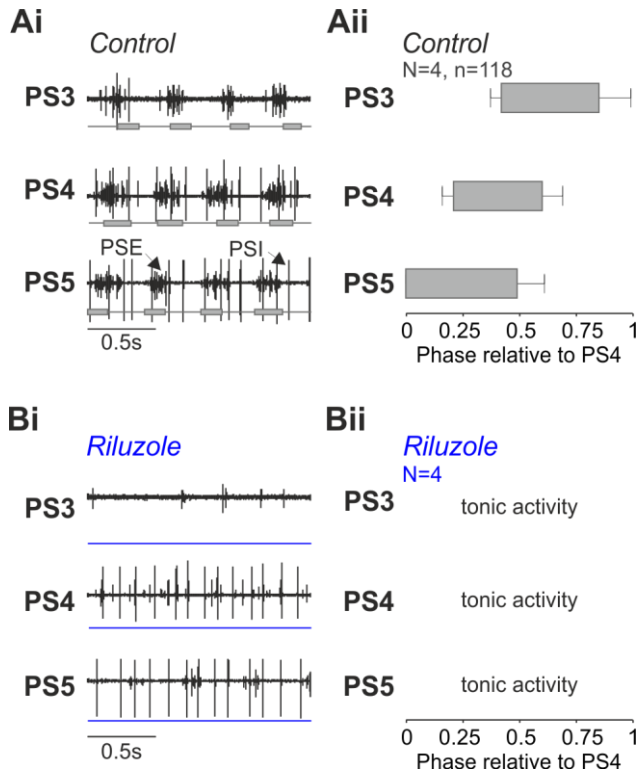

Figure 29: Abolished rhythmic motor activity by block of I_{NaP}. The contribution of I_{NaP} during generation of rhythmic and coordination motor output was investigated by superfusing Riluzole (70 µM) over the abdominal nerve cord. Shown are simultaneous recordings from three ipsilateral PS branches (PS5, PS4, PS3) during control condition (Ai) and tonic activity in Riluzole condition (Bi). Phase histogram shows intersegmental phase relation and duty cycle of PS bursts with reverence to PS5 (N = 4). In control condition characteristic posterior to anterior phase progression between PS activities was observed that was abolished during Riluzole application (Ai, Aii, Bi, Bii). Horizontal box plots show intersegmental phase relation of PS bursts with reverence to PS5 within one cycle (N = 4). PS: Power Stroke.

3.4.3.2 Blocking I_{NaP} abolishes single cell oscillatory activity

By a uniform block of I_{NaP} single cell activity of PSE was altered. During control condition the representative PSE produced membrane potential oscillations that reached spike threshold and led to the generation of mostly one spike per peak oscillation (Figure 30 B). Blocking I_{NaP} in the whole system either abolished or strongly reduced oscillatory activity (mdn = 0.3, IQR = 0.2 – 0.5, N = 4, Wilcoxon signed rank test: $p > 0.05$; Figure 30 C, Di). However, the ability to generate APs was not impaired. Normalized membrane resistance mostly increased when blocking I_{NaP} with Riluzole (mdn = 1.1, IQR = 1.0 – 1.4, N = 5, Wilcoxon signed rank test: $p > 0.05$; Figure 30 Di). Sample sizes varied between R_{IN} measurement and measurements of membrane potential oscillations.

Surprisingly, during this series of experiments not only the coordination between the segments was altered, but rhythmic activity was complete abolished. This result was seen on the network level but also on single cell activity.

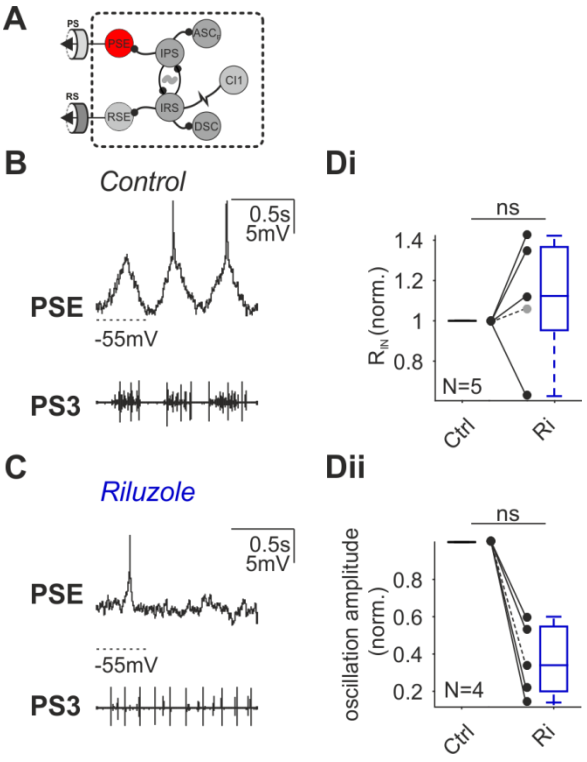

Figure 30: Abolished oscillatory activity of PSE by block of I_{NaP}. Schematic of recorded neuron (A). The contribution of I_{NaP} during generation of oscillatory activity in PSE was investigated by superfusing Riluzole (70 µM) over the abdominal nerve cord. Shown are simultaneous intra- and extracellular recordings from a PSE (upper trace) and its corresponding PS branch (lower trace) in control condition (B) and during application of Riluzole (C). Box plots compare R_{IN} (Di) and oscillation amplitude (Dii) between experimental conditions. Markers: normalized median values of single experiments (black markers: significant change of evaluated parameter, grey makers: represent failed statistical test), dashed lines: results from exemplary PSE recording, PSE: Power Stroke Exciter, PS: Power Stroke, R_{IN}: input resistance, Ctrl: Control, Ri: Riluzole, Wilcoxon signed rank test *: $p < 0.05$, ns: $p > 0.05$ (Supplemental Figures 59).

3.5 Short excurse into roles of outward currents during fictive locomotion - I_A

3.5.1 Contribution of I_A during rhythmic motor activity

Differences can be observed when comparing the shapes of membrane potential oscillations between neurons of different groups. Such differences can be seen when comparing oscillation shapes of ASC_Es and MNs. MNs usually generate membrane potential oscillations with a shallow slope and sparser AP generation during the most depolarized phase of the oscillation. In comparison, some ASC_Es produced membrane potential oscillations with very steep slopes and in general more APs. The variability of oscillations shapes indicates heterogeneity in the ionic currents that promote the oscillation between the two groups. Yet it shields light on ionic currents not been addressed in my experiments thus far, namely outward currents. Outward currents could counteract the depolarizations and thereby influence the slope of an oscillation as it could be seen particularly in PSE compared to ASC_Es. Such a mechanism could achieve precise timing and phasing of neuronal activities which is most likely crucial for proper network activity.

One outward current possibly mediating such a mechanism is the transient outward current (I_A). I_A has been shown to activate transiently at membrane voltages subthreshold and counteracts depolarizing membrane potentials. Chrachri showed the presence of I_A in the soma of dissociated swimmeret MNs (Chrachri, 1995). However, the contribution of I_A during generation of neuronal activity in the dendrites has not been addressed in his study. A contribution of I_A during neuronal activity could explain my findings from chapter 3.2.1.4, where I found a modulation in rebound spike latency that depended on the test potentials. If I_A influenced neural activity in the swimmeret system, this could also explain the slight delayed excitation I saw when hyperpolarizing the neurons to more negative test potentials in ASC_Es and PSEs. Therefore I tested how I_A affected the coordination during fictive swimming. I monitored the motor output of the system while simultaneously recording extracellular activities of two of the Coordinating Neurons, ASC_E and DSC, both projecting onto one target ganglion. Furthermore in contrast to the previous chapters, I recorded also the return stroke (RS) activity in one segment. After observing rhythmic and coordinated activity I bath applied 4-Aminopyridine (4-AP) (4mM, see Material and Methods, chapter 2.4) over the entire abdominal nerve cord to induce uniform block of I_A in all modules of the system. In control condition a steady rhythmic bursting

pattern was observed in all recordings. PS activities in PS5, PS4 and PS3 were characterized by a metachronal wave from posterior to anterior segments with a phase lag of approximately 22.6 ± 6.5 (N = 3). Activity of ASC_E was always in time with its corresponding PS burst, while DSC fired bursts of APs always in anti-phase to its home ganglion PS activity. PS and RS always fired bursts of APs alternating to one another (Figure 31 Ai, Aii). By application of 4-AP, the overall activity of the system increased, bursting became less precise, and regularity of bursting pattern decreased. The coordination between segments was strongly altered and was characterized by synchronous, in phase burst discharges between PS3, PS4 (mdn = -0.005, IQR = -0.02 – 0.03, N = 10, Wilcoxon signed rank test: $p < 0.02$; Figure 31 Dii) and ASC_Es. Thereby, coordination between the segments was less coordinated compared to control condition as shown in the slightly reduced normalized maximum correlation values (PS3 vs. PS4, mdn = 0.9, IQR = 0.8 – 1.0, N = 10, Wilcoxon signed rank test: $p > 0.05$; Figure 31 Cii, Di). Periods increased when blocking I_A (mdn = 3.4, IQR = 2.2 - 6.6, N = 9, Wilcoxon signed rank test: $p < 0.004$), however, during single experiments a wide variety of different periods were evoked. During 4-AP treatment, sequences of tonic activity alternated with synchronous PS bursting, whereas durations of tonic activities increased over time. Likewise, with an increase in periods, the burst duration increased when blocking I_A (mdn = 2.7, IQR = 2.3 - 6.3, N = 9, Wilcoxon signed rank test: $p < 0.004$) while duty cycle was not consistently affected (mdn = 0.8, IQR = 0.6 – 1.3, N = 9, Wilcoxon signed rank test: $p > 0.05$; Figure 31 Ei, Eii, Eiii). Alternation between PS3 and RS3 was maintained in 4-AP, however, DSC`s rhythmic bursting lost its phase relation to its home module before turning silent (Figure 31 Bi, Bii). PS5 activity was characterized by tonic activity in five experiments, but was also observed to burst in phase with the other segments in the other four experiments.

In a system that usually maintains its phase relation blocking I_A caused a severe impact on intersegmental coordination but also slowed down rhythm generation drastically. The contribution of I_A during single cell oscillatory activity was further investigated. PSE, ASC_E, ComInt1 and IPS were recorded intracellularly, while I_A was blocked by treatment with 4-AP.

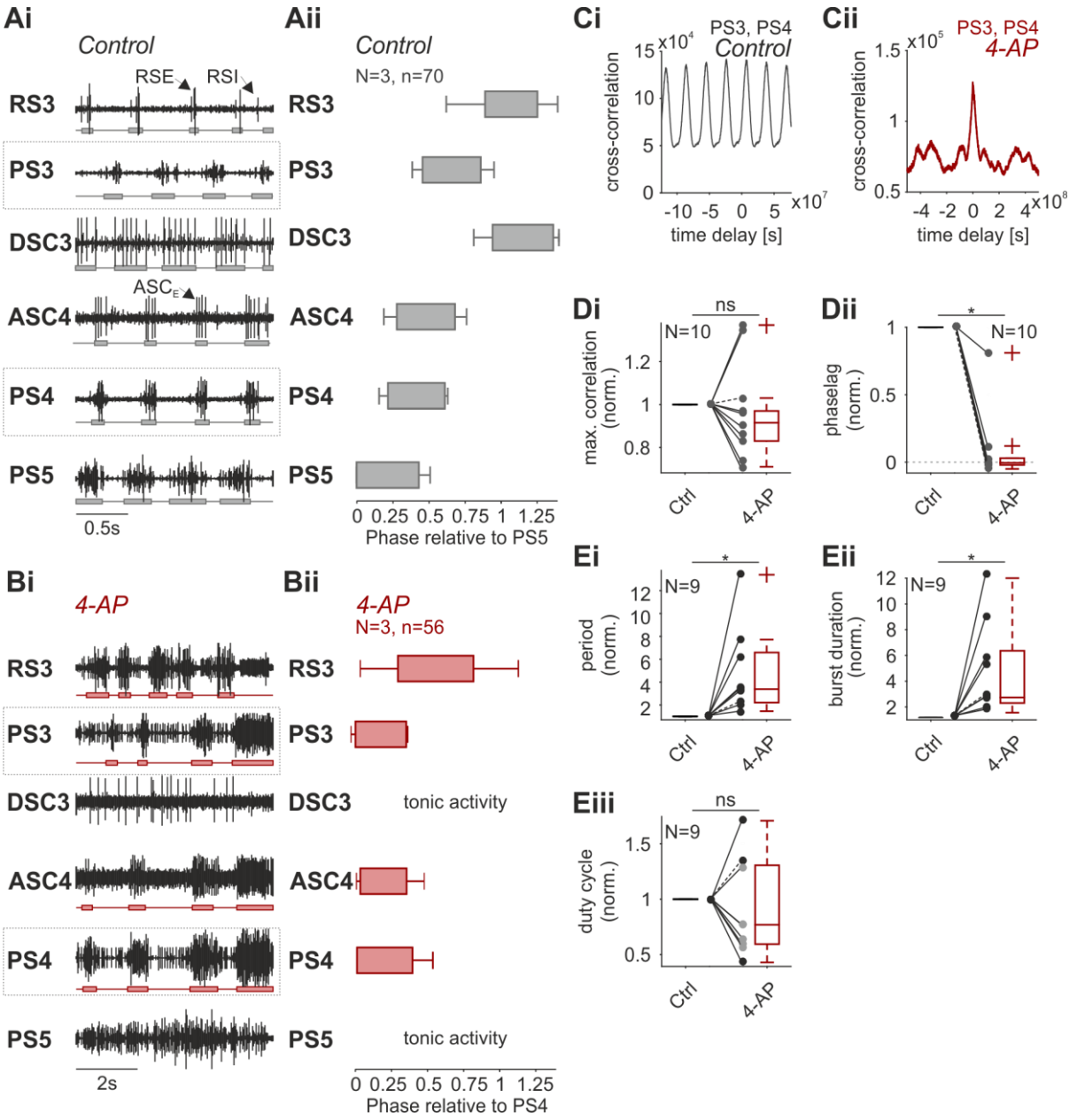

Figure 31: Synchronous motor activity induced by block of I_A. The contribution of I_A during generation of rhythmic and coordination motor output was investigated by superfusing 4-AP (4 mM) over the abdominal nerve cord. Shown are simultaneous recordings from three ipsilateral PS branches (PS5, PS4, PS3), one corresponding RS branch (RS3) and additional suction electrode recordings of ASC_E (A4) and DSC (A3). Characteristic posterior to anterior phase progression between PS activities could be seen (PS5). PS3 and RS3 are always alternatingly active (Ai). Phase histogram shows intersegmental phase relation and duty cycle of PS, ASC_E, DSC, and RS bursts with reverence to PS5 (N = 3) within one cycle of activity (Aii). Blocking I_A caused in phase PS4, PS3, ASC_E activity. DSC and PS5 fired tonically. Alternating activity between PS3 and RS3 was maintained (Bii, note that PS4 was used as a reference during 4-AP treatment). Ci, Cross correlation as a function of time delay compares correlation and synchronicity of PS3 vs.PS4 activity in control and during 4-AP application (dashed boxes in Ai, Bi). See the sharp peak in the cross correlation at zero, indicating strong synchronicity between both PS signals. Box plots compare normalized peak absolute cross correlation values (Di), phase lag (Dii), period (Ei), burst duration (Eii) and duty cycle (Eiii) between experimental conditions. Markers: normalized median values of single experiments (black markers: significant change of evaluated parameter, grey makers:

represent failed statistical test, dark grey markers: unpaired median values were not compared in a statistical test), dashed lines: results from exemplary PS4 recording, PS: Power Stroke, Ctrl: Control, 4-AP: 4-Aminopyridine, Wilcoxon signed rank test *: $p < 0.05$, ns: $p > 0.05$ (Supplemental Figures 60 - 63).

3.5.1.1 Blocking I_A alters single cell activity - PSE

In control condition the activity of PSE was characterized by steady membrane potential oscillations and one to two APs generated at the peak of the depolarization (Figure 32 Bi, Bii). During application of 4-AP, oscillation shapes and regularity of intracellular activity changed. Broadness of membrane potential oscillations varied, while the depolarizing slope of the oscillations appeared steeper, however oscillation amplitudes slightly decreased (mdn = 0.7, IQR = 0.5 – 0.9, N = 4, Wilcoxon signed rank test: $p > 0.05$). Despite this, the amount of generated APs increased (Figure 32 Bi, Bii), while no consistent effect on normalized R_{IN} was observed during 4-AP application (mdn = 0.9, IQR = 0.8 – 1.0, N = 4, Wilcoxon signed rank test: $p > 0.05$).

Similar as observed during Nifedipine and Zd7288 treatment, also 4-AP caused a change in AP propagation velocity. During treatment with 4-AP the duration between intracellularly recorded APs, until they arrived at the extracellular recording electrode at the axon of the MN, increased from 3.05 ms (Ctrl) to 4.11 ms (4-AP).

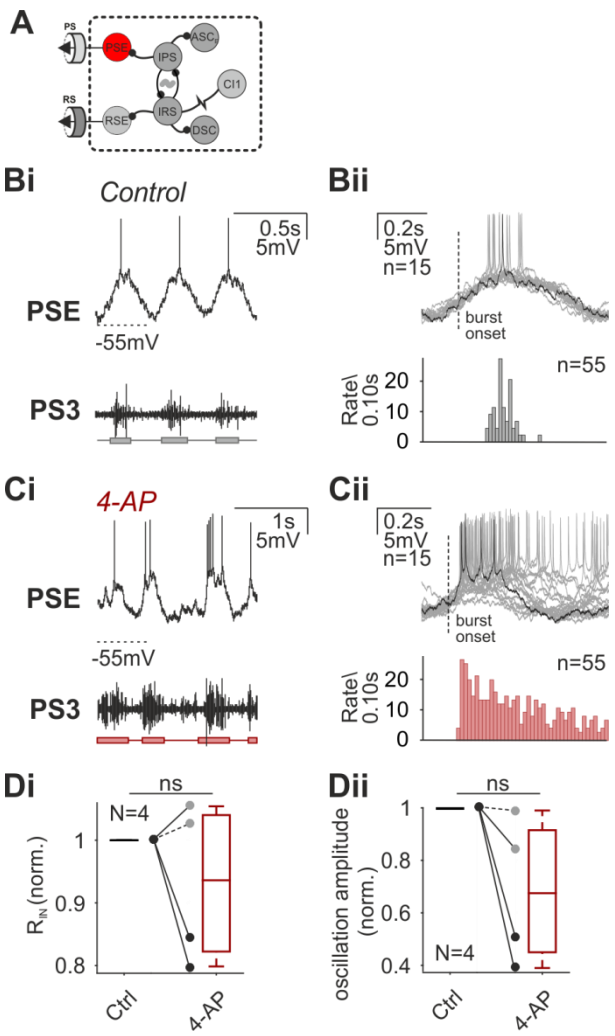

Figure 32: Altered oscillatory activity of PSE by block of I_A. Schematic of recorded neuron (A). The contribution of I_A during generation of oscillatory activity in PSE was investigated by superfusing 4-AP (4 mM) over the abdominal nerve cord. Shown are simultaneous intra- and extracellular recordings from a PSE (upper trace) and its corresponding PS branch (lower trace) in control condition (Bi) and during application of 4-AP (Ci). Multiple recordings from PSE aligned to PS burst onset (15 traces superimposed) emphasize the difference between control (Bii) and block of I_A (Cii) during oscillatory activity. Spike correlation triggered to PS burst onset show distribution of APs during the oscillation (bin size = 8 ms). Box plots compare R_{IN} (Di) and oscillation amplitude (Dii) between experimental conditions. Markers: normalized median values of single experiments (black markers: significant change of evaluated parameter, grey makers: represent failed statistical test), dashed lines: results from exemplary PSE recording, PSE: Power Stroke Exciter, PS: Power Stroke, R_{IN}: input resistance, Ctrl: Control, 4-AP: 4-Aminopyridine, Wilcoxon signed rank test *: $p < 0.05$, ns: $p > 0.05$ (Supplemental Figures 64).

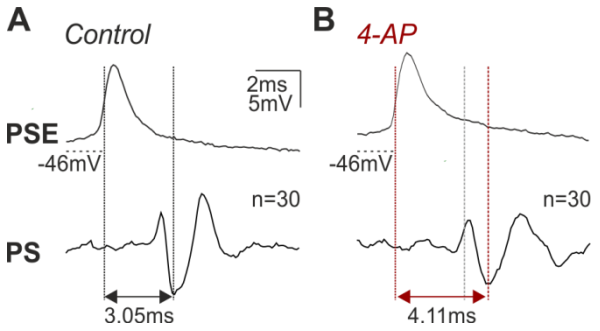

Figure 33: Reduced action potential propagation velocity by block of I_A. Single PSE APs recorded intracellularly and mean voltage traces from extracellularly recorded PS branch (n = 30) in control condition (A) and during 4-AP treatment (B). PSE: Power Stroke Exciter, PS: Power Stroke, AP: action potential.

3.5.1.2 Blocking I_A alters single cell activity - ASC_E

Similar effects as previously observed in intracellularly recorded PSE when blocking I_A, could be observed during ASC_E activity.

In control condition ASC_E was characterized by shallow membrane potential oscillation slopes and approximately one AP generated during peak depolarization of the oscillation (Figure 34 Bi, Bii). When blocking I_A, similar as in PSE, regularity of the oscillations decreased while membrane potential oscillations amplitudes increased (mdn = 1.7, IQR = 1.6 – 2.0, N = 1, Wilcoxon signed rank test: p << 0.001; Figure 34 Ci, Cii, Dii). This effect was accompanied by an increase in the amount of generated APs as well as in the R_{IN} (mdn = 1.1, IQR = 1.1 – 1.1, N = 1, Wilcoxon signed rank test: p << 0.001; Figure 34 Di). Oscillation shapes of ASC_E in 4-AP, resembled the steeper ones sometimes generated in ASC_E during control conditions.

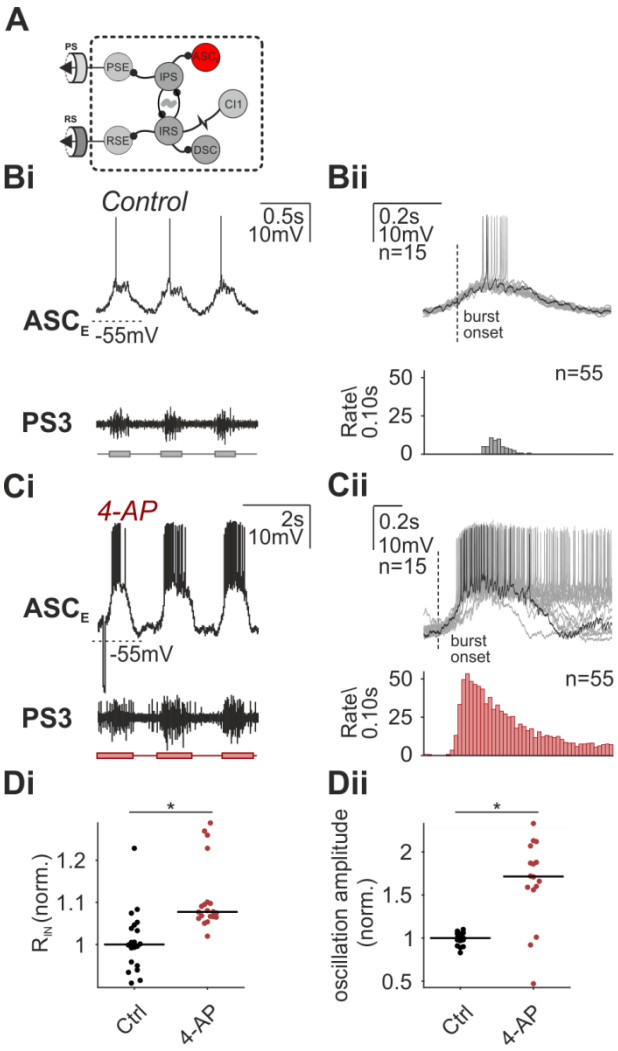

Figure 34: Altered oscillatory activity of ASC_E by block of I_A Schematic of recorded neuron (A). The contribution of I_A during generation of oscillatory activity in ASC_E was investigated by superfusing 4-AP (4 mM) over the abdominal nerve cord. Shown are simultaneous intra- and extracellular recordings from an ASC_E (upper trace) and its corresponding PS branch (lower trace) in control condition (Bi) and during application of 4-AP (Ci). Multiple recordings from ASC_E aligned to PS burst onset (15 traces superimposed) emphasize the difference between control (Bii) and block of I_A (Cii) during oscillatory activity. Spike correlation triggered to PS burst onset show distribution of APs during the oscillation (bin size = 8 ms). Plots compare R_{IN} (Di) and oscillation amplitude (Dii) between experimental conditions. Dots: single normalized R_{IN} and oscillations amplitude measurements, Horizontal lines: median values, ASC_E: Ascending Coordinating Neuron, PS: Power Stroke, R_{IN}: input resistance, Ctrl: Control, 4-AP: 4-Aminopyridine, Wilcoxon signed rank test *: p < 0.05, ns: p > 0.05.

3.5.1.3 Blocking I_A alters single cell activity – ComInt1

Regarding that ComInt1 integrates the information transmitted by ASC_E and DSC and transfers it to the CPG I wondered how the observed increase in ASC_E activity would affect ComInt1 activity. As ASC_E activity was characterized by very strong bursts of APs, I expected ComInt1 to receive an increased amount of EPSPs. However blocking I_A strongly diminished ComInt1 activitx. Comparing to control condition (Figure 35 Bi, Bii) oscillations amplitudes decreased drastically (mdn = 0.01, IQR = 0.01 – 0.03, N = 1, Wilcoxon signed rank test: p << 0.001; Figure 35 Ci, D) and synaptic transmission to ComInt1 seemed almost abolished since only small EPSPs were detected during this experimental condition (Figure 35 Ci).

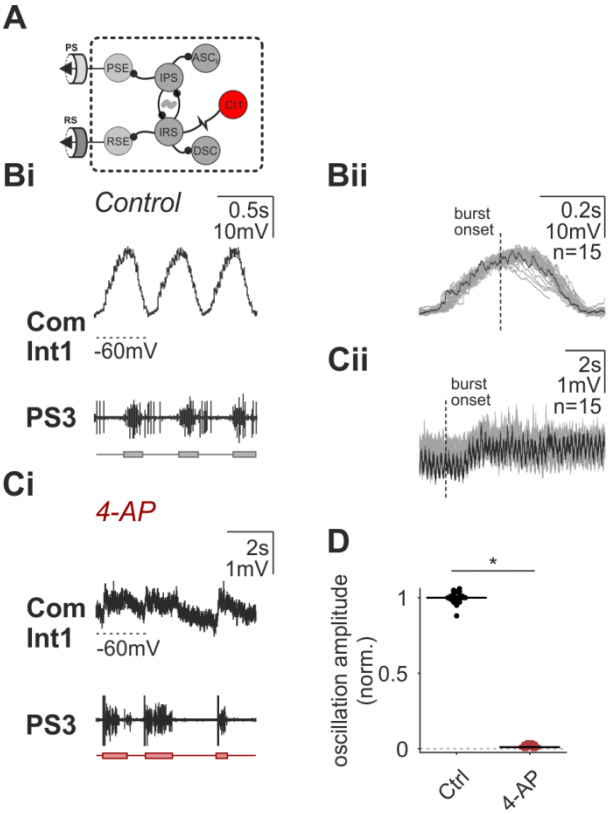

Figure 35: Altered oscillatory activity of ComInt1 by block of I_A. Schematic of recorded neuron (A). The contribution of I_A during generation of oscillatory activity in ComInt1 was investigated by superfusing 4-AP (4 mM) over the abdominal nerve cord. Shown are simultaneous intra- and extracellular recordings from ComInt1 (upper trace) and its corresponding PS branch (lower trace) in control condition (Bi) and during application of 4-AP (Ci). Multiple recordings from ComInt1 aligned to PS burst onset (15 traces superimposed) emphasize the difference between control (Bii) and block of I_A (Cii) during oscillatory activity. Plot compares oscillation amplitude (D) between experimental conditions. Horizontal lines: median values, ComInt1: Commissural Interneuron 1, PS: Power Stroke, Ctrl: Control, 4-AP: 4-Aminopyridine, Wilcoxon signed rank test *: p < 0.05, ns: p > 0.05.

3.5.1.4 Blocking I_A alters single cell activity – IPS

Blocking I_A, by application of 4-AP induced synchronous, in phase burst discharges between PS3 and PS4, however CPG activity seemed to be maintained because PS and RS alternation was preserved. However, the strong increase in cycle periods and burst duration indicates that I_A is directly or indirectly involved in generating cellular activities of the CPG neurons.

I recorded one IPS intracellularly while treating the abdominal nerve cord with 4-AP to test the functional implications of I_A during oscillatory activity. By comparing oscillatory activity of IPS between control condition (Figure 36 Bi, Dii) and 4-AP application, differences in the slops of the membrane potential oscillations became apparent. During control the membrane potential of IPS oscillated regularly which was marked by steady up- and down strokes. When blocking I_A membrane potential oscillations became broader with sharper transition between up- and down strokes, while simultaneously the amplitudes of membrane potential oscillations increased (mdn = 1.1, IQR = 1.0 – 1.4, N = 1, Wilcoxon signed rank test: $p < 0.0074$; Figure 36 Ci, D).

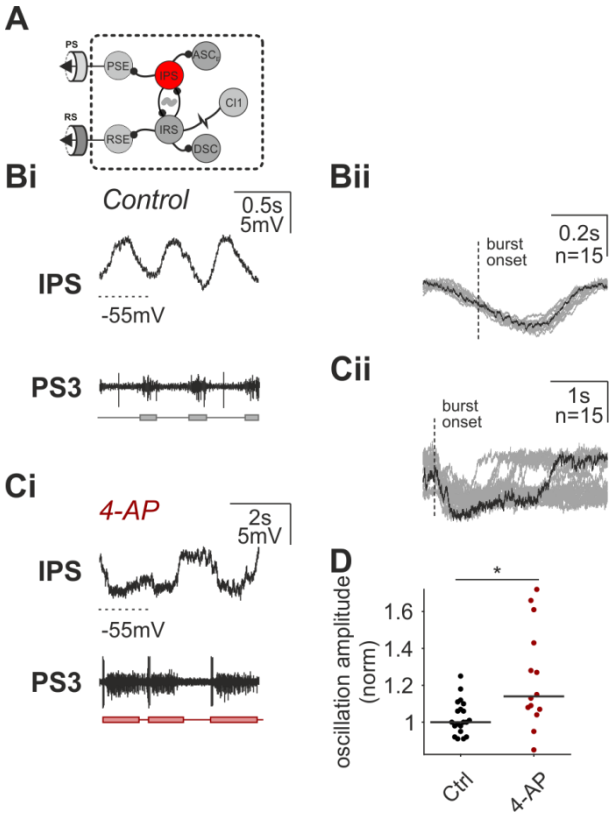

Figure 36: Altered oscillatory activity of IPS by block of I_A. Schematic of recorded neuron (A). The contribution of I_A during generation of oscillatory activity in IPS was investigated by superfusing 4-AP (4 mM) over the abdominal nerve cord. Shown are simultaneous intra- and extracellular recordings from IPS (upper trace) and its corresponding PS branch (lower trace) in control condition (Bi) and during application of 4-AP (Ci). Multiple recordings from IPS triggered to PS burst onset (15 traces superimposed) emphasize the difference between control (Bii) and block of I_A (Cii) during oscillatory activity. Plot compares oscillation amplitude (D) between experimental conditions. Dots represent single normalized measurements. Horizontal lines represent median values. IPS: Inhibitor of Power Stroke, PS: Power Stroke, Ctrl: Control, 4-AP: 4-Aminopyridine, Wilcoxon signed rank test *: $p < 0.05$, ns: $p > 0.05$.

During my experiments I gained insights about the contribution of I_A during fictive swimmeret activity. The absence of I_A strongly affected rhythm generation, coordination between the segments as well as single cell activities of PSE, ASC_E, IPS and ComInt1.

3.6 Different composition of ionic conductances mediate similar CPG activities – A computational model approach

In chapter 3.2.2 I observed disparate neuronal responses to hyperpolarizing current injections in IPS. Some IPSs responded with the generation of a rebound depolarization when being released from hyperpolarizing current pulses and some did not. These results indicated an inhomogeneous distribution in ion channels either within the dendritic aborizations or between individual IPS neurons. A third explanation could arise from changing ionic conductances depending on the internal state of the animal. Implying that all IPS neurons have the same functional relevance in the system, the latter two explanations suggest that analogue neuronal network activities can evolve from different ionic conductances, in this case resulting in alternating activity of the half center oscillator. A mathematical model was used to test whether the composition of different ionic currents was able to perform similar alternating activity of IPS and IRS. In collaboration with Prof. Dr. Silvia Daun and Dr. Azamat Yeldesbay a previously published Hodgkin-Huxley type half center oscillator model was used to simulate alternating IPS and IRS activity (Daun et al., 2009). I added ionic conductances of I_H, I_A to the previously published I_{NaP} and a leak current (I_L) to simulate more adequate representation of the CPG neurons. The model furthermore implied that both neurons received equal excitatory central drive as well as inhibitory synaptic input from another. When setting the levels of ionic conductances to g_H = 2.15 nS, g_{NaP} = 8.733 nS, g_A = 0.58 nS, g_L = 2.9 nS alternating activity of the modeled IPS and IRS could be observed with cycle periods of 0.56 s (Figure 37 Aii). In order to simulate the absence of PIR responses during my experiments I shut off I_H in both neuron types by setting the conductance of this current to g_H = 0 nS (Figure 37 Bii). As expected this abolished alternating IPS and IRS activity. However by increasing g_{NaP} = 14.45 nS rhythmic CPG activity was reestablished (Figure 37 Cii). Furthermore the alternating activity was characterized by similar periods, however, oscillation amplitudes increased in this simulation.

These presented mathematical simulations provided powerful insights, how a central pattern generating network of two neurons was able to accomplish similar activity pattern established by different ionic currents. With regard to my experimental findings from chapter 3.2.2 and 3.3.3 these results indicate how different PIR expressing IPS can still achieve the same functional rhythmic activity.

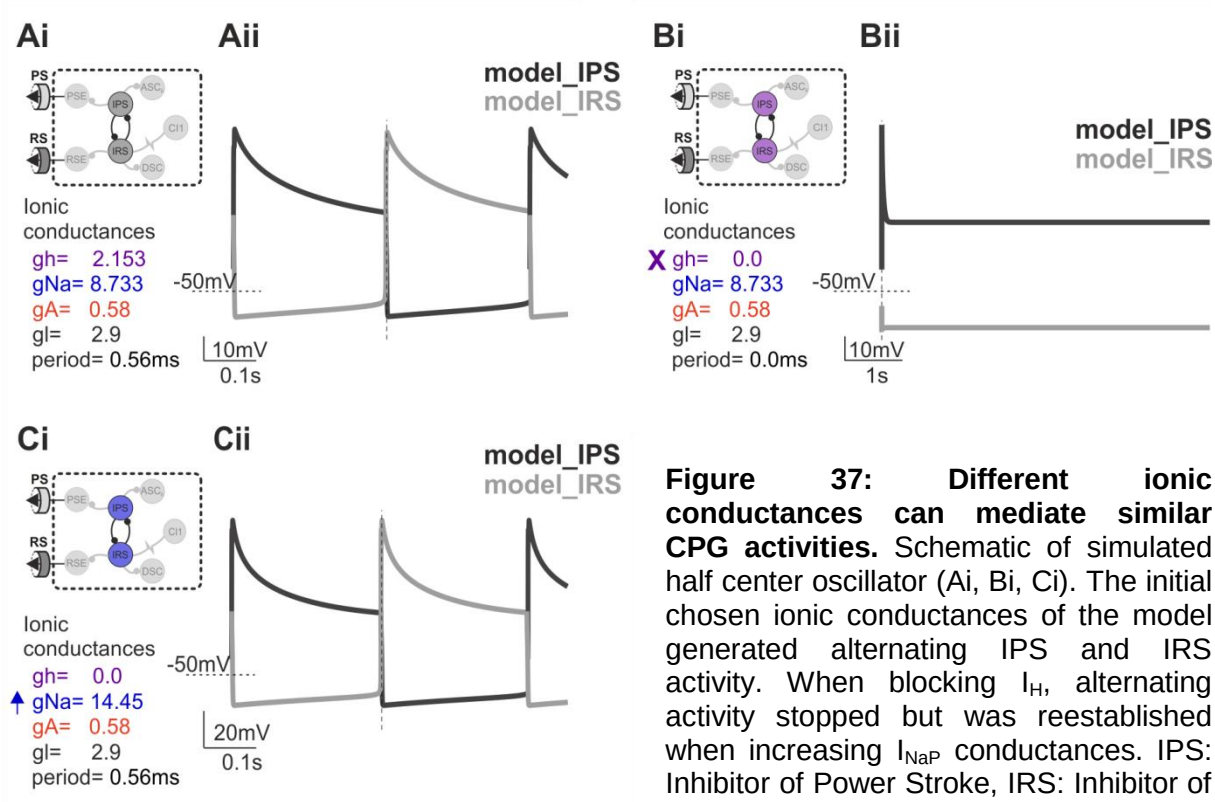

Figure 37: Different ionic conductances can mediate similar CPG activities. Schematic of simulated half center oscillator (Ai, Bi, Ci). The initial chosen ionic conductances of the model generated alternating IPS and IRS activity. When blocking I_H, alternating activity stopped but was reestablished when increasing I_{NaP} conductances. IPS: Inhibitor of Power Stroke, IRS: Inhibitor of Return Stroke, g: conductance.

4. Discussion

The goal of this thesis was to improve the understanding of how the nervous system generates behaviors such as coordinated limb movement during locomotion.

During my work I gathered insights in the complex intrinsic neuronal mechanisms that enable the swimmeret system to generate rhythmic and coordinated activity. In key swimmeret neurons I was able to identify the post-inhibitory rebound (PIR) (Getting, 1989), a membrane property that is able to increase new neuronal excitability during inhibition, and explored the underlying ionic bases. Following, I tested the functional relevance of the identified currents during fictive locomotion in order to gain a better understanding of how PIR responses are involved in generating rhythmic neuronal activity pattern in this system.

4.1 Membrane properties in key interneurons of the swimmeret system - PIR

In a rhythmically oscillating network with predominantly inhibitory synaptic connections, like the swimmeret system, the PIR was a likely membrane mechanism contributing to rhythmic neuronal activities (Wang et al., 2011).

I could detect PIR responses in the two tested groups of motor neurons (MNs) (Power Stroke Exciter (PSE), Return Stroke Exciter (RSE)), in the Coordinating Neurons, Ascending Coordinating Neuron (ASC_E), and Descending Coordinating Neuron (DSC), as well as in some Inhibitor of Power Stroke (IPS), and in the Commissural Interneuron 1 (ComInt1). Therefore, it can be expected that (1) the reliable execution of motor commands, (2) the coordination between segments, and (3), at least in some cases rhythm generation between IPS and Inhibitor of Return Stroke (IRS), is predominantly mediated by “escape” mechanisms. Thereby this mechanism can support the maintenance of rhythmic oscillatory activity (Angstadt et al., 2005; Marder and Calabrese, 1996; Matsushima et al., 1993; Satterlie, 1985). The detection of such a membrane mechanism opens the possibility to analyze ionic conductances that are likely to play an important role in generating neuronal activities. By a precise interplay of inward and outward currents, the correct phasing and magnitudes of neuronal activities can be generated to ultimately allow a functional motor output.

4.1.1 PIR responses in four groups of spiking neurons

The generated PIR responses in four groups of spiking neurons (PSE, RSE, ASC_E, and DSC) showed similar attributes. In all tested neurons, hyperpolarizing current stimulations modulated rebound spike frequency, which mostly depended on the test potential. However, neither change in test potentials nor in holding potentials reliably affected the magnitude of rebound depolarization or voltage sags in those neuron groups. Furthermore, within the neuron groups, the evoked PIR amplitudes were highly variable.

4.1.1.1 Lacking voltage dependence of PIR responses

In most other systems, PIR depolarizations are highly dependent on the membrane voltage before and during the stimulation (Angstadt et al., 2005; Bertrand and Cazalets, 1998; Tegnér et al., 1997; Wang et al., 2011), yet, PIR amplitudes were not voltage-dependent in my experiments. PIR responses in lamprey MNs and commissural interneurons, for example, result in larger rebound depolarization amplitudes at more depolarized holding potentials (Wang et al., 2011). On the other hand, leech dorsal excitatory neurons show similar PIR amplitudes at holding potentials between -55 mV and -35 mV. PIR amplitudes at more depolarized- or hyperpolarized holding potentials were shown to decline (Angstadt et al., 2005). The holding potential range used during the PIR stimulations in my experiment (between -40 mV and -60 mV) was comparable to the observed holding potential range inducing similar PIR amplitudes in the leech. This could indicate that the executed current stimulations in my experiments did not reach the necessary voltage levels to reliably decrease PIR amplitudes (more depolarized than -35 mV or more hyperpolarized than -55 mV).

Another plausible explanation for undetectable voltage dependence during PIR responses could be the contribution of the transient potassium current (I_A). In several species I_A, tunes PIR responses by counteracting the depolarization during the PIR responses (Ascoli et al., 2010; Athanasiades et al., 2000; Harris-Warrick et al., 1995; Tarfa et al., 2017). The importance of I_A for the generation of neuronal activity pattern was, for example, examined in CA1 pyramidal neurons. In these neurons, no PIR phenotype is present under physiological conditions. However it could be revealed that a strong I_A conductance suppresses all rebound responses by strongly counteracting the PIR mediating current, I_H (Ascoli et al., 2010). Only blocking I_A

could reveal the PIR phenotype in these cells. A similar contribution of I_A, however less strong, was detected in parasol cells in *Procambarus clarki* (Mellon, 2016).

I_A has been detected in the soma of dissociated swimmeret MNs (Chrachri, 1995). During hyperpolarizing current injections, inactivation of I_A is removed, ultimately leading to channel activation when releasing the neurons from hyperpolarization. Therefore, it is likely that, at least in MNs, I_A could play a role in shaping PIR responses. Thereby, I_A could counteract the depolarization during PIR responses in spiking swimmeret neurons and thus result in undetectable differences between generated PIR amplitudes elicited from different holding potentials. Because deinactivation of I_A is also voltage dependent (Athanasiades et al., 2000; Harris-Warrick et al., 1995) more transient potassium channels could be released from inactivation at more hyperpolarized potentials. This could lead to an increased I_A conductance that would compensate an increased I_H conductance at the respective test potential. This hypothesis is corroborated by the observed slight delay of first rebound spikes in PSE and ASC_E when stimulating to more hyperpolarized test potentials. If I_A contributes to shaping PIR responses this could also explain the high variance in evoked sag potential amplitudes. Likewise, as I_A could counteract the rebound depolarization, it could also reduce sag potentials. Future experiments to test if I_A contributes in shaping PIR responses would be to increase I_A by stepping to more hyperpolarized test potentials and compare the latency until first rebound spikes were elicited with or without the application of the transient potassium channel antagonist 4-Aminopyridine (4-AP) (Athanasiades et al., 2000; Tarfa et al., 2017).

4.1.1.2 Variances of PIR amplitudes within groups of spiking swimmeret neurons

The evoked PIR responses within the four groups of spiking neurons were characterized by large variances. Several factors can influence the variance of evoked PIR responses. A possible explanation could be a non-uniform distribution of ion channels along the dendritic aborizations of the neurons that contribute to the induction of PIR responses. Passive cable properties of the dendrites reduce the longitudinal current flow. Therefore the placement of the intracellular electrode, close to, or far away from the ion channels, could have strong influences on the recorded PIR amplitudes.

The high variance of PIR responses in MNs can also be explained by functional heterogeneity in the large group of neurons. The muscles of the swimmerets are innervated by 70 excitatory MNs (Davis, 1971; Mulloney and Hall, 2000). When referring to swimmeret beating, it is always simplified as Power- and Return-Stroke movements. However, when looking closer at forward and backward movements of the swimmerets also curling and turning of the rami can be observed. In *Homarus gammarus,* it was found that different groups of muscles are responsible for Power- and Return-Stroke movements than for curling and turning of the rami (Cattaert and Clarac, 1987). Furthermore, the authors could detect that different groups of MNs innervate these different muscles. In this regard it is possible that the MNs innervating those different types of muscles are characterized by heterogeneity in their PIR responses. Because rami curler MNs, have been shown to be highly sensitive to so sensory feedback (Cattaert and Clarac, 1987), these MNs could rely less on strong PIR mediating mechanisms.

Furthermore some MNs have been shown to be able to strongly interfere with the activity pattern of other MNs which led to the dismissed hypothesis that some MNs are part of the pattern generating kernel (Heitler, 1978). Regarding that electrical synapses have been found between MNs innervating synergistic muscle groups (Sherff and Mulloney, 1996), it indicates that the electrical coupling between the MNs could be heterogeneous. Thereby strong intrinsic membrane properties in one neuron could influence the activity pattern of another electrically neuron. This could influence the recorded PIR amplitudes depending on which MN was recorded from.

4.1.1.3 Ionic bases for PIR responses in four classes of spiking neurons

4.1.1.3.1 I_{CaL} contributes to PIR responses in four groups of spiking neurons

PIR responses can be generated by several ionic conductances, none of which are mutual exclusive. They include activation of hyperpolarization-activated cation channels or deinactivation of depolarization-activated channels. The low voltage-gated calcium channels have been shown to be frequently involved (Fan et al., 2000; Wang et al., 2011; Zheng and Raman, 2011). At hyperpolarized membrane voltages, inactivation of low voltage-gated calcium channels is removed, leading to increased availability of these channels when neurons are released from hyperpolarization. Influx of positively charged calcium ions thus results in rebound depolarization of the

neuron. Low voltage-gated calcium channels have been found to be important in generating PIR responses for example in leech swim MNs (Angstadt et al., 2005) or in spinal cord MNs of the turtle (Simon et al., 2003). In the lamprey, different kinds of low voltage-gated calcium channels are identified to mediate PIR responses, the T-type calcium channel as well as a low voltage activated subtype of the L-type calcium channel (Wang et al., 2011). In a study by Chrachri (1995) the L-type calcium current (I_{CaL}) was identified in the soma of dissociated swimmeret MNs next to I_A, delayed rectifier current (I_{KD}), and the transient sodium current. Regarding that I_{CaL} contributes in generating PIR responses in the lamprey and has been detected in swimmeret MNs, I tested its contribution during PIR generation in four groups of spiking swimmeret neurons. Blocking I_{CaL} with the dihydropyridine, Nifedipine, caused divers effects on PIR generation. In each neuron group increasing as well as decreasing effects on PIR depolarizations were observed. Furthermore, in three of six RSEs as well as one of two DSCs, plateau-like rebound depolarizations were evoked upon blockage of I_{CaL}.

The reduction of PIR amplitudes attributable to Nifedipine treatment, indicate the contribution of I_{CaL} during PIR depolarizations in these neurons.

An increase of PIR amplitudes during Nifedipine application is less clearly explained but could point towards secondary effects of reduced intracellular calcium concentration on other calcium-dependent currents. This hypothesis is supported by a general increase in input resistances (R_{IN}), regardless of whether Nifedipine had an increasing or decreasing effect on PIR amplitudes. Intracellular calcium accumulation mediated via the N-type calcium current as well as I_{CaL} has been shown to activate the big conductance calcium-gated potassium current (I_{BKCa}) (Sun et al., 2003). More precisely the authors demonstrated in mouse neocortical pyramidal neurons, that the application of Nifedipine reduced the transient I_{BKCa}. Blocking I_{CaL} with Nifedipine in neurons of the swimmeret system is also likely to reduce the intracellular calcium concentration. Therefore, it could be possible that calcium-gated potassium currents also decline. This could lead to the observed increase in PIR amplitudes in case a strong I_{KCa} usually counteracts PIR depolarizations during control conditions.

Another explanation for the increasing effects of Nifedipine application on PIR depolarization amplitudes is a possible interaction of Nifedipine with delayed rectifier potassium channels. A study working on human embryonic kidney cells (HEK293

cells) expressing rat potassium channels of the *shab* subfamily demonstrated a reduction of I_K by Nifedipine treatment (Li et al., 2015). Such an effect could account for the observed increase in PIR amplitudes if potassium currents (I_K) counteracted PIR depolarization in control condition.

The divergent effects caused by Nifedipine treatment indicate inhomogeneous distribution of either directly or indirectly affected ion channels along the dendrites of the recorded neurons. In lumbar spinal cord MNs of the turtle, a non-uniform distribution of L-type calcium channels was demonstrated (Simon et al., 2003). $Ca_V1.3$ channels were shown to be predominantly localized at irregular patches in the dendritic aborizations. In this study these regions could be identified as the target sites for synaptic transmission by double labeling with antibodies against synapsin of presynaptic neurons. In case of an uneven distribution of calcium channels in swimmeret neurons, the decay of voltage signals caused by passive conductance properties could result in varying PIR amplitudes depending on the placement of the recording electrode. Likewise, the distribution of calcium dependent potassium channels, as well as delayed rectifier potassium channels, has also been shown to be non-uniform within the dendritic aborizations in Purkinje neurons (Westenbroek, 2009) as well as in hippocampal neurons respectively, which could also result in the observed differences in the recorded PIR responses during Nifedipine application (Antonucci et al., 2001; Westenbroek, 2009).

The observed difference in PIR response by Nifedipine application can also be explained by varying conductances of I_{CaL} in control condition. Proctolin treatment, for example, has been shown to increase L-type calcium channel conductances in the crustacean *Idotea* and *Eriphia spinfrons* skeletal muscles (Rathmayer et al., 2002). In the swimmeret system of the crayfish, possible sources for proctolin are excitatory command- like neurons projecting though the entire nervous system (Acevedo et al., 1994). When stimulating axon fiber bundles containing some of these neurons, rhythmic swimmeret motor output was induced (Acevedo, 1990). Proctolin release can therefore be assumed to have an important function on neurons of the swimmeret system, possibly by changing the conductances of the L-type calcium channels. The isolated abdominal nervous system of crayfish produces in approximately 50 % of the time spontaneous rhythmic activity. Following this argumentation it can be hypothesized that between preparations the content of

released proctolin could be different. This in turn could affect L-type calcium channel conductances leading to the observed variance of Nifedipine application on PIR responses.

4.1.1.3.2 I_H contributes to PIR responses in four groups of spiking neurons

In different studies PIR responses have been shown to be mediated by a hyperpolarization-activated cyclic nucleotide-gated cation (HCN) channel (Angstadt and Calabrese, 1989; Bertrand and Cazalets, 1998; Harris-Warrick et al., 1995; Surges et al., 2006). These channels are known to activate at membrane potentials sub spike threshold. Upon activation, the hyperpolarization-activated non-selective cation current (I_H), induces a characteristic voltage sag during sustained hyperpolarization (Angelo and Margrie, 2011). Upon release from hyperpolarization the typically slow closing kinetics of these channels evoke a rebound depolarization.

I applied a blocker against I_H (Zd7288) in addition to Nifedipine, to elucidate the underlying ionic conductances of the remaining PIR responses in the two groups of MNs as well as Coordinating Neurons ASC_E and DSC. Both MN groups responded with a drastic reduction in PIR amplitudes upon Zd7288 treatment which was accompanied by a decrease in voltage sag amplitudes. This indicates that the remaining PIR depolarizations in the previous experimental condition (during Nifedipine treatment) were induced by I_H. This was supported by an increase in R_{IN} in most of the tested neurons. These results are in line with several studies working on sensitivity of I_H to Zd7288 (Ascoli et al., 2010; Cheng et al., 2007; Surges et al., 2006). In four ASC_Es, the same effects of Zd7288 application on PIR amplitudes and sag potential amplitudes as in MNs could be observed, leading to the conclusion that I_H mediated PIR depolarization as well as sag potentials. However, in the remaining two ASC_Es as well as in both recorded DSCs, Zd7288 failed to abolish PIR responses. In both ASC_Es PIR amplitudes increased while in both DSCs, PIR amplitudes slightly declined during Zd7288 treatment. Addition of Riluzole, a blocker against the persistent sodium current (I_{NaP}), decreased PIR responses in all neurons. This leads to the conclusion that the remaining PIR responses were elicited by low voltage-gated I_{NaP}. A similar contribution of I_{NaP} was seen to mediate PIR in leech dorsal- and ventral excitatory MNs (Angstadt and Simone, 2014; Angstadt et al., 2005). The previously observed increase in PIR responses during Zd7288 application is likely to be explained by a change in sodium conductances. During block of I_H, a

shift in the driving force of sodium ions could have been evoked that ultimately increased the the observed PIR amplitudes mediated by a stronger I_{NaP}.

The obtained results from ASC_E indicate that either I_{CaL} and I_H or I_{CaL}, I_H, as well as I_{NaP} are involved in generating the observed PIR responses. These results correlate with the differently expressed membrane potential oscillation shapes of ASC_E in control condition. As described in chapter 3.3.2.1, oscillation shapes in ASC_Es were characterized either by steep- or by shallow slopes. ASC_Es with steeper oscillation shapes produced PIR responses mediated by I_{CaL}, I_H, and I_{NaP}. The other ASC_Es with shallower oscillation shapes produced PIR responses by I_{CaL}, and I_H. This indicates that the additional contribution of I_{NaP} could function as an enhancement mechanism during the depolarizing up-stroke of the oscillations. Furthermore, these results suggest that the ion channels underlying PIR responses in this neuron type might be similarly inhomogenously distributed as I hypothesized for the MNs. This could explain the detection of different ion channel compositions mediating PIR responses in ASC_E neurons.

In three RSE and one DSC, the application of Nifedipine caused the induction of plateau-like depolarizations upon releasing the neurons from hyperpolarizing current pulses. The generation of plateau potentials is usually mediated either by I_{CaL} (Morisset and Nagy, 1999), or by I_{NaP} (Barrio et al., 1991) in other systems. Regarding that I_{CaL} was supposedly blocked during the experimental condition, the generation of the plateau-like depolarization was likely to be induced then by the remaining current I_{NaP}. This hypothesis is supported by the detection of I_{NaP} in DSCs. In RSEs however, the plateau-like depolarizations were abolished by application of Zd7288. Regarding this effect, it can be assumed that a Zd7288-sensitive current mediated the plateau-like potentials in RSEs. Although Zd7288 is used to block specifically I_H, a study by Wu and colleagues (2012) demonstrated in HEK293 cells expressing sodium channels a sensitivity of I_{Na} to Zd7288. However, this was tested in the case of transient sodium channels. Regarding the similarities of transient- and persistent sodium channels, it is possible that Zd7288 could also have an effect on persistent sodium channels. This could indicate that the observed plateau potentials in RSEs could possibly be evoked by a persistent sodium channel, similarly as in DSC. This hypothesis is further supported by the detection of Tetrodotoxin (TTX)-sensitive

plateau potentials in stretch receptor neurons in the abdominal nervous system of crayfish (Barrio et al., 1991).

Summarizing, I could detect I_{CaL} and I_H to mediate PIR responses in two groups of excitatory MNs (PSE and RSE), while PIR responses in the Coordinating Neurons were mediated either by I_{CaL} and I_H or by a combination of I_{CaL}, I_H and I_{NaP}.

4.1.2 PIR responses in the nonspiking CPG neuron - IPS

Next to the neurons enabling the conduction of motor commands to the muscles and the intersegmental coordination, I analyzed the ability to elicit PIR responses in rhythm generating central pattern generator (CPG) neurons. I focused on one representative CPG neuron group, IPS. This neuron group responded differently to hyperpolarizing current injections. Some IPS produced PIR responses when released from hyperpolarizing current injections while others did not. It was not possible to investigate possible correlations of IPSs expressing PIR, with any of the three published IPS neuron groups by Smarandache and colleagues (2013). In many stained neurons the injected dye disappeared during the fixation process which prevented closer examinations of dendritic aborizations which would have been needed to assign the recorded neurons to one of the three homologues IPS neurons.

Similar to the spiking neurons, PIR responses, generated in IPS, did not depend on the test potential. However, PIR responses were clearly affected by changes in holding potentials. Larger PIR amplitudes were evoked at more hyperpolarized holding potentials. These observed voltage sensitivities are in contrast to most published voltage sensitivities of PIR responses mediated by a combination of I_{CaL} and the T-type calcium current (I_{CaT}) or I_{CaT} and I_H. In lamprey commissural interneurons and MNs (Wang et al., 2011), in spinal grey matter neurons (Matsushima et al., 1993), as well as in rat hippocampal CA1 pyramidal neurons (Surges et al., 2006), stronger PIR responses are evoked at more depolarized holding potentials. However, in case PIR responses were exclusively mediated by I_H, the voltage dependence observed during PIR responses of IPS is likely to be explained. The reversal potential of I_H is described in different neuron populations of different species to range between similar voltages of -38 mV in rat hypoglossal MNs (Bayliss et al., 1994) to -35 mV in different leech sensory- and MNs to (Gerard et al., 2012) -32 mV in rat olfactory bulb mitral cells (Angelo and Margrie, 2011). Therefore,

PIR stimulations originating from holding potentials near the reversal potential can be expected to evoke at best small depolarizing inward currents. This could ultimately lead to smaller PIR amplitudes compared to PIR stimulations originating from more hyperpolarized holding potentials, further distant from the reversal potential of I_H.

I performed a similar occlusion experiment as previously explained in spiking neurons to elucidate the underlying ionic conductance mediating PIR responses. The application of Nifedipine, blocking I_{CaL}, failed to reduce PIR amplitudes in IPS. This indicates that I_{CaL} does not contribute to the generation of PIR responses in IPS. However variances in PIR amplitudes decreased during Nifedipine application. In a study working on substantia nigra pars compacta neurons, L-type calcium channels were detected at the presynaptic terminals (Bonci et al. 1998). Blocking I_{CaL} with Nifedipine reduced excitatory postsynaptic currents in the postsynaptic neuron in this study. Therefore the authors concluded that presynaptic calcium influx, by I_{CaL} induced transmitter release at the synapse. Therefore it is likely that blocking I_{CaL} by Nifedipine could also abolish remaining synaptic transmission to IPS, which might have been still present despite synaptic blocker application. During this experiment the R_{IN} of IPS increased during Nifedipine application, which could be a result from reduced synaptic input and could also account for the reduced variance in generated PIR responses in IPS.

In contrast, the subsequent treatment with the blocker against I_H, Zd7288, abolished PIR depolarizations and reduced sag potential amplitudes. Therefore, it can be concluded that PIR responses in IPS are mainly generated by I_H. This was further supported by an additional increase in R_{IN}. Similar findings of I_H establishing PIR responses were found in olfactory bulb mitral cells (Angelo and Margrie, 2011), hippocampal neurons (Surges et al., 2006), as well as in layer II medial entorhinal cortex stellate neurons (Shay et al., 2016).

These findings correlate with the published decline in membrane potential oscillation amplitudes of IPS during depolarizing current injections (Smarandache-Wellmann et al., 2013). If I_H represents an important current for the induction of oscillatory activity in this neuron type, it is likely that membrane potential oscillations close to the reversal potential of this current have smaller amplitudes. Similar observations could also be found in thalamocortical relay neurons (McCormick and Pape, 1990) or subthalamic nucleus neurons (Kass and Mintz, 2006). In both neuron groups the

neuronal activities are shown to be highly sensitive to baseline membrane potentials. Both neuron groups responded upon depolarizing current injections with a decrease in oscillation amplitudes and changed their spiking pattern from rhythmically bursting to tonic spiking at the more depolarized potentials.

4.1.2.1 Heterogeneous expression of PIR responses in IPS

I observed varying abilities of IPS to produce PIR responses. Some IPS responded with PIR when released from hyperpolarization and some did not. I_H was the underlying ionic current when IPS was able to produce a PIR. Different explanations can account for the heterogeneous expression of PIR responses in these cells. One possible reason could be an uneven distribution of HCN channel along the dendritic aborizations of IPS. In different studies, a non-uniform distribution of HCN channels between different dendritic compartments have been described (Angelo and Margrie, 2011; Goeritz et al., 2011; Harnett et al., 2015; Magee and Johnston, 1995). In these studies, varying conductances of I_H were detected that depended on the location of the recording electrode at the dendrites. Such uneven distribution of I_H could account for the undetectable PIR expression in some of the recorded IPSs. If the recording electrode was far away from the localization of HCN channels, the passive cable properties of the dendrites could cause attenuation of I_H. This could ultimately result in an undetectable I_H, thus resulting in no PIR expression at the recording site during my experiments.

On the other hand, the heterogeneous expression of rebound responses could also be explained by functional diversity of individual IPS neurons within the class of IPS. Three different IPS neurons have been identified according to their physiological similarities but morphological differences (Smarandache-Wellmann et al., 2013). At this point, it is not known what the functional implications of three homologues copies for rhythmic generation are. IPS_{Wedge} however, seems to have a stronger diminishing effect on PS activity, when depolarized, than the other two IPS neurons, $IPS_{Tangend}$ and $IPS_{Orthogonal}$ (personal communication C. Smarandache-Wellmann). This could imply functional diversity within the class of IPS which could correlate with biophysical differences within these neurons. This could be manifested in IPSs by different membrane mechanisms. As I have shown, some IPSs were able to escape from inhibition while others did not show this characteristic. These other IPSs could possibly rely on a “release” mechanism from IRS, rather than an “escape”

mechanism. During the “release” mechanism, slowly inactivating inward currents or activating outward currents as well as synaptic fatigue, reduces the provided synaptic inhibition to the other CPG neuron (Miles et al., 2005; Skinner et al., 1994).

Such functional diversity is reasonable when taking into account that the group of MNs can also be classified into functional groups according to the muscles they innervate. As mentioned above the group of MNs can be categorized next to Power- and Return Stroke MNs into rami curler MNs as well as rami turner MNs (Cattaert and Clarac, 1987). Thus, it is likely that the different IPS could provide synaptic input to different MNs groups. This assumption is supported by findings in other arthropods where different CPG are expected to mediate the activity pattern of different leg joints (Büschges et al., 1995).

Homeostatic plasticity between preparations can also account for the differences in PIR responses within the IPS neuron group. A study by Goldman and colleagues (Goldman et al., 2001) could demonstrate that very similar network activity can be generated by different network parameters. It was shown that different conductances of ionic currents were able to elicit the same neuronal activity pattern. Such a phenomenon could also account for the observations in IPS. All recorded IPSs in my experiments produced similar rhythmic oscillatory activity in control condition, but where then differently characterized by the ability to produce a PIR. Therefore, it is likely that different ionic conductances underlie the generation of oscillatory activities in these neurons.

Differences in ionic currents could also be caused by the action of different neuromodulators. Much is known about neuromodulatory influences on ionic conductances in the stomatogastric nervous system of the crab. Dopamine and serotonin, for example, have been shown to be able to shift the working ranges of I_H to more depolarized voltages in different neurons of this network (Flamm and Harris-Warrick, 1986a, 1986b; Kiehn and Harris-Warrick, 1992). As the content of neuromodulators in the hemolymph of individual crayfish cannot be controlled for during the experiments, it is likely that variation in the concentration between animals can influence the expression of PIR responses in IPS. Different concentrations of serotonin in the hemolymph were shown to correlate to excessive stress of the animals prior experiments (Fossat et al., 2015) or the social rank within groups of crayfish (Bacqué-Cazenave et al., 2018). Possible sources for serotonin in the

abdominal nervous system are serotonergic neurons originating in the fifth thoracic and first abdominal ganglia as described by Beltz and Kravitz (1983, 1987). In a recent study it was shown that exogenous application of serotonin on the isolated abdominal nervous system of the crayfish ceased rhythmic motor activity (Schneider et al., 2018). This study provides evidence that serotonergic receptors are expressed in neurons that are involved in generating the rhythmic motor output. Possible modulatory effects of serotonin on the conductance of I_H could be a target for future experiments.

4.1.3 'PIR-like' responses in ComInt1

When hyperpolarizing ComInt1 also rebound responses were elicited. ComInt1 has been shown to receive excitatory synaptic input from the Coordinating Neuron (Mulloney and Hall, 2003; Smarandache et al., 2009) and transmits this information to the CPG via an electrical synapse to IRS_{Hook} (Smarandache-Wellmann et al., 2014). Giving its function as a hub neuron it seems unlikely that a PIR response would play a significant role for its function. Regarding the electrical synapse to IRS is seems more likely that the observed 'PIR-like' responses in ComInt1 could be influenced by IRS activity. If this is true the responses observed in ComInt1 could possibly provide indirect insights on IRS ability to elicit rebound excitation following a phase of inhibitory synaptic input. This could be an important characteristic to establish rhythmic activity of the CPG, regarding that I could detect PIR responses in some of the tested IPS neurons (chapter 4.1.2.1).

Furthermore no conclusive identification of the underlying ionic currents mediating the 'PIR-like' responses in ComInt1 could be made. However some experiments indicated a possible contribution of I_{NaP}. Though regarding the electrical synapse to IRS is remains questionable if these channels are expressed in ComInt1 or in IRS.

4.2 Functional relevance of identified ionic currents during fictive locomotion

During phases of inhibitory synaptic input from CPG neurons, low voltage-activated inward currents are likely to play a role in promoting the depolarization of membrane potential oscillations. Hence, the combination of synaptic input, together with intrinsic neuronal properties, tightly control timing and magnitude of rhythmic neuronal activities of all contributing neurons in the swimmeret system. In the previous

chapters I demonstrated the ability of key swimmeret neurons to produce PIR responses and identified possible underlying ionic conductances.

I identified three low voltage-gated inward currents to be differently involved in generating PIR responses. Thereby I_{CaL} and I_H contributed to PIR induction in two groups of MNs (PSE, RSE), while in some of the Coordinating Neurons, next to I_{CaL} and I_H, also I_{NaP} was involved. In one of the CPG neurons, IPS, on the other hand, only I_H mediated PIR responses.

I performed occlusion experiments to examine the functional implications of these different ionic conductances for the generation of fictive swimming. Therefore I monitored rhythmic and coordinated motor output, as well as single MN activity during application of different ion channel antagonists previously used when examining the ionic bases for PIR responses in the different neuron groups.

4.2.1 Functional relevance of I_{CaL} during rhythmic motor activity

As I detected I_{CaL} to be involved in generating rebound responses in the Coordinating Neurons, ASC_E, DSC, as well as the MNs, PSE, and RSE, I tested the contribution of this current for the activity of these neurons during fictive swimming. Therefore, I blocked I_{CaL} in all modules of the swimmeret system by bath application of Nifedipine. Power-Stroke Inhibitor MNs activity increased while PSE bursts became weaker and less defined. This observation was met by a reduction in PSE membrane potential oscillation amplitudes. Together with the detected contribution of I_{CaL} in generating rebound responses, the reduction in oscillation amplitudes supports the assumption that I_{CaL} contributes to inducing escape mechanisms in PSE. By binding to L-type calcium channels in the active conformation, Nifedipine reduces inward calcium currents (Snutch et al., 2013). Thereby fewer positively charged calcium ions could accumulate inside the neurons, thus resulting in less depolarization of the membrane potential. This notion is supported by an increase in R_{IN} attributable to Nifedipine application in these MNs. However, the observation that membrane potential oscillations were not abolished during Nifedipine treatment indicate that next to I_{CaL} other depolarizing inward currents are involved in generating the up-stroke of the oscillations, likely being I_H (discussed further below, chapter 4.2.2).

During treatment with Nifedipine I could also observe a reduction in the amount of generated action potential (APs), as well as a decline in spike frequency adaptation.

Spike frequency adaptation can be mediated by multiple processes, including saturation of calcium buffering capacity (Powers et al., 1999), activation of electrogenic sodium / potassium pumps (Sawczuk et al., 1997), slowly increasing inactivation of sodium currents (Miles et al., 2005), or by slowly developing hyperpolarizing currents that are either voltage-dependent or depend on intracellular concentrations of either sodium (Bhattacharjee and Kaczmarek, 2005) or calcium ions (Peron and Gabbiani, 2009; Powers et al., 1999; Sah, 1996). The observed changes in spike frequency adaptation during Nifedipine treatment, indicate that this membrane property to be a calcium dependent process. Thereby the reduction in intracellular calcium concentration could result in a reduced calcium-gated potassium outward current (Sun et al., 2003). This observation supports my hypothesis from chapter 4.1.1.3, that I_{KCa} could be involved in shaping PIR responses.

Next to changes in AP pattern I could also observe changes in AP propagation velocity. A study working on sciatic nerve axons could detect a functional contribution of N- and L-type calcium channels during AP propagation (Barzan et al., 2016). In this study the authors saw a decrease in AP propagation velocity when treating the axons with Nifedipine. This in turn could also indicate presence of L-type calcium channels in the axons of swimmeret MNs, which could have been blocked during treatment with Nifedipine, thus leading to an increased in propagation velocity.

When analyzing the underlying ionic currents mediating PIR responses I found I_{CaL} to contribute in shaping the activity of the Coordinating Neurons as well. Therefore it can be assumed that the rhythmic activity pattern of Coordinating Neurons could be similarly affected by block of I_{CaL} as seen in MNs. This could explain how the slight effect on intersegmental coordination was caused. If Nifedipine application altered signal transmission of the Coordinating Neurons it would interfere with the information the postsynaptic ComInt1 receives.

On the other hand, a study on CA1 pyramidal neurons showed that Nifedipine had an enhancing effect on synaptic transmission (O'Regan et al., 1991). The authors observed that Nifedipine application was able to increase excitatory postsynaptic potentials (EPSPs) amplitudes and area but also changed the slope of EPSPs. Both effects could have an influence on how the synaptic information is integrated in ComInt1. Therefore also the information transmitted to the CPG could be altered and thus resulting in a changed CPG activity. Such an effect could cause the increase in

PSI recruitment, but also the varying effects on periods, burst duration, and duty cycle as observed during my experiments. This is one example of how the entirety of a rhythmically active nervous system can be altered by changing presumably the activity of only single components within the network.

4.2.2 Functional relevance of I_H during rhythmic motor activity

My results analyzing ionic conductances mediating PIR responses could show that I_H contributes to the generation of PIR responses in almost all tested swimmeret neurons. To test the implications of this hyperpolarization-activated current for the generation of rhythmic and coordinated motor output, I performed similar occlusion experiments as described in the previous chapter 4.2.1. The rhythmic motor pattern was severely impaired upon application of Zd7288. Stochastic bursting pattern in each segments occurred that was significantly less coordinated between the segments. Furthermore I could detect almost uniform increase in period and burst duration, while no reliable effect on the duty cycle could be observed.

These results are in line with a strong effect of Zd7288 on single PSE activity. The membrane potential oscillations became irregular with single oscillations failing to reach spike threshold while membrane potential oscillations broadened and oscillation amplitudes declined during Zd7288 application. The reduction in oscillation amplitudes indicates that the applied channel blocker was able to diminish a depolarizing inward current, most likely mediated by I_H. This observation is met by an increase in R_{IN} in the recorded neurons, supporting the notion that ion channels closed during blocker application. Similar observations were made in rat hippocampal dentate gyrus cells (Aponte et al., 2006) or CA1 neurons (Maccaferri and McBain, 1996) during treatment with Zd7288. Furthermore, I could observe a decline in AP propagation velocity. Similar observations have been made in pyramidal neurons of rat. More specifically the propagation of dendritic spikes was observed to be prolonged under Zd7288 treatment (Harnett et al., 2015).

Neither Zd7288, nor Nifedipine (chapter 4.2.1) treatment alone, were sufficient to abolish the generation of membrane potential oscillations. This indicates a combined action of I_{CaL} and I_H to initiate the depolarization of the membrane potential after receiving inhibitory synaptic input from the CPG. This hypothesis is supported by my

results identifying both I_{CaL} and I_H mediating PIR responses in PSE neurons in chapter 3.3.1.1.

Given the knowledge that PSE activity is strictly shaped by IPS activity (Mulloney, 2003) it can be assumed that the irregular activity observed in PSE arises from impaired CPG activity. This seems likely since only I_H seemed to mediate PIR responses in IPS.

As ASC_E is known to receive the same synaptic input from IPS than PSE (Smarandache-Wellmann and Grätsch, 2014), and I could show that PIR responses in ASC_E are similarly shaped by I_H as in PSE, it can be hypothesized that the activity in ASC_E could similarly be affected by Zd7288 treatment as in PSE. This could explain the impairment of intersegmental coordination in this experimental condition. If the activity pattern in ASC_E and DSC were characterized by irregular AP burst discharges,like in PSEs, the information received in ComInt1 would arrive without the correct phasing. The altered transmission to the CPG could therefore increase the irregularity of CPG activity.

These results indicate that I_H plays an important role for the activity of the CPG, but also for the Coordinating Neurons and MNs.

4.2.3 Functional relevance of I_{NaP} during rhythmic motor activity

The PIR responses in some ASC_Es (2 out of 6), and all DSCs were mediated by I_{CaL}, I_H, and I_{NaP}. The other neuron groups seemed not to rely on I_{NaP} during PIR generation. When treating the abdominal nervous system with Riluzole, to block I_{NaP}, rhythmic motor activity was abolished in all segments, suggesting that I_{NaP} is significant for the generation of rhythmic, coordinated activity in the swimmeret system. This effect was unlikely a sole effect on the Coordinating Neurons. In case the activity pattern of Coordinating Neurons was obstructed by blocking $I_{NaP'}$, it is unlikely that this would cause a total loss of motor activity in all segments. Murchison and colleagues (1993) tested the necessity of intersegmental signals for the generation of rhythmic activity in individual segments of the swimmeret system. The authors detected that each microcircuit was able to produce rhythmic activity even in the absence of intersegmental information, transmitted through the connectives (Murchison et al., 1993).

Regarding that Riluzole abolished all rhythmic motor output it can be assumed that either MNs and/or CPG neurons also dependend on I_{NaP}. Thereby I_{NaP} is likely to be high voltage-gated (Kiss, 2003) because a low voltage-gated subtype would have been revealed during the executed PIR stimulations.

4.2.4 Functional relevance of I_A during rhythmic motor activity

During my experiments analyzing PIR responses I found indications about a possible contribution of I_A. As discussed in chapter 4.1.1.1 a putative influence of this current could have resulted in the undetectable voltage dependence of PIR responses in the four tested spiking neuron groups. This assumption is supported by several studies observing I_A to contribute in tuning of PIR responses by counteracting the depolarization of the membrane potential (Ascoli et al., 2010; Harris-Warrick et al., 1995; MacLean et al., 2003).

A possible influence of I_A could also account for the observed variances in shapes of membrane potential oscillations during control condition between neuron groups, but also between recordings of neurons from the same group. As discussed in chapter 4.1.1.3.2, membrane potential oscillations recorded in different ASC_Es are characterized by different shapes. These differences indicate heterogeneity in the intrinsic properties underlying the generation of the oscillations. However, besides a possible contribution of I_{NaP}, as discussed above, the divergence in oscillations amplitudes can be also be explained by divergent contribution of I_A. Thereby this current could counteract the depolarization of the membrane potential, thus leading to smaller amplitudes and shallower slopes as observed in some of the recorded ASC_Es. If I_A contributes to shaping membrane potential oscillations in some ASC_Es, the variances in shapes between recordings could be manifested by an uneven distribution of ion channels along the dendritic aborizations of the recorded neurons. In CA1 pyramidal neurons it has been shown that the density of transient potassium channels increases with distance from the soma in the apical dendrites (Hoffman et al., 1997). To test the contribution of I_A for a functional motor output I performed an occlusion experiment with 4-AP.

During 4-AP treatment episodes of synchronized in phase PS and ASC_E bursts occurred. Additionally, DSC's activity first lost its phase relation to its home module, before turning silent.

Similar network synchronization under 4-AP treatment was observed during the expression of fictive locomotion in rat (Taccola and Nistri, 2005) and cat (Dubuc and Rossignol, 1989).

However CPG activity seemed to be preserved during this experimental condition as the alternation between PS and RS was maintained and the intracellularly recorded IPS was still oscillating. Yet, the activity of the CPG was clearly altered since the PS period and burst duration increased. Membrane potential oscillations amplitudes of IPS increased during 4-AP treatment, with sharper transitions between up- and down-strokes. These changes are likely to be explained by a loss of I_A. As transient potassium channels open at membrane voltages subthreshold, the evoked I_A could dampen the depolarization of the membrane during the oscillation (Yuan and Chen, 2006). These outward currents could therefore account for the smooth transitions between up- and drown-strokes of IPS in control condition. Similar effects of 4-AP have been observed in a study elucidating the role of I_A in neurons of the preBötzinger complex (Hayes et al., 2008). The authors observed a more abrupt rise of the membrane potential during the inspiratory bursts during 4-AP treatment, while also higher bursts amplitudes were reached.

Intracellular recordings of PSE and ASC_E revealed similar effects of 4-AP on membrane potential oscillations shapes. In both neurons types, 4-AP induced steeper up-strokes of the oscillation and increased the amount of generated APs. Especially in ASC_E the contribution of I_A seems to be the cause of the variances in oscillations shapes observed in control condition. This could be assumed because 4-AP treatment changed the slopes of the generated membrane potential oscillations in ASC_E from the shallow oscillation category to a steeper oscillation, which resempled closer the steep category of membrane potential oscillations during control condition.

During 4-AP treatment, I additionally observed a decrease in AP propagation velocity in PSE which can be explained by an increase in leak conductance attributable to 4-AP treatment (personal communication N. Daur). Regarding the similar effects of 4-AP on the shape of membrane potential oscillations in PSE and ASC_E, I assume AP propagation velocity in ASC_E to be similarly affected by 4-AP treatment. This in turn could indicate that information transmitted by ASC_E would reach ComInt1 in the next anterior segment later, and could possibly fail to reach further distant segments.

Regarding this and the obvious cessation of DSC activity could cause the change in phase delay between the segments in the experimental condition.

The observed in phase synchronization of all PS MN bursts, during 4-AP treatment, could be simulated in a mathematical model (Zhang, Schläger, Smarandache-Wellmann, 2018 in preparation). The simplified mathematical model express in phase synchronization of PS activity when assuming, in accordance with the experimental results, that each microcircuit only receives intersegmental information from the nearest neighboring ASC_E, while no information was received from any DSC. Both assumptions would result in a loss of the gradient of synaptic strength (Smarandache et al., 2009). This assumption is supported by intracellular recordings of ComInt1. In control condition, ComInt1 is known to integrate the information of three different Coordinating Neurons, thereby three different sizes of EPSPs are are always observed during intracellular recordings (Mulloney and Hall, 2003; Smarandache et al., 2009). During 4-AP treatment only one size of EPSPs was elicited in ComInt1. This is in line with the assumption that only information from the closest posterior neighbor is received as postulated in the model.

These results could demonstrate a significant importance of I_A for the generation of a rhyhtmic motor output. By counteracting the depolarization of membrane potential oscillation this current is likely to be of great importance for the generation of the correct phasing of neuronal activities.

4.3 Different composition of ionic conductances mediate similar CPG activities

Mathematical models are a useful tool to test hypotheses from experimental data and to predict the outcome of future experiments. Modeling can easily be applied to ionic currents because most of them are readily approximated by Hodgkin and Huxley equations. The aim of this modeling approach was to improve the previously published representations of the swimmeret system. The neuronal network of the swimmeret system producing rhythmic and coordinated motor output has been simulated in different models (Jones et al., 2003; Skinner and Mulloney, 1998; Spardy and Lewis, 2018; Zhang et al., 2014). Thereby, a lot of progress has been made in understanding how different intersegmental connections could account for the 0.25 cycle phase delay between the segments. However, lacking physiological

data, neither of the published mathematical models was able to simulate a realistic representation of the neurons in the half center oscillator with the appropriate ionic conductances.

In this study, I aimed at establishing a more realistic half center oscillator model that includes the ionic currents that were observed to influence the activity of the CPG in my experiments.

During my experiments I found indications that I_A (chapter 4.2.4) and I_{NaP} (chapter 4.2.3) might contribute to shaping the activity pattern of IPSs. Furthermore when analyzing membrane properties of IPSs, I detected different abilities of these neurons to produce a PIR response. Some IPSs were able to produce a PIR when being released from hyperpolarization, while others were not. Furthermore, I could identify the PIR to be generated by I_H. Given the different abilities of IPS to express a PIR, it is likely that these neurons are characterized by a different ion channel composition. However all recorded IPS produced the same oscillatory rhythmic activity in control condition. Therefore this indicates that the same neuronal activity pattern can be expressed by the combination of different ionic conductances. This hypothesis was tested in a mathematical model based on a Hodgkin and Huxley type representation of a half center oscillator published by Daun and colleagues (2009). I incorporated the ionic conductances of I_A and I_H to the previously published conductances of I_{NaP} and I_L. In this condition steady alternating CPG activity could be simulated.

However, when reducing the conductance of I_H to replicate IPS activity without rebound properties, the half center oscillator failed to establish alternating CPG activity. When increasing the conductances of I_{NaP} in the follwoing, I could simulate similar alternating CPG activity that was then only mediated by a combination I_{NaP}, I_L, and I_A compared to the previous combinations of ionic currents (I_H, I_{NaP}, I_L, and I_A). These results are in line with several theoretical investigations showing that similar network activities can arise from different combinations of ionic conductances (Goaillard et al., 2009; Prinz et al., 2004). This can explain how similar rhythmic IPS activities can arise with or without the contribution of I_H. The divergence of I_H conductances can either be a result of different HCN channel expression between individual IPS neurons (Angelo and Margrie, 2011) or heterogeneity in the channel distribution along the dendrites (Ascoli et al., 2010), but could also arise from actions of different neuromodulators (Daur et al., 2016).

4.4 Comments on synaptic isolation

When analyzing cellular properties of the swimmeret system, it was crucial that the neurons were synaptically isolated. Only if synaptic transmission was blocked, the achieved results could be related to the intrinsic channel composition and were not attributable to synaptic input. In a recent study Acetylcholine was shown to be a transmitter of the Coordinating Neurons (Schneider et al., 2018). A study by B. Schneider (2017) investigated the effect of the Acetylcholine receptor antagonist Tubocurarin on the generation of rhythmic and coordinated swimmeret motor output. Treatment with Tubocurarin increased the PS burst duration and cycle period, which provides evidence that the Coordinating Neurons might release Acetylcholine at their synapse to ComInt1.

The transmitters of the remaining synapses have not been identified yet. However, a study by Sherff and Mulloney (1996) indicated the transmitters released at the synapse between the CPG neurons and MNs to be GABA and Glutamate. This hypothesis was further analyzed by B. Schneider and Schneider and colleagues (2018), evaluating the effects of Picrotoxin, a blocker against GABAergic receptors on the swimmeret motor output. In both studies, rhythmic activity was impaired by application of Picrotoxin, supporting the assumption of GABA mediated synaptic transmission, either between CPG neurons or between CPG and MNs.

To synaptically isolate the neurons of the swimmeret system, I applied synaptic blockers against Acetylcholine (Tubocurarin), GABA (Picrotoxin), and Glutamate (DL-AP5, CNQX and DNXQ). Treatment with the mixture of synaptic blockers induced tonic motor activity in 65 % of the preparations. This indicates that CPG activity had crashed in most of the preparations in this experimental condition, which was supported by the observation that oscillatory activity in IPS also ceased during synaptic blocker application. Regarding that most tested spiking neurons were tonically active during synaptic blocker application additionaly indicates that inhibitory synaptic input from the CPG neurons to these neurons was reduced.

I measured the R_{IN} of the neurons to confirm this hypothesis and to test the effectiveness of the applied synaptic blockers to close ion channels. An increase in R_{IN} in PSE, RSE, IPS, and ComInt1 gives evidence that ion channels closed during blocker application. In ASC_E and DSC, however, the R_{IN} was not reliably affected.

This might suggest that synaptic transmission was not fully blocked in these neurons. Furthermore it could be observed that membrane noise, likely being mediated by small inhibitory postsynaptic potentials (IPSPs) or EPSPs, remained during synaptic blocker application in all recorded neurons. This was most obvious during recordings of ComInt1. The detection of remaining EPSPs could indicate that synaptic transmission was not fully eliminated. On the other hand it could indicate the presence of an electrical synapse between the Coordinating Neurons and ComInt1, as it has been suggested in the work by Schneider and colleagues (2018).

Regarding the above described arguments it is likely that synaptic transmission was partially still functional, especially because electrical synapses between the neurons were not blocked in these experimental conditions. However I found promising evidence that the activity of the CPG was halted. This validates that the observed cellular responses I characterized during my thesis were mediated directly by the intracellularly recorded neuron and were not a cause by rhythmic network effects.

4.5 Summary - Ionic currents in a chain of coupled oscillators

The swimmeret system of the crayfish is a unique neuronal network in which all cellular components responsible for rhythm generation, coordination between the segments, but also for the conduction of motor commands to the muscles have been identified. During this thesis I could show that the neurons of the swimmeret system possess the ability to produce a PIR when being released from hyperpolarization. Thereby hyperpolarization-activated inward currents induced a depolarization of the membrane potential leading to new excitability of the neurons. When elucidating the underlying ionic conductances I detected I_{CaL}, I_H and I_{NaP} to differently establish the PIR properties in different neuron groups. The additional contribution of I_A seems to be a mechanism to tune PIR responses. The PIR, or rather the ability to escape from inhibitory synaptic input, seems to be of significant importance for initiation of rhythmic CPG activity, but also for the Coordinating Neurons ASC_E, and DSC as well as for the MNs, PSE, and RSE. By a precise interplay of the different ionic conductances with appropriate synaptic input the activity patterns of individual neurons can be modulated to maintain constant phase relationships within individual segments but also between segments.

4.6 Outlook

This thesis provides a first insight into ionic conductances important for the generation of rhythmic and coordinated motor output in the swimmeret system. Thereby, I found promising evidence for the differential contribution of I_{CaL}, I_H and I_{NaP} in establishing PIR responses in different neuron groups. Furthermore, I hypothesized I_{KCa} to contribute in shaping PIR responses in some of the neurons of the swimmeret system. As a possible mechanism to decrease neuronal activity and thus weaken synaptic output (Harris-Warrick et al., 1992), this ion channel could be important especially for the Coordinating Neurons to achieve the correct coordination between the segments.

I could also detect the contribution of I_A in generating a functional motor output. I_A has been shown in different studies to be dynamically regulated in accordance to changes in I_H to keep a correct phasing of neuronal activities during episodes of higher or lower frequencies of motor activities (Daur et al., 2016; Tang et al., 2010). This mechanism has been shown to be tightly regulated by neuromodulators like dopamine or serotonin (Harris-Warrick et al., 1995; Rodgers et al., 2011; Wang et al., 2011). Because the activity of the swimmeret system needs to adapt in accordance to environmental cues, as for example stronger water current, it seems likely that such a regulatory mechanism established by homeostatic plasticity could be present in the swimmeret system. Therefore, experiments elucidating the role of I_A during the generation of PIR responses, in combination with neuromodulatory substances, could enhance the understanding of tightly tuned escape mechanisms in the swimmeret system. Furthermore immunocytochemical stainings of the identified ion channels could explain the observed variances in evoked PIR responses. Voltage clamp experiments at the dendritic aborizations of the neurons could further support my experimental findings because this technique directly addresses the conductances of ion channels. Thereby further insights could be gained on opening and closing kinetics and precise voltage sensitivities of ion channels in this system.

5. Appendix

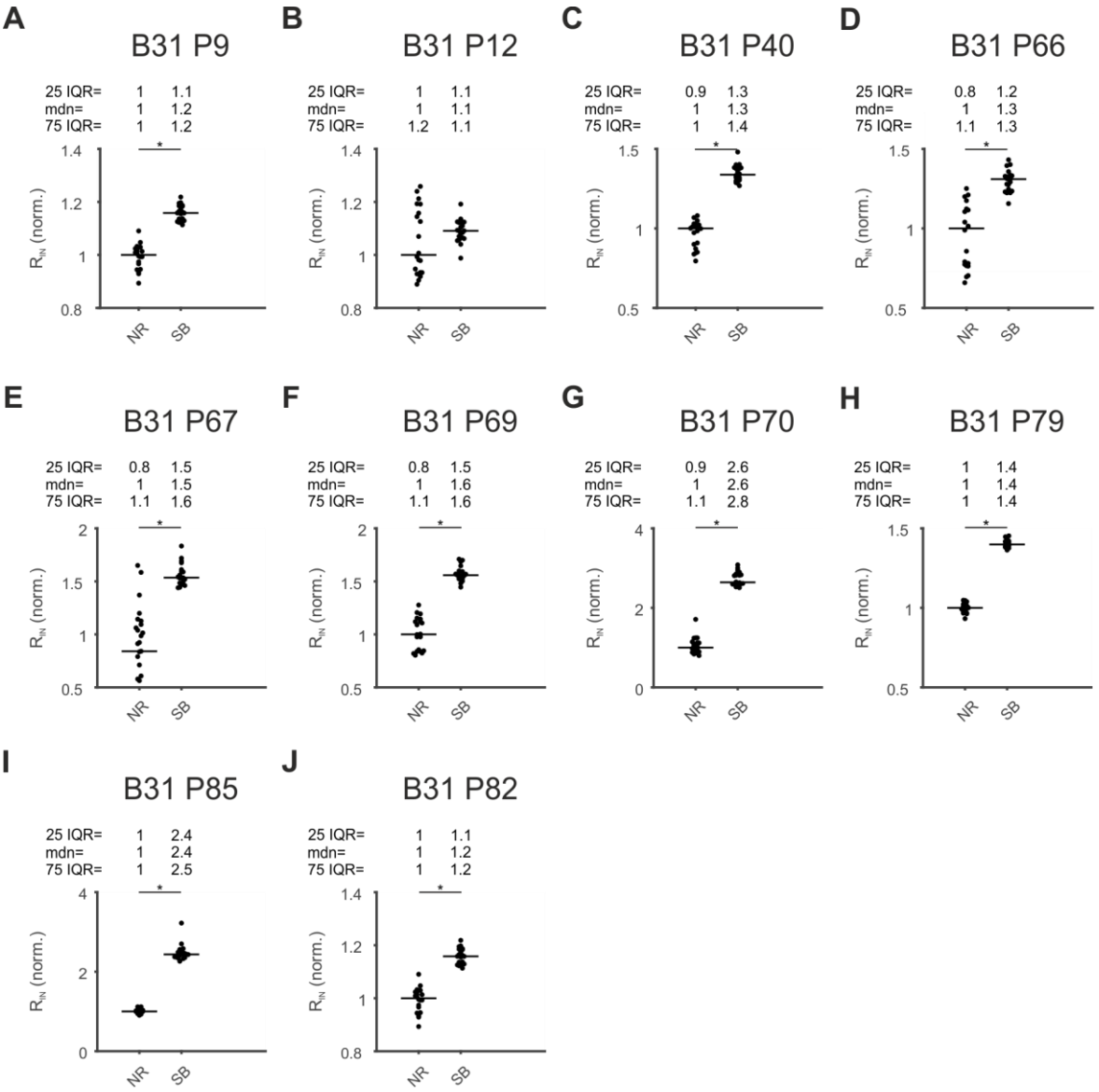

Supplemental Figure 1: Synaptic isolation of PSE. Normalized input resistances during control condition and during synaptic blocker application. Horizontal lines represent normalized median values. BXX and PXX represent numbering of experiments according to laboratory book- and respective page number. R_{IN}: input resistance, PSE: Power Stroke Exciter, NR: normal ringer, SB: synaptic blocker, IQR: interquartile range, mdn: median, *: $p < 0.05$.

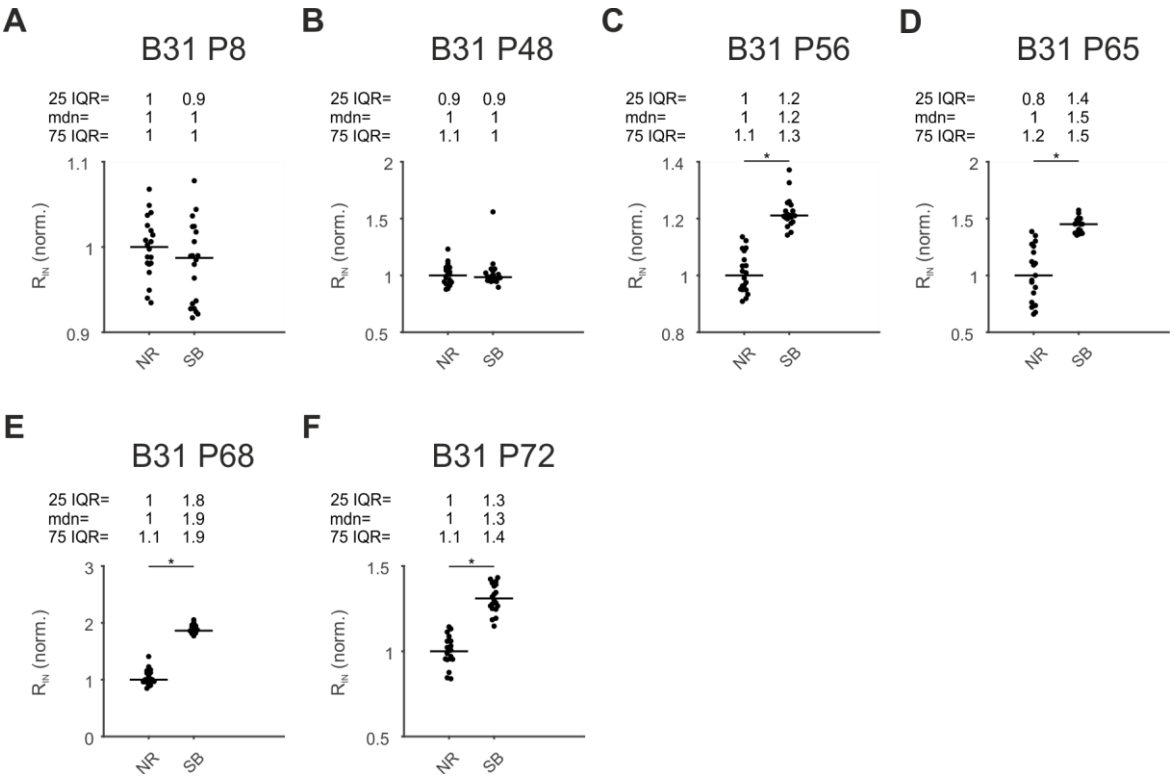

Supplemental Figure 2: Synaptic isolation of RSE. Normalized input resistances during control condition and during synaptic blocker application. Horizontal lines represent normalized median values. BXX and PXX represent numbering of experiments according to laboratory book- and respective page number. R_{IN}: input resistance, RSE: Return Stroke Exciter, NR: normal ringer, SB: synaptic blocker, IQR: interquartile range, mdn: median, *: $p < 0.05$.

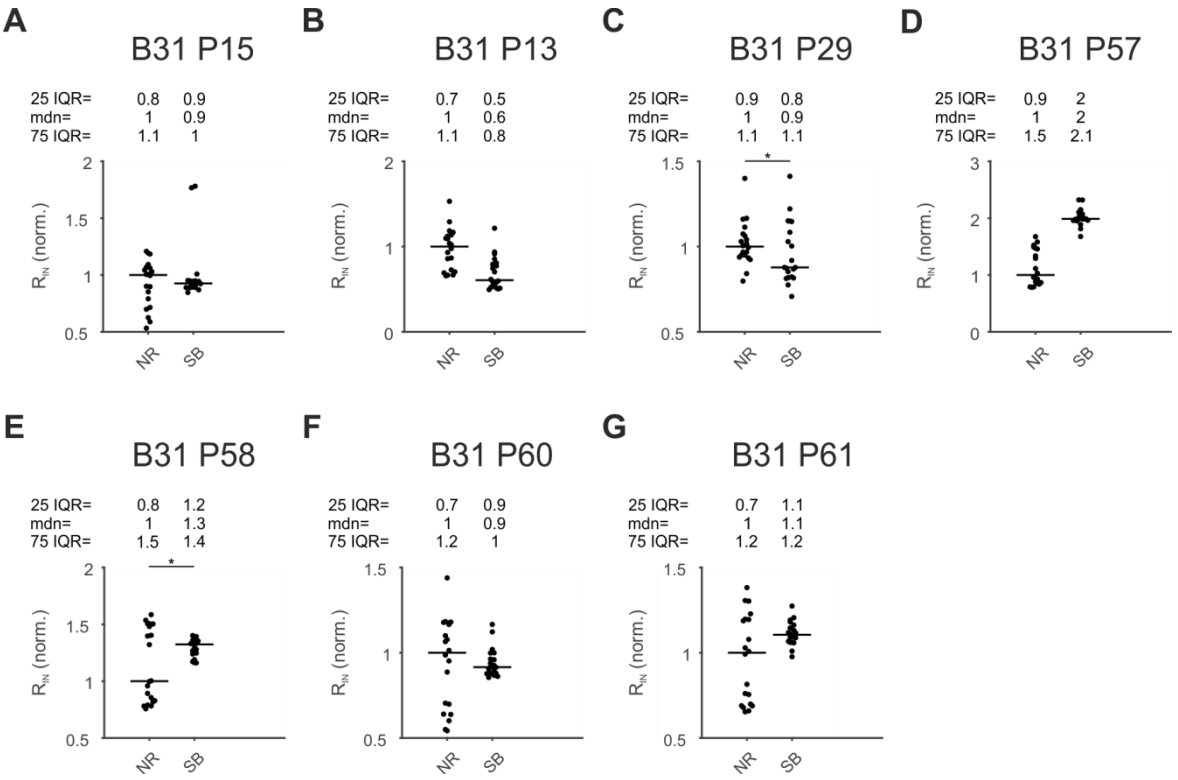

Supplemental Figure 3: Synaptic isolation of ASC_E. Normalized input resistance during control condition and during synaptic blocker application. Horizontal lines represent normalized median values. BXX and PXX represent numbering of experiments according to laboratory book- and respective page number. R_{IN}: input resistance, ASC_E: Ascending Coordinating Neuron, NR: normal ringer, SB: synaptic blocker, IQR: interquartile range, mdn: median, *: $p < 0.05$.

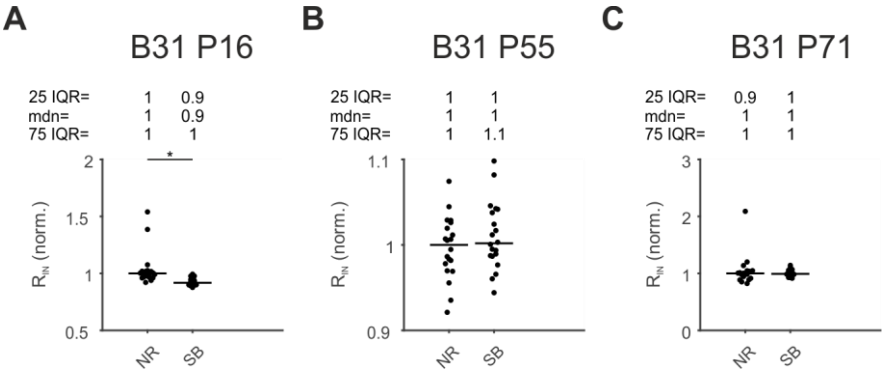

Supplemental Figure 4: Synaptic isolation of DSC. Normalized input resistances during control condition and during synaptic blocker application. Horizontal lines represent normalized median values. BXX and PXX represent numbering of experiments according to laboratory book- and respective page number. R_{IN}: input resistance, DSC: Descending Coordinating Neuron, NR: normal ringer, SB: synaptic blocker, IQR: interquartile range, mdn: median, *: $p < 0.05$.

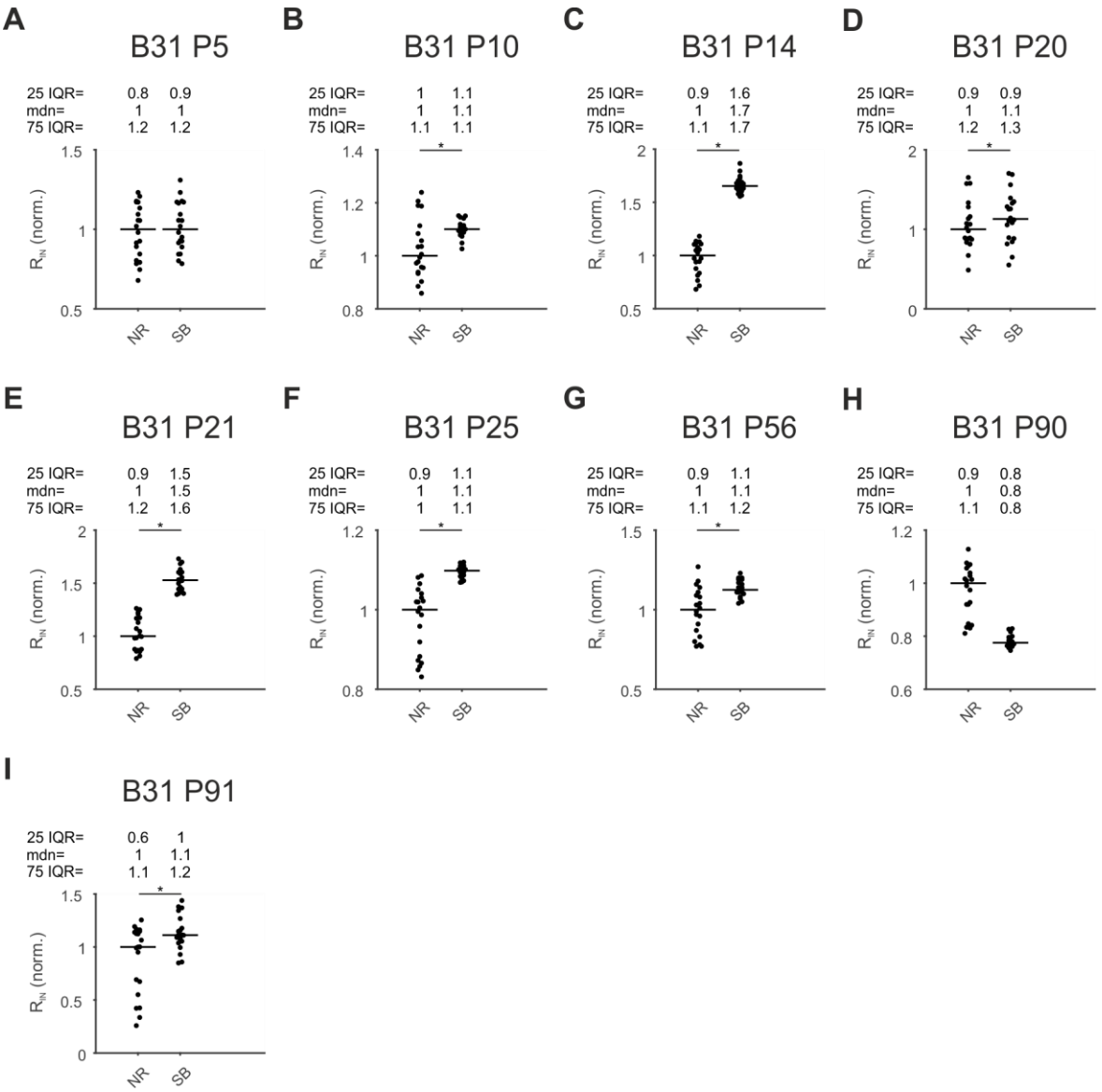

Supplemental Figure 5: Synaptic isolation of IPS. Normalized input resistances during control condition and during synaptic blocker application. Horizontal lines represent normalized median values. BXX and PXX represent numbering of experiments according to laboratory book- and respective page number. R_{IN}: input resistance, IPS: Inhibitor of Power Stroke, NR: normal ringer, SB: synaptic blocker, IQR: interquartile range, mdn: median, *: $p < 0.05$.

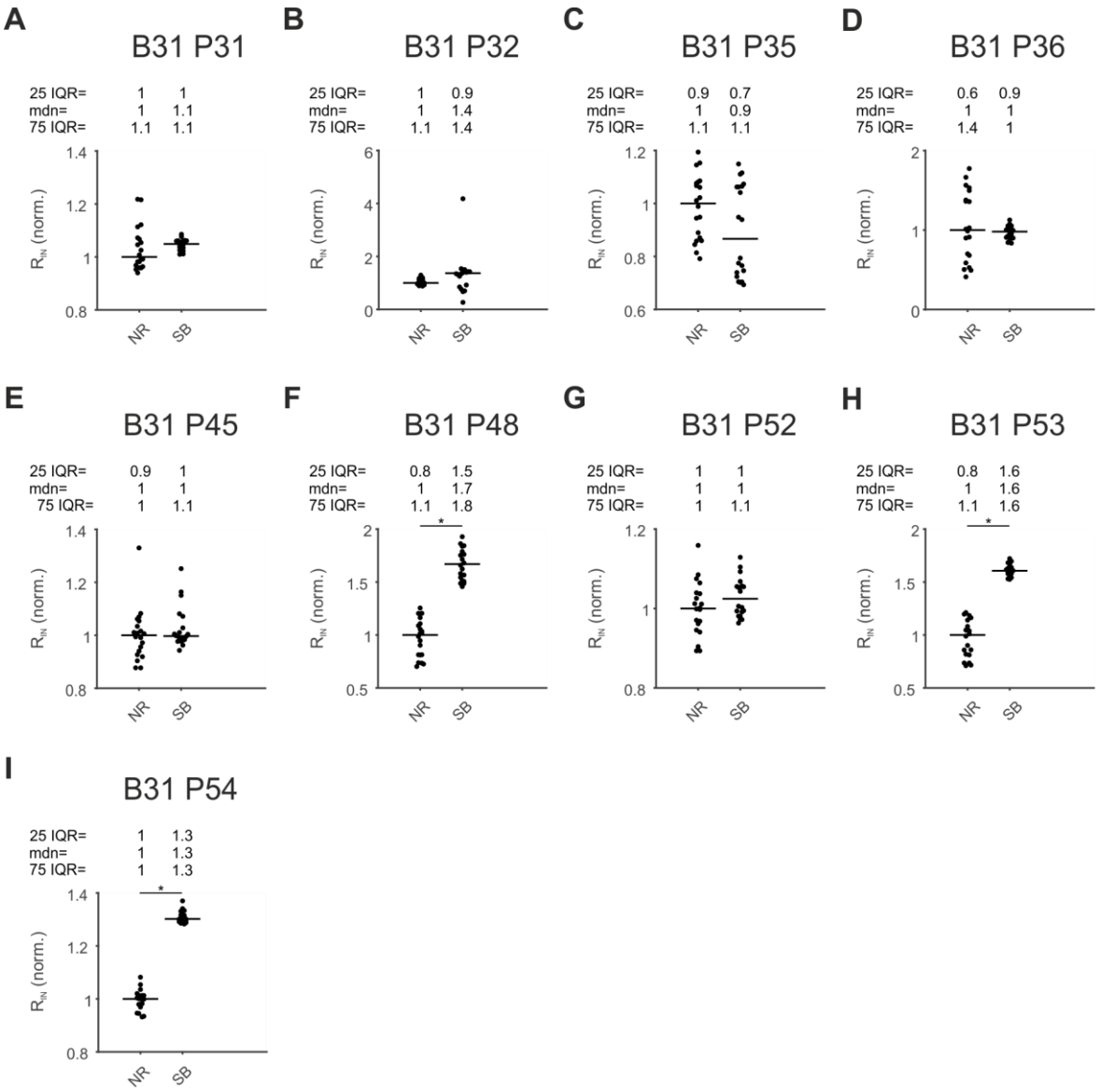

Supplemental Figure 6: Synaptic isolation of ComInt1. Normalized input resistances during control condition and during synaptic blocker application. Horizontal lines represent normalized median values. BXX and PXX represent numbering of experiments according to laboratory book- and respective page number. R_{IN}: input resistance, ComInt1: Commissural Interneuron 1, NR: normal ringer, SB: synaptic blocker, IQR: interquartile range, mdn: median, *: $p < 0.05$.

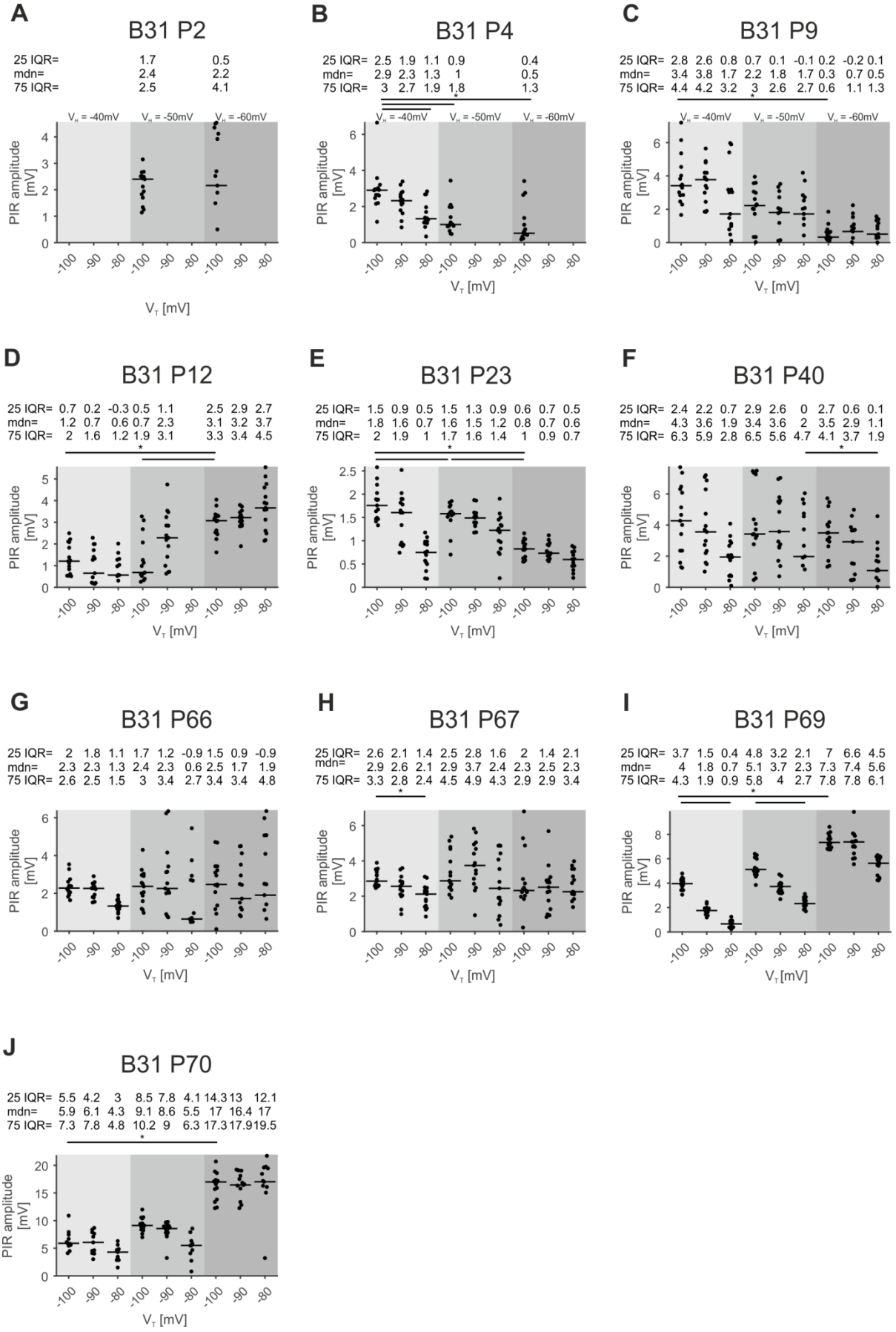
A
B31 P2
25 IQR= 1.7 0.5
mdn= 2.4 2.2
75 IQR= 2.5 4.1
B
B31 P4
25 IQR= 2.5 1.9 1.1 0.9 0.4
mdn= 2.9 2.3 1.3 1 0.5
75 IQR= 3 2.7 1.9 1.8 1.3
C
B31 P9
25 IQR= 2.8 2.6 0.8 0.7 0.1 -0.1 0.2 -0.2 0.1
mdn= 3.4 3.8 1.7 2.2 1.8 1.7 0.3 0.7 0.5
75 IQR= 4.4 4.2 3.2 3 2.6 2.7 0.6 1.1 1.3
D
B31 P12
25 IQR= 0.7 0.2 -0.3 0.5 1.1 2.5 2.9 2.7
mdn= 1.2 0.7 0.6 0.7 2.3 3.1 3.2 3.7
75 IQR= 2 1.6 1.2 1.9 3.1 3.3 3.4 4.5
E
B31 P23
25 IQR= 1.5 0.9 0.5 1.5 1.3 0.9 0.6 0.7 0.5
mdn= 1.8 1.6 0.7 1.6 1.5 1.2 0.8 0.7 0.6
75 IQR= 2 1.9 1 1.7 1.6 1.4 1 0.9 0.7
F
B31 P40
25 IQR= 2.4 2.2 0.7 2.9 2.6 0 2.7 0.6 0.1
mdn= 4.3 3.6 1.9 3.4 3.6 2 3.5 2.9 1.1
75 IQR= 6.3 5.9 2.8 6.5 5.6 4.7 4.1 3.7 1.9
G
B31 P66
25 IQR= 2 1.8 1.1 1.7 1.2 -0.9 1.5 0.9 -0.9
mdn= 2.3 2.3 1.3 2.4 2.3 0.6 2.5 1.7 1.9
75 IQR= 2.6 2.5 1.5 3 3.4 2.7 3.4 3.4 4.8
H
B31 P67
25 IQR= 2.6 2.1 1.4 2.5 2.8 1.6 2 1.4 2.1
mdn= 2.9 2.6 2.1 2.9 3.7 2.4 2.3 2.5 2.3
75 IQR= 3.3 2.8 2.4 4.5 4.9 4.3 2.9 2.9 3.4
I
B31 P69
25 IQR= 3.7 1.5 0.4 4.8 3.2 2.1 7 6.6 4.5
mdn= 4 1.8 0.7 5.1 3.7 2.3 7.3 7.4 5.6
75 IQR= 4.3 1.9 0.9 5.8 4 2.7 7.8 7.8 6.1
J
B31 P70
25 IQR= 5.5 4.2 3 8.5 7.8 4.1 14.3 13 12.1
mdn= 5.9 6.1 4.3 9.1 8.6 5.5 17 16.4 17
75 IQR= 7.3 7.8 4.8 10.2 9 6.3 17.3 17.9 19.5
PIR amplitude [mV]
V_T [mV]
V_H = -40mV
V_H = -50mV
V_H = -60mV

Supplemental Figure 7: PIR amplitudes – PSE. Normalized PIR amplitudes (elicited by hyperpolarizing current injections from different V_H to different V_T) from single experiments. Horizontal lines represent normalized median values. BXX and PXX represent numbering of experiments according to laboratory book- and respective page number. PIR: post-inhibitory rebound, PSE: Power Stroke Exciter, IQR: interquartile range, mdn: median, V_H: holding potential, V_T: test potential, *: $p < 0.05$.

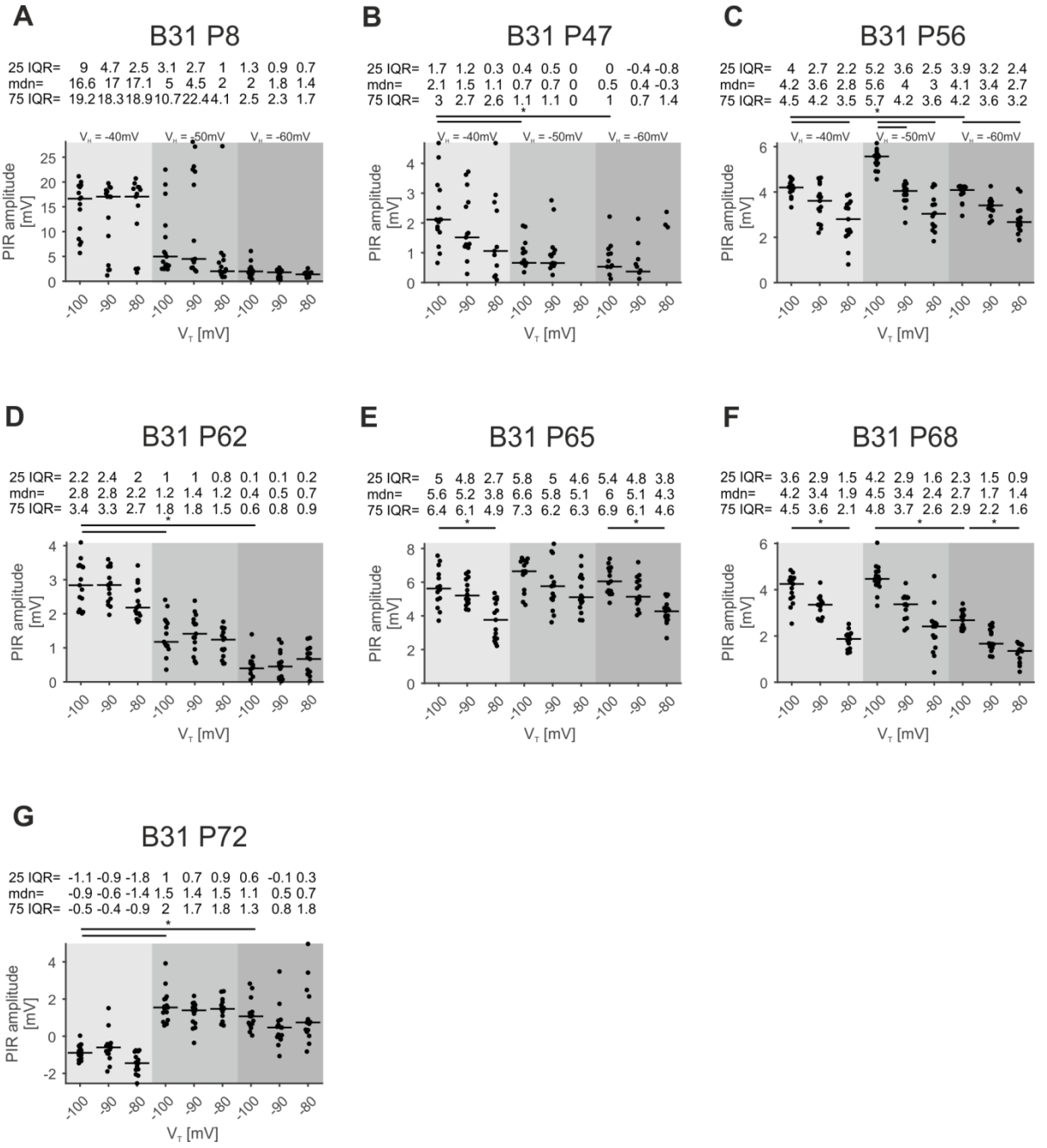

Supplemental Figure 8: PIR amplitudes – RSE. Normalized PIR amplitudes (elicited by hyperpolarizing current injections from different V_H to different V_T) from single experiments. Horizontal lines represent normalized median values. BXX and PXX represent numbering of experiments according to laboratory book- and respective page number. RSE: Return Stroke Exciter, IQR: interquartile range, mdn: median, V_H: holding potential, V_T: test potential, *: $p < 0.05$.

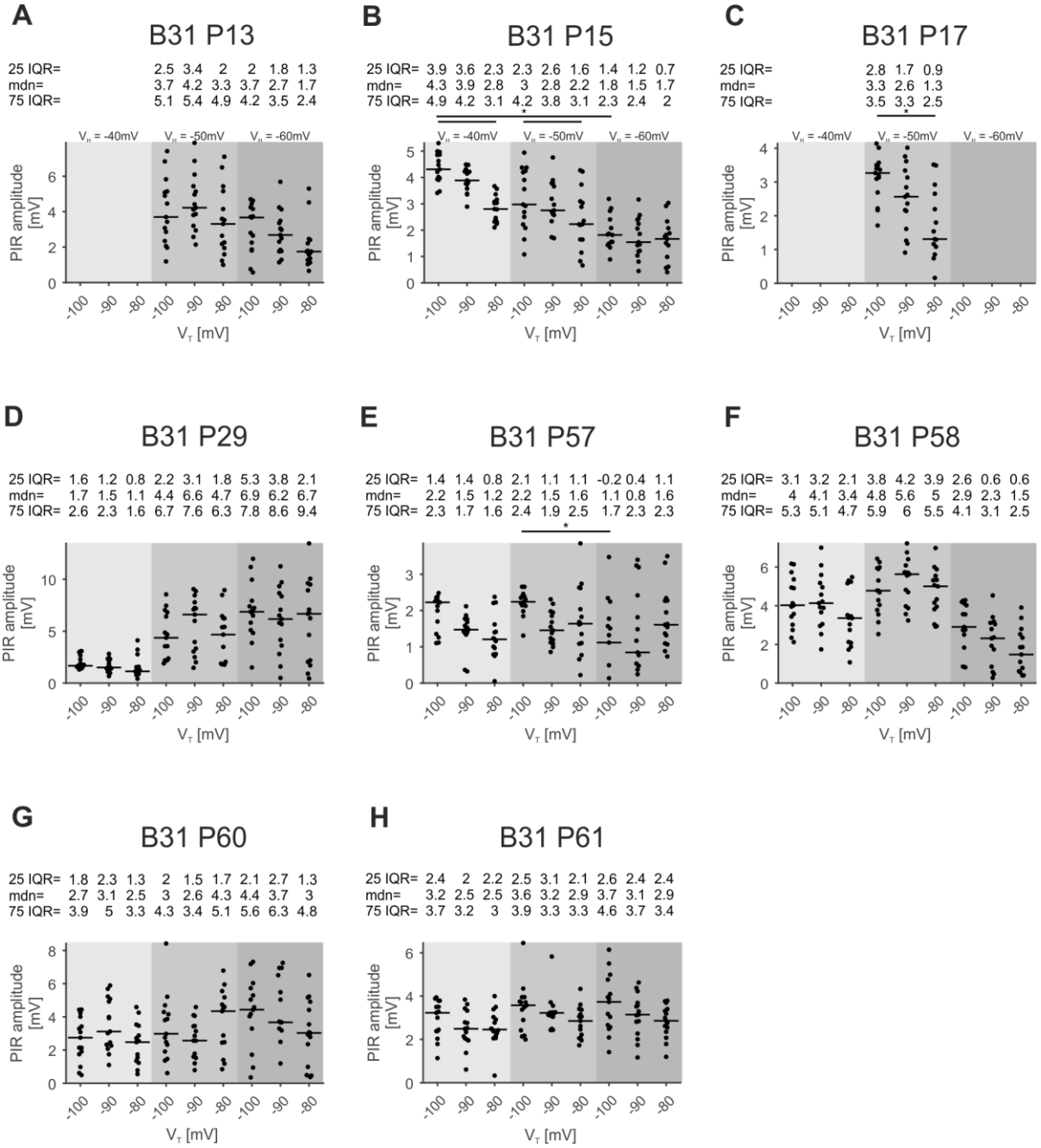

Supplemental Figure 9: PIR amplitudes – ASC_Es. Normalized PIR amplitudes (elicited by hyperpolarizing current injections from different V_H to different V_T) from single experiments. Horizontal lines represent normalized median values. BXX and PXX represent numbering of experiments according to laboratory book- and respective page number. ASC_E: Ascending Coordinating Neuron, IQR: interquartile range, mdn: median, V_H: holding potential, V_T: test potential, *: $p < 0.05$.

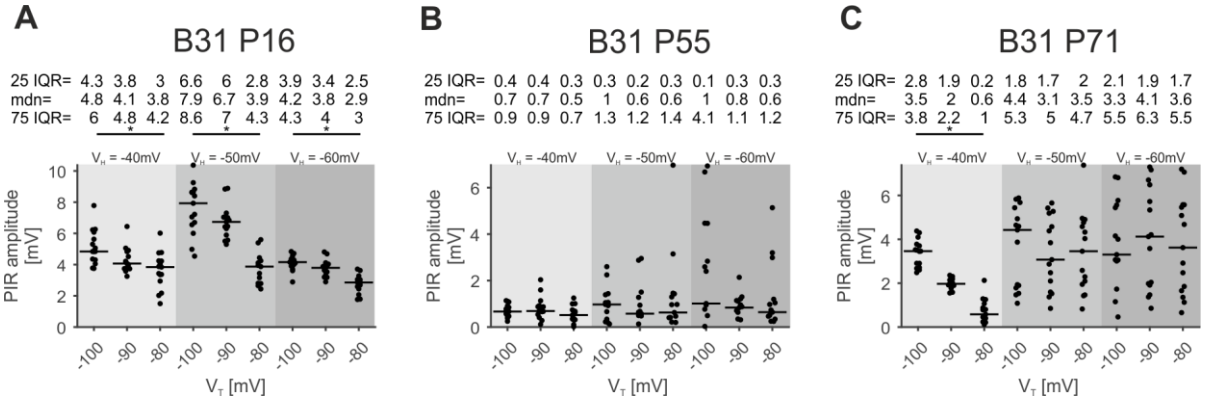

Supplemental Figure 10: PIR amplitudes – DSC. Normalized PIR amplitudes (elicited by hyperpolarizing current injections from different V_H to different V_T) from single experiments. Horizontal lines represent normalized median values. BXX and PXX represent numbering of experiments according to laboratory book- and respective page number. DSC: Descending Coordinating Neuron, IQR: interquartile range, mdn: median, V_H: holding potential, V_T: test potential, *: $p < 0.05$.

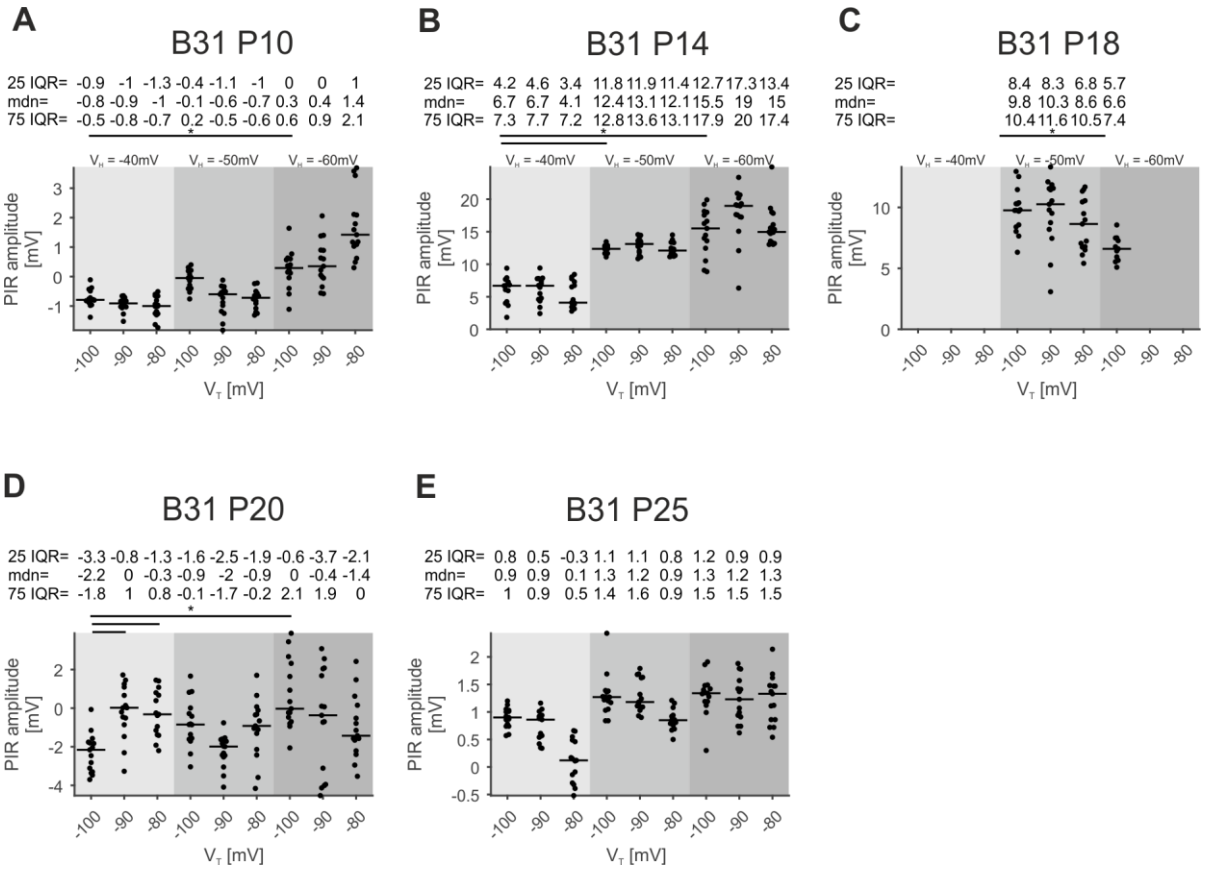

Supplemental Figure 11: PIR amplitudes – IPS. Normalized PIR amplitudes (elicited by hyperpolarizing current injections from different V_H to different V_T) from single experiments. Horizontal lines represent normalized median values. BXX and PXX represent numbering of experiments according to laboratory book- and respective page number. IPS: Inhibitor of Power Stroke, IQR: interquartile range, mdn: median, V_H: holding potential, V_T: test potential, *: $p < 0.05$.

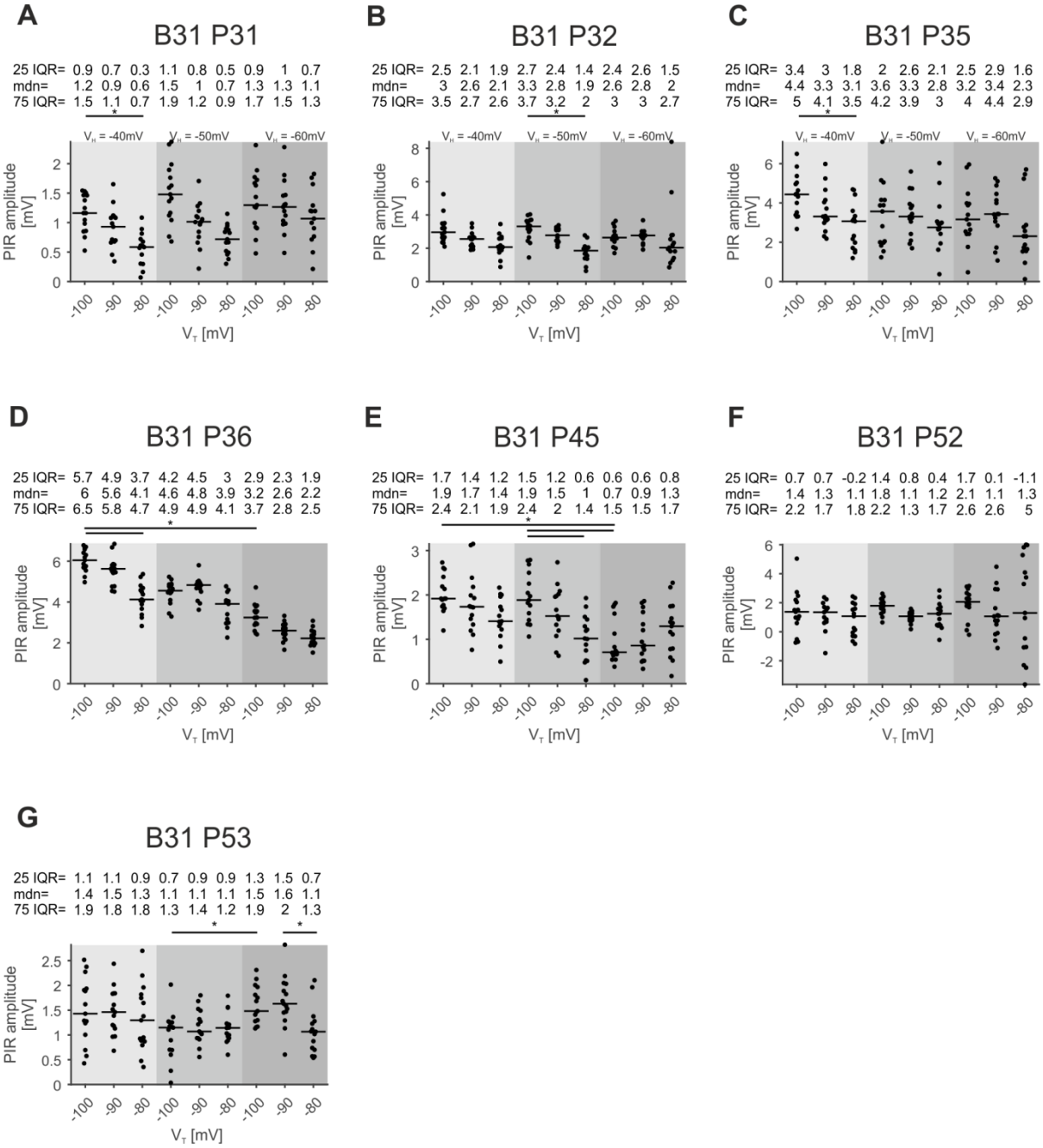

Supplemental Figure 12: PIR amplitudes – ComInt1. Normalized PIR amplitudes (elicited by hyperpolarizing current injections from different V_H to different V_T) from single experiments. Horizontal lines represent normalized median values. BXX and PXX represent numbering of experiments according to laboratory book- and respective page number. ComInt1: Commissural Interneuron 1, IQR: interquartile range, mdn: median, V_H: holding potential, V_T: test potential, *: $p < 0.05$.

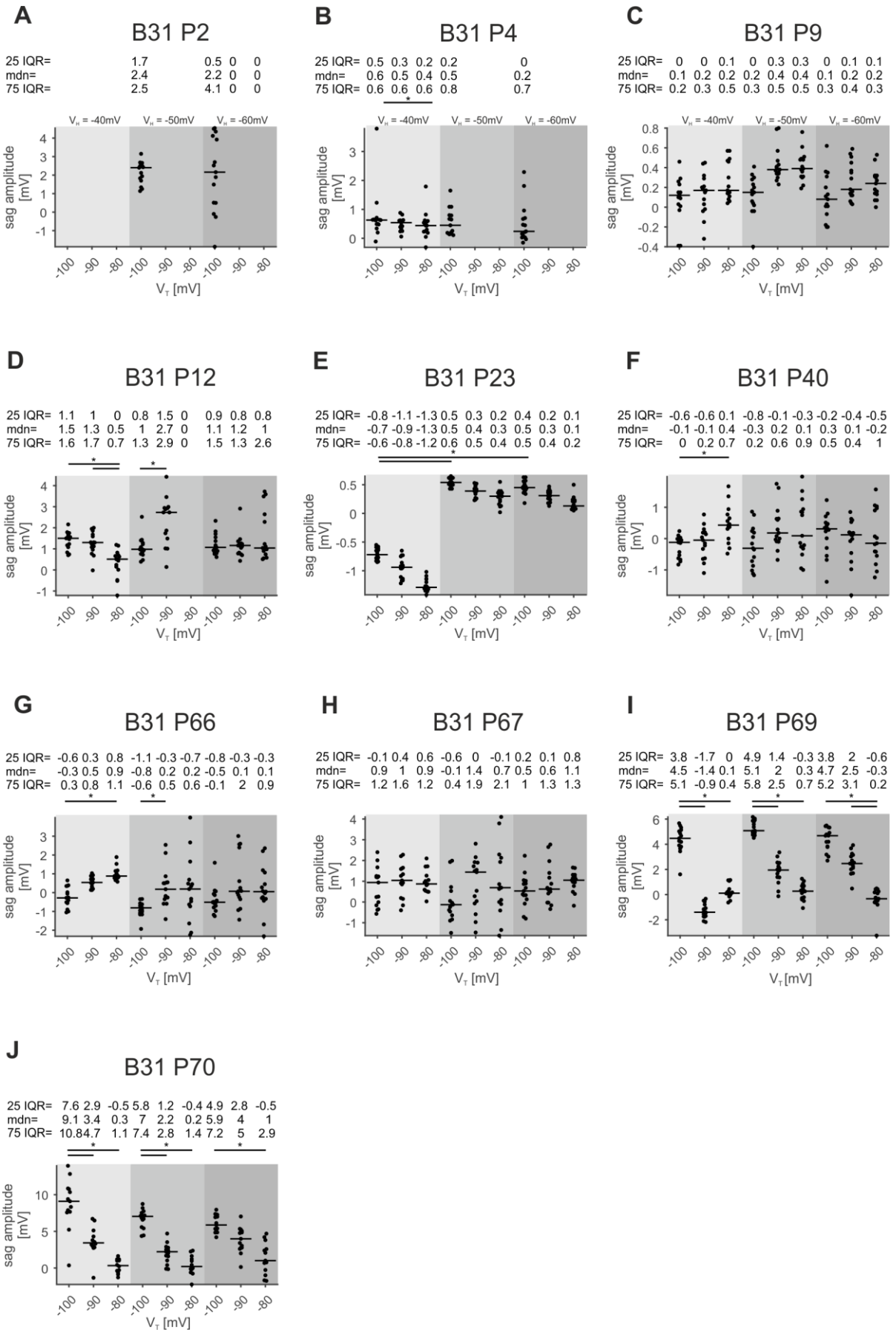
A
B31 P2
25 IQR= 1.7 0.5 0 0
mdn= 2.4 2.2 0 0
75 IQR= 2.5 4.1 0 0
B
B31 P4
25 IQR= 0.5 0.3 0.2 0.2 0
mdn= 0.6 0.5 0.4 0.5 0.2
75 IQR= 0.6 0.6 0.6 0.8 0.7
C
B31 P9
25 IQR= 0 0 0.1 0 0.3 0.3 0 0.1 0.1
mdn= 0.1 0.2 0.2 0.2 0.4 0.4 0.1 0.2 0.2
75 IQR= 0.2 0.3 0.5 0.3 0.5 0.5 0.3 0.4 0.3
D
B31 P12
25 IQR= 1.1 1 0 0.8 1.5 0 0.9 0.8 0.8
mdn= 1.5 1.3 0.5 1 2.7 0 1.1 1.2 1
75 IQR= 1.6 1.7 0.7 1.3 2.9 0 1.5 1.3 2.6
E
B31 P23
25 IQR= -0.8 -1.1 -1.3 0.5 0.3 0.2 0.4 0.2 0.1
mdn= -0.7 -0.9 -1.3 0.5 0.4 0.3 0.5 0.3 0.1
75 IQR= -0.6 -0.8 -1.2 0.6 0.5 0.4 0.5 0.4 0.2
F
B31 P40
25 IQR= -0.6 -0.6 0.1 -0.8 -0.1 -0.3 -0.2 -0.4 -0.5
mdn= -0.1 -0.1 0.4 -0.3 0.2 0.1 0.3 0.1 -0.2
75 IQR= 0 0.2 0.7 0.2 0.6 0.9 0.5 0.4 1
G
B31 P66
25 IQR= -0.6 0.3 0.8 -1.1 -0.3 -0.7 -0.8 -0.3 -0.3
mdn= -0.3 0.5 0.9 -0.8 0.2 0.2 -0.5 0.1 0.1
75 IQR= 0.3 0.8 1.1 -0.6 0.5 0.6 -0.1 2 0.9
H
B31 P67
25 IQR= -0.1 0.4 0.6 -0.6 0 -0.1 0.2 0.1 0.8
mdn= 0.9 1 0.9 -0.1 1.4 0.7 0.5 0.6 1.1
75 IQR= 1.2 1.6 1.2 0.4 1.9 2.1 1 1.3 1.3
I
B31 P69
25 IQR= 3.8 -1.7 0 4.9 1.4 -0.3 3.8 2 -0.6
mdn= 4.5 -1.4 0.1 5.1 2 0.3 4.7 2.5 -0.3
75 IQR= 5.1 -0.9 0.4 5.8 2.5 0.7 5.2 3.1 0.2
J
B31 P70
25 IQR= 7.6 2.9 -0.5 5.8 1.2 -0.4 4.9 2.8 -0.5
mdn= 9.1 3.4 0.3 7 2.2 0.2 5.9 4 1
75 IQR= 10.8 4.7 1.1 7.4 2.8 1.4 7.2 5 2.9
sag amplitude [mV]
V_T [mV]
V_H = -40mV
V_H = -50mV
V_H = -60mV

Supplemental Figure 13: Sag amplitudes – PSE. Normalized sag amplitudes (elicited by hyperpolarizing current injections from different V_H to different V_T) from single experiments. Horizontal lines represent normalized median values. BXX and PXX represent numbering of experiments according to laboratory book- and respective page number. PSE: Power Stroke Exciter, IQR: interquartile range, mdn: median, V_H: holding potential, V_T: test potential, *: $p < 0.05$.

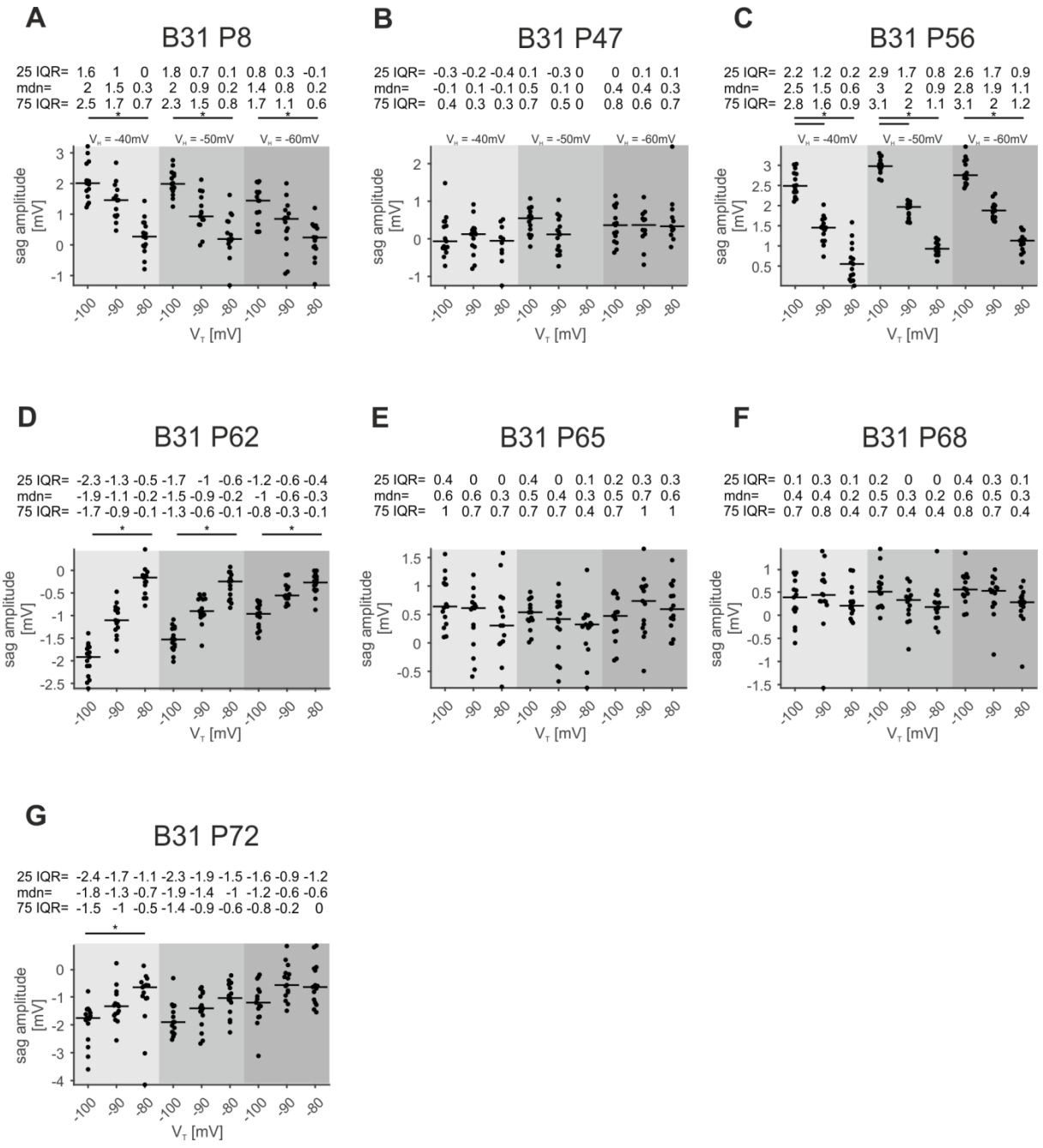

Supplemental Figure 14: Sag amplitudes – RSE. Normalized sag amplitudes (elicited by hyperpolarizing current injections from different V_H to different V_T) from single experiments. Horizontal lines represent normalized median values. BXX and PXX represent numbering of experiments according to laboratory book- and respective page number. RSE: Return Stroke Exciter, IQR: interquartile range, mdn: median, V_H: holding potential, V_T: test potential, *: $p < 0.05$.

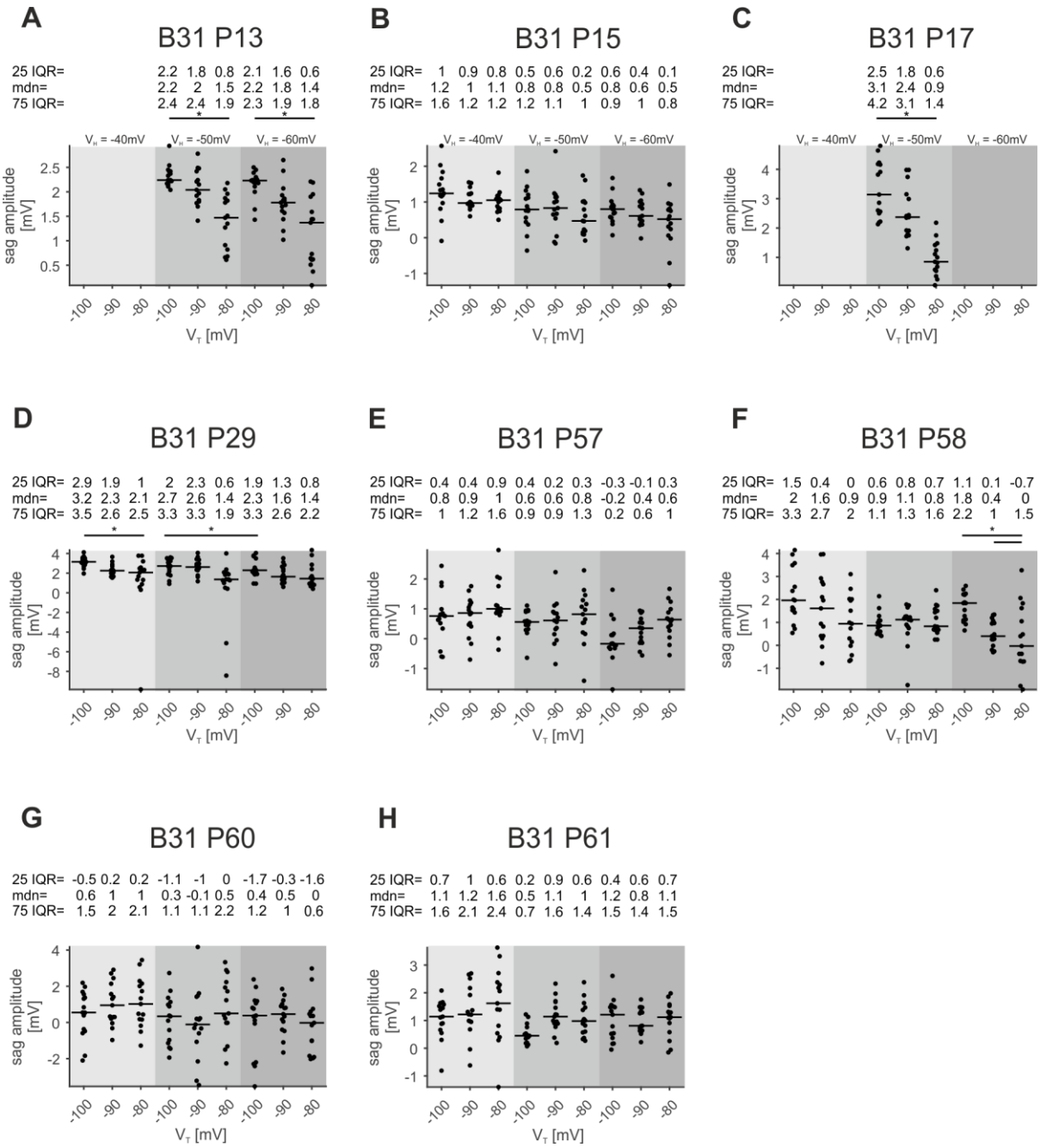

Supplemental Figure 15: Sag amplitudes – ASC_Es. Normalized sag amplitudes (elicited by hyperpolarizing current injections from different V_H to different V_T) from single experiments. Horizontal lines represent normalized median values. BXX and PXX represent numbering of experiments according to laboratory book- and respective page number. ASC_E: Ascending Coordinating Neuron, IQR: interquartile range, mdn: median, V_H: holding potential, V_T: test potential, *: $p < 0.05$.

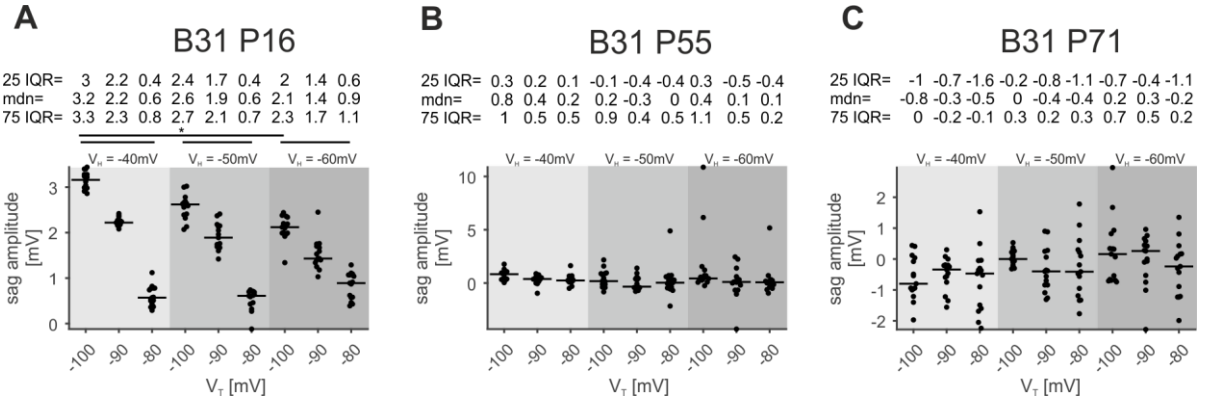

Supplemental Figure 16: Sag amplitudes – DSC. Normalized sag amplitudes (elicited by hyperpolarizing current injections from different V_H to different V_T) from single experiments. Horizontal lines represent normalized median values. BXX and PXX represent numbering of experiments according to laboratory book- and respective page number. DSC: Descending Coordinating Neuron, IQR: interquartile range, mdn: median, V_H: holding potential, V_T: test potential, *: $p < 0.05$.

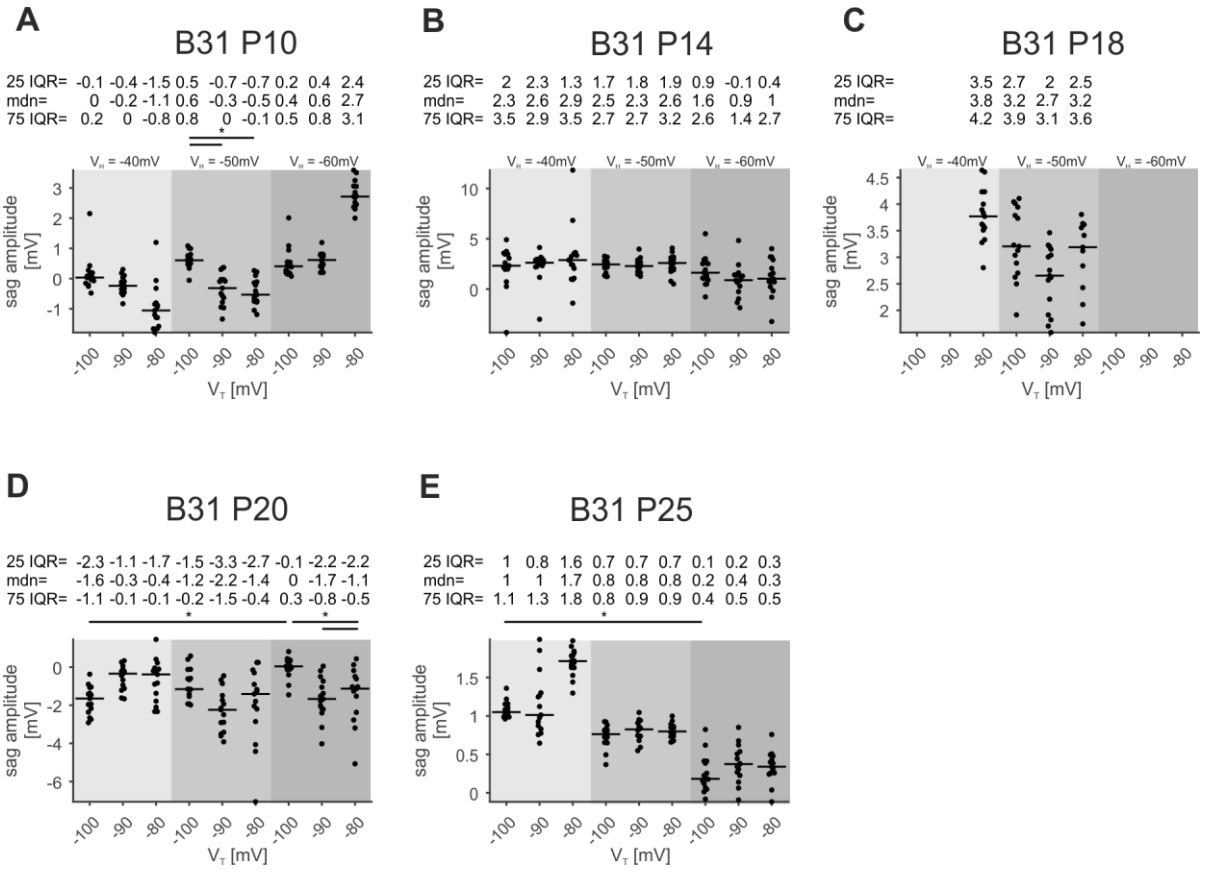

Supplemental Figure 17: Sag amplitudes – IPS. Normalized sag amplitudes (elicited by hyperpolarizing current injections from different V_H to different V_T) from single experiments. Horizontal lines represent normalized median values. BXX and PXX represent numbering of experiments according to laboratory book- and respective page number. IPS: Inhibitor of Power Stroke, IQR: interquartile range, mdn: median, V_H: holding potential, V_T: test potential, *: $p < 0.05$.

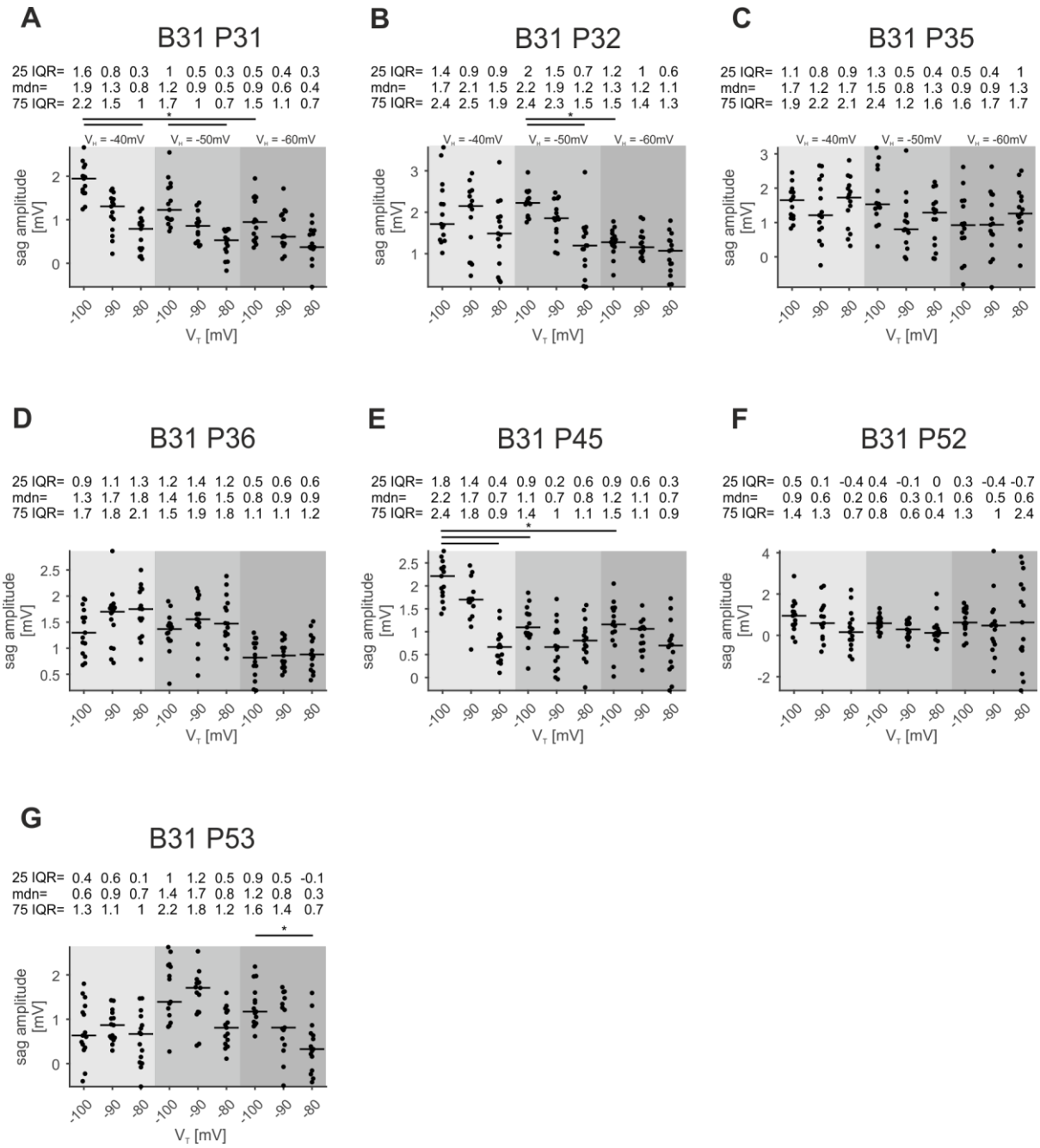

Supplemental Figure 18: Sag amplitudes – ComInt1. Normalized sag amplitudes (elicited by hyperpolarizing current injections from different V_H to different V_T) from single experiments. Horizontal lines represent normalized median values. BXX and PXX represent numbering of experiments according to laboratory book- and respective page number. ComInt1: Commissural Interneuron 1, IQR: interquartile range, mdn: median, V_H: holding potential, V_T: test potential, *: $p < 0.05$.

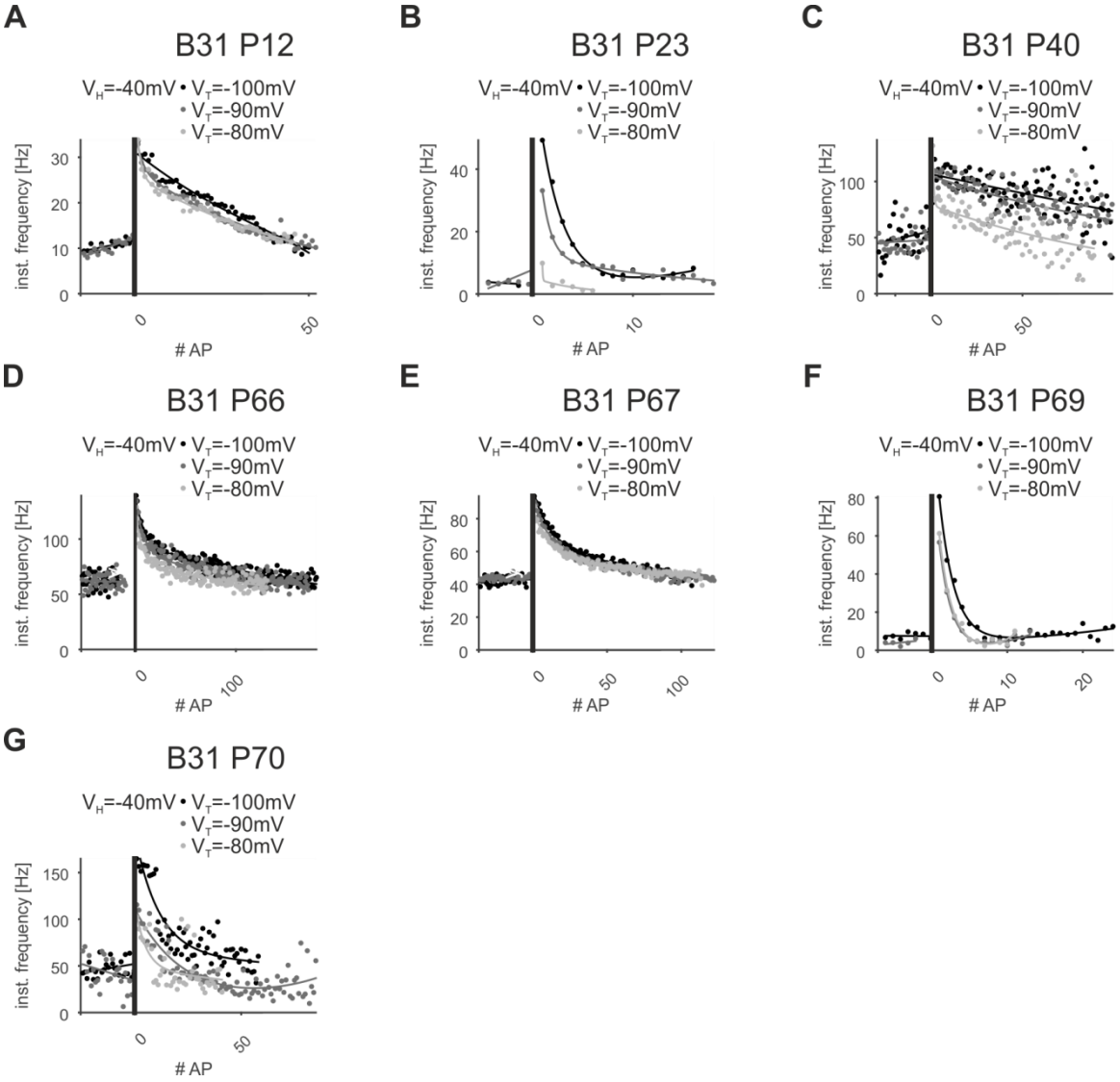

Supplemental Figure 19: Modulated instantaneous rebound spike frequencies – PSE. Mean instantaneous firing frequencies (15 stimulations) from single experiments, plotted against the number of APs, before- and following the stimulation. BXX and PXX represent numbering of experiments according to laboratory book- and respective page number. PSE: Power Stroke Exciter, V_H: holding potential, V_T: test potential, *: $p < 0.05$.

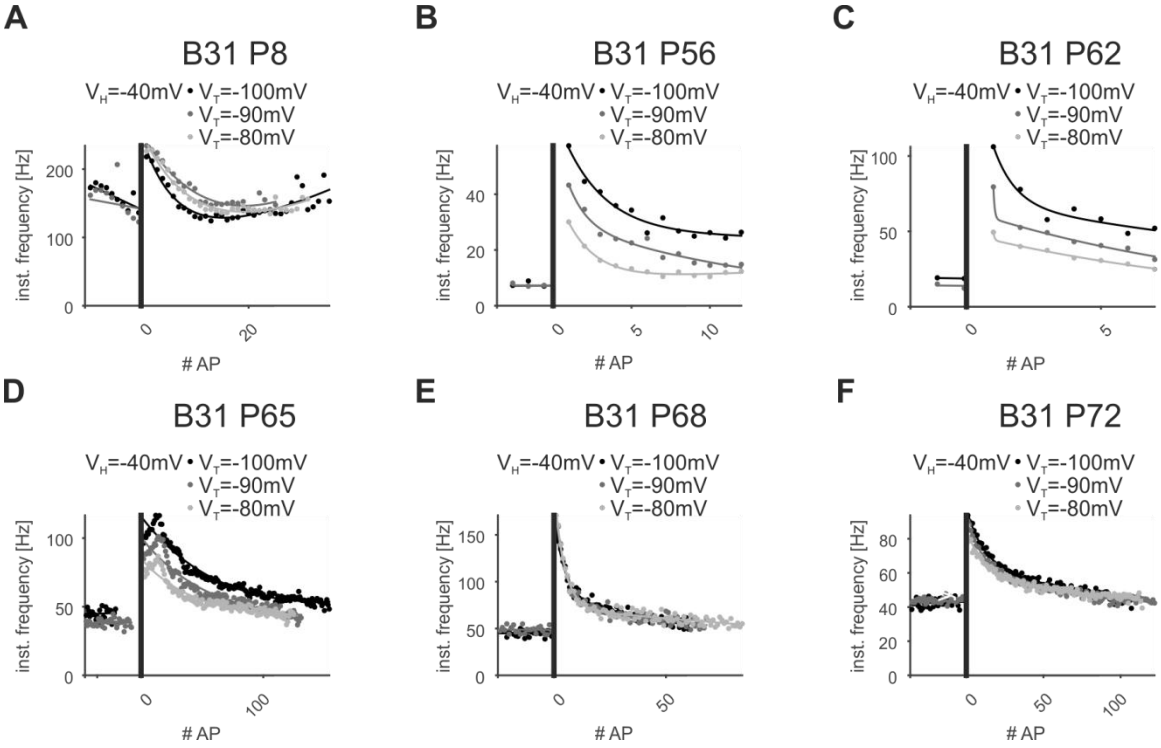

Supplemental Figure 20: Modulated instantaneous rebound spike frequencies – RSE. Mean instantaneous firing frequencies (15 stimulations) from single experiments, plotted against the number of APs, before- and following the stimulation. BXX and PXX represent numbering of experiments according to laboratory book- and respective page number. RSE: Return Stroke Exciter, V_H: holding potential, V_T: test potential, *: $p < 0.05$.

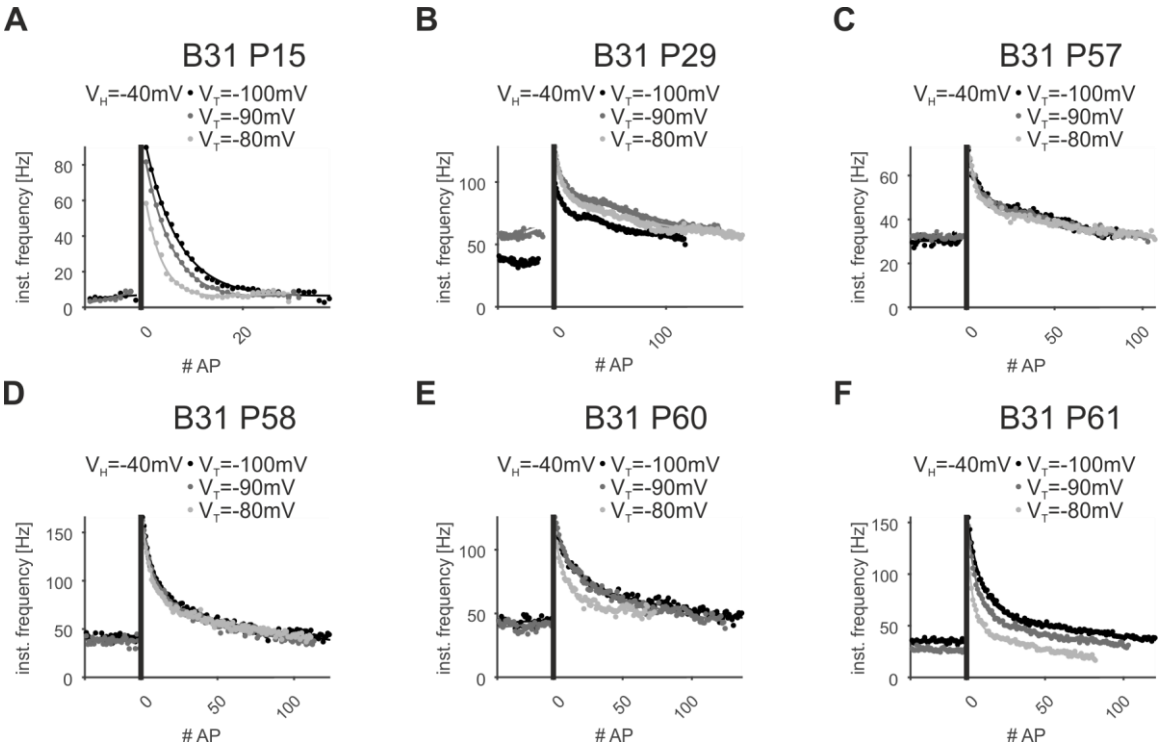

Supplemental Figure 21: Modulated instantaneous rebound spike frequencies – ASC_E. Mean instantaneous firing frequencies (15 stimulations) from single experiments, plotted against the number of APs, before- and following the stimulation. BXX and PXX represent numbering of experiments according to laboratory book- and respective page number. ASC_E: Ascending Coordinating Neuron, V_H: holding potential, V_T: test potential, *: $p < 0.05$.

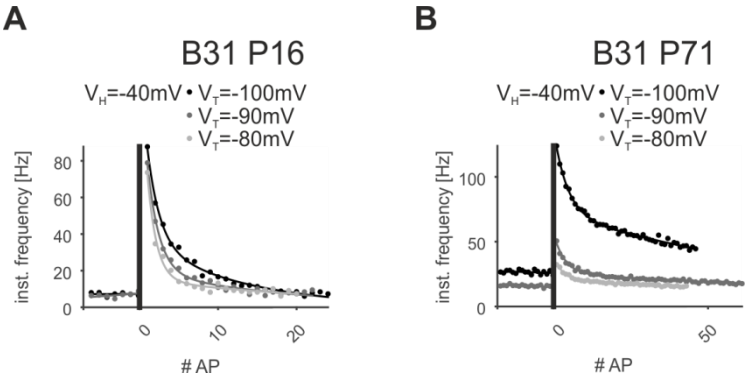

Supplemental Figure 22: Instantaneous rebound spike frequencies – DSC. Mean instantaneous firing frequencies (15 stimulations) from single experiments, plotted against the number of APs, before- and following the stimulation. BXX and PXX represent numbering of experiments according to laboratory book- and respective page number. DSC: Descending Coordinating Neuron, V_H: holding potential, V_T: test potential, *: $p < 0.05$.

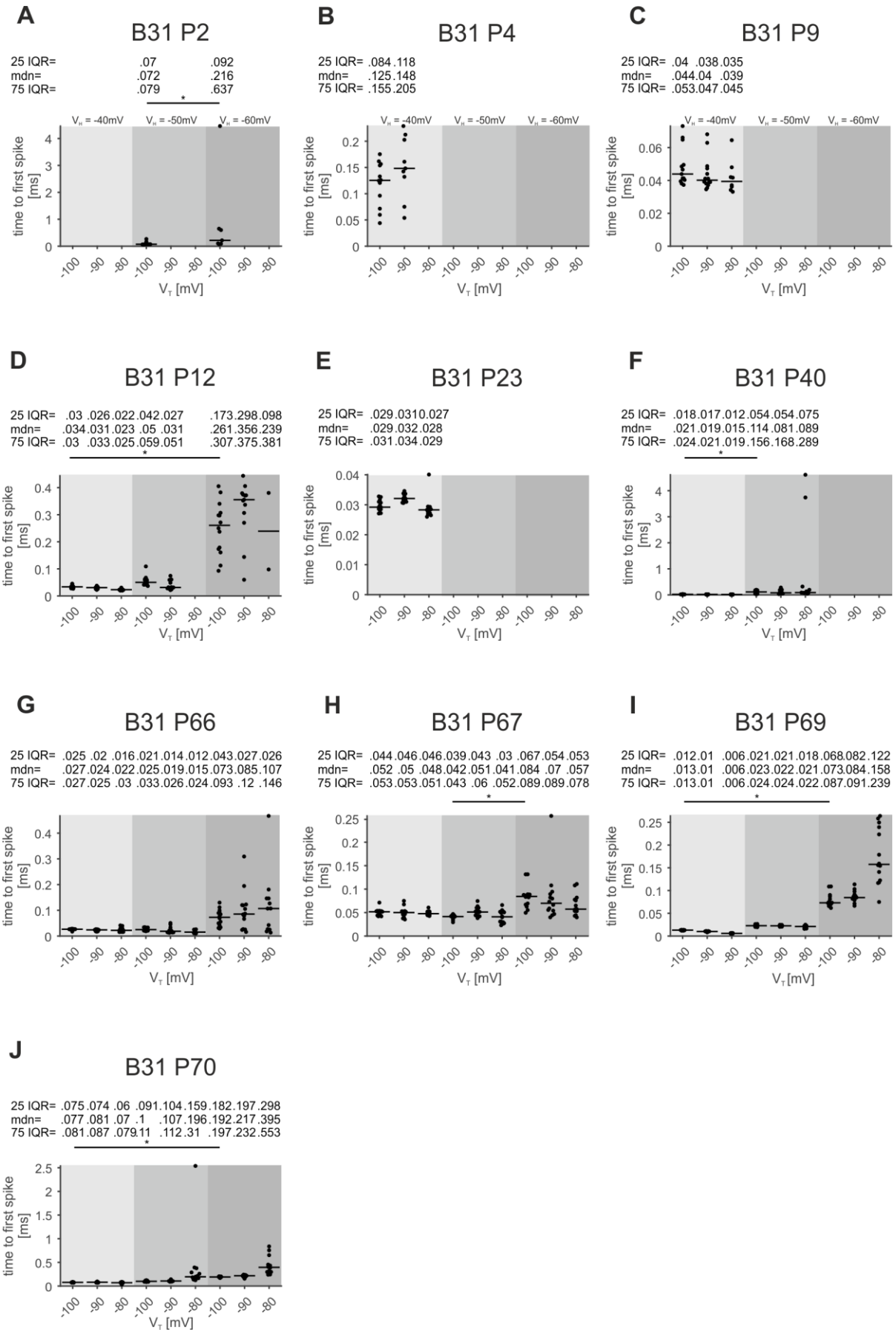
A
B31 P2
25 IQR= .07 .092
mdn= .072 .216
75 IQR= .079 .637
B
B31 P4
25 IQR= .084 .118
mdn= .125 .148
75 IQR= .155 .205
C
B31 P9
25 IQR= .04 .038 .035
mdn= .044 .04 .039
75 IQR= .053 .047 .045
D
B31 P12
25 IQR= .03 .026 .022 .042 .027 .173 .298 .098
mdn= .034 .031 .023 .05 .031 .261 .356 .239
75 IQR= .03 .033 .025 .059 .051 .307 .375 .381
E
B31 P23
25 IQR= .029 .031 0.027
mdn= .029 .032 .028
75 IQR= .031 .034 .029
F
B31 P40
25 IQR= .018 .017 .012 .054 .054 .075
mdn= .021 .019 .015 .114 .081 .089
75 IQR= .024 .021 .019 .156 .168 .289
G
B31 P66
25 IQR= .025 .02 .016 .021 .014 .012 .043 .027 .026
mdn= .027 .024 .022 .025 .019 .015 .073 .085 .107
75 IQR= .027 .025 .03 .033 .026 .024 .093 .12 .146
H
B31 P67
25 IQR= .044 .046 .046 .039 .043 .03 .067 .054 .053
mdn= .052 .05 .048 .042 .051 .041 .084 .07 .057
75 IQR= .053 .053 .051 .043 .06 .052 .089 .089 .078
I
B31 P69
25 IQR= .012 .01 .006 .021 .021 .018 .068 .082 .122
mdn= .013 .01 .006 .023 .022 .021 .073 .084 .158
75 IQR= .013 .01 .006 .024 .024 .022 .087 .091 .239
J
B31 P70
25 IQR= .075 .074 .06 .091 .104 .159 .182 .197 .298
mdn= .077 .081 .07 .1 .107 .196 .192 .217 .395
75 IQR= .081 .087 .079 .11 .112 .31 .197 .232 .553
V_H = -40mV
V_H = -50mV
V_H = -60mV
time to first spike [ms]
V_T [mV]

Supplemental Figure 23: Rebound spike latencies – PSE. Normalized rebound spike latencies (elicited by hyperpolarizing current injections from different V_H to different V_T) from single experiments. Horizontal lines represent normalized median values. BXX and PXX represent numbering of experiments according to laboratory book- and respective page number. PSE: Power Stroke Exciter, IQR: interquartile range, mdn: median, V_H: holding potential, V_T: test potential, *: $p < 0.05$.

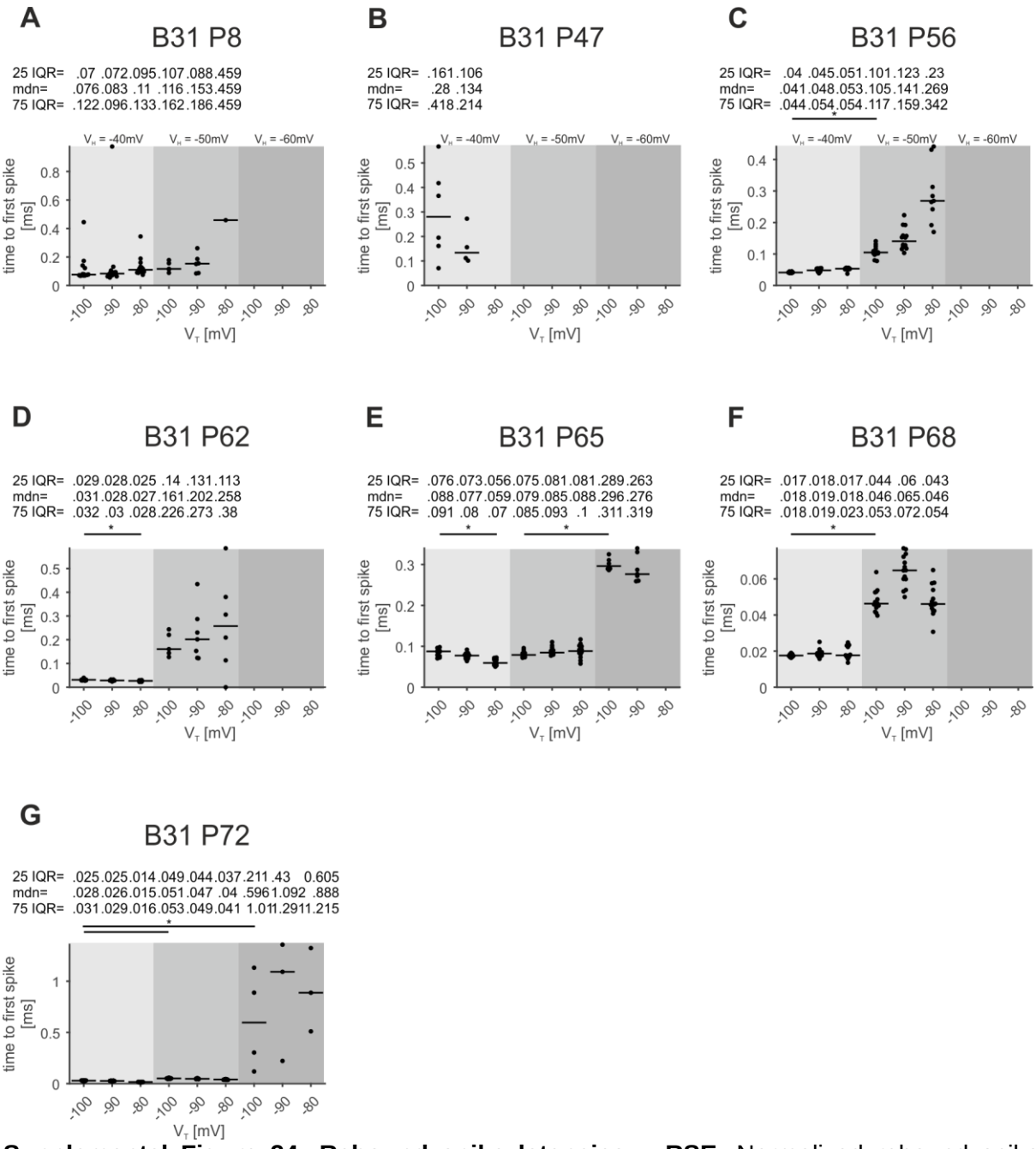

Supplemental Figure 24: Rebound spike latencies – RSE. Normalized rebound spike latencies (elicited by hyperpolarizing current injections from different V_H to different V_T) from single experiments. Horizontal lines represent normalized median values. BXX and PXX represent numbering of experiments according to laboratory book- and respective page number. RSE: Return Stroke Exciter, IQR: interquartile range, mdn: median, V_H: holding potential, V_T: test potential, *: $p < 0.05$.

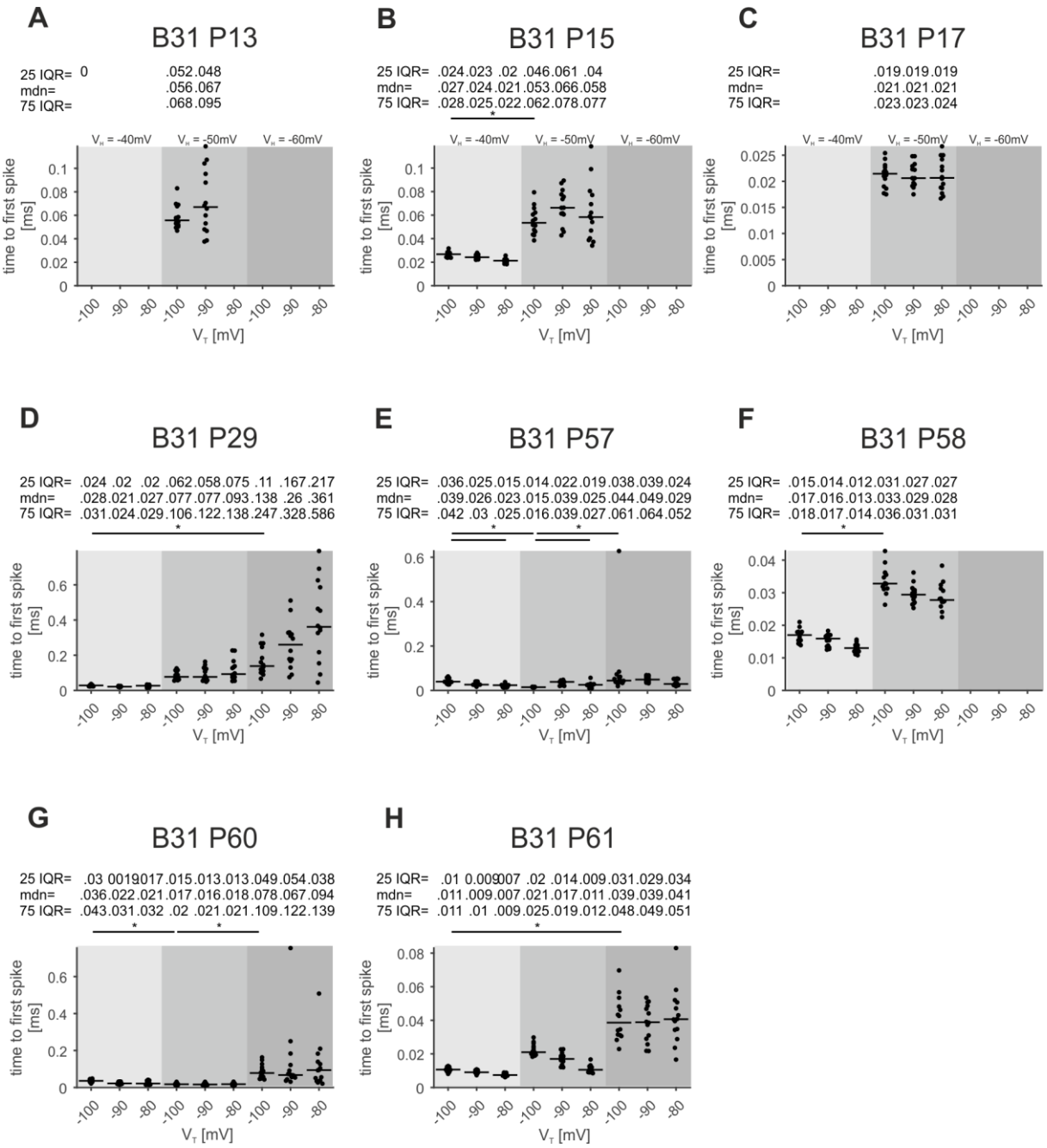

Supplemental Figure 25: Rebound spike latencies – ASC_Es. Normalized rebound spike latencies (elicited by hyperpolarizing current injections from different V_H to different V_T) from single experiments. Horizontal lines represent normalized median values. BXX and PXX represent numbering of experiments according to laboratory book- and respective page number. ASC_E: Ascending Coordinating Neuron, IQR: interquartile range, mdn: median, V_H: holding potential, V_T: test potential, *: $p < 0.05$.

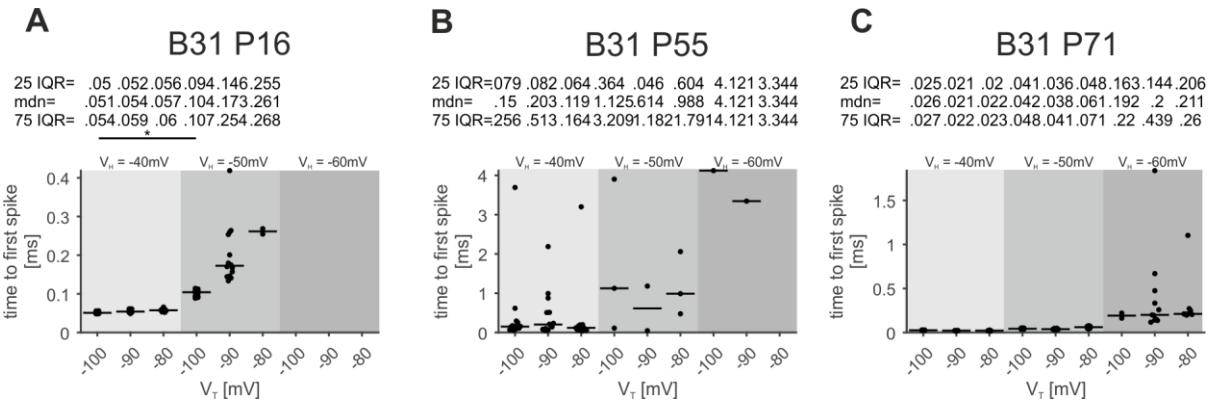

Supplemental Figure 26: Rebound spike latencies – DSC. Normalized rebound spike latencies (elicited by hyperpolarizing current injections from different V_H to different V_T) from single experiments. Horizontal lines represent normalized median values. BXX and PXX represent numbering of experiments according to laboratory book- and respective page number. DSC: Descending Coordinating Neuron, IQR: interquartile range, mdn: median, V_H: holding potential, V_T: test potential, *: $p < 0.05$.

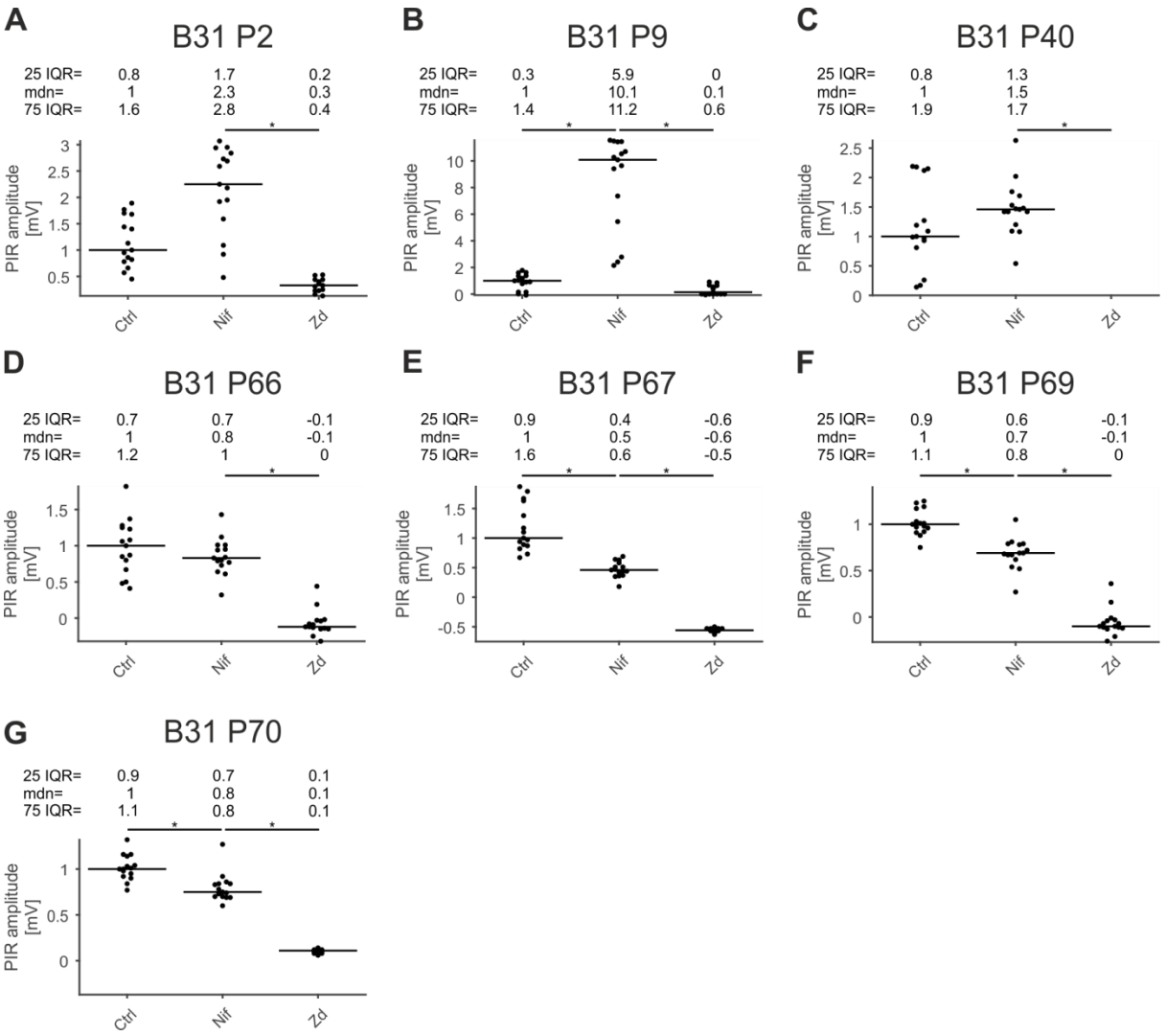

Supplemental Figure 27: Effects of channel blockers application on PIR amplitudes – PSE. Normalized PIR amplitudes from single experiments elicited by hyperpolarizing current injections during control condition and during treatment with Nifedipine, and Zd7288. Horizontal lines represent normalized median values. BXX and PXX represent numbering of experiments according to laboratory book- and respective page number. PIR: post-inhibitory rebound, PSE: Power Stroke Exciter, IQR: interquartile range, mdn: median, Ctrl: control, Nif: Nifedipine, Zd: Zd7288, *: $p < 0.05$.

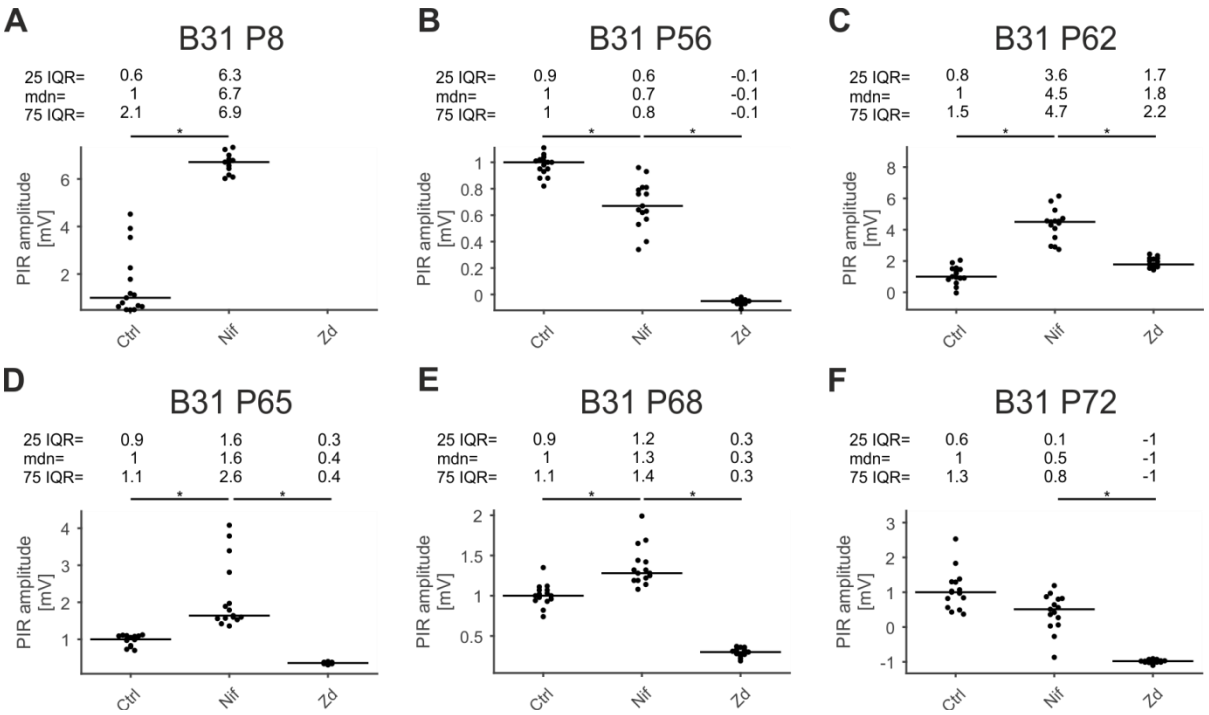

Supplemental Figure 28: Effects of channel blockers application on PIR amplitudes – RSE. Normalized PIR amplitudes from single experiments elicited by hyperpolarizing current injections during control condition and during treatment with Nifedipine, and Zd7288. Horizontal lines represent normalized median values. BXX and PXX represent numbering of experiments according to laboratory book- and respective page number. PIR: post-inhibitory rebound, RSE: Return Stroke Exciter, IQR: interquartile range, mdn: median, Ctrl: control, Nif: Nifedipine, Zd: Zd7288, *: $p < 0.05$.

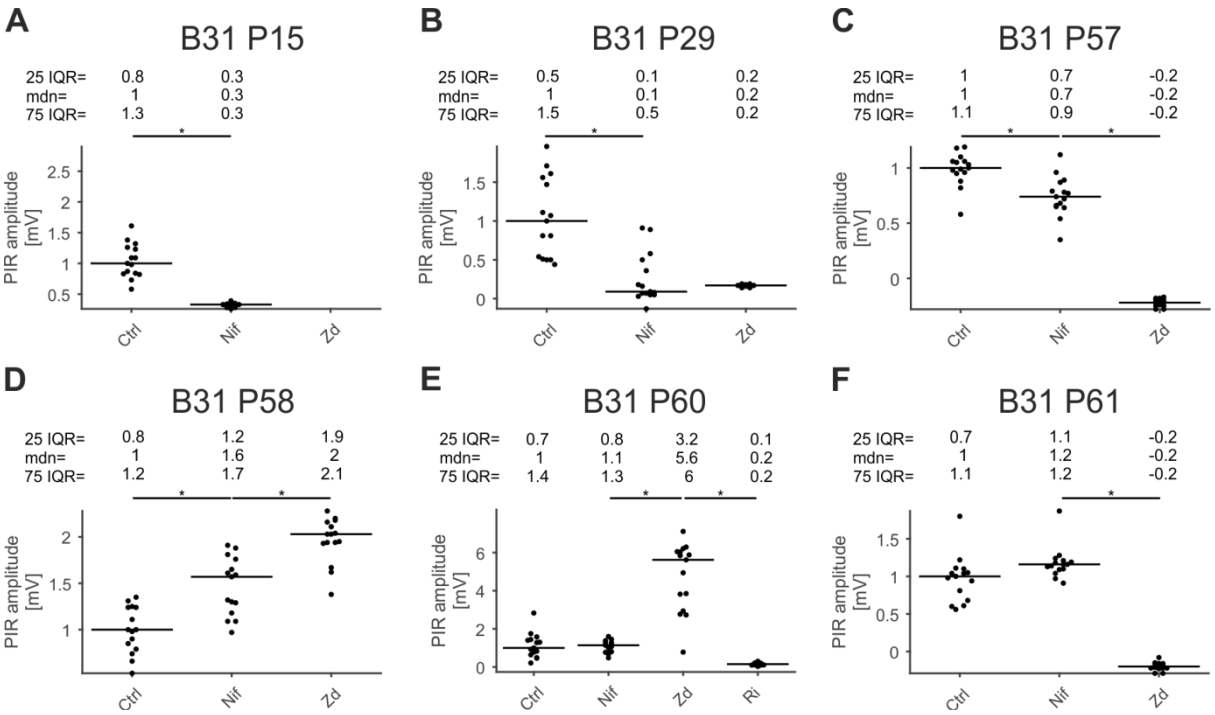

Supplemental Figure 29: Effects of channel blockers application on PIR amplitudes – ASC_E. Normalized PIR amplitudes from single experiments elicited by hyperpolarizing current injections during control condition and during treatment with Nifedipine, Zd7288, and Riluzole. Horizontal lines represent normalized median values. BXX and PXX represent numbering of experiments according to laboratory book- and respective page number. PIR: post-inhibitory rebound, ASC_E: Ascending Coordinating Neuron, IQR: interquartile range, mdn: median, Ctrl: control, Nif: Nifedipine, Zd: Zd7288, Ri: Riluzole, *: $p < 0.05$.

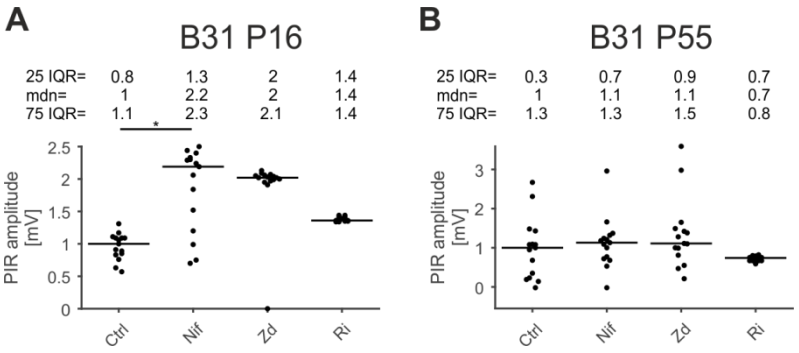

Supplemental Figure 30: Effects of channel blockers application on PIR amplitudes – DSC. Normalized PIR amplitudes from single experiments elicited by hyperpolarizing current injections during control condition and during treatment with Nifedipine, Zd7288, and Riluzole. Horizontal lines represent normalized median values. BXX and PXX represent numbering of experiments according to laboratory book- and respective page number. PIR: post-inhibitory rebound, DSC: Descending Coordinating Neuron, IQR: interquartile range, mdn: median, Ctrl: control, Nif: Nifedipine, Zd: Zd7288, Ri: Riluzole, *: $p < 0.05$.

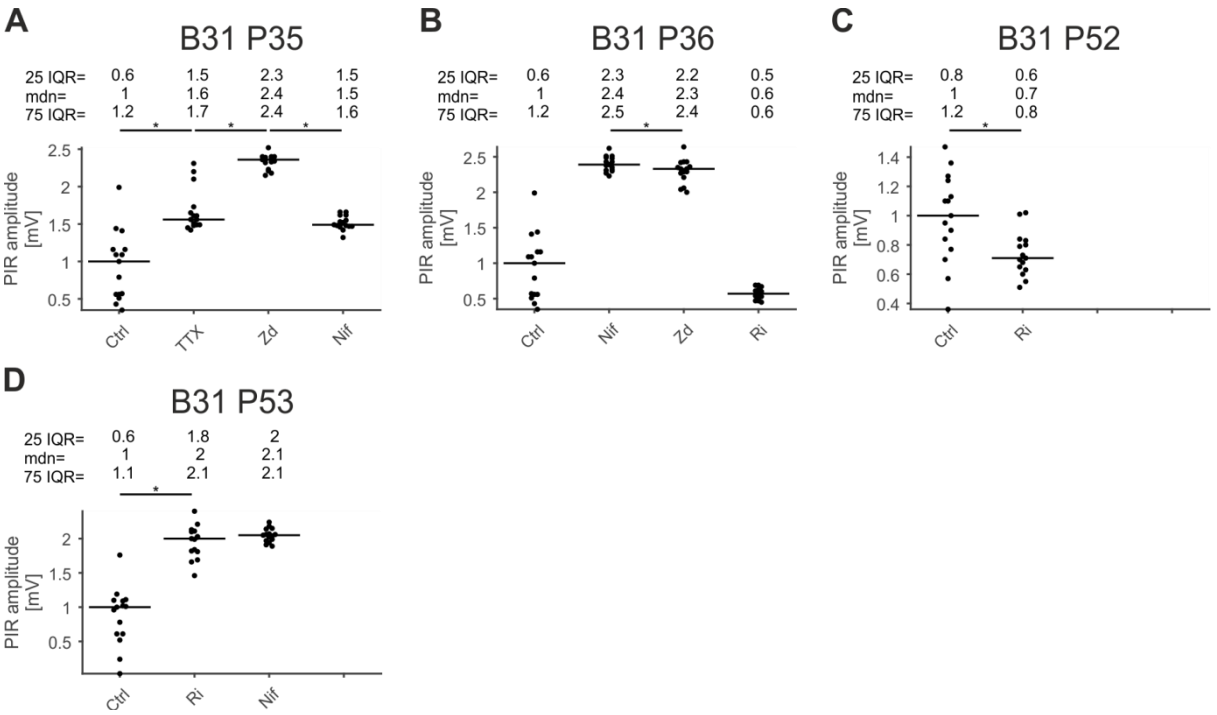

Supplemental Figure 31: Effects of channel blockers application on PIR amplitudes – ComInt1. Normalized PIR amplitudes from single experiments elicited by hyperpolarizing current injections during control condition and during treatment with Nifedipine, Zd7288, TTX or Riluzole. Horizontal lines represent normalized median values. BXX and PXX represent numbering of experiments according to laboratory book- and respective page number. PIR: post-inhibitory rebound, ComInt1: Commissural Interneuron 1, IQR: interquartile range, mdn: median, Ctrl: control, Nif: Nifedipine, Zd: Zd7288, Ri: Riluzole, TTX: Tetrodotoxin, *: $p < 0.05$.

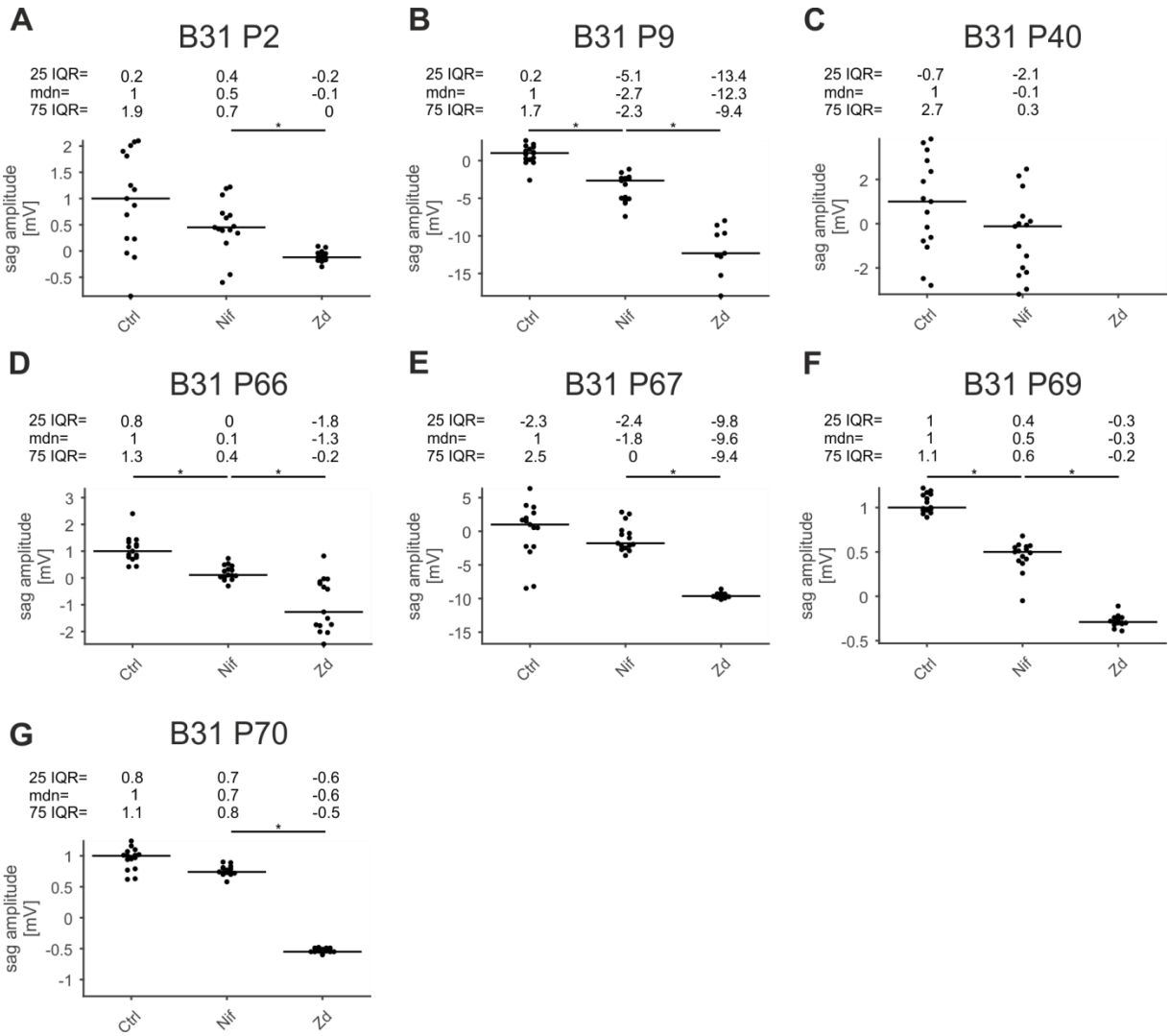

Supplemental Figure 32: Effects of channel blockers application on sag amplitudes – PSE. Normalized sag potential amplitudes from single experiments elicited by hyperpolarizing current injections during control condition and during treatment with Nifedipine, and Zd7288. Horizontal lines represent normalized median values. BXX and PXX represent numbering of experiments according to laboratory book- and respective page number. PSE: Power Stroke Exciter, IQR: interquartile range, mdn: median, Ctrl: control, Nif: Nifedipine, Zd: Zd7288, *: $p < 0.05$.

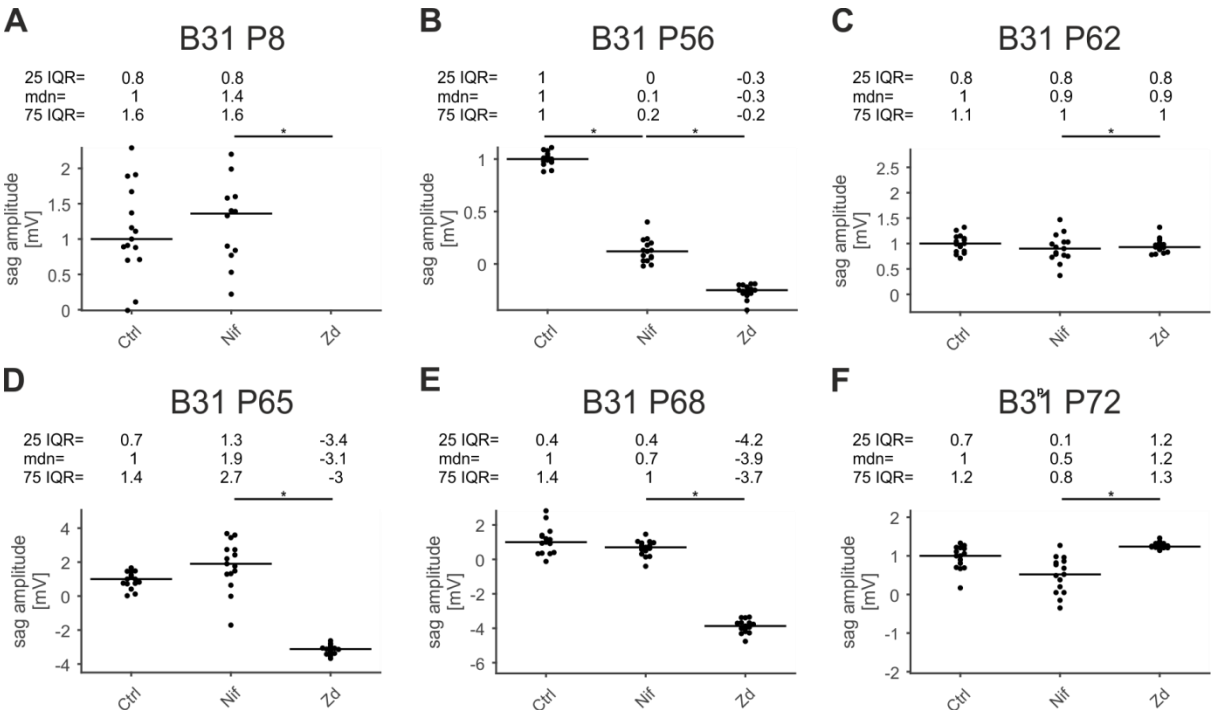

Supplemental Figure 33: Effects of channel blockers application on sag amplitudes – RSE. Normalized sag potential amplitudes from single experiments elicited by hyperpolarizing current injections during control condition and during treatment with Nifedipine, and Zd7288. Horizontal lines represent normalized median values. BXX and PXX represent numbering of experiments according to laboratory book- and respective page number. RSE: Return Stroke Exciter, IQR: interquartile range, mdn: median, Ctrl: control, Nif: Nifedipine, Zd: Zd7288, *: $p < 0.05$.

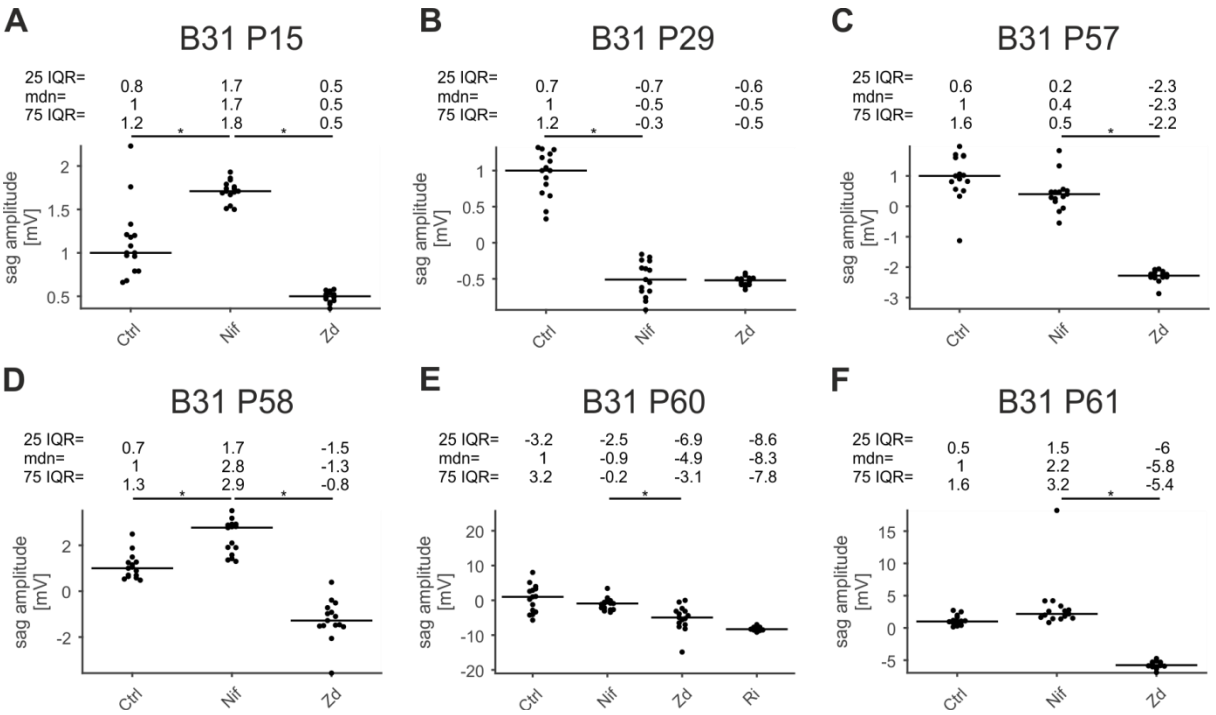

Supplemental Figure 34: Effects of channel blockers application on sag amplitudes – ASC_E. Normalized sag potential amplitudes from single experiments elicited by hyperpolarizing current injections during control condition and during treatment with Nifedipine, Zd7288, TTX, and Riluzole. Horizontal lines represent normalized median values. BXX and PXX represent numbering of experiments according to laboratory book- and respective page number. ASC_E: Ascending Coordinating Neuron, IQR: interquartile range, mdn: median, Ctrl: control, Nif: Nifedipine, Zd: Zd7288, Ri: Riluzole, *: $p < 0.05$.

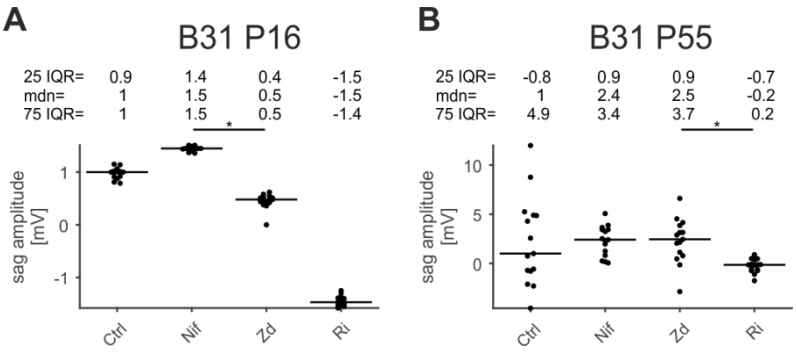

Supplemental Figure 35: Effects of channel blockers application on sag amplitudes – DSC. Normalized sag potential amplitudes from single experiments elicited by hyperpolarizing current injections during control condition and during treatment with Nifedipine, Zd7288, and Riluzole. Horizontal lines represent normalized median values. BXX and PXX represent numbering of experiments according to laboratory book- and respective page number. DSC: Descending Coordinating Neuron, IQR: interquartile range, mdn: median, Ctrl: control, Nif: Nifedipine, Zd: Zd7288, Ri: Riluzole, *: $p < 0.05$.

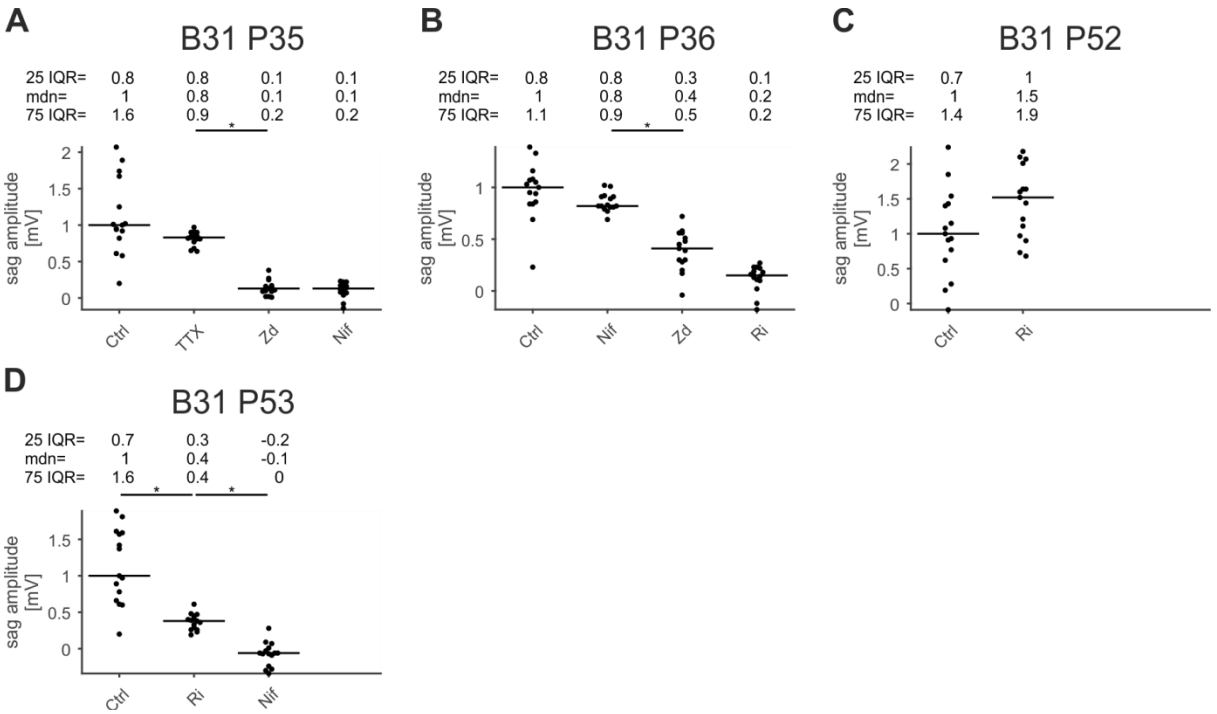

Supplemental Figure 36: Effects of channel blockers application on sag amplitudes – ComInt1. Normalized sag potential amplitudes from single experiments elicited by hyperpolarizing current injections during control condition and during treatment with Nifedipine, Zd7288, TTX, and Riluzole. Horizontal lines represent normalized median values. BXX and PXX represent numbering of experiments according to laboratory book- and respective page number. ComInt1: Commissural Interneuron 1, IQR: interquartile range, mdn: median, Ctrl: control, Nif: Nifedipine, Zd: Zd7288, Ri: Riluzole, TTX: Tetrodotoxin, *: $p < 0.05$.

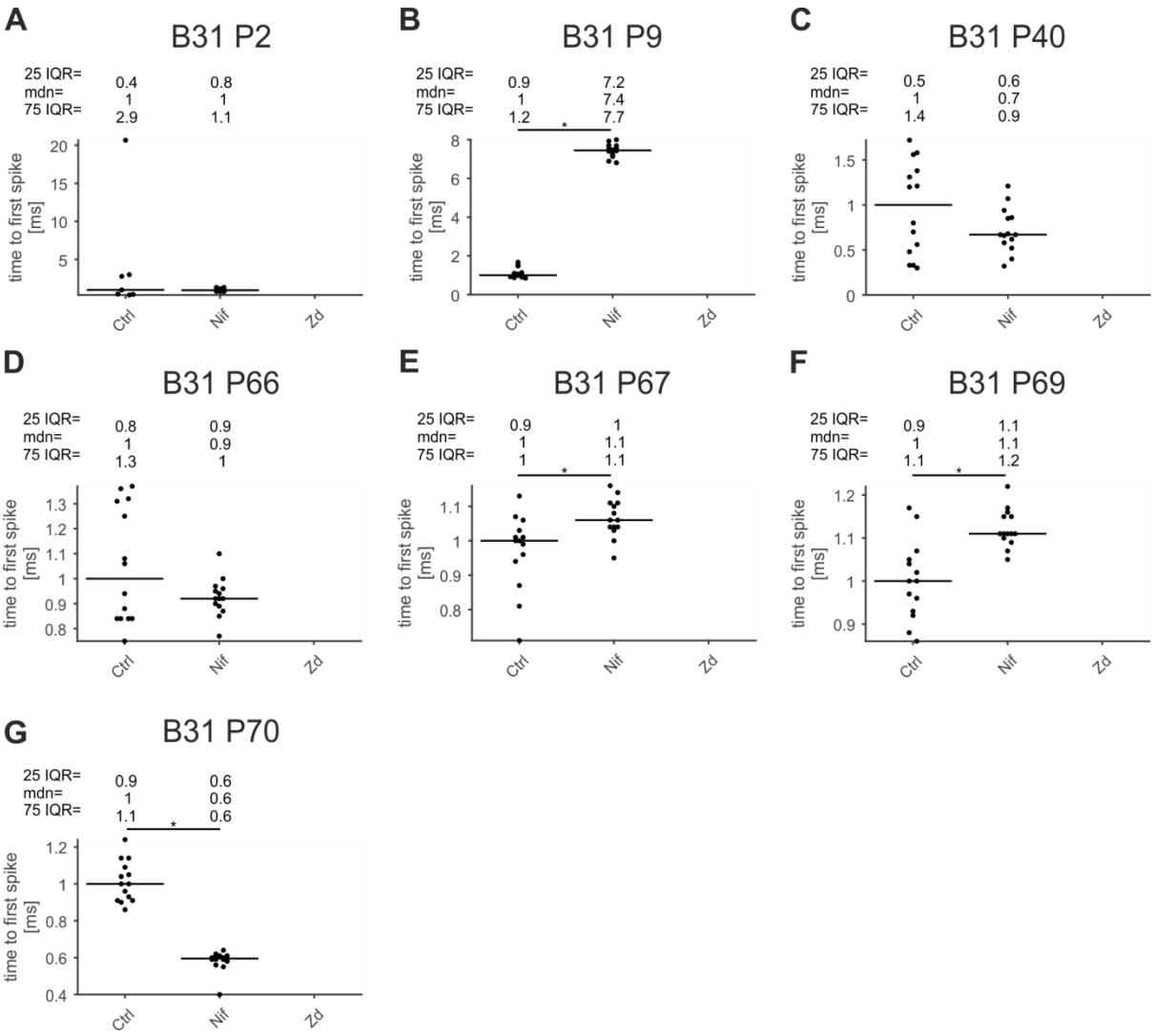

Supplemental Figure 37: Effects of channel blockers application on rebound latencies – PSE. Normalized rebound spike latencies from single experiments elicited by hyperpolarizing current injections during control condition and during treatment with Nifedipine, and Zd7288. Horizontal lines represent normalized median values. BXX and PXX represent numbering of experiments according to laboratory book- and respective page number. PSE: Power Stroke Exciter, IQR: interquartile range, mdn: median, Ctrl: control, Nif: Nifedipine, Zd: Zd7288, *: $p < 0.05$.

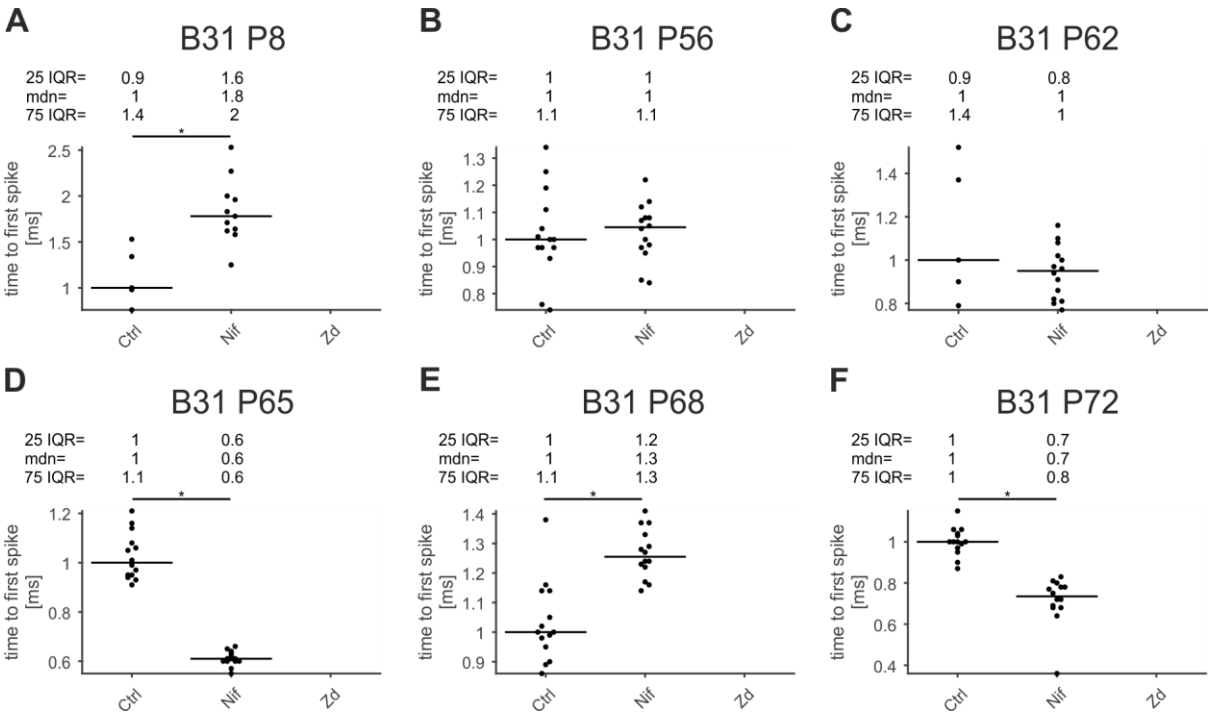

Supplemental Figure 38: Effects of channel blockers application on rebound latencies – RSE. Normalized rebound spike latencies from single experiments elicited by hyperpolarizing current injections during control condition and during treatment with Nifedipine, and Zd7288. Horizontal lines represent normalized median values. BXX and PXX represent numbering of experiments according to laboratory book- and respective page number. RSE: Return Stroke Exciter, IQR: interquartile range, mdn: median, Ctrl: control, Nif: Nifedipine, Zd: Zd7288, *: $p < 0.05$.

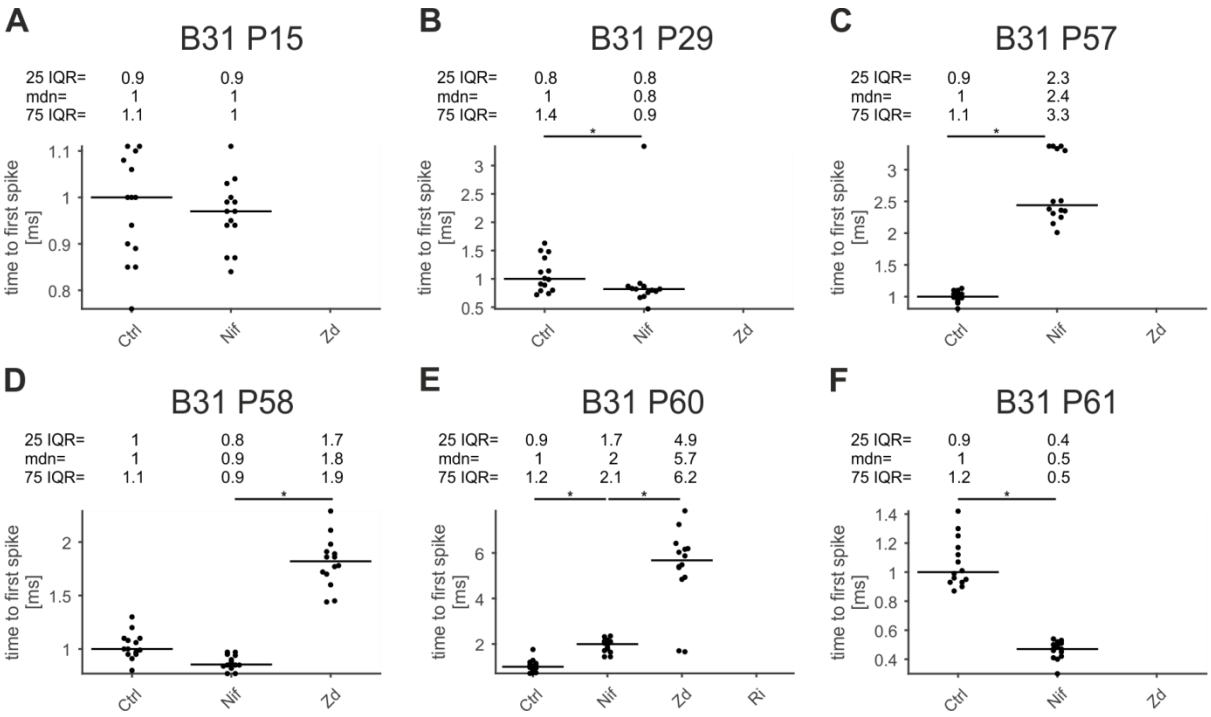

Supplemental Figure 39: Effects of channel blockers application on rebound latencies – ASC_E. Normalized rebound spike latencies from single experiments elicited by hyperpolarizing current injections during control condition and during treatment with Nifedipine, and Zd7288. Horizontal lines represent normalized median values. BXX and PXX represent numbering of experiments according to laboratory book- and respective page number. ASC_E: Ascending Coordinating Neuron, IQR: interquartile range, mdn: median, Ctrl: control, Nif: Nifedipine, Zd: Zd7288, Ri: Riluzole, *: $p < 0.05$.

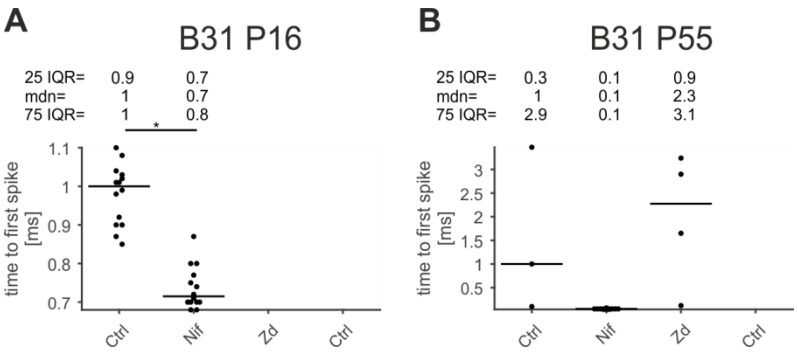

Supplemental Figure 40: Effects of channel blockers application on rebound latencies – DSC. Normalized rebound spike latencies from single experiments elicited by hyperpolarizing current injections during control condition and during treatment with Nifedipine, and Zd7288. Horizontal lines represent normalized median values. BXX and PXX represent numbering of experiments according to laboratory book- and respective page number. DSC: Descending Coordinating Neuron, IQR: interquartile range, mdn: median, Ctrl: control, Nif: Nifedipine, Zd: Zd7288, Ri: Riluzole, *: $p < 0.05$.

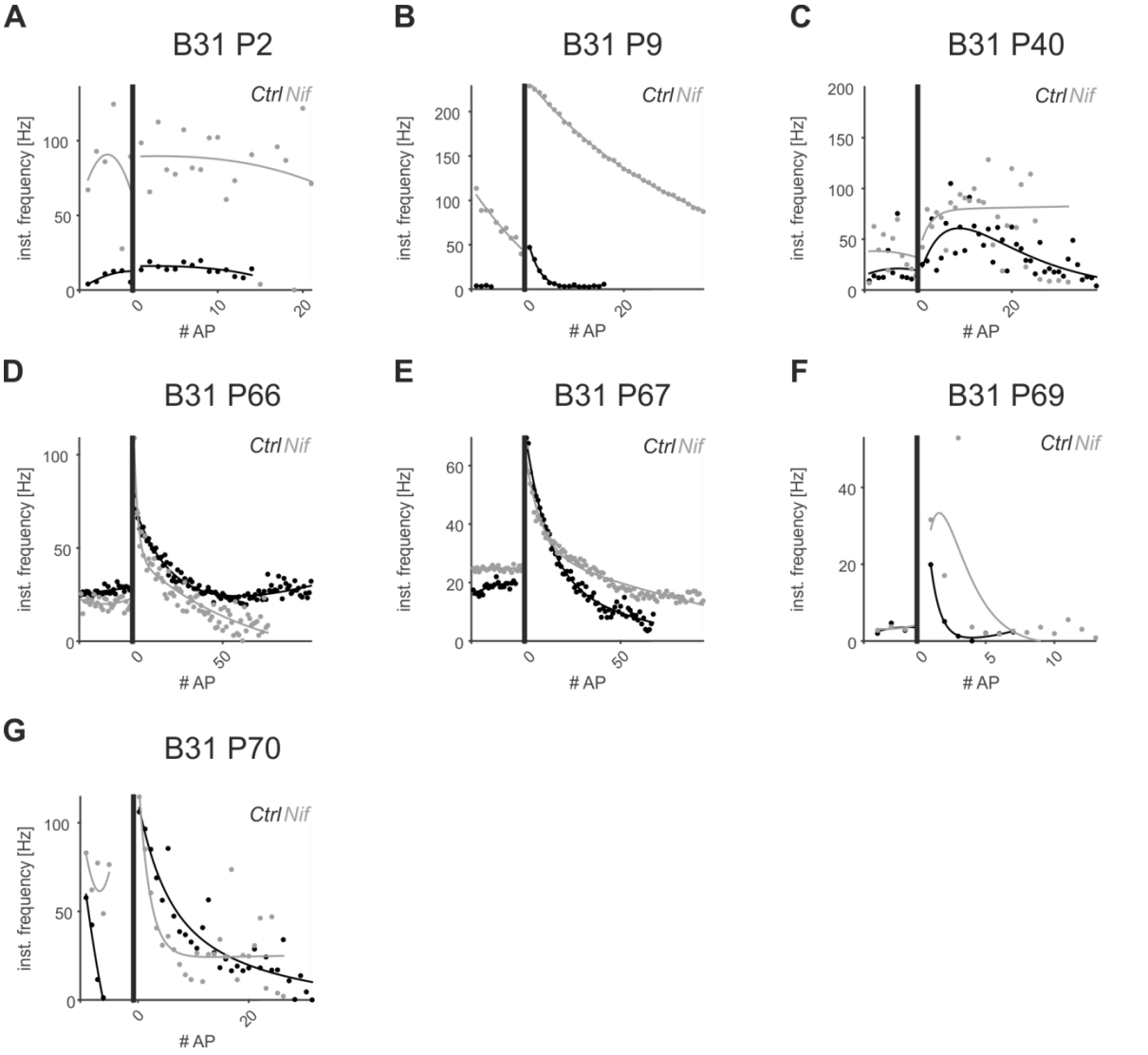

Supplemental Figure 41: Effects of channel blockers application on instantaneous rebound frequencies – PSE. Mean instantaneous firing frequencies (15 stimulations) from single experiments, plotted against the number of APs, before- and following the stimulation (control condition (black markers), treatment with Nifedipine (Grey markers)). BXX and PXX represent numbering of experiments according to laboratory book- and respective page number. PSE: Power Stroke Exciter, Ctrl: control, Nif: Nifedipine, *: $p < 0.05$.

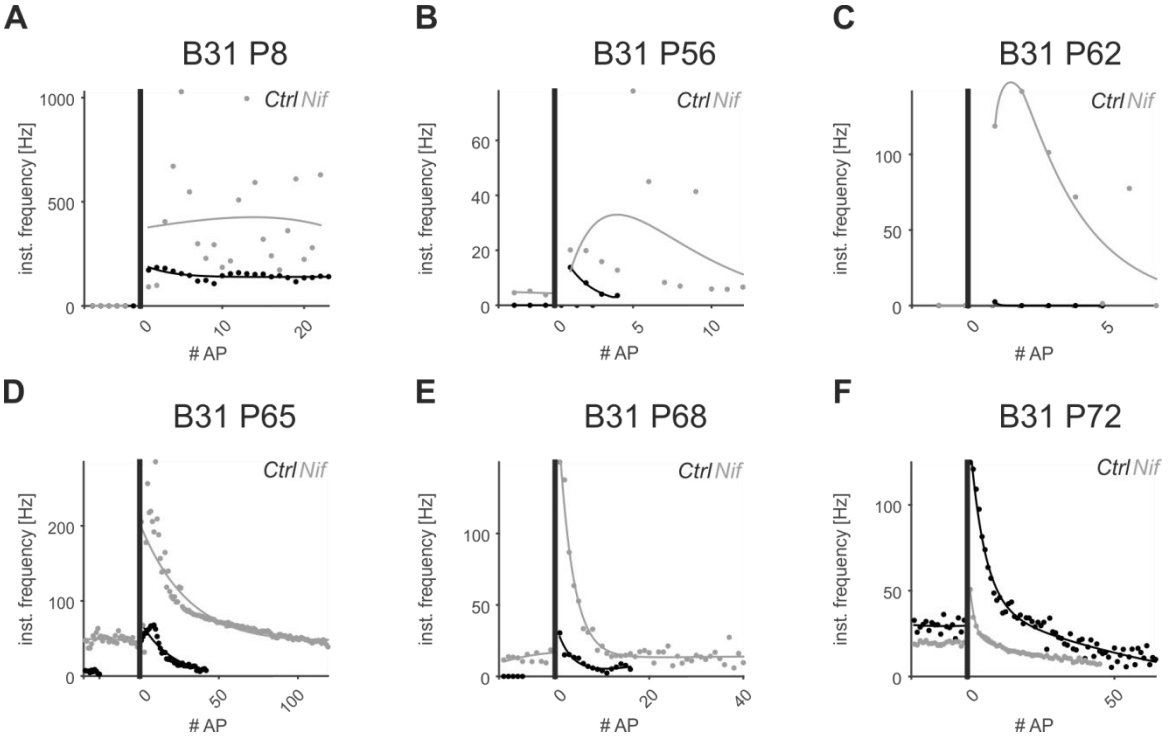

Supplemental Figure 42: Effects of channel blockers application on instantaneous rebound frequencies – RSE. Mean instantaneous firing frequencies (15 stimulations) from single experiments, plotted against the number of APs, before- and following the stimulation (control condition (black markers), treatment with Nifedipine (Grey markers)). BXX and PXX represent numbering of experiments according to laboratory book- and respective page number. RSE: Return Stroke Exciter, Ctrl: control, Nif: Nifedipine, *: $p < 0.05$.

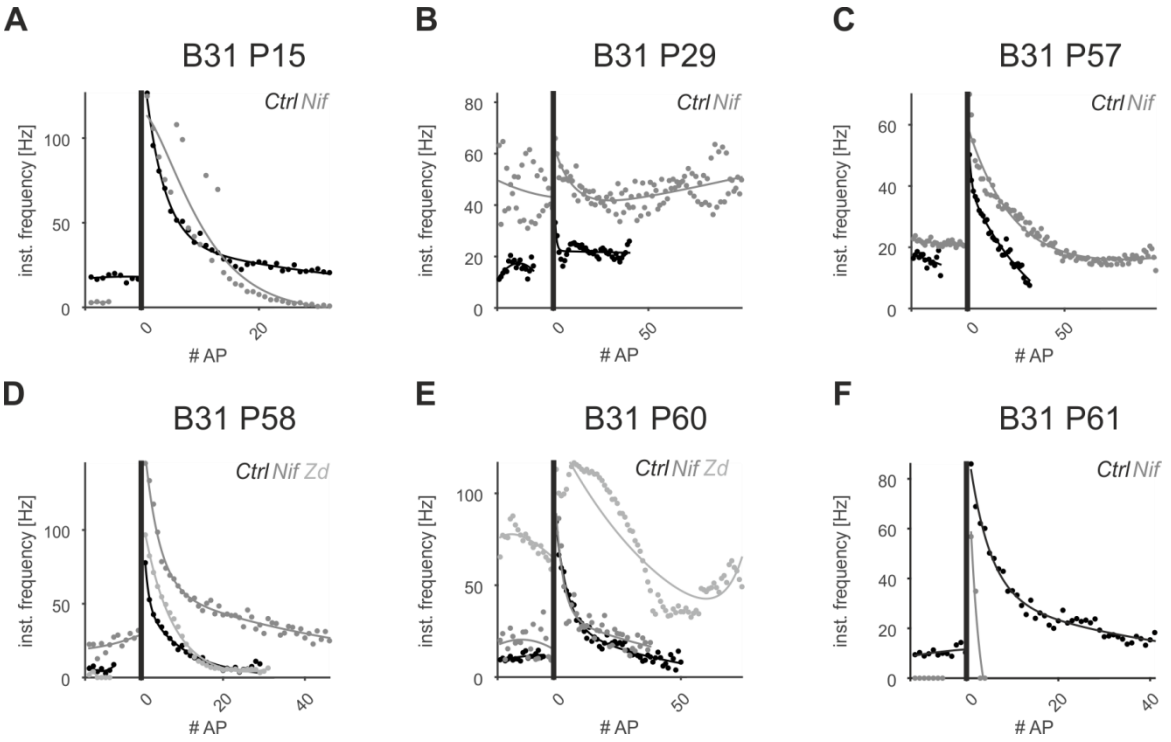

Supplemental Figure 43: Effects of channel blockers application on instantaneous rebound frequencies – ASC. Mean instantaneous firing frequencies (15 stimulations) from single experiments, plotted against the number of APs, before- and following the stimulation (control condition (black markers), treatment with Nifedipine (Grey markers)). BXX and PXX represent numbering of experiments according to laboratory book- and respective page number. ASC_E: Ascending Coordinating Neuron, Ctrl: control, Nif: Nifedipine, Zd: Zd7288, *: $p < 0.05$.

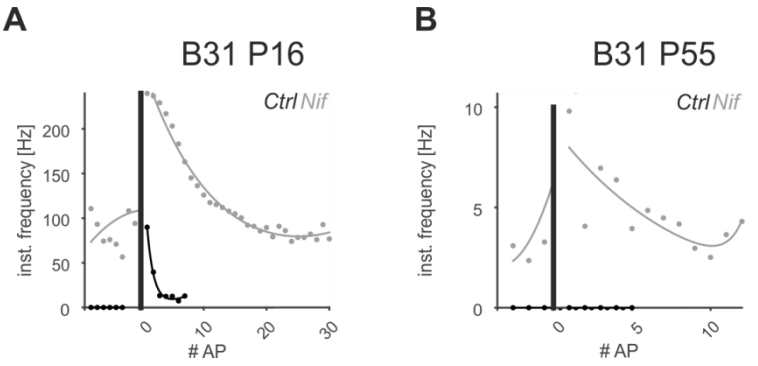

Supplemental Figure 44: Effects of channel blockers application on instantaneous rebound frequencies – DSC. Mean instantaneous firing frequencies (15 stimulations) from single experiments, plotted against the number of APs, before- and following the stimulation (control condition (black markers), treatment with Nifedipine (Grey markers)). BXX and PXX represent numbering of experiments according to laboratory book- and respective page number. DSC: Descending Coordinating Neuron, Ctrl: control, Nif: Nifedipine, *: $p < 0.05$.

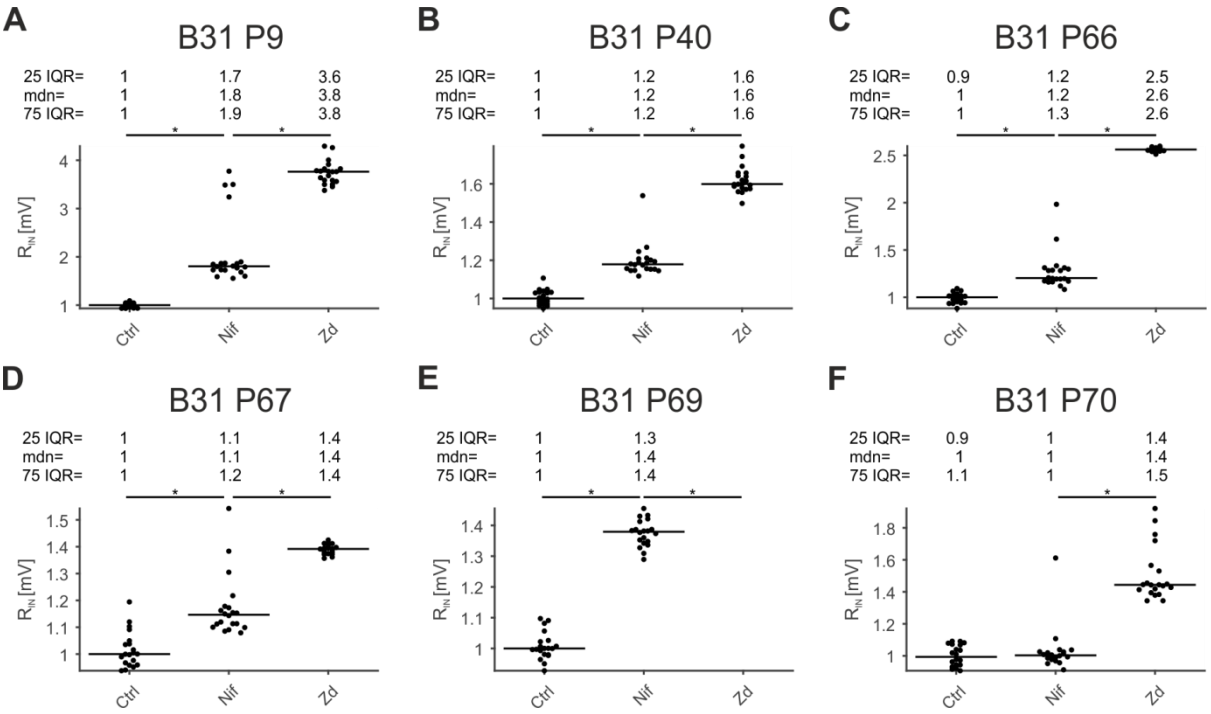

Supplemental Figure 45: Effects of channel blockers application on input resistances – PSE. Normalized input resistances from single experiments during control condition and during treatment with Nifedipine, and Zd7288. Horizontal lines represent normalized median values. BXX and PXX represent numbering of experiments according to laboratory book- and

respective page number. R_{IN}: input resistance, PSE: Power Stroke Exciter, IQR: interquartile range, mdn: median, Ctrl: control, Nif: Nifedipine, Zd: Zd7288, *: $p < 0.05$.

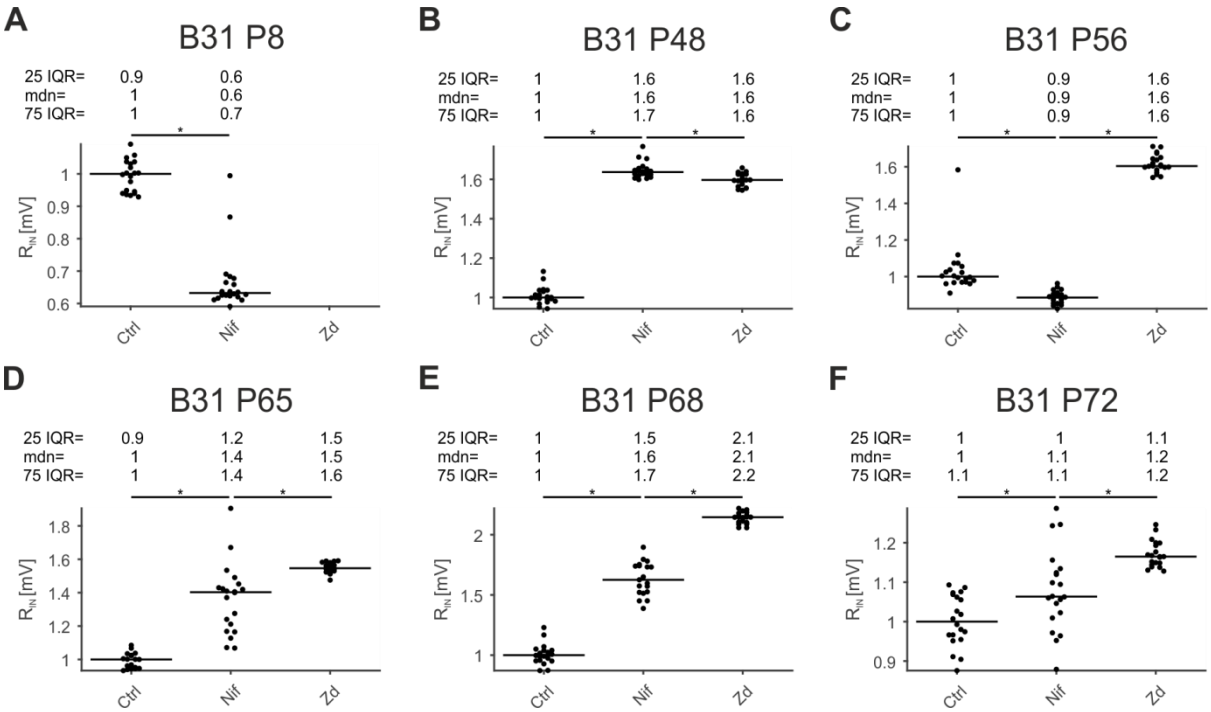

Supplemental Figure 46: Effects of channel blockers application on input resistances – RSE. Normalized input resistances from single experiments during control condition and during treatment with Nifedipine, and Zd7288. Horizontal lines represent normalized median values. BXX and PXX represent numbering of experiments according to laboratory book- and respective page number. R_{IN}: input resistance, RSE: Return Stroke Exciter, IQR: interquartile range, mdn: median, Ctrl: control, Nif: Nifedipine, Zd: Zd7288, *: $p < 0.05$.

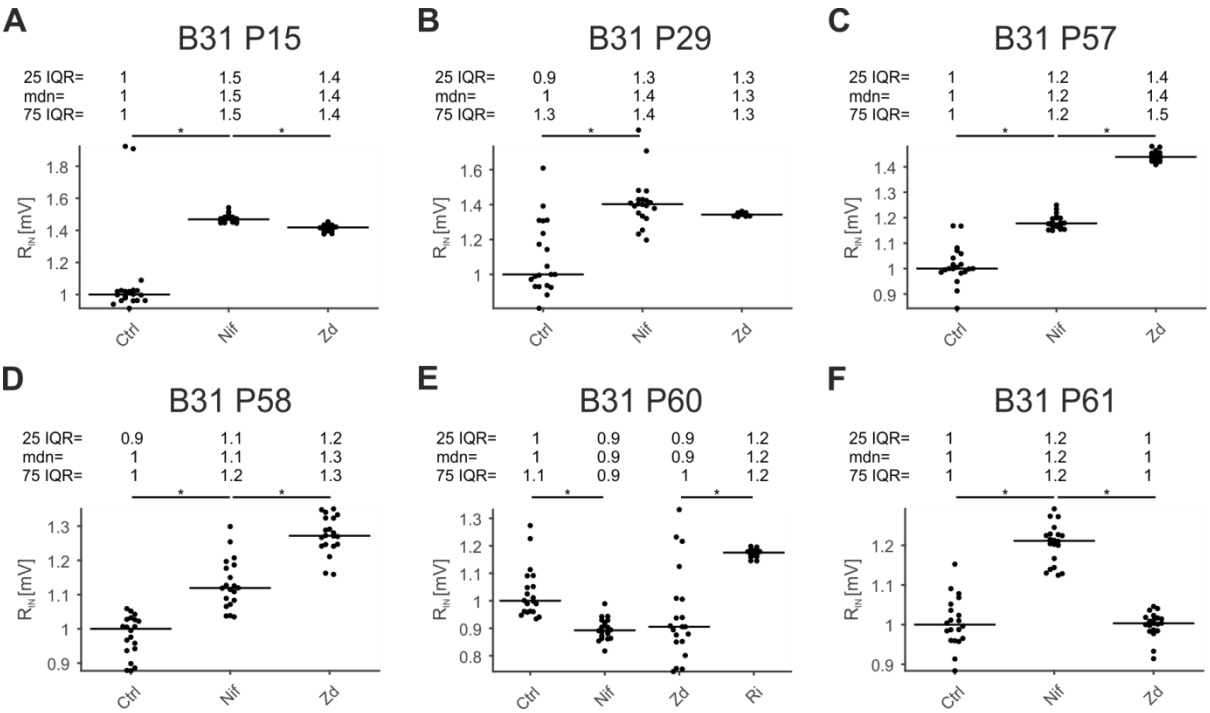

Supplemental Figure 47: Effects of channel blockers application on input resistances – ASC. Normalized input resistances from single experiments during control condition and during treatment with Nifedipine, Zd7288, and Riluzole. Horizontal lines represent normalized median values. BXX and PXX represent numbering of experiments according to laboratory book- and respective page number. R_{IN}: input resistance, ASC_E: Ascending Coordinating Neuron, IQR: interquartile range, mdn: median, Ctrl: control, Nif: Nifedipine, Zd: Zd7288, Ri: Riluzole, *: $p < 0.05$.

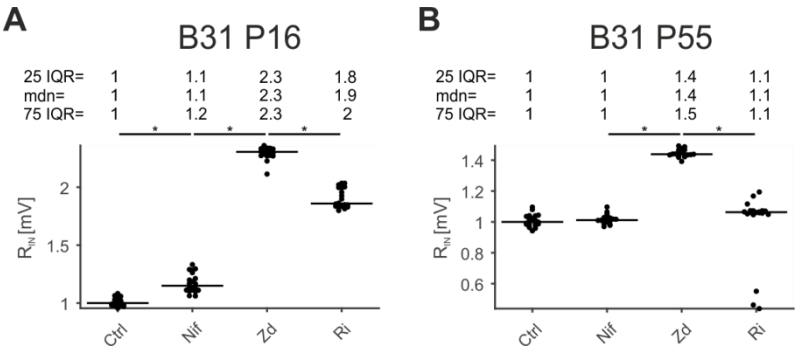

Supplemental Figure 48: Effects of channel blockers application on input resistances – DSC. Normalized input resistances from single experiments during control condition and during treatment with Nifedipine, Zd7288, and Riluzole. Horizontal lines represent normalized median values. BXX and PXX represent numbering of experiments according to laboratory book- and respective page number. R_{IN}: input resistance, DSC: Descending Coordinating Neuron, IQR: interquartile range, mdn: median, Ctrl: control, Nif: Nifedipine, Zd: Zd7288, Ri: Riluzole, *: $p < 0.05$.

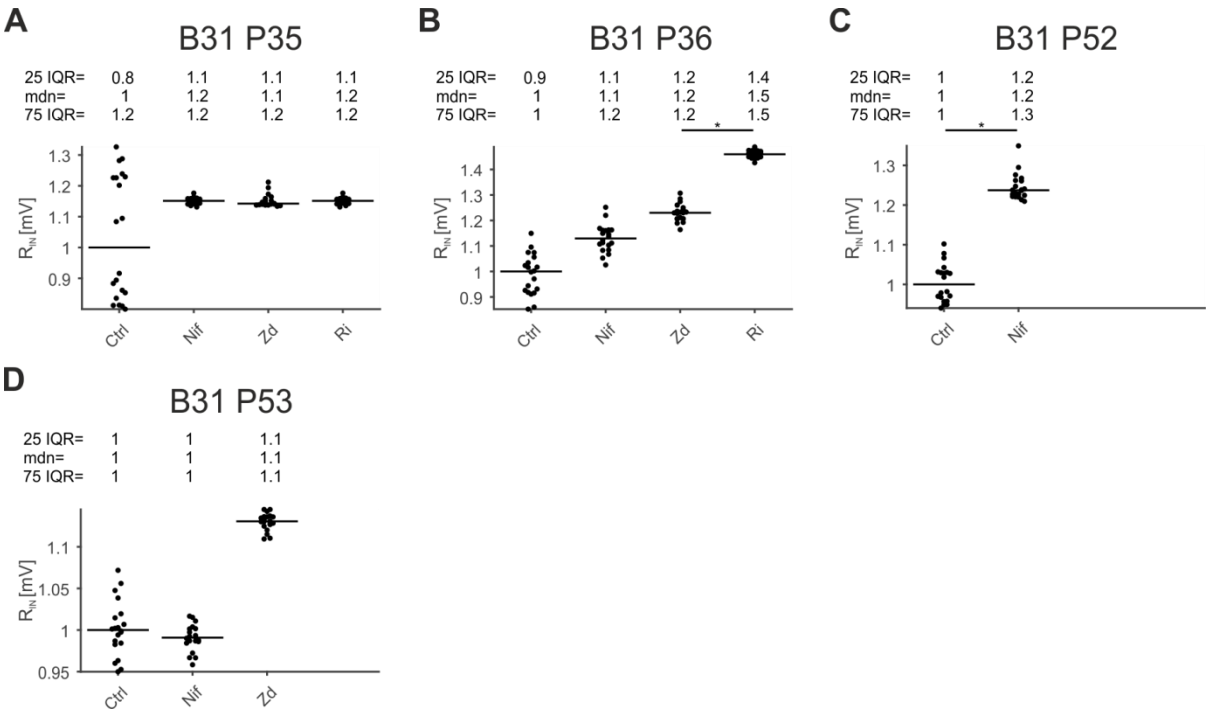

Supplemental Figure 49: Effects of channel blockers application on input resistances – ComInt1. Normalized input resistances from single experiments during control condition and during treatment with Nifedipine, Zd7288, TTX, or Riluzole. Horizontal lines represent normalized median values. BXX and PXX represent numbering of experiments according to laboratory book- and respective page number. R_{IN}: input resistance, ComInt1: Commissural Interneuron 1, IQR: interquartile range, mdn: median, Ctrl: control, Nif: Nifedipine, Zd: Zd7288, Ri: Riluzole, TTX: Tetrodotoxin, *: $p < 0.05$.

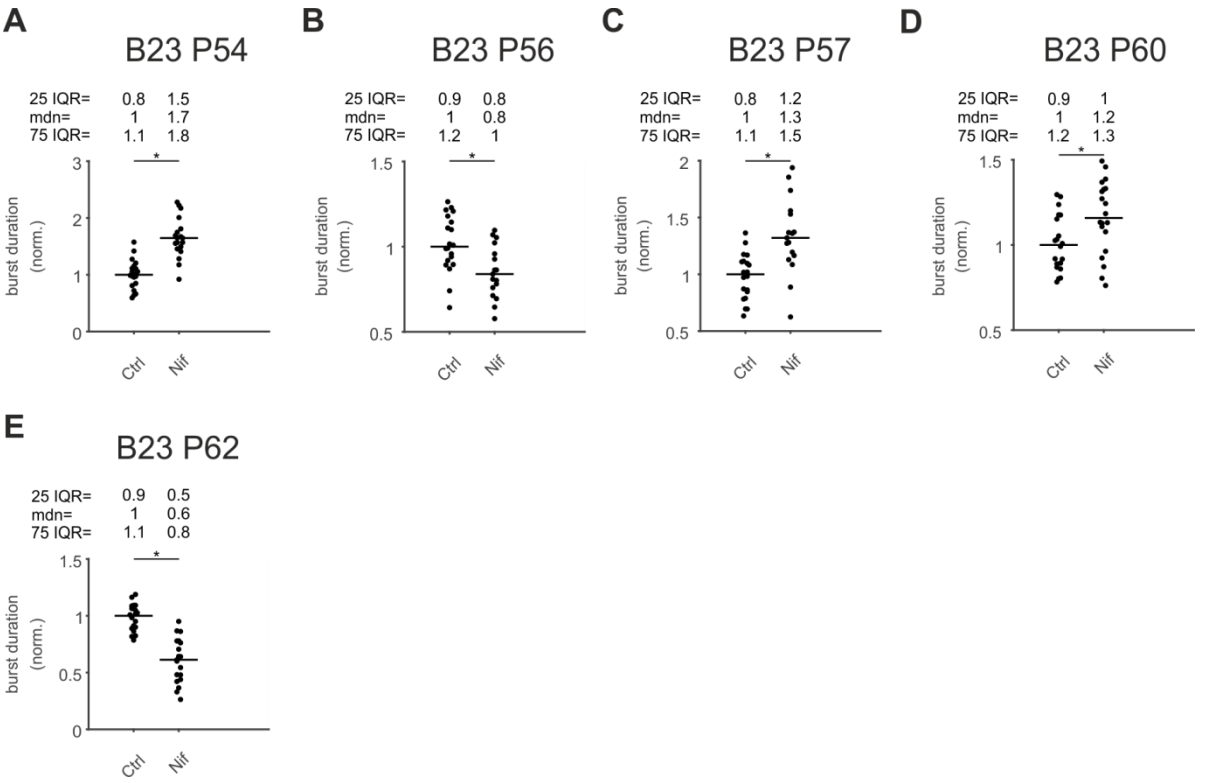

Supplemental Figure 50: Effects of Nifedipine application on PS burst duration. Normalized PS burst duration from single experiments during control condition and during treatment with Nifedipine. Horizontal lines represent normalized median values. BXX and PXX represent numbering of experiments according to laboratory book- and respective page number. PSE: Power Stroke Exciter, IQR: interquartile range, mdn: median, Ctrl: control, Nif: Nifedipine, *: $p < 0.05$.

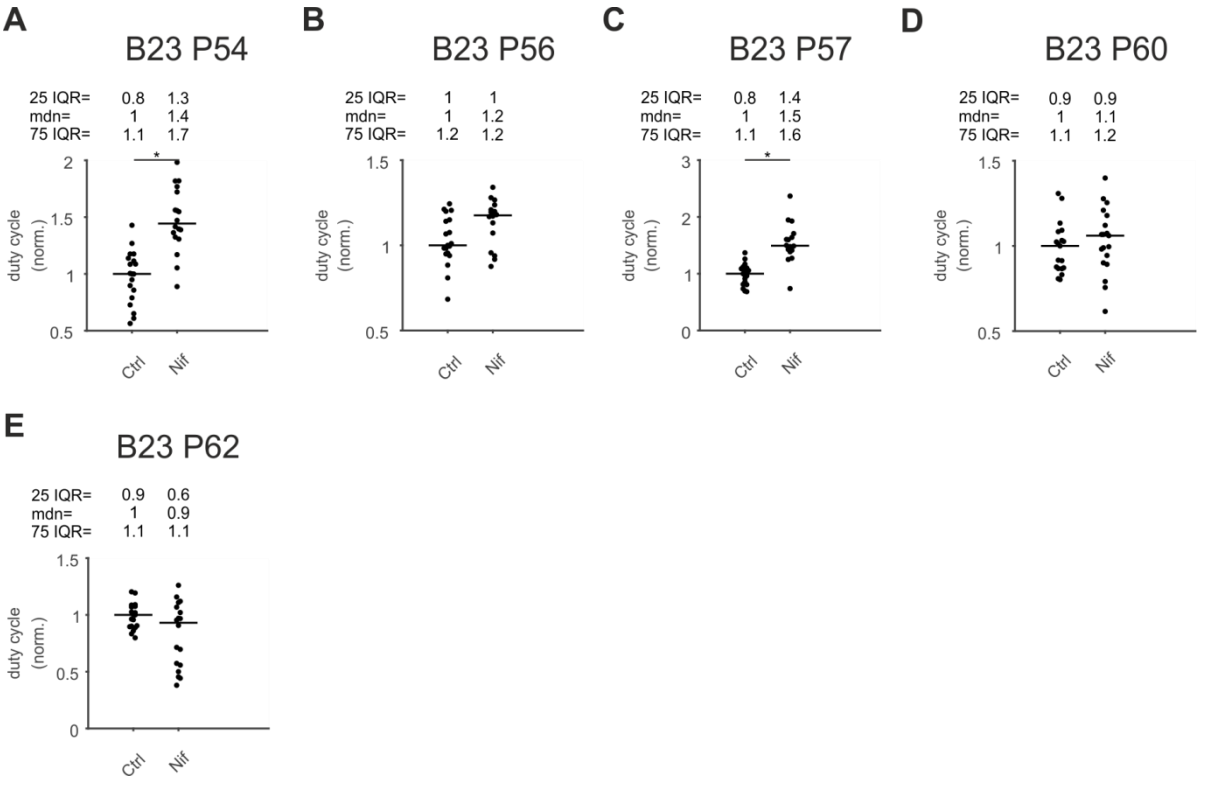

Supplemental Figure 51: Effects of Nifedipine application on PS duty cycle. Normalized PS duty cycle from single experiments during control condition and during treatment with Nifedipine. Horizontal lines represent normalized median values. BXX and PXX represent numbering of experiments according to laboratory book- and respective page number. PSE: Power Stroke Exciter, IQR: interquartile range, mdn: median, Ctrl: control, Nif: Nifedipine, *: $p < 0.05$.

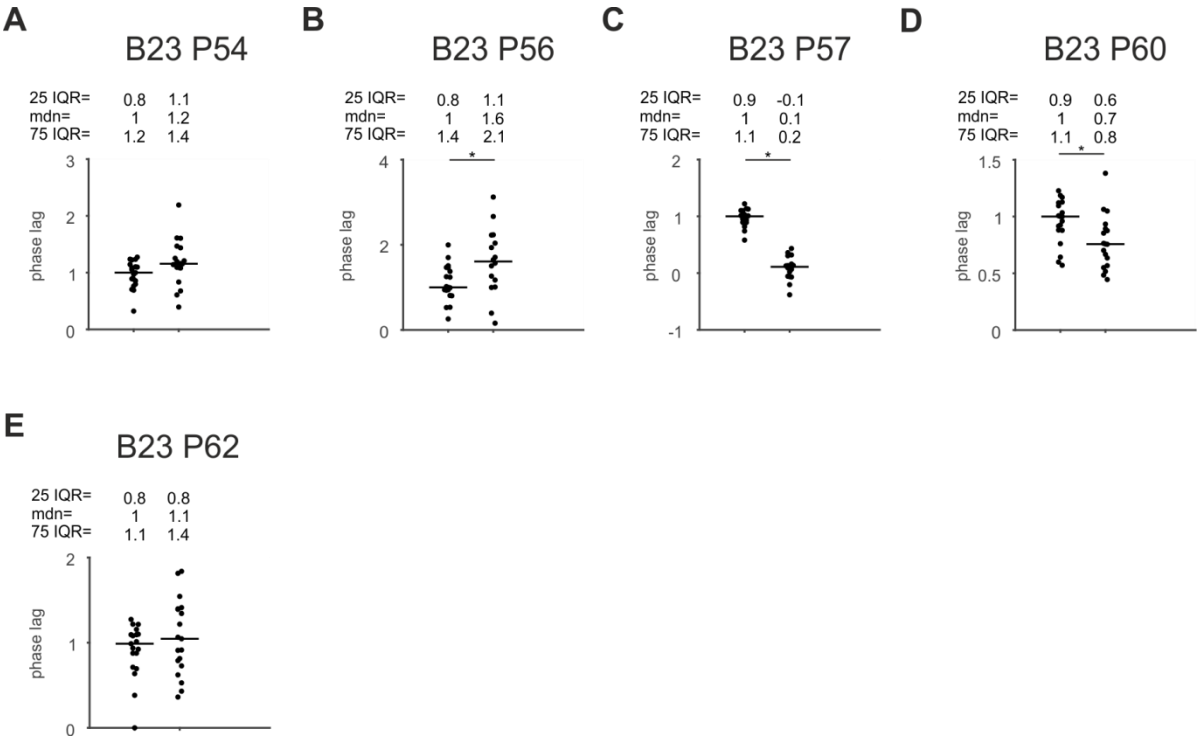

Supplemental Figure 52: Effects of Nifedipine application on PS phase lags. PS phase lag from single experiments during control condition and during treatment with Nifedipine. Horizontal lines represent normalized median values. BXX and PXX represent numbering of experiments according to laboratory book- and respective page number. PSE: Power Stroke Exciter, IQR: interquartile range, mdn: median, Ctrl: control, Nif: Nifedipine, *: $p < 0.05$.

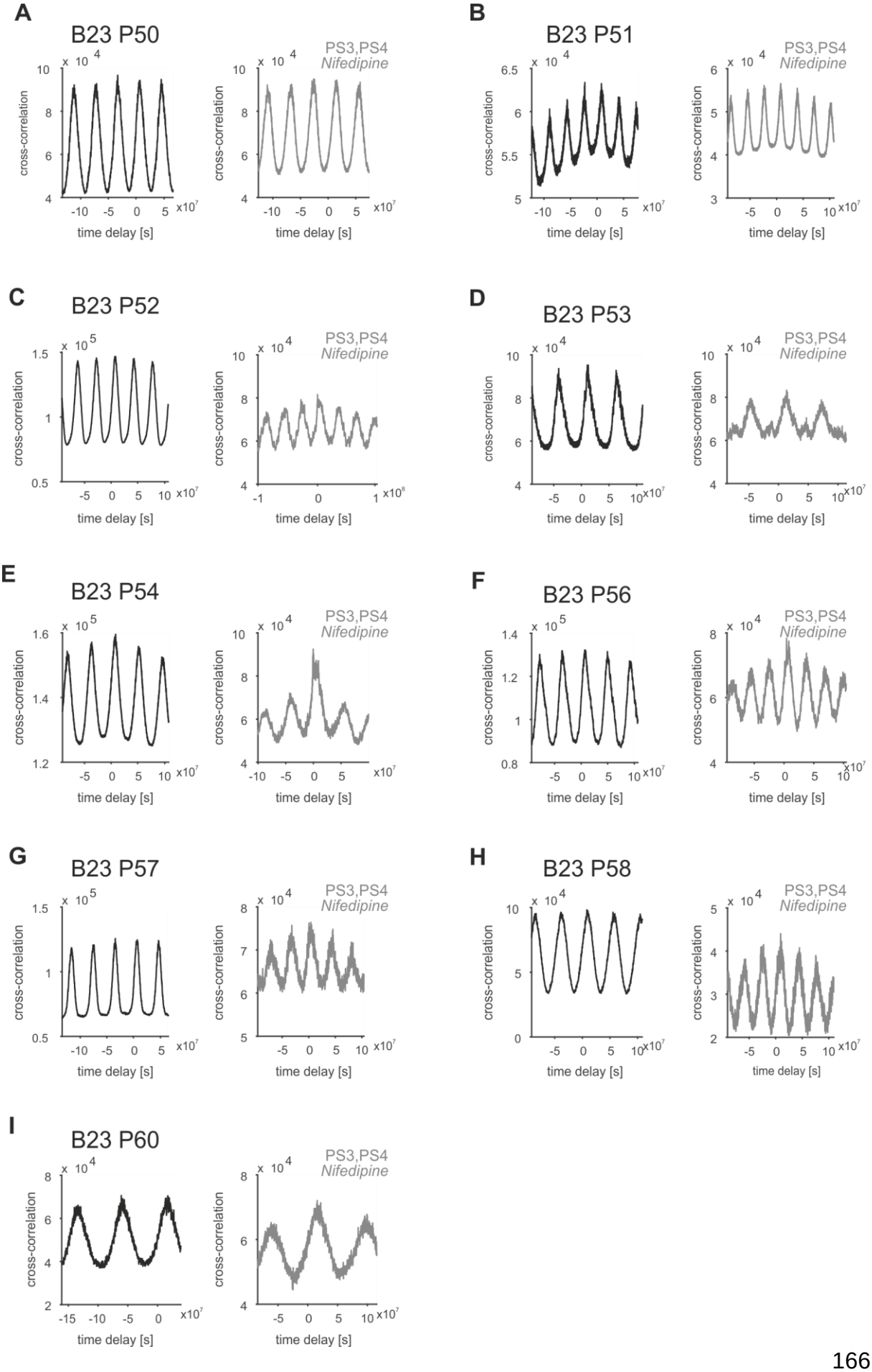
A
B23 P50
PS3,PS4
Nifedipine
B
B23 P51
PS3,PS4
Nifedipine
C
B23 P52
PS3,PS4
Nifedipine
D
B23 P53
PS3,PS4
Nifedipine
E
B23 P54
PS3,PS4
Nifedipine
F
B23 P56
PS3,PS4
Nifedipine
G
B23 P57
PS3,PS4
Nifedipine
H
B23 P58
PS3,PS4
Nifedipine
I
B23 P60
PS3,PS4
Nifedipine
cross-correlation
time delay [s]

Supplemental Figure 53: Effects of Nifedipine application on PS3-PS4 relation. Cross correlation as a function of time delay compares similarity and synchronicity of PS3 vs.PS4 activity in control condition and during Nifedipine treatment. BXX and PXX represent numbering of experiments according to laboratory book- and respective page number.

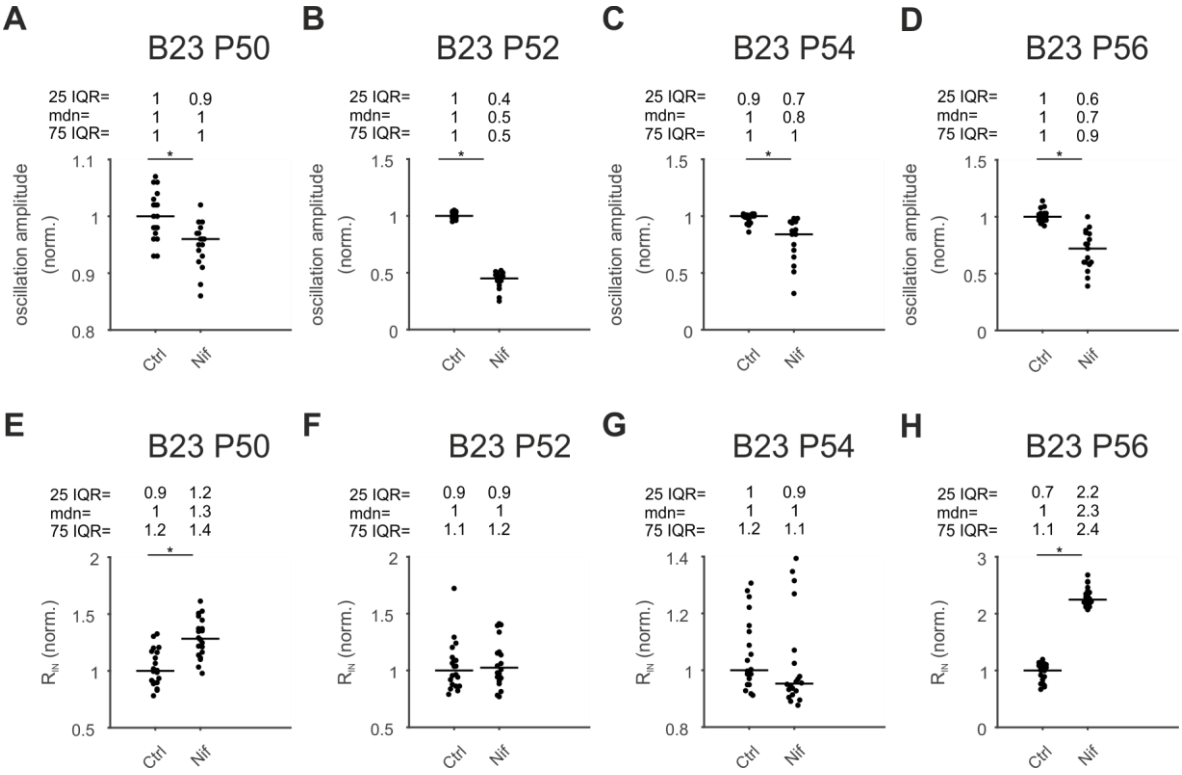

Supplemental Figure 54: Effects of Nifedipine application on oscillation amplitudes and input resistances from single PSE neurons. Normalized oscillation amplitudes and input resistances from single experiments during control condition and during treatment with Nifedipine. Horizontal lines represent normalized median values. BXX and PXX represent numbering of experiments according to laboratory book- and respective page number. R_{IN}: input resistance, IQR: interquartile range, mdn: median, Ctrl: control, Nif: Nifedipine, *: $p < 0.05$.

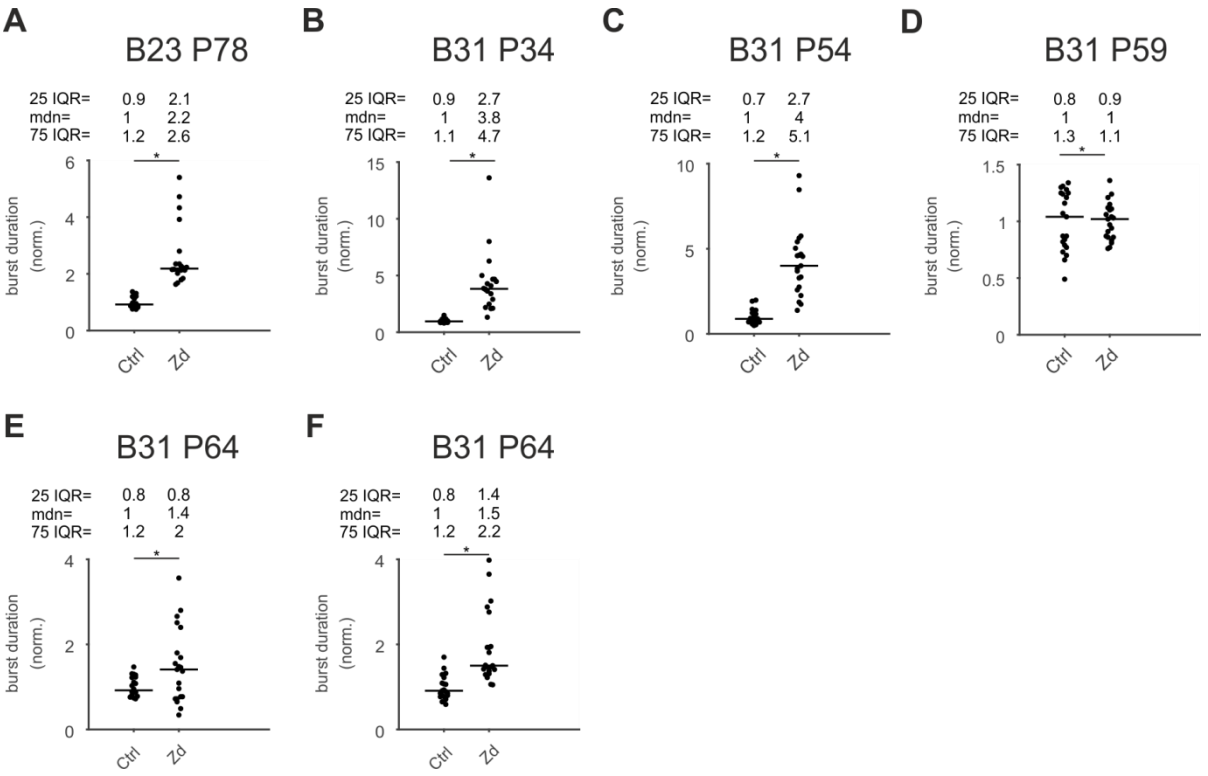

Supplemental Figure 55: : Effects of Zd7288 application on PS burst duration. Normalized PS burst duration from single experiments during control condition and during treatment with Zd7288. Horizontal lines represent normalized median values. BXX and PXX represent numbering of experiments according to laboratory book- and respective page number. PSE: Power Stroke Exciter, IQR: interquartile range, mdn: median, Ctrl: control, Zd: Zd7288, *: $p < 0.05$.

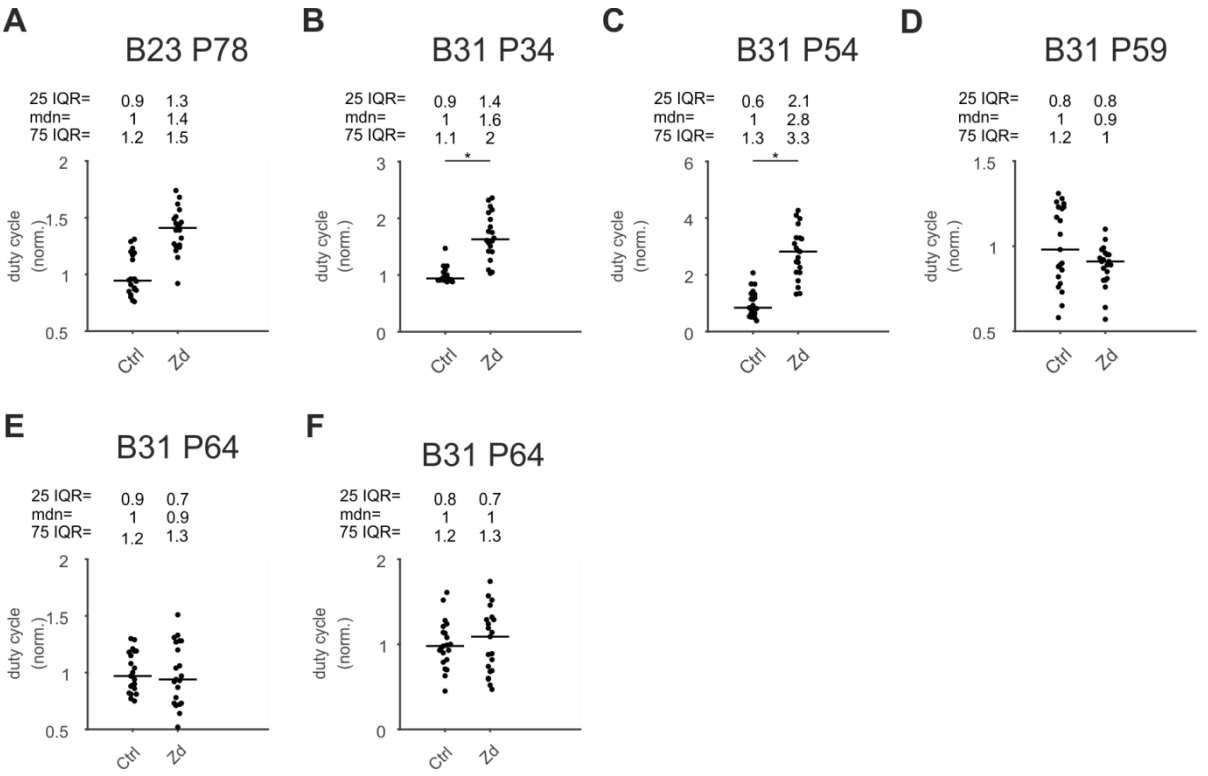

Supplemental Figure 56: Effects of Zd7288 application on PS duty cycle. Normalized PS duty cycle from single experiments during control condition and during treatment with Zd7288. Horizontal lines represent normalized median values. BXX and PXX represent numbering of experiments according to laboratory book- and respective page number. PSE: Power Stroke Exciter, IQR: interquartile range, mdn: median, Ctrl: control, Zd: Zd7288, *: $p < 0.05$.

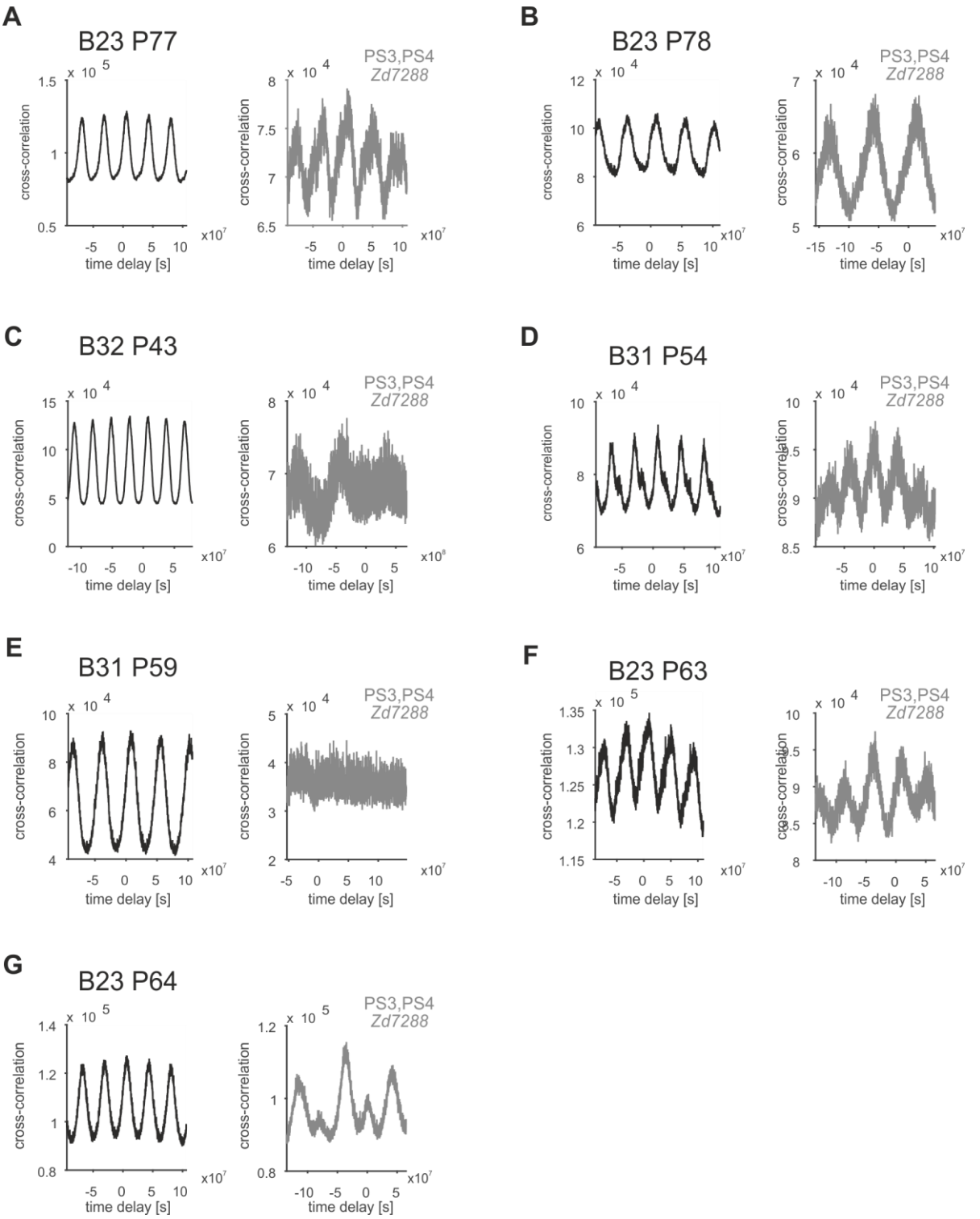

Supplemental Figure 57: Effects of Zd7288 application on PS3-PS4 relation. Cross correlation as a function of time delay compares similarity and synchronicity of PS3 vs.PS4 activity in control condition and during Zd7288 treatment. BXX and PXX represent numbering of experiments according to laboratory book- and respective page number.

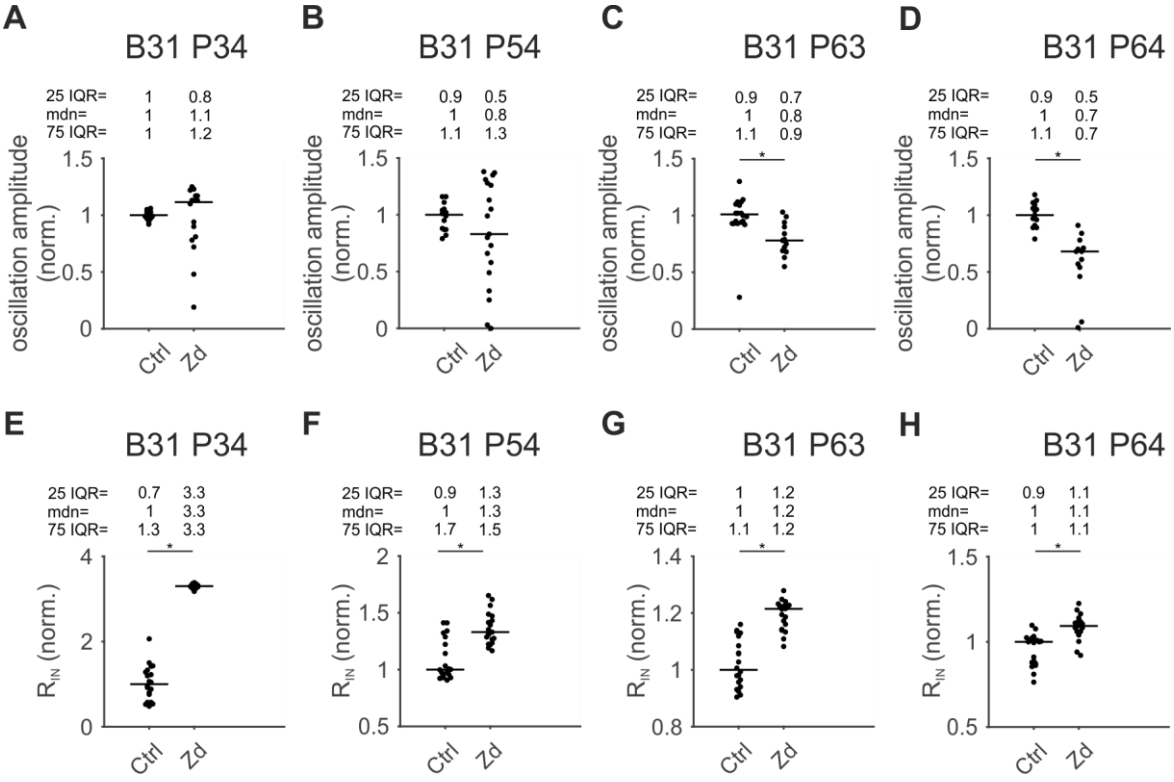

Supplemental Figure 58: Effects of Zd7288 application on oscillation amplitudes and input resistances from single PSE neurons. Normalized oscillation amplitudes and input resistances from single experiments during control condition and during treatment with Zd7288. Horizontal lines represent normalized median values. BXX and PXX represent numbering of experiments according to laboratory book- and respective page number. R_{IN}: input resistance, IQR: interquartile range, mdn: median, Ctrl: control, Zd: Zd7288, *: $p < 0.05$.

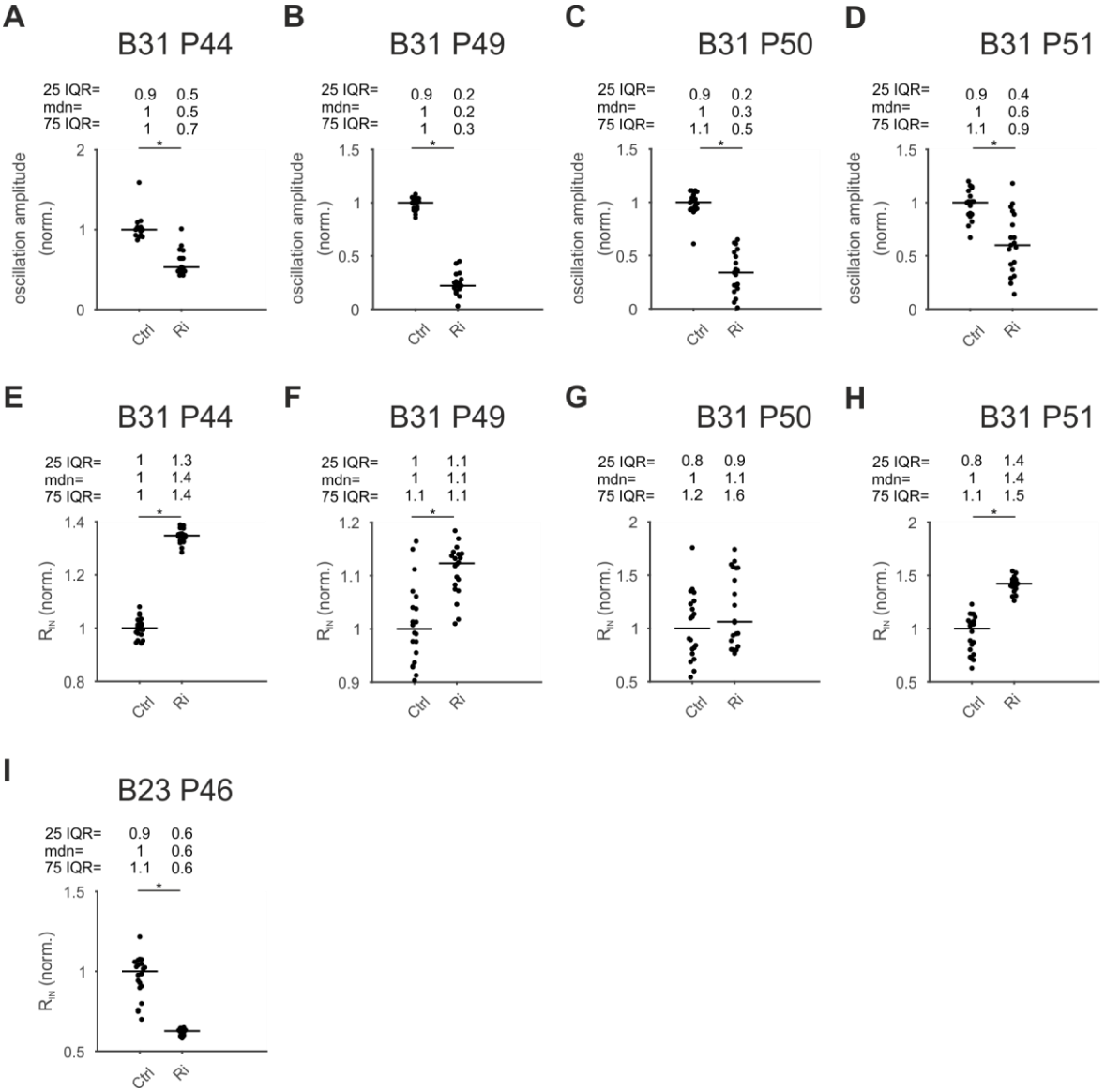

Supplemental Figure 59: Effects of Riluzole application on oscillation amplitudes and input resistances from single PSE neurons. Normalized oscillation amplitudes and input resistances from single experiments during control condition and during treatment with Riluzole. Horizontal lines represent normalized median values. BXX and PXX represent numbering of experiments according to laboratory book- and respective page number. R_{IN}: input resistance, IQR: interquartile range, mdn: median, Ctrl: control, Ri: Riluzole, *: $p < 0.05$.

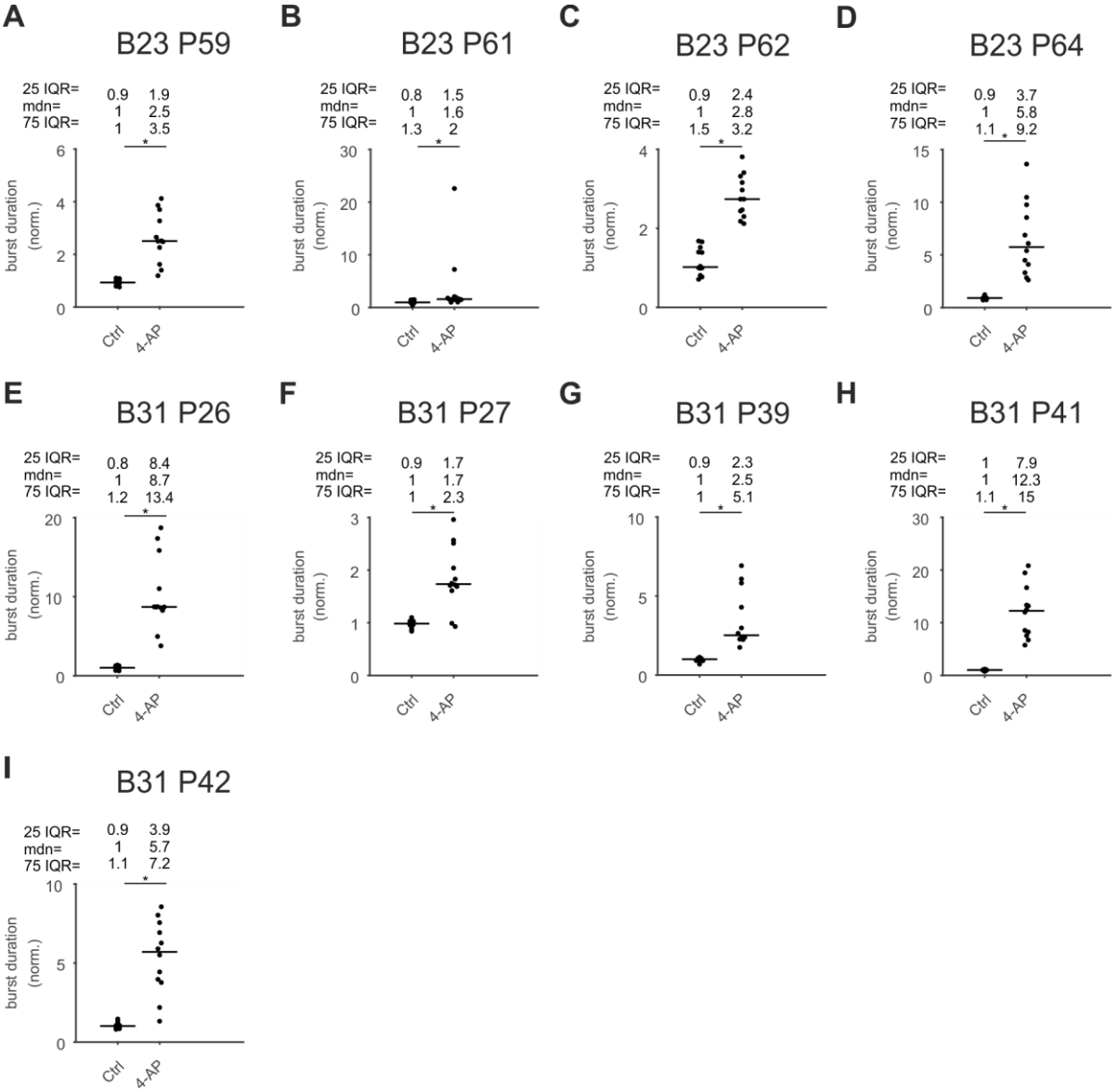

Supplemental Figure 60: Effects of 4-AP application on PS burst durations. Normalized PS burst duration from single experiments during control condition and during treatment with 4-AP. Horizontal lines represent normalized median values. BXX and PXX represent numbering of experiments according to laboratory book- and respective page number. PSE: Power Stroke Exciter, IQR: interquartile range, mdn: median, Ctrl: control, 4-AP: 4-Aminopyridine, *: $p < 0.05$.

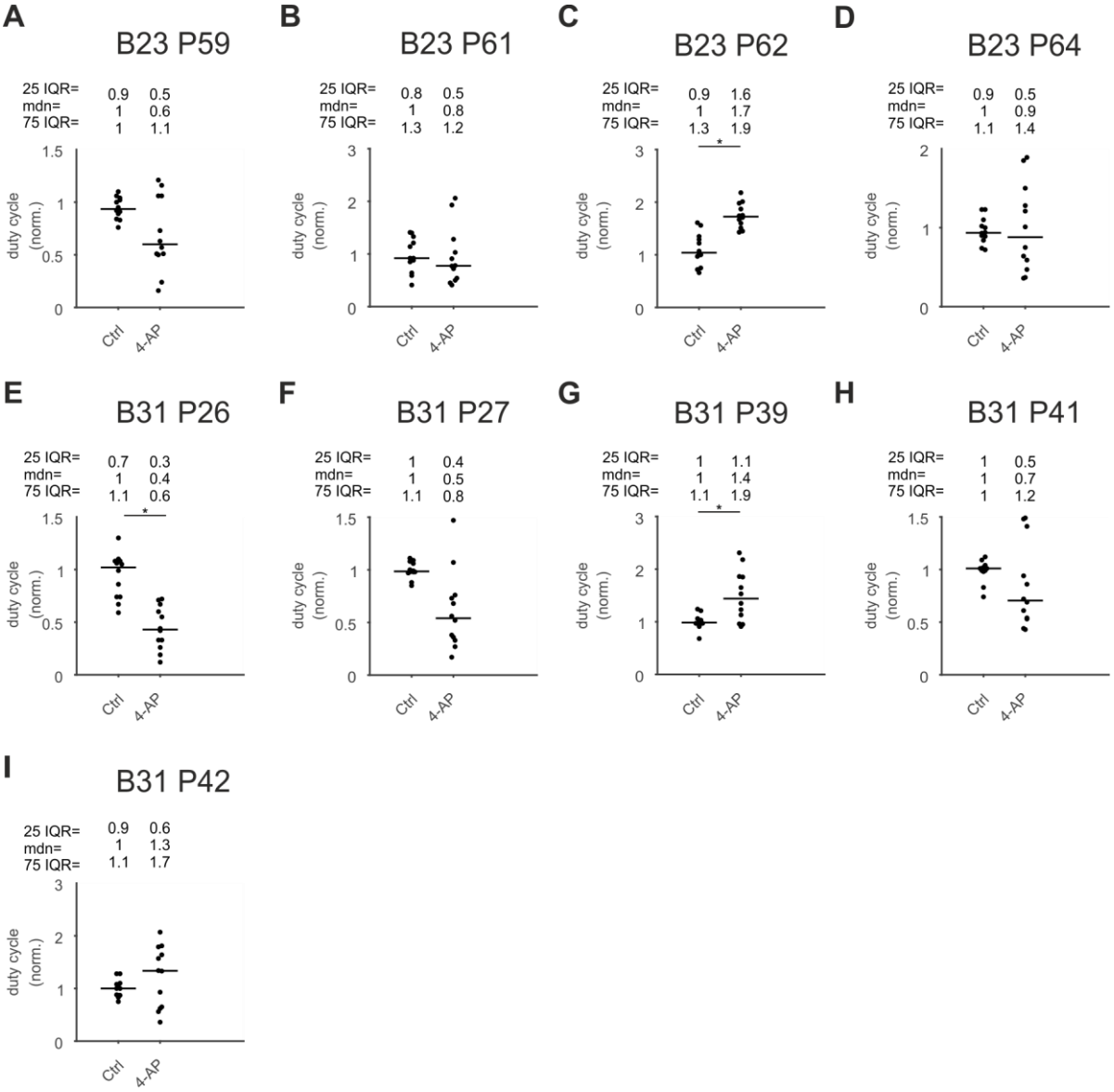

Supplemental Figure 61: Effects of 4-AP application on PS duty cycle. Normalized PS duty cycle from single experiments during control condition and during treatment with 4-AP. Horizontal lines represent normalized median values. BXX and PXX represent numbering of experiments according to laboratory book- and respective page number. PSE: Power Stroke Exciter, IQR: interquartile range, mdn: median, Ctrl: control, 4-AP: 4-Aminopyridine, *: $p < 0.05$.

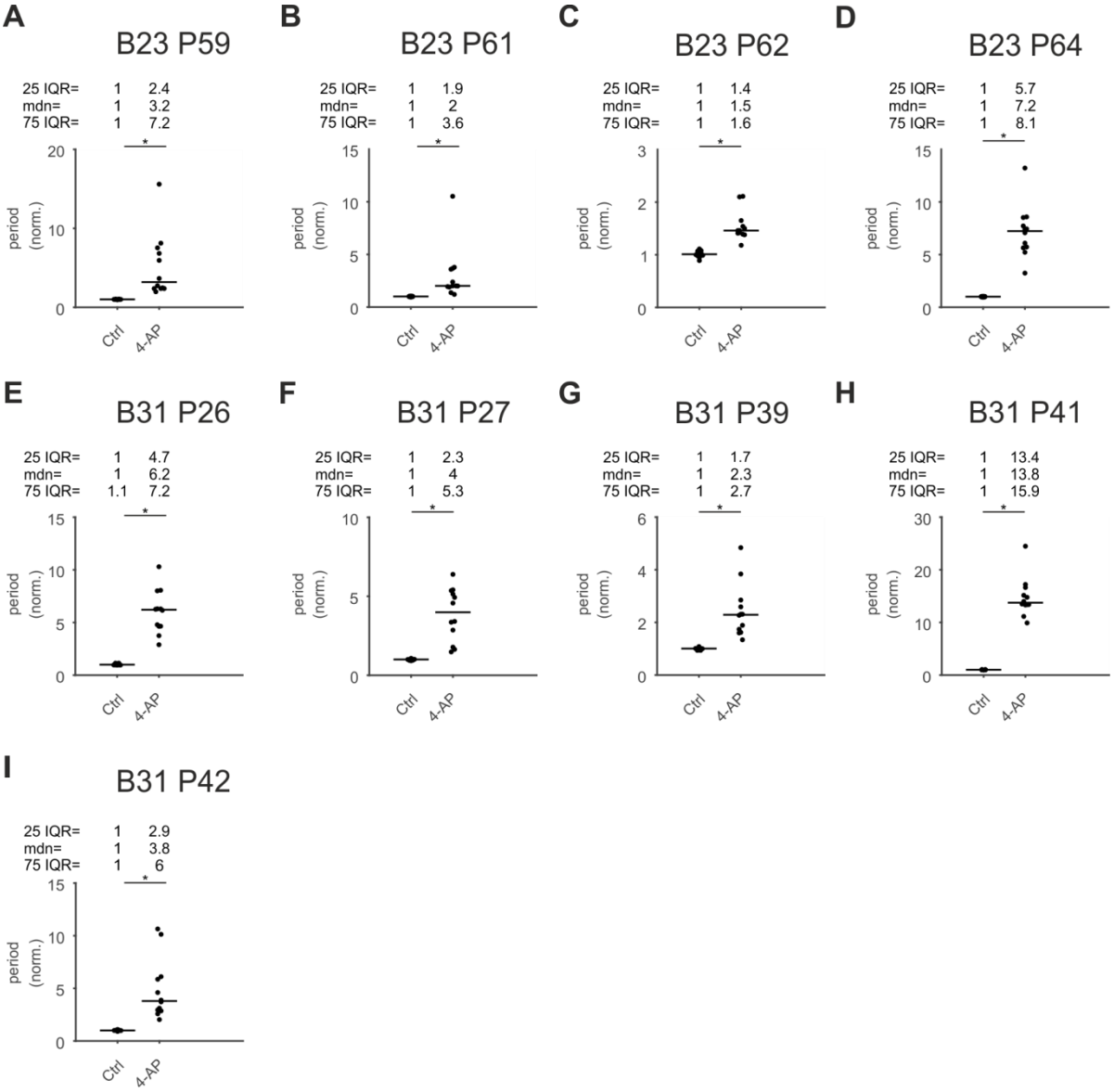

Supplemental Figure 62: Effects of 4-AP application on PS period. Normalized PS period from single experiments during control condition and during treatment with 4-AP. Horizontal lines represent normalized median values. BXX and PXX represent numbering of experiments according to laboratory book- and respective page number. PSE: Power Stroke Exciter, IQR: interquartile range, mdn: median, Ctrl: control, 4-AP: 4-Aminopyridine, *: $p < 0.05$.

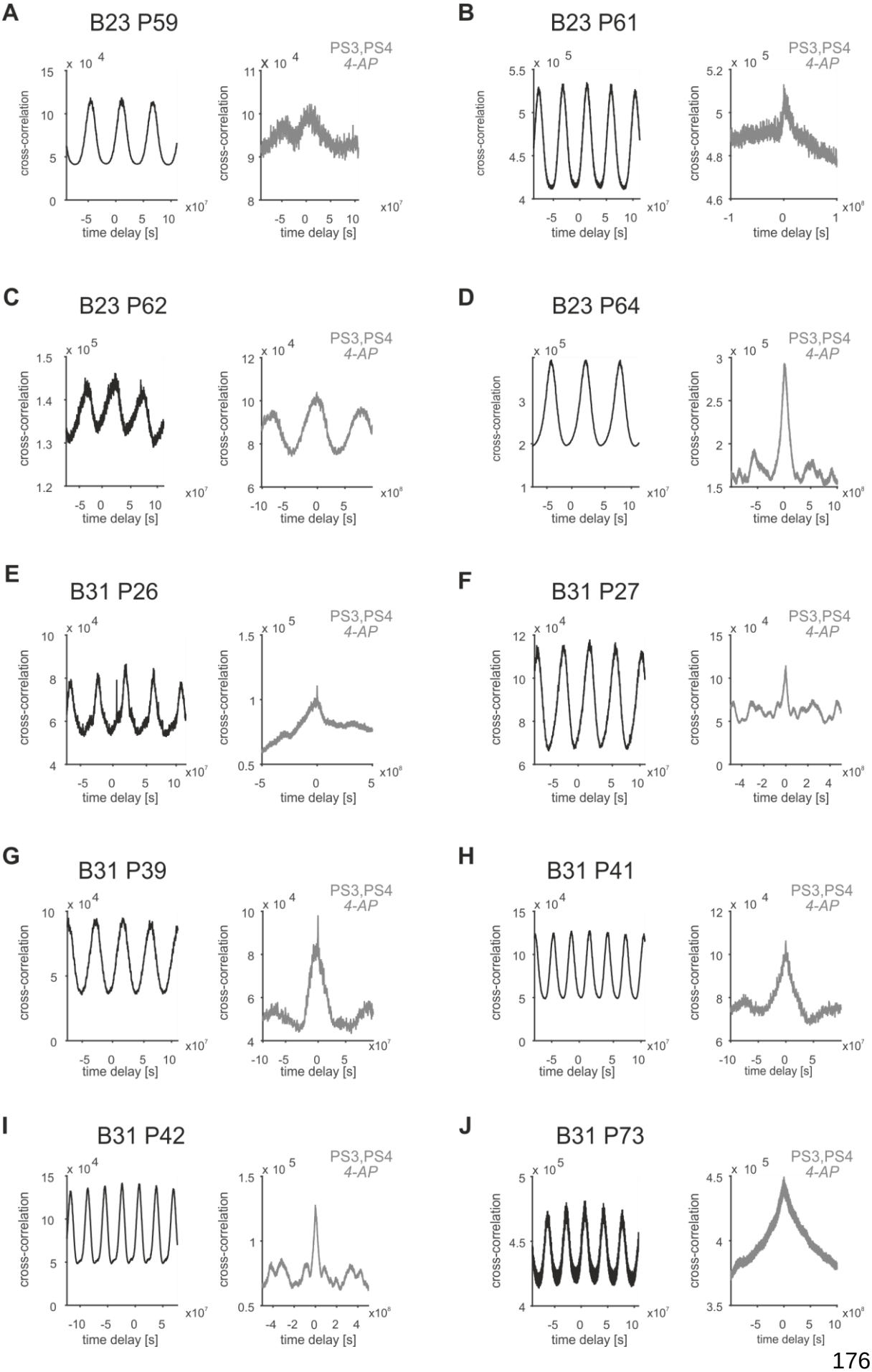
A
B23 P59
PS3,PS4
4-AP
cross-correlation
time delay [s]
B
B23 P61
C
B23 P62
D
B23 P64
E
B31 P26
F
B31 P27
G
B31 P39
H
B31 P41
I
B31 P42
J
B31 P73

Supplemental Figure 63: : Effects of 4-AP application on PS3-PS4 relation. Cross correlation as a function of time delay compares similarity and synchronicity of PS3 vs.PS4 activity in control condition and during 4-AP treatment. BXX and PXX represent numbering of experiments according to laboratory book- and respective page number, 4-AP: 4-Aminopyridine.

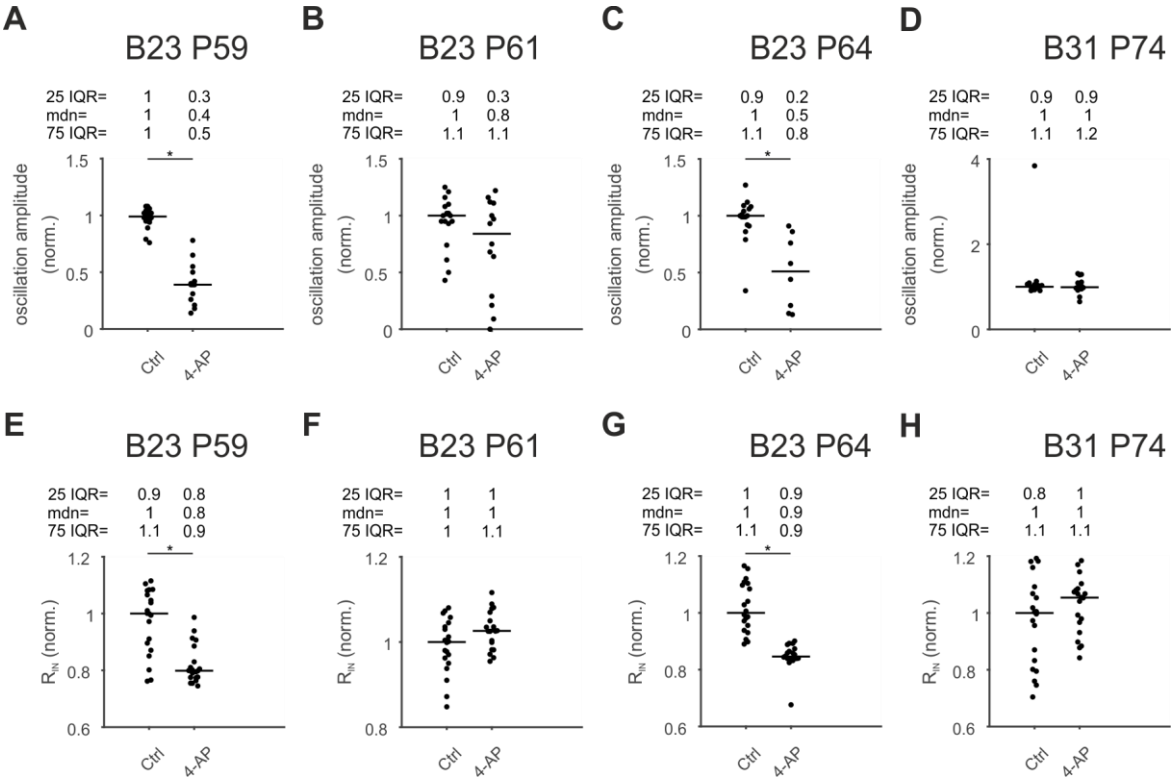

Supplemental Figure 64: Effects of 4-AP application on oscillation amplitudes and input resistances from single PSE neurons. Normalized oscillation amplitudes and input resistances from single experiments during control condition and during treatment with 4-AP. Horizontal lines represent normalized median values. BXX and PXX represent numbering of experiments according to laboratory book- and respective page number. R_{IN}: input resistance, IQR: interquartile range, mdn: median, Ctrl: control, 4-AP: 4-Aminopyridine, *: $p < 0.05$.

6. References

Acevedo, L.D. (1990). Control of the expression of a simple behavior: Activation and inhibition of the crayfish swimmeret rhythm by command neurons and their transmitters. Ph.D. University of California, Davis.

Acevedo, L.D., Hall, W.M., and Mulloney, B. (1994). Proctolin and excitation of the crayfish swimmeret system. J. Comp. Neurol. *345*, 612–627.

Alberts, B., Johnson, A., Lewis, J., Raff, M., Roberts, K., and Walter, P. (2002). Ion Channels and the Electrical Properties of Membranes. Mol. Biol. Cell 4th Ed.

Anderson, P. a. V. (1987). Properties and Pharmacology of a TTX-insensitive Na^+ Current in Neurones of the Jellyfish Cyanea Capillata. J. Exp. Biol. *133*, 231–248.

Andersson, O., Forssberg, H., Grillner, S., and Lindquist, M. (1978). Phasic gain control of the transmission in cutaneous reflex pathways to motoneurones during “fictive” locomotion. Brain Res. *149*, 503–507.

Angelo, K., and Margrie, T.W. (2011). Population diversity and function of hyperpolarization-activated current in olfactory bulb mitral cells. Sci. Rep. *1*, 50.

Angstadt, J.D., and Calabrese, R.L. (1989). A hyperpolarization-activated inward current in heart interneurons of the medicinal leech. J. Neurosci. Off. J. Soc. Neurosci. *9*, 2846–2857.

Angstadt, J.D., and Simone, A.M. (2014). Riluzole suppresses postinhibitory rebound in an excitatory motor neuron of the medicinal leech. J. Comp. Physiol. A *200*, 759–775.

Angstadt, J.D., Grassmann, J.L., Theriault, K.M., and Levasseur, S.M. (2005). Mechanisms of postinhibitory rebound and its modulation by serotonin in excitatory swim motor neurons of the medicinal leech. J. Comp. Physiol. A *191*, 715–732.

Antonucci, D.E., Lim, S.T., Vassanelli, S., and Trimmer, J.S. (2001). Dynamic localization and clustering of dendritic Kv2.1 voltage-dependent potassium channels in developing hippocampal neurons. Neuroscience *108*, 69–81.

Aponte, Y., Lien, C.-C., Reisinger, E., and Jonas, P. (2006). Hyperpolarization-activated cation channels in fast-spiking interneurons of rat hippocampus. J. Physiol. *574*, 229–243.

Armstrong, C.M., and Matteson, D.R. (1985). Two distinct populations of calcium channels in a clonal line of pituitary cells. Science *227*, 65–67.

Armstrong, C.M., Bezanilla, F., and Rojas, E. (1973). Destruction of Sodium Conductance Inactivation in Squid Axons Perfused with Pronase. J. Gen. Physiol. *62*, 375–391.

Ascoli, G.A., Gasparini, S., Medinilla, V., and Migliore, M. (2010). Local Control of Postinhibitory Rebound Spiking in CA1 Pyramidal Neuron Dendrites. J. Neurosci. *30*, 6434–6442.

Athanasiades, A., Clark, J., Fathi, H., and Bidani, A. (2000). An Ionic Current Model for Medullary Respiratory Neurons. J. Comput. Neurosci. *9*, 237–257.

Bacqué-Cazenave, J., Cattaert, D., Delbecque, J.P., and Fossat, P. (2018). Alteration of size perception: serotonin has opposite effects on the aggressiveness of crayfish confronting either a smaller or a larger rival. J. Exp. Biol. *221*, jeb177840.

Barrio, L., Clarac, F., and Buño, W. (1991). TTX sensitive plateau potentials in the crayfish slowly adapting stretch receptor neuron. J. Comp. Physiol. A *168*.

Barzan, R., Pfeiffer, F., and Kukley, M. (2016). N- and L-Type Voltage-Gated Calcium Channels Mediate Fast Calcium Transients in Axonal Shafts of Mouse Peripheral Nerve. Front. Cell. Neurosci. *10*.

Bayliss, D.A., Viana, F., Bellingham, M.C., and Berger, A.J. (1994). Characteristics and postnatal development of a hyperpolarization-activated inward current in rat hypoglossal motoneurons in vitro. J. Neurophysiol. *71*, 119–128.

Beaumont, V., and Zucker, R.S. (2000). Enhancement of synaptic transmission by cyclic AMP modulation of presynaptic I_h channels. Nat. Neurosci. *3*, 133–141.

Beltz, B.S., and Kravitz, E.A. (1983). Mapping of serotonin-like immunoreactivity in the lobster nervous system. J. Neurosci. *3*, 585–602.

Beltz, B.S., and Kravitz, E.A. (1987). Physiological identification, morphological analysis, and development of identified serotonin-proctolin containing neurons in the lobster ventral nerve cord. J. Neurosci. Off. J. Soc. Neurosci. *7*, 533–546.

Benoit, E., and Escande, D. (1991). Riluzole specifically blocks inactivated Na channels in myelinated nerve fibre. Pflügers Arch. Eur. J. Physiol. *419*, 603–609.

Bertrand, S., and Cazalets, J.-R. (1998). Postinhibitory Rebound During Locomotor-Like Activity in Neonatal Rat Motoneurons In Vitro. J. Neurophysiol. *79*, 342–351.

Bhattacharjee, A., and Kaczmarek, L.K. (2005). For K^+ channels, Na^+ is the new Ca^{2+}. Trends Neurosci. *28*, 422–428.

Biel, M. (2010). Chapter 185 - Cyclic Nucleotide-Regulated Cation Channels. In Handbook of Cell Signaling (Second Edition), R.A. Bradshaw, and E.A. Dennis, eds. (San Diego: Academic Press), pp. 1519–1523.

Biggin, P.C., Roosild, T., and Choe, S. (2000). Potassium channel structure: domain by domain. Curr. Opin. Struct. Biol. *10*, 456–461.

Bonci, A., Grillner, P., Mercuri, N.B., and Bernardi, G. (1998). L-Type calcium channels mediate a slow excitatory synaptic transmission in rat midbrain dopaminergic neurons. J. Neurosci. Off. J. Soc. Neurosci. *18*, 6693–6703.

Borgmann, A., Scharstein, H., and Büschges, A. (2007). Intersegmental coordination: influence of a single walking leg on the neighboring segments in the stick insect walking system. J. Neurophysiol. *98*, 1685–1696.

Borgmann, A., Toth, T.I., Gruhn, M., Daun-Gruhn, S., and Büschges, A. (2012). Dominance of local sensory signals over inter-segmental effects in a motor system: experiments. Biol. Cybern.

Branch, S.Y., Sharma, R., and Beckstead, M.J. (2014). Aging Decreases L-Type Calcium Channel Currents and Pacemaker Firing Fidelity in Substantia Nigra Dopamine Neurons. J. Neurosci. *34*, 9310–9318.

Brodfuehrer, P.D., Debski, E.A., O'Gara, B.A., and Friesen, W.O. (1995). Neuronal control of leech swimming. J. Neurobiol. *27*, 403–418.

Bucher, D. (2009). Central Pattern Generators. In Encyclopedia of Neuroscience, L.R. Squire, ed. (Oxford: Academic Press), pp. 691–700.

Büschges, A. (2012). Lessons for circuit function from large insects: towards understanding the neural basis of motor flexibility. Curr. Opin. Neurobiol. *22*, 602–608.

Büschges, A., and Gruhn, M. (2007). Mechanosensory Feedback in Walking: From Joint Control to Locomotor Patterns. In Advances in Insect Physiology, J. Casas and S. J. Simpson, ed. (Academic Press), pp. 193–230.

Büschges, A., Schmitz, J., and Bässler, U. (1995). Rhythmic patterns in the thoracic nerve cord of the stick insect induced by pilocarpine. J. Exp. Biol. *198*, 435–456.

Calabrese, R.L., Nadim, F., and Olsen, O.H. (1995). Heartbeat control in the medicinal leech: a model system for understanding the origin, coordination, and modulation of rhythmic motor patterns. J. Neurobiol. *27*, 390–402.

Cattaert, D., and Clarac, F. (1987). Rami motor neurons and motor control of the swimmeret system of *Homarus gammarus*. J. Comp. Physiol. A *160*, 55–68.

Catterall, W.A. (1992). Cellular and molecular biology of voltage-gated sodium channels. Physiol. Rev. *72*, S15-48.

Catterall, W.A. (2011). Voltage-Gated Calcium Channels. Cold Spring Harb. Perspect. Biol. *3*, a003947.

Cheng, L., Kinard, K., Rajamani, R., and Sanguinetti, M.C. (2007). Molecular Mapping of the Binding Site for a Blocker of Hyperpolarization-Activated, Cyclic Nucleotide-Modulated Pacemaker Channels. J. Pharmacol. Exp. Ther. *322*, 931–939.

Chrachri, A. (1995). Ionic currents in identified swimmeret motor neurones of the crayfish Pacifastacus leniusculus. J. Exp. Biol. *198*, 1483–1492.

Cohen, A.H., and Wallén, P. (1980). The neuronal correlate of locomotion in fish. "Fictive swimming" induced in an in vitro preparation of the lamprey spinal cord. Exp. Brain Res. *41*, 11–18.

Cohen, A.H., Ermentrout, G.B., Kiemel, T., Kopell, N., Sigvardt, K.A., and Williams, T.L. (1992). Modelling of intersegmental coordination in the lamprey central pattern generator for locomotion. Trends Neurosci. *15*, 434–438.

Conway, B.A., Hultborn, H., and Kiehn, O. (1987). Proprioceptive input resets central locomotor rhythm in the spinal cat. Exp. Brain Res. *68*, 643–656.

Crill, W.E. (1996). Persistent Sodium Current in Mammalian Central Neurons. Annu. Rev. Physiol. *58*, 349–362.

Dale, N. (1986). Excitatory Synaptic Drive for Swimming Mediated by Amino Acid Receptors in the Lamprey. J. Neurosci. *6*, 14.

Daun, S., Rubin, J.E., and Rybak, I.A. (2009). Control of oscillation periods and phase durations in half-center central pattern generators: a comparative mechanistic analysis. J. Comput. Neurosci. *27*, 3–36.

Daur, N., Nadim, F., and Bucher, D. (2016). The complexity of small circuits: the stomatogastric nervous system. Curr. Opin. Neurobiol. *41*, 1–7.

Davis, W.J. (1971). Functional significance of motorneuron size and soma position in swimmeret system of the lobster. J. Neurophysiol. *34*, 274–288.

Del Negro, C.A., Morgado-Valle, C., and Feldman, J.L. (2002). Respiratory rhythm: an emergent network property? Neuron *34*, 821–830.

Dubuc, R., Rossignol S. (1989). The effects of 4-aminopyridine on the cat spinal cord: rhythmic antidromic discharges recorded from the dorsal roots. Brain Research. 491: 335-48.

Eaholtz, G., Scheuer, T., and Catterall, W.A. (1994). Restoration of inactivation and block of open sodium channels by an inactivation gate peptide. Neuron *12*, 1041–1048.

Edman, A., Gestrelius, S., and Grampp, W. (1987). Current activation by membrane hyperpolarization in the slowly adapting lobster stretch receptor neurone. J. Physiol. *384*, 671–690.

Elliott, A.A., and Elliott, J.R. (1993). Characterization of TTX-sensitive and TTX-resistant sodium currents in small cells from adult rat dorsal root ganglia. J. Physiol. *463*, 39–56.

Fan, Y.-P., Horn, E.M., and Waldrop, T.G. (2000). Biophysical Characterization of Rat Caudal Hypothalamic Neurons: Calcium Channel Contribution to Excitability. J. Neurophysiol. *84*, 2896–2903.

Ferrus, A., LLamazares, S., de la Pompa, J.L., Tanouye, M.A., and Pongs, O. (1990). Genetic Analysis of the Shaker Gene Complex of Drosophila Melanogaster. Genetics *125*, 383–398.

Flamm, R.E., and Harris-Warrick, R.M. (1986). Aminergic modulation in lobster stomatogastric ganglion. I. Effects on motor pattern and activity of neurons within the pyloric circuit. J. Neurophysiol. *55*, 847–865.

Flamm, R.E., and Harris-Warrick, R.M. (1986b). Aminergic modulation in lobster stomatogastric ganglion. II. Target neurons of dopamine, octopamine, and serotonin within the pyloric circuit. J. Neurophysiol. *55*, 866–881.

Fossat, P., Bacqué-Cazenave, J., De Deurwaerdère, P., Cattaert, D., and Delbecque, J.-P. (2015). Serotonin, but not dopamine, controls the stress response and anxiety-like behavior in the crayfish Procambarus clarkii. J. Exp. Biol. *218*, 2745–2752.

Friesen, W.O. (1989). Neuronal control of leech swimming movements. J. Comp. Physiol. A *166*, 205–215.

Friesen, W.O. (1994). Reciprocal inhibition: a mechanism underlying oscillatory animal movements. Neurosci. Biobehav. Rev. *18*, 547–553.

Gauss, R., Seifert, R., and Kaupp, U.B. (1998). Molecular identification of a hyperpolarization-activated channel in sea urchin sperm. Nature *393*, 583–587.

Gerard, E., Hochstrate, P., Dierkes, P.-W., and Coulon, P. (2012). Functional properties and cell type specific distribution of Ih channels in leech neurons. J. Exp. Biol. *215*, 227–238.

Getting, P.A. (1989). Emerging Principles Governing the Operation of Neural Networks. Annu. Rev. Neurosci. *12*, 185–204.

Getting, P., R Lennard, P., and Hume, R. (1980). Central pattern generator mediating swimming in Tritonia. I. Identification and synaptic interactions. J. Neurophysiol. *44*, 151–164.

Gilly, W.F., Gillette, R., and McFarlane, M. (1997). Fast and slow activation kinetics of voltage-gated sodium channels in molluscan neurons. J. Neurophysiol. *77*, 2373–2384.

Goaillard, J.-M., Taylor, A.L., Schulz, D.J., and Marder, E. (2009). Functional consequences of animal-to-animal variation in circuit parameters. Nat. Neurosci. *12*, 1424–1430.

Goeritz, M.L., Ouyang, Q., and Harris-Warrick, R.M. (2011). Localization and function of Ih channels in a small neural network. J. Neurophysiol. *106*, 44–58.

Goldman, M.S., Golowasch, J., Marder, E., and Abbott, L.F. (2001). Global Structure, Robustness, and Modulation of Neuronal Models. J. Neurosci. *21*, 5229–5238.

Golowasch, J., Buchholtz, F., Epstein, I.R., and Marder, E. (1992). Contribution of individual ionic currents to activity of a model stomatogastric ganglion neuron. J. Neurophysiol. *67*, 341–349.

Grillner, S. (2003). The motor infrastructure: from ion channels to neuronal networks. Nat. Rev. Neurosci. *4*, 573–586.

Guan, L., Kiemel, T., and Cohen, A.H. (2001). Impact of movement and movement-related feedback on the lamprey central pattern generator for locomotion. J. Exp. Biol. *204*, 2361–2370.

Harnett, M.T., Magee, J.C., and Williams, S.R. (2015). Distribution and Function of HCN Channels in the Apical Dendritic Tuft of Neocortical Pyramidal Neurons. J. Neurosci. *35*, 1024–1037.

Harris-Warrick, R.M., Marder, E., Selverston, A.I., and Moulins, M. (1992). Dynamic Biological Networks: The Stomatogastric Nervous System (MIT Press).

Harris-Warrick, R.M., Coniglio, L.M., Levini, R.M., Gueron, S., and Guckenheimer, J. (1995a). Dopamine modulation of two subthreshold currents produces phase shifts in activity of an identified motoneuron. J. Neurophysiol. *74*, 1404–1420.

Harris-Warrick, R.M., Coniglio, L.M., Barazangi, N., Guckenheimer, J., and Gueron, S. (1995b). Dopamine modulation of transient potassium current evokes phase shifts in a central pattern generator network. J. Neurosci. *15*, 342–358.

Hartline, D.K., and Gassie, D.V. (1979). Pattern generation in the lobster (Panulirus) stomatogastric ganglion. I. Pyloric neuron kinetics and synaptic interactions. Biol. Cybern. *33*, 209–222.

Harvey, P.J., Li, Y., Li, X., and Bennett, D.J. (2006). Persistent Sodium Currents and Repetitive Firing in Motoneurons of the Sacrocaudal Spinal Cord of Adult Rats. J. Neurophysiol. *96*, 1141–1157.

Hayes, J.A., Mendenhall, J.L., Brush, B.R., and Del Negro, C.A. (2008). 4-Aminopyridine-sensitive outward currents in preBötzinger complex neurons influence respiratory rhythm generation in neonatal mice. J. Physiol. *586*, 1921–1936.

Heitler, W.J. (1978). Coupled motoneurones are part of the crayfish swimmeret central oscillator. Nature *275*, 231.

Heitler, W.J., and Pearson, K.G. (1980). Non-spiking interactions and local interneurones in the central pattern generator of the crayfish swimmeret system. Brain Res. *187*, 206–211.

Hille, B. (1992). Axons, ions, and dons. Science *258*, 144–145.

Hille, B. (2001). Ion Channels of Excitable Membranes.

Hodgkin, A.L., and Huxley, A.F. (1952). A quantitative description of membrane current and its application to conduction and excitation in nerve. J. Physiol. *117*, 500–544.

Hoffman, D.A., Magee, J.C., Colbert, C.M., and Johnston, D. (1997). K^+ channel regulation of signal propagation in dendrites of hippocampal pyramidal neurons. Nature *387*, 869–875.

Hughes, G.M., and Wiersma, C. a G. (1960). The Co-ordination of Swimmeret Movements in the Crayfish, Procambarus Clarkii (Girard). J. Exp. Biol. *37*, 657–670.

Ikeda, K., and Wiersma, C.A.G. (1964). Autogenic rhythmicity in the abdominal ganglia of the crayfish: The control of swimmeret movements. Comp. Biochem. Physiol. *12*, 107–115.

Izhikevich, E.M. (2007). Dynamical systems in neuroscience: the geometry of excitability and bursting (Cambridge, Mass: MIT Press).

Johnson, S.M., and Getting, P.A. (1991). Electrophysiological properties of neurons within the nucleus ambiguus of adult guinea pigs. J. Neurophysiol. *66*, 744–761.

Johnston, R.M., and Levine, R.B. (1996). Crawling motor patterns induced by pilocarpine in isolated larval nerve cords of Manduca sexta. J. Neurophysiol. *76*, 3178–3195.

Jones, S.R., Mulloney, B., Kaper, T.J., and Kopell, N. (2003). Coordination of cellular pattern-generating circuits that control limb movements: the sources of stable differences in intersegmental phases. J. Neurosci. Off. J. Soc. Neurosci. *23*, 3457–3468.

Kass, J.I., and Mintz, I.M. (2006). Silent plateau potentials, rhythmic bursts, and pacemaker firing: Three patterns of activity that coexist in quadristable subthalamic neurons. Proc. Natl. Acad. Sci. *103*, 183–188.

Kaupp, U.B., and Seifert, R. (2001). Molecular Diversity of Pacemaker Ion Channels. Annu. Rev. Physiol. *63*, 235–257.

Kay, A.R., Sugimori, M., and Llinás, R. (1998). Kinetic and Stochastic Properties of a Persistent Sodium Current in Mature Guinea Pig Cerebellar Purkinje Cells. J. Neurophysiol. *80*, 1167–1179.

Kiehn, O., and Harris-Warrick, R.M. (1992). 5-HT modulation of hyperpolarization-activated inward current and calcium-dependent outward current in a crustacean motor neuron. J. Neurophysiol. *68*, 496–508.

Kim, J., Wei, D.-S., and Hoffman, D.A. (2005). Kv4 potassium channel subunits control action potential repolarization and frequency-dependent broadening in rat hippocampal CA1 pyramidal neurones. J. Physiol. *569*, 41–57.

Kiss, T. (2003). Evidence for a persistent Na-conductance in identified command neurones of the snail, Helix pomatia. Brain Res. *989*, 16–25.

Kiss, T., László, Z., and Szabadics, J. (2002). Mechanism of 4-aminopyridine block of the transient outward K-current in identified Helix neuron. Brain Res. *927*, 168–179.

Kristan, W.B., and Calabrese, R.L. (1976). Rhythmic swimming activity in neurones of the isolated nerve cord of the leech. J. Exp. Biol. *65*, 643–668.

Li, W.-C., and Moult, P.R. (2012). The control of locomotor frequency by excitation and inhibition. J. Neurosci. Off. J. Soc. Neurosci. *32*, 6220–6230.

Li, X.-T., Li, X.-Q., Hu, X.-M., and Qiu, X.-Y. (2015). The Inhibitory Effects of Ca^{2+} Channel Blocker Nifedipine on Rat Kv2.1 Potassium Channels. PloS One *10*, e0124602.

Lipkind, G.M., and Fozzard, H.A. (1994). A structural model of the tetrodotoxin and saxitoxin binding site of the Na+ channel. Biophys. J. *66*, 1–13.

Ludwig, A., Zong, X., Jeglitsch, M., Hofmann, F., and Biel, M. (1998). A family of hyperpolarization-activated mammalian cation channels. Nature *393*, 587–591.

Maccaferri, G., and McBain, C.J. (1996). The hyperpolarization-activated current (Ih) and its contribution to pacemaker activity in rat CA1 hippocampal stratum oriens-alveus interneurones. J. Physiol. *497*, 119–130.

MacLean, J.N., Zhang, Y., Johnson, B.R., and Harris-Warrick, R.M. (2003). Activity-independent homeostasis in rhythmically active neurons. Neuron *37*, 109–120.

Macmillan, D.L., and Kien, J. (1983). Intra- And Intersegmental Pathways Active during Walking in the Locust. Proc. R. Soc. Lond. B Biol. Sci. *218*, 287–308.

Magee, J.C., and Johnston, D. (1995). Characterization of single voltage-gated Na^{+} and Ca^{2+} channels in apical dendrites of rat CA1 pyramidal neurons. J. Physiol. *487*, 67–90.

el Manira, A., Tegnér, J., and Grillner, S. (1994). Calcium-dependent potassium channels play a critical role for burst termination in the locomotor network in lamprey. J. Neurophysiol. *72*, 1852–1861.

Mantziaris, C., Bockemühl, T., Holmes, P., Borgmann, A., Daun, S., and Büschges, A. (2017). Intra- and intersegmental influences among central pattern generating networks in the walking system of the stick insect. J. Neurophysiol. *118*, 2296–2310.

Marban, E., Yamagishi, T., and Tomaselli, G.F. (1998). Structure and function of voltage-gated sodium channels. J. Physiol. *508*, 647–657.

Marder, E., and Calabrese, R.L. (1996). Principles of rhythmic motor pattern generation. Physiol. Rev. *76*, 687–717.

Marder, E., and Prinz, A.A. (2002). Modeling stability in neuron and network function: the role of activity in homeostasis. BioEssays News Rev. Mol. Cell. Dev. Biol. *24*, 1145–1154.

Marder, E., Bucher, D., Schulz, D.J., and Taylor, A.L. (2005). Invertebrate Central Pattern Generation Moves along. Curr. Biol. *15*, R685–R699.

Matsumoto-Makidono, Y., Nakayama, H., Yamasaki, M., Miyazaki, T., Kobayashi, K., Watanabe, M., Kano, M., Sakimura, K., and Hashimoto, K. (2016). Ionic Basis for Membrane Potential Resonance in Neurons of the Inferior Olive. Cell Rep. *16*, 994–1004.

Matsushima, T., and Grillner, S. (1992). Neural mechanisms of intersegmental coordination in lamprey: local excitability changes modify the phase coupling along the spinal cord. J. Neurophysiol. *67*, 373–388.

Matsushima, T., Tegner, J., Hill, R.H., and Grillner, S. (1993). $GABA_B$ receptor activation causes a depression of low- and high-voltage-activated Ca^{2+} currents, postinhibitory rebound, and postspike afterhyperpolarization in lamprey neurons. J. Neurophysiol. *70*, 2606–2619.

McCormick, D.A., and Pape, H.C. (1990). Properties of a hyperpolarization-activated cation current and its role in rhythmic oscillation in thalamic relay neurones. J. Physiol. *431*, 291–318.

Mellon, D. (2016). Electrophysiological Evidence for Intrinsic Pacemaker Currents in Crayfish Parasol Cells. PLoS ONE *11*.

Mellor, J., Nicoll, R.A., and Schmitz, D. (2002). Mediation of hippocampal mossy fiber long-term potentiation by presynaptic Ih channels. Science *295*, 143–147.

Miles, G.B., Dai, Y., and Brownstone, R.M. (2005). Mechanisms underlying the early phase of spike frequency adaptation in mouse spinal motoneurones. J. Physiol. *566*, 519–532.

Morisset, V., and Nagy, F. (1999). Ionic Basis for Plateau Potentials in Deep Dorsal Horn Neurons of the Rat Spinal Cord. J. Neurosci. *19*, 7309–7316.

Mulloney, B. (2003). During Fictive Locomotion, Graded Synaptic Currents Drive Bursts of Impulses in Swimmeret Motor Neurons. J. Neurosci. *23*, 5953–5962.

Mulloney, B., and Hall, W.M. (2000). Functional organization of crayfish abdominal ganglia. III. Swimmeret motor neurons. J. Comp. Neurol. *419*, 233–243.

Mulloney, B., and Hall, W.M. (2003). Local commissural interneurons integrate information from intersegmental coordinating interneurons. J. Comp. Neurol. *466*, 366–376.

Mulloney, B., Tschuluun, N., and Hall, W.M. (2003). Architectonics of crayfish ganglia. Microsc. Res. Tech. *60*, 253–265.

Mulloney, B., Harness, P.I., and Hall, W.M. (2006). Bursts of information: coordinating interneurons encode multiple parameters of a periodic motor pattern. J. Neurophysiol. *95*, 850–861.

Mulloney, B., and Smarandache-Wellmann, C. (2012). Neurobiology of the crustacean swimmeret system. Prog. Neurobiol. *96*, 242–267.

Murchison, D., Chrachri, A., and Mulloney, B. (1993). A separate local pattern-generating circuit controls the movements of each swimmeret in crayfish. J. Neurophysiol. *70*, 2620–2631.

Namba, H., and Mulloney, B. (1999). Coordination of limb movements: three types of intersegmental interneurons in the swimmeret system and their responses to changes in excitation. J. Neurophysiol. *81*, 2437–2450.

Opdyke, C.A., and Calabrese, R.L. (1994). A persistent sodium current contributes to oscillatory activity in heart interneurons of the medicinal leech. J. Comp. Physiol. A *175*.

O'Regan, M.H., Kocsis, J.D., and Waxman, S.G. (1991). Nimodipine and nifedipine enhance transmission at the Schaffer collateral CA1 pyramidal neuron synapse. Exp. Brain Res. *84*, 224–228.

Pape, H.C. (1996). Queer current and pacemaker: the hyperpolarization-activated cation current in neurons. Annu. Rev. Physiol. *58*, 299–327.

Paul, D.H., and Mulloney, B. (1985a). Local interneurons in the swimmeret system of the crayfish. J. Comp. Physiol. A *156*, 489–502.

Paul, D.H., and Mulloney, B. (1985b). Nonspiking local interneuron in the motor pattern generator for the crayfish swimmeret. J. Neurophysiol. *54*, 28–39.

Peña, F., Parkis, M.A., Tryba, A.K., and Ramirez, J.-M. (2004). Differential contribution of pacemaker properties to the generation of respiratory rhythms during normoxia and hypoxia. Neuron *43*, 105–117.

Peron, S.P., and Gabbiani, F. (2009). Role of spike-frequency adaptation in shaping neuronal response to dynamic stimuli. Biol. Cybern. *100*, 505–520.

Pirtle, T.J., and Satterlie, R.A. (2004). Cellular Mechanisms Underlying Swim Acceleration in the Pteropod Mollusk Clione limacina. Integr. Comp. Biol. *44*, 37–46.

Powers, R.K., Sawczuk, A., Musick, J.R., and Binder, M.D. (1999). Multiple mechanisms of spike-frequency adaptation in motoneurones. J. Physiol.-Paris *93*, 101–114.

Prinz, A.A., Bucher, D., and Marder, E. (2004). Similar network activity from disparate circuit parameters. Nat. Neurosci. *7*, 1345–1352.

Ramirez, J.M., and Pearson, K.G. (1993). Alteration of bursting properties in interneurons during locust flight. J. Neurophysiol. *70*, 2148–2160.

Rathmayer, W., Erxleben, C., Djokaj, S., Gaydukov, A., Kreissl, S., and Weiss, T. (2002). Antagonistic Modulation of Neuromuscular Parameters in Crustaceans by the Peptides Proctolin and Allatostatin, Contained in Identified Motor Neurons. pp. 2–19.

Rodgers, E.W., Fu, J.J., Krenz, W.-D.C., and Baro, D.J. (2011). Tonic Nanomolar Dopamine Enables an Activity-Dependent Phase Recovery Mechanism That Persistently Alters the Maximal Conductance of the Hyperpolarization-Activated Current in a Rhythmically Active Neuron. J. Neurosci. *31*, 16387–16397.

Roy, M.L., and Narahashi, T. (1992). Differential properties of tetrodotoxin-sensitive and tetrodotoxin-resistant sodium channels in rat dorsal root ganglion neurons. J. Neurosci. Off. J. Soc. Neurosci. *12*, 2104–2111.

Sah, P. (1996). $Ca(^{2+})$-activated K^+ currents in neurones: types, physiological roles and modulation. Trends Neurosci. *19*, 150–154.

Sakurai, A., and Katz, P.S. (2009). State-, timing-, and pattern-dependent neuromodulation of synaptic strength by a serotonergic interneuron. J. Neurosci. Off. J. Soc. Neurosci. *29*, 268–279.

Salkoff, L., Baker, K., Butler, A., Covarrubias, M., Pak, M.D., and Wei, A. (1992). An essential 'set' of K^+ channels conserved in flies, mice and humans. Trends Neurosci. *15*, 161–166.

Satterlie, R.A. (1985). Reciprocal inhibition and postinhibitory rebound produce reverberation in a locomotor pattern generator. Science *229*, 402–404.

Sawczuk, A., Powers, R.K., and Binder, M.D. (1997). Contribution of Outward Currents to Spike-Frequency Adaptation in Hypoglossal Motoneurons of the Rat. J. Neurophysiol. *78*, 2246–2253.

Schneider, A.C. (2017). Encoding of Coordinating Information in a Network of Coupled Oscillators. text.thesis.doctoral. Universität zu Köln.

Schneider, A.C., Seichter, H.A., Neupert, S., Hochhaus, A.M., and Smarandache-Wellmann, C.R. (2018). Profiling neurotransmitters in a crustacean neural circuit for locomotion. PloS One *13*, e0197781.

Schneider, B. (2017) Der Effekt von PTX, Tubocurarin & DL-AP5 auf das abdominale Nervensystem von Flusskrebsen. Bachelor Thesis, University of Cologne

Schreiber, M., and Salkoff, L. (1997). A novel calcium-sensing domain in the BK channel. Biophys. J. *73*, 1355–1363.

Seichter, H.A., Blumenthal, F., and Smarandache-Wellmann, C.R. (2014). The Swimmeret System of Crayfish: A Practical Guide for the Dissection of the Nerve Cord and Extracellular Recordings of the Motor Pattern. J. Vis. Exp.

Serrano, E.E., and Getting, P.A. (1989). Diversity of the transient outward potassium current in somata of identified molluscan neurons. J. Neurosci. Off. J. Soc. Neurosci. *9*, 4021–4032.

Shay, C.F., Ferrante, M., Chapman, G.W., and Hasselmo, M.E. (2016). Rebound spiking in layer II medial entorhinal cortex stellate cells: Possible mechanism of grid cell function. Neurobiol. Learn. Mem. *129*, 83–98.

Sherff, C.M., and Mulloney, B. (1996). Tests of the motor neuron model of the local pattern-generating circuits in the swimmeret system. J. Neurosci. *16*, 2839–2859.

Sherff, C.M., and Mulloney, B. (1997). Passive Properties of Swimmeret Motor Neurons. J. Neurophysiol. *78*, 92–102.

Simms, B.A., and Zamponi, G.W. (2014). Neuronal Voltage-Gated Calcium Channels: Structure, Function, and Dysfunction. Neuron *82*, 24–45.

Simon, M., Perrier, J.-F., and Hounsgaard, J. (2003). Subcellular distribution of L-type Ca^{2+} channels responsible for plateau potentials in motoneurons from the lumbar spinal cord of the turtle. Eur. J. Neurosci. *18*, 258–266.

Skinner, F.K., and Mulloney, B. (1998). Intersegmental Coordination of Limb Movements during Locomotion: Mathematical Models Predict Circuits That Drive Swimmeret Beating. J. Neurosci. *18*, 3831–3842.

Skinner, F.K., Kopell, N., and Marder, E. (1994). Mechanisms for oscillation and frequency control in reciprocally inhibitory model neural networks. J. Comput. Neurosci. *1*, 69–87.

Smarandache, C., Hall, W.M., and Mulloney, B. (2009). Coordination of rhythmic motor activity by gradients of synaptic strength in a neural circuit that couples modular neural oscillators. J. Neurosci. Off. J. Soc. Neurosci. *29*, 9351–9360.

Smarandache-Wellmann, C., and Grätsch, S. (2014). Mechanisms of Coordination in Distributed Neural Circuits: Encoding Coordinating Information. J. Neurosci. *34*, 5627–5639.

Smarandache-Wellmann, C., Weller, C., Wright, T.M., and Mulloney, B. (2013). Five types of nonspiking interneurons in local pattern-generating circuits of the crayfish swimmeret system. J. Neurophysiol. *110*, 344–357.

Smarandache-Wellmann, C., Weller, C., and Mulloney, B. (2014). Mechanisms of coordination in distributed neural circuits: decoding and integration of coordinating information. J. Neurosci. Off. J. Soc. Neurosci. *34*, 793–803.

Snutch, T.P., Peloquin, J., Mathews, E., and McRory, J.E. (2013). Molecular Properties of Voltage-Gated Calcium Channels (Landes Bioscience).

Song, S.C., Beatty, J.A., and Wilson, C.J. (2016). The ionic mechanism of membrane potential oscillations and membrane resonance in striatal LTS interneurons. J. Neurophysiol. *116*, 1752–1764.

Soofi, W., Archila, S., and Prinz, A.A. (2012). Co-variation of ionic conductances supports phase maintenance in stomatogastric neurons. J. Comput. Neurosci. *33*, 77–95.

Spardy, L.E., and Lewis, T.J. (2018). The role of long-range coupling in crayfish swimmeret phase-locking. Biol. Cybern.

Stein, P.S.G. (2008). Motor pattern deletions and modular organization of turtle spinal cord. Brain Res. Rev. *57*, 118–124.

Storch, V., and Welsch, U. (2014). Kükenthal - Zoologisches Praktikum (Springer-Verlag).

Stühmer, W., Conti, F., Suzuki, H., Wang, X.D., Noda, M., Yahagi, N., Kubo, H., and Numa, S. (1989). Structural parts involved in activation and inactivation of the sodium channel. Nature *339*, 597–603.

Sun, X., Gu, X.Q., and Haddad, G.G. (2003). Calcium influx via L- and N-type calcium channels activates a transient large-conductance Ca^{2+}-activated K^{+} current in mouse neocortical pyramidal neurons. J. Neurosci. Off. J. Soc. Neurosci. *23*, 3639–3648.

Surges, R., Sarvari, M., Steffens, M., and Els, T. (2006). Characterization of rebound depolarization in hippocampal neurons. Biochem. Biophys. Res. Commun. *348*, 1343–1349.

Taccola, G., and Nistri, A. (2005). Electrophysiological effects of 4-aminopyridine on fictive locomotor activity of the rat spinal cord in vitro. Acta Neurochir. Suppl. *93*, 151–154.

Tang, L.S., Goeritz, M.L., Caplan, J.S., Taylor, A.L., Fisek, M., and Marder, E. (2010). Precise Temperature Compensation of Phase in a Rhythmic Motor Pattern. PLOS Biol. *8*, e1000469.

Tarfa, R.A., Evans, R.C., and Khaliq, Z.M. (2017). Enhanced Sensitivity to Hyperpolarizing Inhibition in Mesoaccumbal Relative to Nigrostriatal Dopamine Neuron Subpopulations. J. Neurosci. *37*, 3311–3330.

Tegnér, J., Hellgren-Kotaleski, J., Lansner, A., and Grillner, S. (1997). Low-voltage-activated calcium channels in the lamprey locomotor network: simulation and experiment. J. Neurophysiol. *77*, 1795–1812.

Thoby-Brisson, M., Telgkamp, P., and Ramirez, J.M. (2000). The role of the hyperpolarization-activated current in modulating rhythmic activity in the isolated respiratory network of mice. J. Neurosci. Off. J. Soc. Neurosci. *20*, 2994–3005.

Tierney, A.J., and Harris-Warrick, R.M. (1992). Physiological role of the transient potassium current in the pyloric circuit of the lobster stomatogastric ganglion. J. Neurophysiol. *67*, 599–609.

Tikhonov, D.B., and Zhorov, B.S. (2009). Structural model for dihydropyridine binding to L-type calcium channels. J. Biol. Chem. *284*, 19006–19017.

Tschuluun, N., Hall, W.M., and Mulloney, B. (2001). Limb movements during locomotion: Tests of a model of an intersegmental coordinating circuit. J. Neurosci. Off. J. Soc. Neurosci. *21*, 7859–7869.

Tsuruyama, K., Hsiao, C.-F., and Chandler, S.H. (2013). Participation of a persistent sodium current and calcium-activated nonspecific cationic current to burst generation in trigeminal principal sensory neurons. J. Neurophysiol. *110*, 1903–1914.

Urbani, A., and Belluzzi, O. (2000). Riluzole inhibits the persistent sodium current in mammalian CNS neurons. Eur. J. Neurosci. *12*, 3567–3574.

Vassilev, P.M., Scheuer, T., and Catterall, W.A. (1988). Identification of an intracellular peptide segment involved in sodium channel inactivation. Science *241*, 1658–1661.

Vergara, C., Latorre, R., Marrion, N.V., and Adelman, J.P. (1998). Calcium-activated potassium channels. Curr. Opin. Neurobiol. *8*, 321–329.

Wallén, P., and Williams, T.L. (1984). Fictive locomotion in the lamprey spinal cord in vitro compared with swimming in the intact and spinal animal. J. Physiol. *347*, 225–239.

Wang, D., Grillner, S., and Wallén, P. (2011). 5-HT and dopamine modulates CaV1.3 calcium channels involved in postinhibitory rebound in the spinal network for locomotion in lamprey. J. Neurophysiol. *105*, 1212–1224.

Westenbroek, R. (2009). Ion Channel Localization in Cell Bodies and Dendrites. In Encyclopedia of Neuroscience, L.R. Squire, ed. (Oxford: Academic Press), pp. 221–228.

Wicher, D., Walther, C., and Wicher, C. (2001). Non-synaptic ion channels in insects--basic properties of currents and their modulation in neurons and skeletal muscles. Prog. Neurobiol. *64*, 431–525.

Wu, X., Liao, L., Liu, X., Luo, F., Yang, T., and Li, C. (2012). Is ZD7288 a selective blocker of hyperpolarization-activated cyclic nucleotide-gated channel currents? Channels *6*, 438–442.

Xu, W., and Lipscombe, D. (2001). Neuronal $Ca_V1.3alpha_1$ L-type channels activate at relatively hyperpolarized membrane potentials and are incompletely inhibited by dihydropyridines. J. Neurosci. Off. J. Soc. Neurosci. *21*, 5944–5951.

Xu, J., Yu, W., Jan, Y.N., Jan, L.Y., and Li, M. (1995). Assembly of voltage-gated potassium channels. Conserved hydrophilic motifs determine subfamily-specific interactions between the alpha-subunits. J. Biol. Chem. *270*, 24761–24768.

Yao, J.A., and Tseng, G.N. (1994). Modulation of 4-AP block of a mammalian A-type K channel clone by channel gating and membrane voltage. Biophys. J. *67*, 130–142.

Yuan, L.-L., and Chen, X. (2006). Diversity of potassium channels in neuronal dendrites. Prog. Neurobiol. *78*, 374–389.

Zhang, C., Guy, R.D., Mulloney, B., Zhang, Q., and Lewis, T.J. (2014). Neural mechanism of optimal limb coordination in crustacean swimming. Proc. Natl. Acad. Sci. *111*, 13840–13845.

Zheng, N., and Raman, I.M. (2011). Prolonged post-inhibitory rebound firing in the cerebellar nuclei mediated by group I mGluR potentiation of L-type Ca currents. J. Neurosci. Off. J. Soc. Neurosci. *31*, 10283–10292.

Acknowledgements

At this point I want to thank all people supporting me in so many ways during the years of my PhD. My special thanks goes to Dr. Carmen Smarandache-Wellmann, for giving me the opportunity to pursue my PhD in her lab, for her steady and unconditional support and the huge trust, giving me the freedom to plan and perform my experiments. I want to thank her especially for putting us always first, in moments in which there was neither time nor energy.

Furthermore I thank Prof. Dr. Ansgar Büschges for accepting to be my second referee and Prof. Dr. Sigrun Korsching to chair my defense.

I would also like to thank Prof. Dr. Ansgar Büschges and Prof. Dr. Silvia Daun for the inspiring input during the development of my thesis and the fruitful discussions on different approaches to solve pressing issue during the development of my project. Furthermore I want to thank Dr. Azamat Yeldesbay for his patience, new ideas and assistance in introducing me into mathematical modeling and its advantages in sciences.

I want to thank Heike for uncountable liters of crayfish ringer and my tiny yellow, orange, or red synaptic blockers. Anna for troubleshooting Matlab “BING” problems and for the lively discussion on any possible interpretation of experimental results (you have been missed in the last year).

I am furthermore grateful to Michael, Jan and Hans- Peter for the constant technical support.

Additionally my gratitude goes to all former and present members of the Wellmann- and Büschges lab, for creating a unique work experience. You have been much more than just colleagues.

I was honored to be accepted in the first cohort of the 2014 established research training group funded by the DFG (1960, RTG-NCA). Participating in in this program gave me the great opportunity to witness outstanding research and meet brilliant people, broadening my horizon on state of the art techniques and new discoveries in different research areas. Thereby I want to thank Dr. Isabell Witt, Kathy Joergens, and Dr. Katherina Vlantis for their frequent organizational help.

At last I want to thank my parents, my sister and especially Felix. Without your unconditional and loving support I probably wouldn’t have made it this far.

Eigenständigkeitserklärung

Ich versichere, dass ich die von mir vorgelegte Dissertation selbständig angefertigt, die benutzten Quellen und Hilfsmittel vollständig angegeben und die Stellen der Arbeit − einschließlich Tabellen, Karten und Abbildungen −, die anderen Werken im Wortlaut oder dem Sinn nach entnommen sind, in jedem Einzelfall als Entlehnung kenntlich gemacht habe; dass diese Dissertation noch keiner anderen Fakultät oder Universität zur Prüfung vorgelegen hat; dass sie − abgesehen von unten angegebenen Teilpublikationen − noch nicht veröffentlicht worden ist, sowie, dass ich eine solche Veröffentlichung vor Abschluss des Promotionsverfahrens nicht vornehmen werde. Die Bestimmungen der Promotionsordnung sind mir bekannt. Die von mir vorgelegte Dissertation ist von Dr. Carmen Wellmann betreut worden.

Köln, den 24.01.19